The Deep Space Network Progress Report 42-39

March and April 1977

National Aeronautics and Space Administration

Jet Propulsion Laboratory
California Institute of Technology
Pasadena, California 91103

The Deep Space Network Progress Report 42-39

March and April 1977

June 15, 1977

National Aeronautics and
Space Administration

Jet Propulsion Laboratory
California Institute of Technology
Pasadena, California 91103

Prepared Under Contract No NAS 7-100
National Aeronautics and Space Administration

Preface

Beginning with Volume XX, the Deep Space Network Progress Report changed from the Technical Report 32- series to the Progress Report 42- series. The volume number continues the sequence of the preceding issues. Thus, Progress Report 42-20 is the twentieth volume of the Deep Space Network series, and is an uninterrupted follow-on to Technical Report 32-1526, Volume XIX.

This report presents DSN progress in flight project support, tracking and data acquisition (TDA) research and technology, network engineering, hardware and software implementation, and operations. Each issue presents material in some, but not all, of the following categories in the order indicated.

Description of the DSN

Mission Support
- Ongoing Planetary/Interplanetary Flight Projects
- Advanced Flight Projects

Radio Science

Special Projects

Supporting Research and Technology
- Tracking and Ground-Based Navigation
- Communications–Spacecraft/Ground
- Station Control and Operations Technology
- Network Control and Data Processing

Network and Facility Engineering and Implementation
- Network
- Network Operations Control Center
- Ground Communications
- Deep Space Stations

Operations
- Network Operations
- Network Operations Control Center
- Ground Communications
- Deep Space Stations

Program Planning
- TDA Planning
- Quality Assurance

In each issue, the part entitled "Description of the DSN" describes the functions and facilities of the DSN and may report the current configuration of one of the five DSN systems (Tracking, Telemetry, Command, Monitor & Control, and Test & Training).

The work described in this report series is either performed or managed by the Tracking and Data Acquisition organization of JPL for NASA.

Contents

DESCRIPTION OF THE DSN

MISSION SUPPORT

Ongoing Planetary/Interplanetary Flight Projects

SUPPORTING RESEARCH AND TECHNOLOGY

Tracking and Ground-Based Navigation

Communications - Spacecraft/Ground

Station Control and Operations Technology

Network Control and Data Processing

NETWORK AND FACILITY ENGINEERING AND IMPLEMENTATION

Network

Ground Communications

Deep Space Stations

OPERATIONS

Network Operations

Network Functions and Facilities

N. A. Renzetti
Office of Tracking and Data Acquisition

The objectives, functions, and organization of the Deep Space Network are summarized; deep space station, ground communication, and network operations control capabilities are described.

The Deep Space Network (DSN), established by the National Aeronautics and Space Administration (NASA) Office of Tracking and Data Acquisition under the system management and technical direction of the Jet Propulsion Laboratory (JPL), is designed for two-way communications with unmanned spacecraft traveling approximately 16,000 km (10,000 miles) from Earth to the farthest planets of our solar system. It has provided tracking and data acquisition support for the following NASA deep space exploration projects Ranger, Surveyor, Mariner Venus 1962, Mariner Mars 1964, Mariner Venus 1967, Mariner Mars 1969, Mariner Mars 1971, and Mariner Venus Mercury 1973, for which JPL has been responsible for the project management, the development of the spacecraft, and the conduct of mission operations, Lunar Orbiter, for which the Langley Research Center carried out the project management, spacecraft development, and conduct of mission operations; Pioneer, for which Ames Research Center carried out the project management, spacecraft development, and conduct of mission operations; and Apollo, for which the Lyndon B. Johnson Space Center was the project center and the Deep Space Network supplemented the Manned Space Flight Network (MSFN), which was managed by the Goddard Space Flight Center (GSFC). It is providing tracking and data acquisition support for Helios, a joint U.S./West German project; and Viking, for which Langley Research Center provides the project management, the Lander spacecraft, and conducts mission operations, and for which JPL also provides the Orbiter spacecraft.

The Deep Space Network is one of two NASA networks. The other, the Spaceflight Tracking and Data Network, is under the system management and technical direction of the Goddard Space Flight Center. Its function is to support manned and unmanned Earth-orbiting satellites The Deep Space Network supports lunar, planetary, and interplanetary flight projects.

From its inception, NASA has had the objective of conducting scientific investigations throughout the solar sys-

tem. It was recognized that in order to meet this objective, significant supporting research and advanced technology development must be conducted in order to provide deep space telecommunications for science data return in a cost effective manner. Therefore, the Network is continually evolved to keep pace with the state of the art of telecommunications and data handling. It was also recognized early that close coordination would be needed between the requirements of the flight projects for data return and the capabilities needed in the Network. This close collaboration was effected by the appointment of a Tracking and Data Systems Manager as part of the flight project team from the initiation of the project to the end of the mission. By this process, requirements were identified early enough to provide funding and implementation in time for use by the flight project in its flight phase.

As of July 1972, NASA undertook a change in the interface between the Network and the flight projects. Prior to that time, since 1 January 1964, in addition to consisting of the Deep Space Stations and the Ground Communications Facility, the Network had also included the mission control and computing facilities and provided the equipment in the mission support areas for the conduct of mission operations. The latter facilities were housed in a building at JPL known as the Space Flight Operations Facility (SFOF). The interface change was to accommodate a hardware interface between the support of the network operations control functions and those of the mission control and computing functions. This resulted in the flight projects assuming the cognizance of the large general-purpose digital computers which were used for both network processing and mission data processing. They also assumed cognizance of all of the equipment in the flight operations facility for display and communications necessary for the conduct of mission operations. The Network then undertook the development of hardware and computer software necessary to do its network operations control and monitor functions in separate computers. This activity has been known as the Network Control System Implementation Project. A characteristic of the new interface is that the Network provides direct data flow to and from the stations; namely, metric data, science and engineering telemetry, and such network monitor data as are useful to the flight project. This is done via appropriate ground communication equipment to mission operations centers, wherever they may be.

The principal deliverables to the users of the Network are carried out by data system configurations as follows:

- The DSN Tracking System generates radio metric data; i.e., angles, one- and two-way doppler and range, and transmits raw data to Mission Control.
- The DSN Telemetry System receives, decodes, records, and retransmits engineering and scientific data generated in the spacecraft to Mission Control.
- The DSN Command System accepts coded signals from Mission Control via the Ground Communications Facility and transmits them to the spacecraft in order to initiate spacecraft functions in flight.

The data system configurations supporting testing, training, and network operations control functions are as follows:

- The DSN Monitor and Control System instruments, transmits, records, and displays those parameters of the DSN necessary to verify configuration and validate the Network. It provides operational direction and configuration control of the Network, and provides primary interface with flight project Mission Control personnel.
- The DSN Test and Training System generates and controls simulated data to support development, test, training and fault isolation within the DSN. It participates in mission simulation with flight projects.

The capabilities needed to carry out the above functions have evolved in three technical areas:

(1) The Deep Space Stations, which are distributed around Earth and which, prior to 1964, formed part of the Deep Space Instrumentation Facility. The technology involved in equipping these stations is strongly related to the state of the art of telecommunications and flight-ground design considerations, and is almost completely multimission in character.

(2) The Ground Communications Facility provides the capability required for the transmission, reception, and monitoring of Earth-based, point-to-point communications between the stations and the Network Operations Control Center at JPL, Pasadena, and to the mission operations centers, wherever they may be. Four communications disciplines are provided: teletype, voice, high-speed, and wideband. The Ground Communications Facility uses the capabilities provided by common carriers throughout the world, engineered into an integrated system by Goddard Space Flight Center, and controlled from the communications Center located in the Space Flight Operations Facility (Building 230) at JPL.

(3) The Network Operations Control Center is the functional entity for centralized operational control of the Network and interfaces with the users. It has two separable functional elements; namely, Network Operations Control and Network Data Processing. The functions of the Network Operations Control are:

- Control and coordination of Network support to meet commitments to Network users.
- Utilization of the Network data processing computing capability to generate all standards and limits required for Network operations.
- Utilization of Network data processing computing capability to analyze and validate the performance of all Network systems.

The personnel who carry out the above functions are located in the Space Flight Operations Facility, where mission operations functions are carried out by certain flight projects. Network personnel are directed by an Operations Control Chief. The functions of the Network Data Processing are:

- Processing of data used by Network Operations Control for control and analysis of the Network.
- Display in the Network Operations Control Area of data processed in the Network Data Processing Area.
- Interface with communications circuits for input to and output from the Network Data Processing Area.
- Data logging and production of the intermediate data records.

The personnel who carry out these functions are located approximately 200 meters from the Space Flight Operations Facility. The equipment consists of minicomputers for real-time data system monitoring, two XDS Sigma 5s, display, magnetic tape recorders, and appropriate interface equipment with the ground data communications.

D2

N78-15069

Viking Mission Support

D. W. H. Johnston
Deep Space Network Operations

This report covers the period 1 January through 28 February 1977 and includes the initial Viking Extended Mission period of DSN "normal" support, following the nonstandard operations during the Solar Conjunction period. The operational testing subsequent to the MK III Data System installations at DSS 12, 44, and 62 during this period is also discussed.

I. Viking Operation Activities

Several maneuvers have been carried out with both VO-1 and VO-2, resulting, at the end of February 1977, with VO-1 in a 23.5-hour orbit and a periapsis altitude of 300 km. This orbit causes the spacecraft to "walk" around Mars progressively and ending at its starting point every 25 days. The low periapsis altitude pictures are the closest ever taken but, although there are some clear areas, a large percentage of the pictures is degraded due to possible dust clouds in the southern hemisphere and the carbon dioxide polar hood in the northern hemisphere. VL-1, 22°N of the equator, is now experiencing temperatures on the Mars surface of about 178 K (-140°F).

VO-2 is in a synchronous orbit over VL-2 with a periapsis altitude of 800 km. VL-2, higher in the northern hemisphere (48°N), which is now in Mars winter, is experiencing outside temperatures of about 150 K (-190°F).

With minor exceptions the four spacecraft are functioning normally.

Both orbiters are experiencing daily occultations, i.e., the RF signal is being interrupted as the spacecraft passes behind Mars as viewed from Earth.

II. DSN Support for Viking

The statistics listing the DSN tracking and command support for Viking during this reporting period are shown in Tables 1 and 2.

The Discrepancy Report status for this period is summarized in Table 3.

III. MK III Data System (MDS) Capabilities

As mentioned in previous articles, the MDS implementation replaces the digital processing equipment at the DSSs with new equipment. At the 26-m stations, the total data processing capability, i.e., supporting a single spacecraft carrier and processing two telemetry channels, nominally a low rate <

33-1/3 bps and a medium rate < 2 kbps, remains unchanged, though either channel can now process from 8-1/3 bps up to 2 kbps. However, the 64-m station capability of processing three spacecraft carriers and six TLM channels simultaneously, i.e., two low, two medium, and two high < 16 kbps (see Fig. 1) will be reduced to nominally two spacecraft carriers with two low/medium channels and two high-rate channels (see Fig. 2).

However, although the telemetry from four subcarriers only can be processed in real time, the 64-m stations will still retain the original four receivers, so the third Viking spacecraft carrier can be recorded on analog tape and replayed and processed in near-real time if required.

IV. Network Operations Plan for Viking Extended Mission

Due to the fact that the MDS modifications will be progressively implemented at all DSN stations over a period of about 18 months, the Viking Extended Mission (VEM) will be supported by both modified and unmodified stations at any time up to May 1978.

As the MDS modifications change the hardware configurations, software programs, and operational procedures, a completely new Network Operations Plan (NOP) is required for the MDS stations. Therefore, the Viking NOP has been updated for use by the modified DSN stations. The unmodified stations are still using the original NOP to support the Viking Extended Mission.

V. MDS Testing

Testing after the MDS modifications to verify the station's capability to support the Viking Extended Mission followed a similar pattern to the prelaunch testing but on a reduced scale.

The stations affected during this reporting period were DSS 12, DSS 44, and DSS 62.

A. DSS 12

(1) System Performance Tests (SPTs)

Completed by 1 January 1977.

(2) Operational Verification Tests (OVTs)

(a) On 8 January 1977, OVT 1 experienced problems caused by known software anomalies and some equipment failures.

(b) On 12 January, OVT 2 met all test acceptance criteria and was considered successful.

(3) DSN-VMCCC System Integration Tests (SITs)

(a) On 14 January 1977, SIT 1 experienced hardware failures.

(b) On 24 January, SIT 2 was successfully completed.

(4) Demonstration Passes

Two demonstration passes were successfully carried out on live tracks of the Viking spacecraft. After the completion of the second pass on 31 January 1977, DSS 12 was placed in configuration control for Viking.

B. DSS 62

During February 1977, DSS 62 completed the OVT portion of the program successfully on schedule with a planned completion of the remainder of the tests in March.

C. DSS 44

The MDS implementation at DSS 44 was near completion at the end of February with the first OVT scheduled for 6 March 1977.

Table 1. VEM tracking support (1977)

DSS	January		February	
	Tracks	Hours	Tracks	Hours
11	23	135	22	142
12	4	11	1	6
14	52	341	59	392
42	21	247	25	226
43	68	721	62	627
44	0	0	0	0
61	35	261	29	227
62	0	0	2	7
63	38	327	28	202
Total	241	2043	228	1829

Table 2. VEM commands transmitted

DSS	January	February
11	1521	1394
12	0	0
14	769	1404
42	2072	953
43	919	2523
44	0	0
61	605	1116
62	0	0
63	795	472
Total	6681	7862

Table 3. DSN VEM discrepancy reports

DSS	January		February	
	Opened	Closed	Opened	Closed
11	4	0	3	4
12	4	0	0	0
14	14	2	11	19
42	0	1	2	3
43	10	13	11	10
44	0	0	0	0
61	1	9	1	6
62	0	0	0	8
63	1	4	7	3
Others*	4	3	3	9
Total	38	32	38	62

*Others = DSN, Network Data Processing Area, Network Operations Control Area

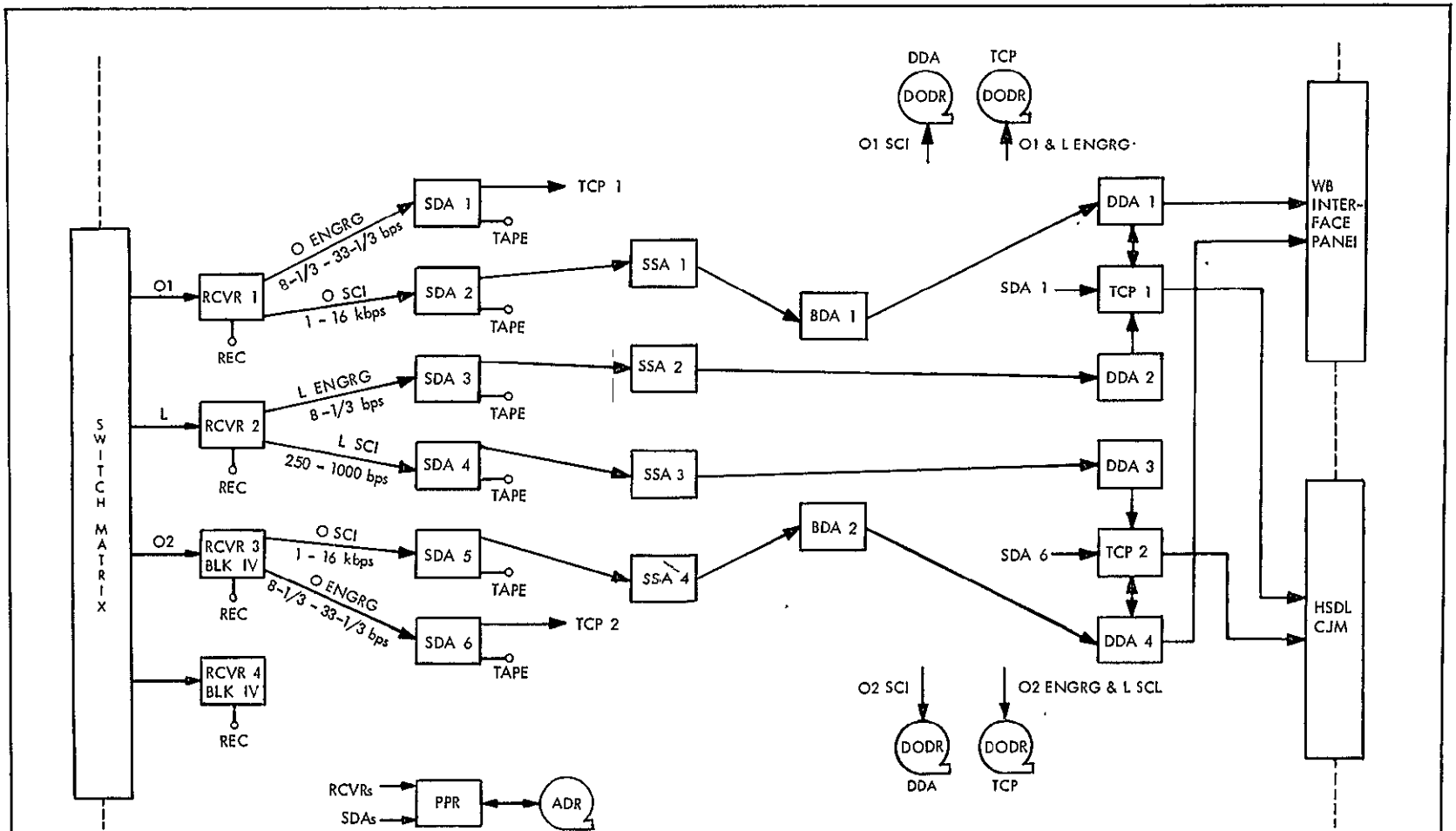

SPACECRAFT	RECEIVER	DATA TYPE	SDA	SSA	BDA	DDA	TCP
ORBITER 1	1	ENGRG	1	0	0	0	1
		SCI	2	1	1	1	
LANDER	2	ENGRG	3	2	0	2	
		SCI	4	3	0	3	2
ORBITER 2	3	SCI	5	4	2	4	
		ENGRG	6	0	0	0	

Fig. 1. Standard planetary configuration, Orbiter-Lander-Orbiter (Code 30)

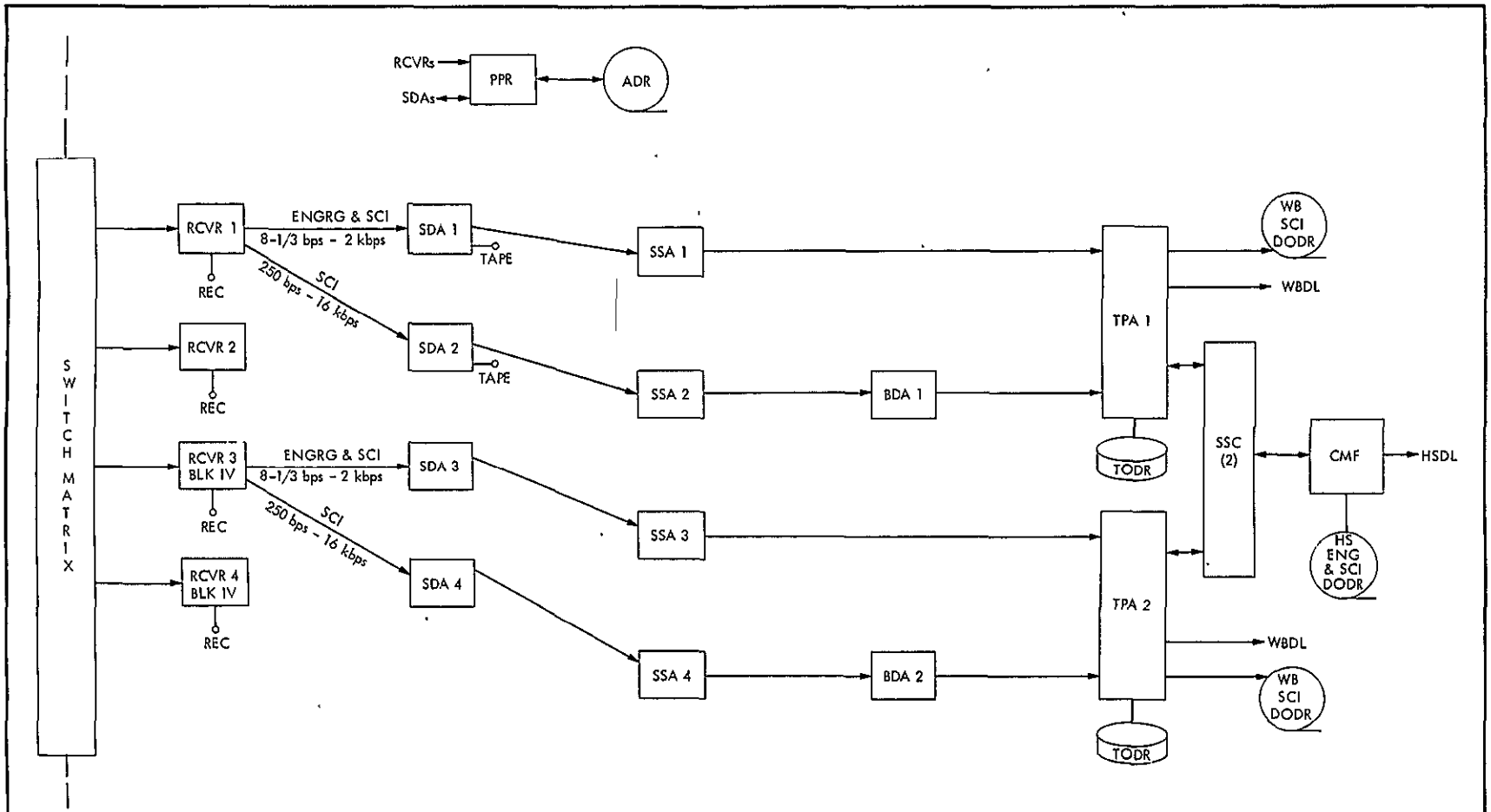

SPACECRAFT	RECEIVER	DATA TYPE	SDA	SSA	BDA	TPA
1	1	ENGRG & SCI	1	1	0	1
		SCI	2	2	1	1
2	3	ENGRG & SCI	3	3	0	2
		SCI	4	4	2	2

Fig. 2. Standard VEM two spacecraft configuration (Code 1)

D3

N78-15070

Pioneer Mission Support

T. P. Adamski

Deep Space Network Operations

This article reports on activities within the Deep Space Network in support of the Pioneer Project's in-flight spacecraft during the period December 1976 through March 1977. The amount of tracking coverage provided by the Network and a summary of operational testing of the Mark III Data Subsystems are presented.

I. Pioneers 6, 7, 8, and 9

Coverage of these spacecraft has continued at minimal levels. During the period December 1976 through March 1977, Pioneers 6 and 9 were each tracked once whereas Pioneer 7 was tracked four times. Total tracking coverage times appear in Table 1.

Tracking of Pioneer 7 was performed in support of an opportunity for the spacecraft to observe the geomagnetic tail. Data obtained early in the Pioneer missions indicated that the position of the geomagnetic tail varies considerably due to interaction with the solar wind. It was anticipated that Pioneer 7 might observe the tail as the Earth passed between the Sun and the spacecraft. However, no net change in flux was observed, indicating that the spacecraft probably did not enter the tail. Figure 1 illustrates the geometry of the event.

II. Pioneers 10 and 11

A. Mission Operations and Status

Pioneer 10 continues to operate satisfactorily. The spacecraft is now more than 13 astronomical units (AU) from the Earth and the round trip light time is over 3 hours 45 minutes. Tracking coverage has decreased from the levels reported earlier (Ref. 1), due primarily to the extreme spacecraft range that requires coverage by the 64-meter stations. Tracking times for the last four months are listed in Table 1. Figure 2 presents a histogram of Pioneer 10 coverage for the last twelve months.

Pioneer 11 is also operating satisfactorily. The distance to the spacecraft is now more than 5 AU and the round trip light time is over 1 hour 25 minutes. Tracking coverage is shown in Table 1 and Fig. 3.

The use of thruster pair No. 2 on Pioneer 11 has been discontinued due to the development of a serious leak in the valve seals. This thruster pair had been used since last October, when a leak was detected in pair No. 1. The leak rate from pair No. 1 has decreased since then and the Project has lengthened the thruster pulse duration from one-eighth to one second to decrease the number of valve actuations required. The velocity change resulting from the use of pair No. 1 has not yet been explained, but the effect will be used to perform a trajectory correction maneuver without using the ΔV thrusters. It has been determined that the use of thruster pair No. 1 in accomplishing precession maneuvers will, by the end of 1977, provide a sufficient ΔV to refine the spacecraft targeting for Saturn encounter.

B. Mark III Data Subsystems Support of Pioneer

Since the previous report (Ref. 1), Mark III Data System (MDS) verification testing for Pioneers 10 and 11 has been completed at DSSs 12, 44, and 62. Configuration control for Pioneer was established on 26 January for DSS 12, 1 March for DSS 62, and on 22 March for DSS 44. Table 2 is a listing of the demonstration passes that were performed by these stations and a summary of the problems encountered. All major anomalies have been cleared by the issuance and successful demonstration of either updated software or hardware changes.

Future updates to the command and telemetry programs will enable the MDS-equipped stations to support the Pioneer 6, 7, 8, and 9 missions. A series of demonstration passes will be conducted with the stations when these programs are completed and released to operations.

DSS 14 is currently undergoing upgrading to a MDS configuration. Verification testing of this station for Pioneer support will follow the same pattern of demonstration passes as was used for DSSs 12, 44, and 62. A future article will report on this testing.

Reference

Adamski, T.P., "Pioneer Mission Support," in *The Deep Space Network Progress Report 42-37*, pp. 35–38, Jet Propulsion Laboratory, Pasadena, Calif., February 15, 1977.

Table 1. Pioneer tracking coverage

Month	Spacecraft	Station type	Tracks	Tracking time, h:m
December	Pioneer 10	26-meter	7	47:31
		64-meter	34	231 14
	Pioneer 11	26-meter	70	513.48
		64-meter	1	2:53
January	Pioneer 10	26-meter	1	2:00
		64-meter	40	328:53
	Pioneer 11	26-meter	66	518:46
		64-meter	4	23.54
February	Pioneer 6	26-meter	1	5:45
	Pioneer 7	26-meter	4	42 34
	Pioneer 9	26-meter	1	3:56
	Pioneer 10	26-meter	2	11.39
		64-meter	29	194·41
	Pioneer 11	26-meter	39	301:34
		64-meter	7	45:06
March	Pioneer 10	26-meter	1	2:52
		64-meter	33	187:41
	Pioneer 11	26-meter	68	521:04
		64-meter	4	23:54

Table 2. Pioneer MDS demonstration pass summary

Date	DSS	Duration (h.m)	Spacecraft		Anomalies
12/28/76	12	6:28	11	(1)	Unable to either receive text predicts at DIS or transfer binary predicts to MDA. No DIS/SSC interface
				(2)	Unable to access CPA for command data transfer. Suspected comm buffer interface or SSC problem
				(3)	Unable to output radio metric data until MDA was reloaded
				(4)	Transmitter failed twice. Bad thermal switch on klystron magnet
				(5)	DIS failed due to blown fuse in memory +25 volt power supply
				(6)	Unable to process radio metric data at NOCC. Procedural error (required software patches had not been made)
				(7)	Lost all output twice due to nondirected reconfigurations of the star switch map
1/3/77	12	5:52	11	(1)	Unable to establish interface between CMF 1 and comm buffer 1 with program DMH-5115-OP-A until (required) patches per ECO 76.249 were deleted
				(2)	Transmitter failed due to insufficient magnet coolant flow
				(3)	Unable to process radio metric data at NOCC. Procedural error (required software patches had not been made)
				(4)	A manual command remained in the command stack after it was confirmed. Procedural error (command had been promoted from the manual buffer twice)
				(5)	TPA failed when receivers dropped lock at two-way acquisition
				(6)	Telemetry time errors following bit rate change. Procedural error due to incorrect documentation
1/13/77	12	2:37	10	(1)	Test terminated early due to severe timing problems on-site
1/21/77	12	5:53	11	(1)	Lost output due to nondirected reconfiguration of the star switch map
				(2)	TPA 2 failed. Stopped processing and did not go into TODR mode (which was enabled)
				(3)	DIS stopped updating, apparently due to bad DIS/SSC interface
				(4)	Unable to restrict telemetry recalls to a single UDT. Procedural error with program initialization
				(5)	Signal level in error by 4 dB due to bad calibration curve
1/26/77	12	5:26	11	(1)	TPA 2 failed three times during the pass
2/2/77	62	7:02	11	(1)	DIS failed after losing interface with TPA 1. Program reloaded
				(2)	Lost all output due to nondirected reconfiguration of star switch map
				(3)	CMF 1 failed, displaying an indeterminable timing error
				(4)	TPA 1 failed. Possible problem with TODR operation

Table 2. (contd)

Date	DSS	Duration (h:m)	Spacecraft		Anomalies
2/5/77	62	6:36	11	(1)	Nondirected reconfiguration of star switch map
				(2)	CMF 1 failed twice. Program reloaded each time
2/6/77	62	8:47	11	(1)	Unable to complete command checkout due to loop-back of HSDL at some unknown location
				(2)	CMF 1 failed twice. Program reloaded each time
				(3)	Both CPAs aborted commands due to data quality alarms. Reconfigured to short-loop (CMA internal) confirmation
2/9/77	62	9:34	11	(1)	Lost output due to nondirected reconfiguration of star switch map
				(2)	Observed erroneous antenna mode status in monitor data. Known software problem
2/15/77	62	12:19	11	(1)	Procedural error in entering manual command (command entered in wrong CMA mode)
				(2)	Lost ten minutes of DODR due to rewind after write errors and no switching to backup transport
2/16/77	62	9:00	11	(1)	Nondirected reconfiguration of star switch map
3/4/77	44	6:31	11	(1)	Lost CMF/comm buffer interface during data transfer
				(2)	DIS incorrectly indicating antenna mode and angle data type. Known software anomaly
				(3)	Unable to initiate or terminate CONSCAN AGC data via DIS CRT keyboard. Entries accepted via DIS local I/O
				(4)	TPA 2 unable to lock to 64 bps coded data due to unstable SSA lock
				(5)	CMF stopped logging a DODR due to no fresh tape available after attempted tape switch
3/8/77	44	4:17	11	(1)	MDA halted due to failure of TermiNet I/O device
				(2)	DIS incorrectly flagging antenna mode and angle data type. Known software anomaly
3/12/77	44	6:15	11	None	
3/17/77	44	3:30	11	None	
3/20/77	44	6:20	11	None	

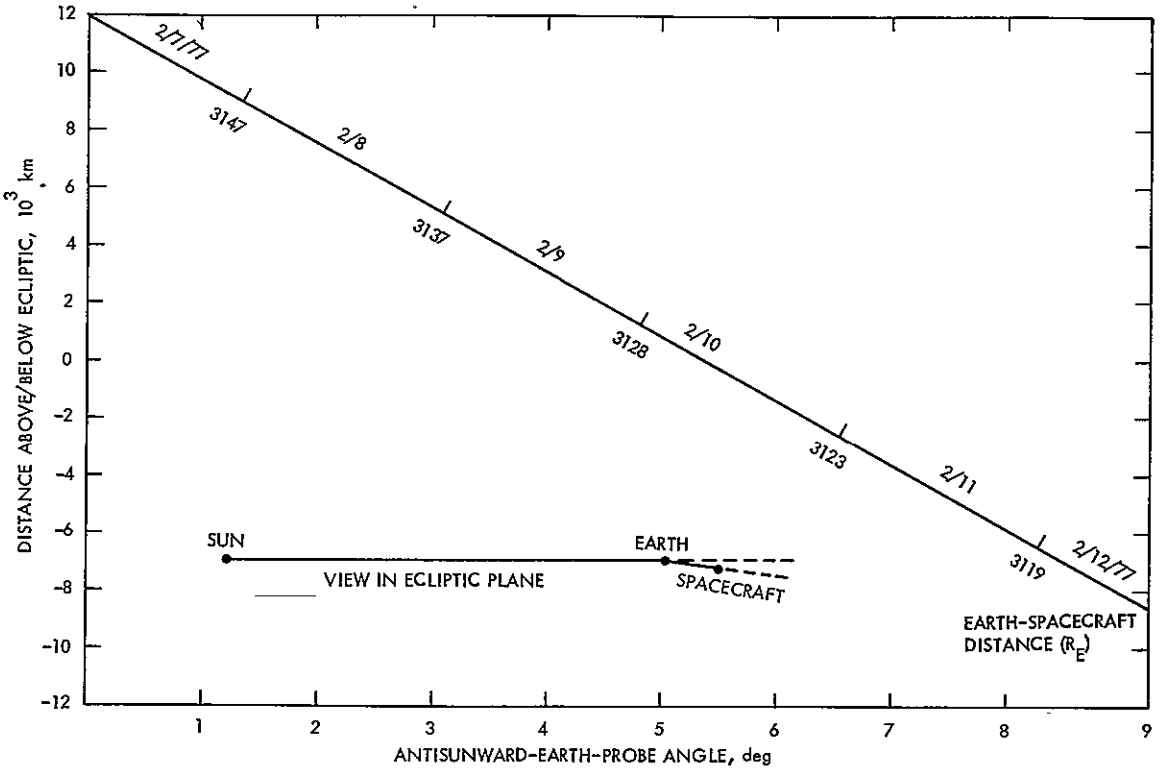

Fig. 1. Pioneer 7 trajectory

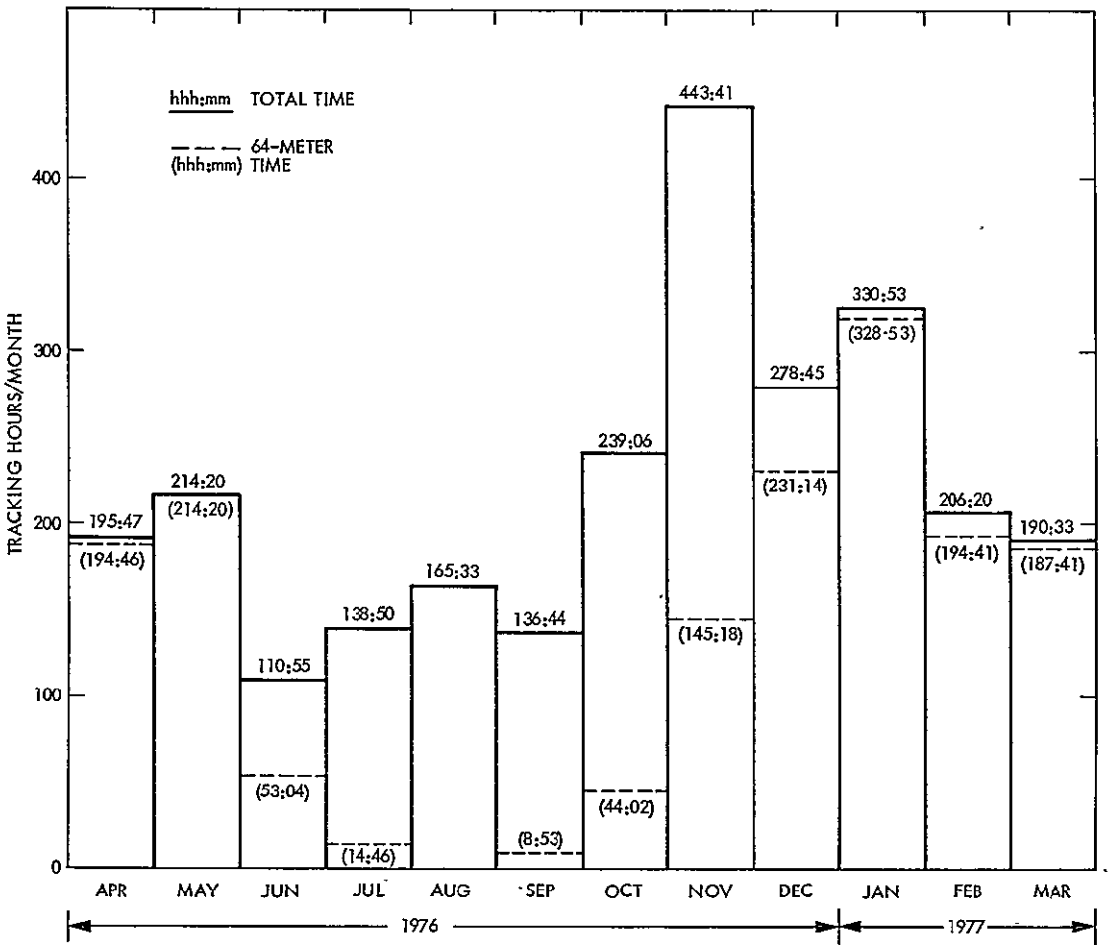

Fig. 2. Pioneer 10 tracking times

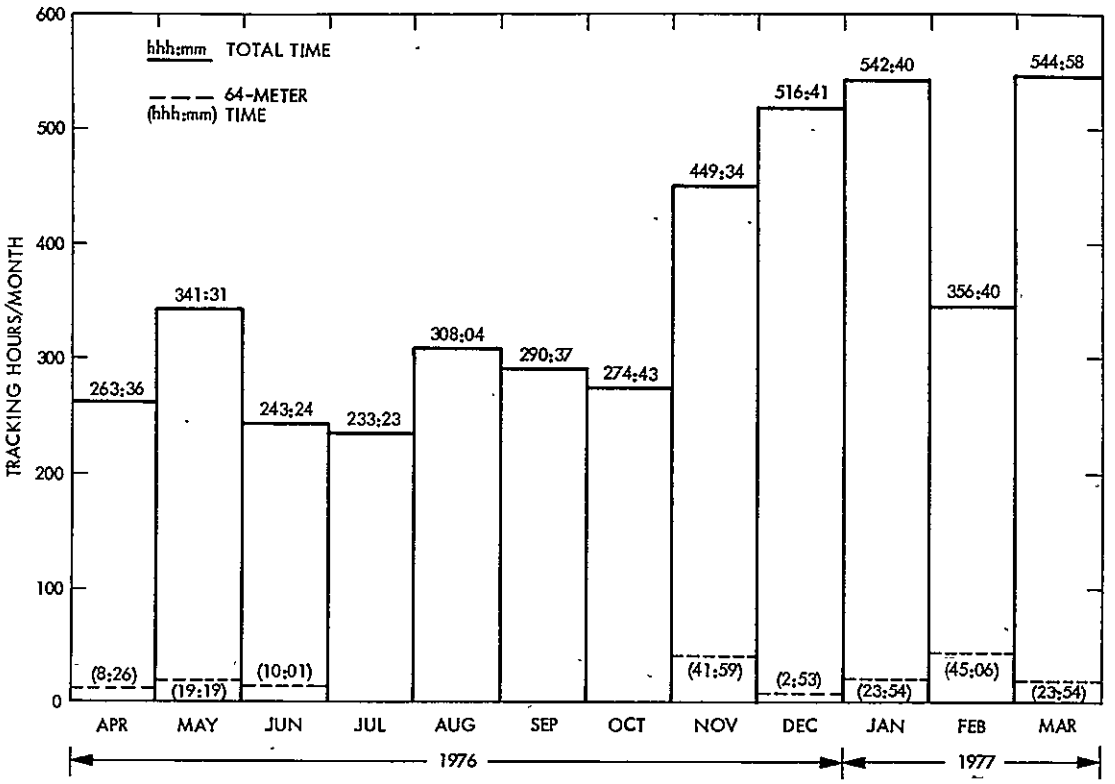

Fig. 3. Pioneer 11 tracking times

Helios Mission Support

P. S. Goodwin
TDA Mission Support

E. S. Burke and G. M. Rockwell
Deep Space Network Operations

This article reports on activities of the Network Operations organization in support of the Helios Project from 1 February 1977 through 15 April 1977.

I. Introduction

This article is the fifteenth in a continuing series of reports that discuss Deep Space Network support of Helios Mission operations. Included in this article is information concerning the inferior solar conjunction periods, demonstration tracks following Mark III Data System implementation, the STDN-DSN telemetry and command cross-support operations, and other mission-oriented activities.

II. Mission Operations and Status

Helios-1 entered a period of inferior solar conjunction from 30 March 1977 until 9 April 1977. The spacecraft entered a grayout period over DSS 42 (Canberra, Australia) on 2 April at a Sun-Earth-Probe (SEP) angle of 0.7734 degrees, and exited over DSS 63 (Madrid, Spain) on 3 April at a SEP angle of 0.4049 degrees. During the grayout the spacecraft was covered by a core memory read-in using format 3, data mode 4, and a bit rate of 8 bits per second (b/s) coded. Following the grayout a spacecraft emergency was declared on 3 April over DSS 14 (Goldstone, California). Apparently a regulator switch onboard put the spacecraft into an undefined (silent) configuration. As a result DSS 14 lost the downlink. The spacecraft was then commanded to reconfigure to the noncoherent mode, Driver 1, and TWT2 to medium power. DSS 14 then reacquired the downlink carrier and subcarrier, but no telemetry data was present. The spacecraft was then commanded to generate 1024 b/s coded and soon the station's telemetry string acquired lock. All experiments were checked and all were functioning properly. From the data received no anomaly was found and it was assumed that a signal spike caused the regulator switch to react as it did. No similar problem has occurred since.

The last major event for Helios-1 during this period occurred on 13 April 1977. On that day the Helios-1 spacecraft passed through its fifth perihelion. At that time the spacecraft was traveling at a velocity of 66.0456 kilometers per second, at a distance of 128 million kilometers from Earth and 46 million kilometers from the Sun. The round-trip light time at that time was 14 minutes and 2.7 seconds. The coverage for this event was provided by DSS 44 (Australia) with a downlink bit rate of 256 b/s. The spacecraft was configured in Format 2 with shock data read in data mode 3, which was triggered by experiment 5. All subsystems and experiments functioned normally.

Helios-2 continues to perform normally minus the use of its receiver 1 (Ref. 1), which is inoperative. Helios-2 entered its period of inferior solar conjunction on 29 March 1977 and ran

until 11 April 1977. The spacecraft entered its grayout period over DSS 12 (Goldstone, California) on 3 April at a Sun-Earth-probe angle of 0.7148 degrees, and exited over DSS 63 on 4 April at a Sun-Earth-probe angle of 0.3534 degrees. As with Helios-1, Helios-2's grayout was covered by a core memory read in, Format 3, data mode 4, and a bit rate of 8 b/s coded.

The next significant event for Helios-2 will be its third perihelion, scheduled to occur on 23 April 1977. The results of this event will be incorporated in the next article of this series.

Total DSN coverage for this period for both Helios-1 and -2 is recorded in Table 1. The coverage is shown for both 26-meter and 64-meter networks.

III. Special Activities

A. Mark III Data System (MDS) Support of Helios

Demonstration tracks were conducted during this period with DSS 63 (Spain) and DSS 44 (Australia). The MDS performance has been greatly improved over what was reported in the previous article (Ref. 1). Personnel at both stations displayed a good understanding of MDS operations, and operator errors were at a minimum. The system problems reported earlier have since been corrected with only a few exceptions. Of these, the most bothersome to operations was the continuing unreliability of the Communications and Monitor Formatter (CMF). To find solutions to CMF problems, a special procedure has been initiated within the DSN to analyze and hopefully find permanent solutions to improve the reliability of the CMF. The progress of this procedure will be documented in future articles.

Following a successful series of demonstration tracks at DSS 62 and DSS 44, both stations were placed under configuration control for support of Helios flight operations.

This was accomplished for DSS 62 on 1 March 1977 and for DSS 44 on 22 March 1977. Both stations have provided excellent support since those dates.

The next station to be reconfigured to the MDS will be DSS 14 at Goldstone, California. DSS 14 will be the first 64-meter antenna station to undergo modification. The station will cease operations on 16 April 1977 and is scheduled to return on 15 June 1977 fully implemented in the MDS configuration for the test and training phase. The status of DSS 14's progress will be reported in future articles.

B. STDN-DSN Cross-Support

On 1 March 1977 the STDN-DSN cross-support was activated to support Helios operations. On that date a demonstration track was conducted using the STDN station at Goldstone, California, and DSS 12 at Goldstone. In this particular pass Helios-2 (spacecraft 91) was tracked by STDN's antenna. The resultant downlink was microwaved to DSS 14, which in turn microwaved the signal to DSS 12. At DSS 12 the signal was processed through the station's back-up telemetry string and the data were transmitted to JPL and Germany via high-speed data line. Commanding was accomplished in the reversed order. During the cross-support period the DSS 12 was tracking another spacecraft with its own antenna and processing this data on its prime telemetry and command system. This overall configuration is shown in Fig. 1. During this first track the main problem encountered was the initial poor signal quality being received at DSS 12 from STDN. After a period of system troubleshooting it was found that the receiver STDN was using was not functioning properly. Having four multifunction receivers available, each one was brought into operation until the most efficient was found. After that was accomplished DSS 12 established a solid lock on the STDN data and the track proceeded without incident. This first track was used primarily for feeling the system out and matching equipment to optimize the data quality and system performance. On 4 March 1977 the same activity was performed using DSS 11 and, except for a few minor operator errors, the system functioned well. Both demonstration tracks were considered successful and the system functional.

Since these initial tracks, the STDN-DSN cross-support has been utilized on a regular basis over Goldstone for Helios support. The configurations used at DSS 11, DSS 12, and STDN are depicted in Fig. 2, 3, and 4, respectively.

Thus far the performance has been the same as was experienced during the first cross-support period which ended on 15 November 1976. As reported in a previous article (Ref. 2) the signal-to-noise ratio from STDN was approximately 4 db below that of a 26-meter DSN station, the reason being a higher system temperature and a lower receiver sensitivity at the STDN site. Table 2 shows a summary comparison between STDN and the DSN, of downlink AGC and SNR residuals for this period of STDN/DSN cross-support.

References

1. Goodwin, P. S., Burke, E. S., and Rockwell, G. M., "Helios Mission Support," in *The Deep Space Network Progress Report 42-38*, pp. 50–54, Jet Propulsion Laboratory, Pasadena, California, April 15, 1977.

2. Goodwin, P. S., Burke, E. S., and Rockwell, G. M., "Helios Mission Support," in *The Deep Space Network Progress Report 42-37*, pp. 39–42, Jet Propulsion Laboratory, Pasadena, California, February 15, 1977.

Table 1. Helios tracking coverage

Month	Spacecraft	Station type	Number of tracks	Tracking time, h, min
February	Helios-1	26 meter	30	211:49
		64 meter	0	0
	Helios-2	26 meter	52	291:04
		64 meter	1	5:00
March	Helios-1	26 meter	51	376:23
		64 meter	6	37:04
	Helios-2	26 meter	90	502:04
		64 meter	1	14:47

Table 2. Comparison of STDN and DSN downlink performance (1 March through 21 April 1977)

Spacecraft	STDN	Standard deviation	Sample size	DSSs 11, 12, 14	Standard deviation	Sample size
Helios-1						
AGC Residual	−1.9	NA	1	+0.4	1.0	60
SNR Residual	NA due to maser problem	NA	NA	+0.4	0.9	48
Helios-2						
AGC Residual	−3.2	3.0	20	−0.9	0 7	38
SNR Residual	−0.2	2.4	21	−1.1	0.8	37

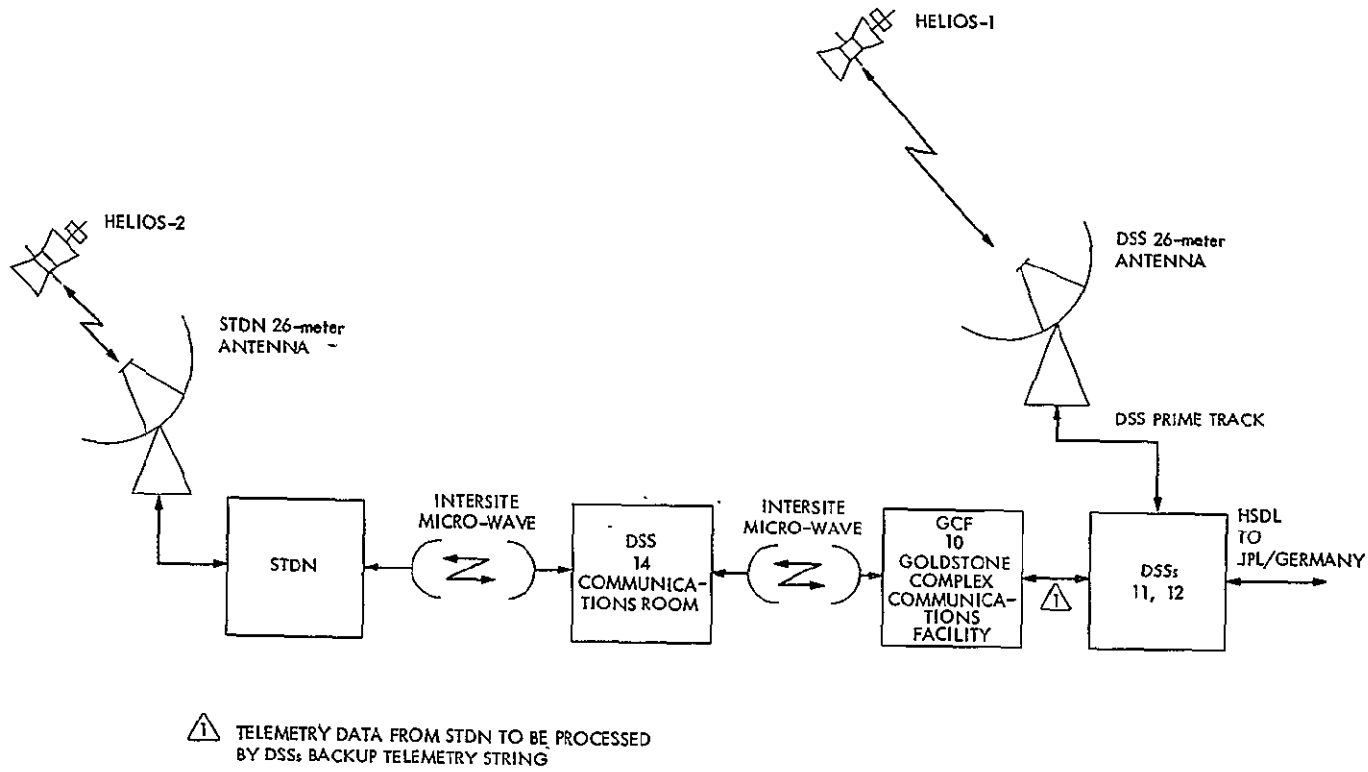

Fig. 1. Goldstone STDN-DSN cross-support configuration

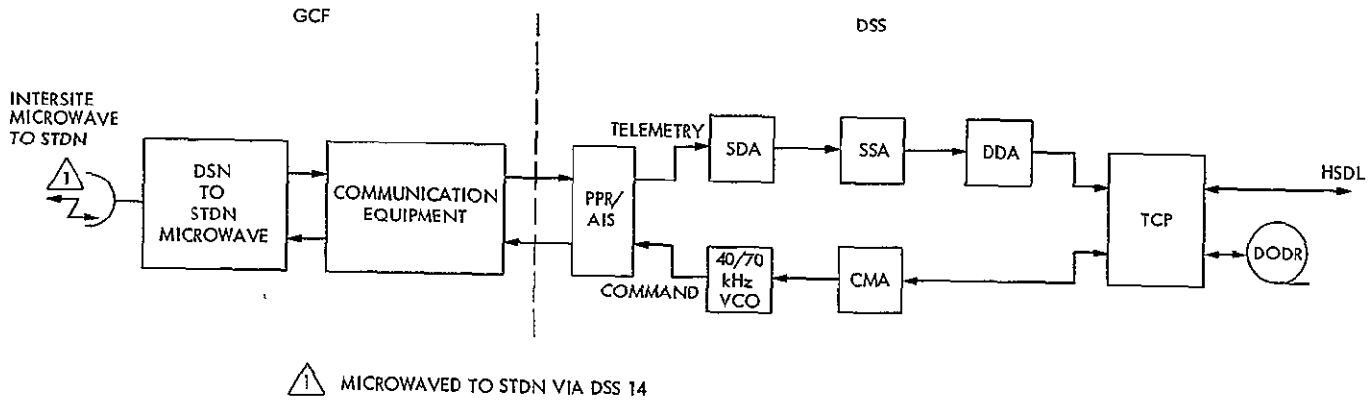

Fig. 2. DSN DSS 11 cross-support configuration

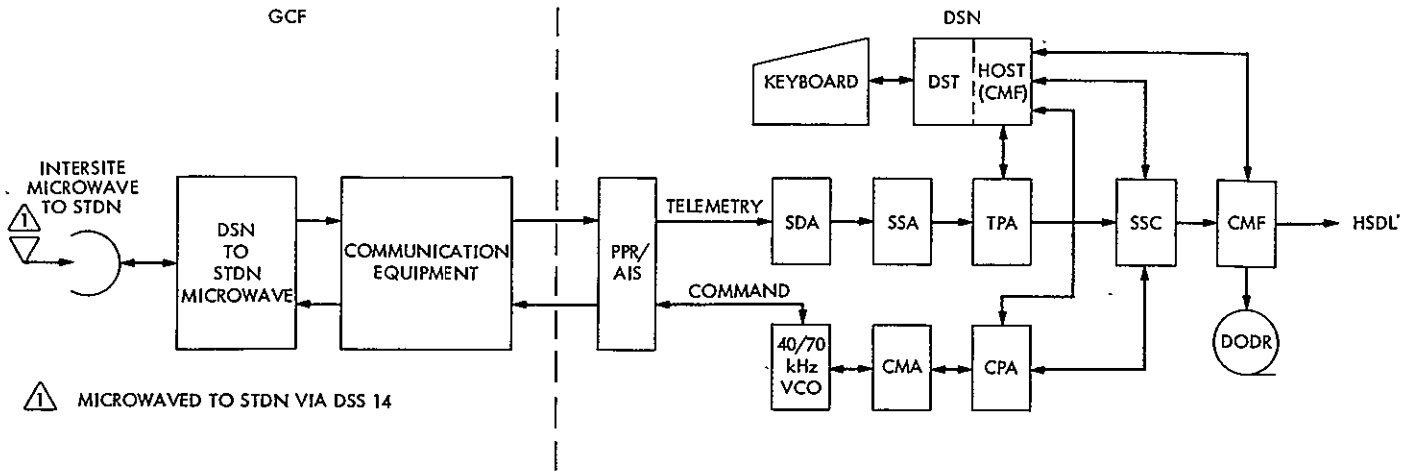

Fig. 3. DSN DSS 12 Helios cross-support configuration

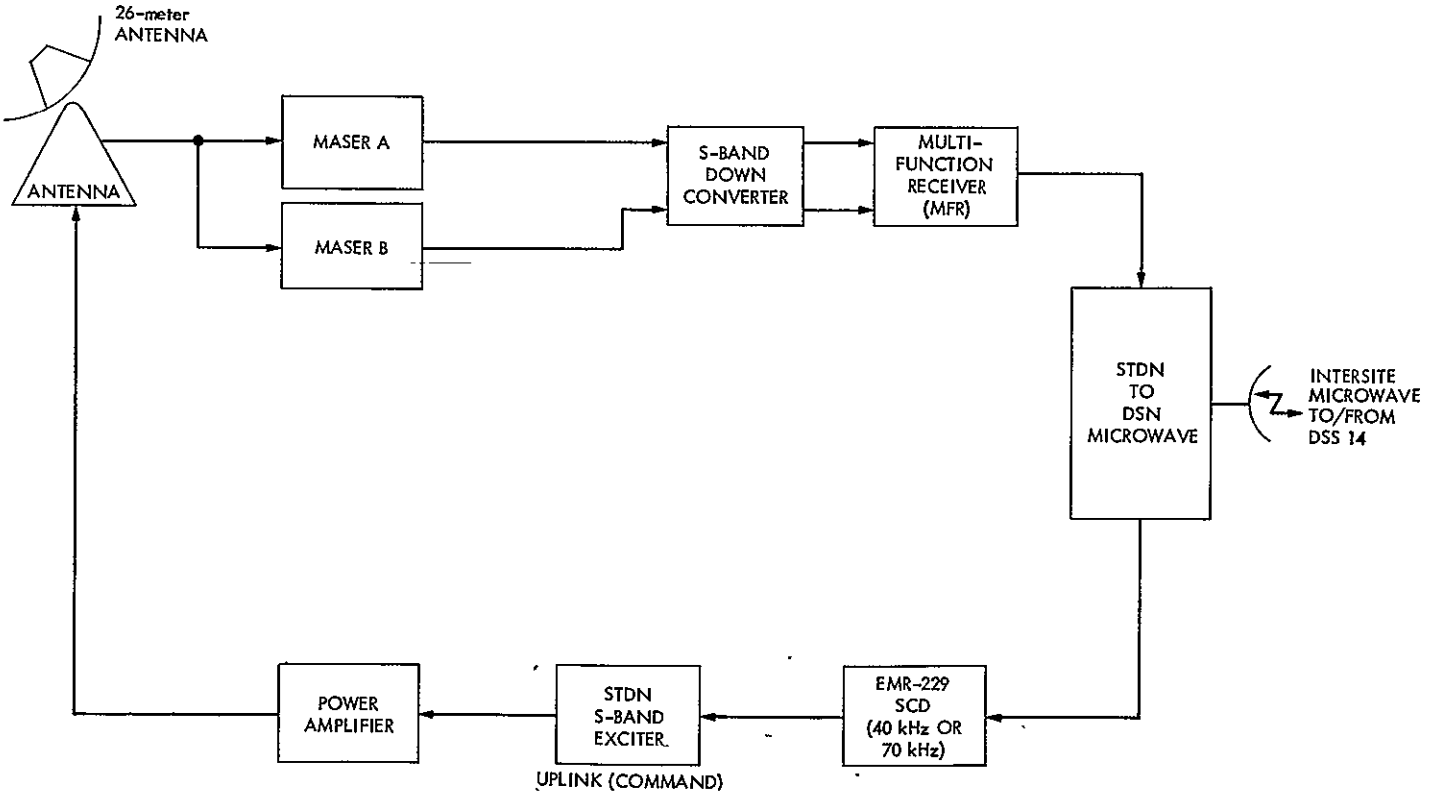

Fig. 4. STDN Helios cross-support configuration

D5

N78-15072

A Preliminary Analysis of Viking S-X Doppler Data and Comparison to Results of Mariner 6, 7, and 9 DRVID Measurements of the Solar Wind Turbulence

P. S. Callahan
Tracking Systems and Applications Section

More than 135 passes of Viking S-X doppler data have been used to investigate the solar wind turbulence from 3 August to 15 December 1976. The results of this analysis are compared to previous investigations using Mariner DRVID data to attempt to find the changes in the turbulence over the sunspot cycle. It is found that: (1) electron density fluctuations decline with heliocentric distance as $r^{-1.8\pm0.2}$; (2) the level of the turbulence may be a factor 2 lower near sunspot minimum than at maximum; and (3) the spectrum of the fluctuations may be steeper (~ -3.0 vs ~ -2.6) near sunspot minimum. The expected range error for various time scales and geometries is derived from the results.

I. Introduction

Critical Voyager pre-encounter correction maneuvers will occur at small SEP angles in 1981. Because 1981 is very near the peak of the sunspot cycle (SSC) which is now beginning, there is concern that the solar wind (SW) plasma and/or its fluctuations will interfere with the stringent radio metric accuracies required. In order to investigate changes over the SSC, columnar content data from Viking have been processed in the same way as DRVID data from Mariners 1969 and 1971 (Ref. 1) obtained near the peak of the past SSC.

This is a preliminary report of that investigation. Only 15 passes of Viking data from after superior conjunction (~27 November 1976) have been processed. The long passes available from tying together doppler passes or using S-X range data to set an absolute scale have not been exploited. Furthermore, only limited comparisons to other SW or solar surface data have been made. A predictive model of radio metric data quality would be likely to emerge from such analysis. Viking data continue to be collected, and there is now a span of post-conjunction data equal to the preconjunction data investigated here. The longer time base and more complete radial (heliocentric) coverage will allow better estimates of the radial dependence and the SSC modulation of the SW turbulence.

The data coverage for this analysis is described in Section II. The analysis techniques are outlined in Section III. Section IV gives the results and discusses the implications for radio metric data.

II. Data Coverage

The data coverage for this analysis is shown in Table 1. Data from 23 September to 17 October 1976 exist but were not included because of lack of time. The second column gives the number of passes (from various 64-meter stations) included in each grouping.

All of the passes used in this analysis were at least 5 hours long and contained at least 275 points. Thus, some gaps were allowed, but none exceeding 1 hour. Most of the data were 1-minute samples, but stretches of 10-second data occur in some passes. The net average sample spacings ranged from about 55 to 65 seconds. Individual passes lasted up to 12 hours. Near and after conjunction 10-second (and even some 1 second) data were obtained in large amounts. Ten-second data from 8 to 15 December 1976 have been included in this analysis by averaging the data to 30-second sample times and then treating the data to give the same spectral resolution as the 60-second passes. The 10-second data have also been examined by themselves and show that the power spectrum continues smoothly to higher frequencies.

The coverage of one or both spacecraft is often continuous. When the doppler data overlap (or nearly), it is possible to continue the record by continuing to add the change in columnar content at each step. Records up to 32 hours (typically 15-20 hours) have been constructed in this way. The spectra from these longer records have not yet been averaged in the same way as the results presented here but will be presented in a future report.

III. Data Analysis

In order to investigate the columnar content changes under a wide range of conditions, it is necessary to have an objective measure of these changes. The power spectra of the data provide such a measure. The spectra give the mean squared fluctuation per unit frequency interval in a range of frequencies. Thus, given the power density at some frequency, $P_{\Delta I}(\nu)$, the expected change in the columnar content on a time scale $t_1 = 1/\nu$ is

$$\Delta I(t_1) \cong (P_{\Delta I}(\nu) * \nu)^{1/2} \qquad (1)$$

where for rapidly falling spectra at low frequencies we have approximated the frequency interval $\Delta\nu$ (spectral resolution) by ν.

The frequencies over which one can obtain reliable estimates of the spectrum from discretely sampled records of limited length are $1/2\,\Delta t \geqslant \nu \gtrsim 5/T$, where Δt is the sample rate, and T is the length of the record. For most of the data used here $1 \times 10^{-4}\text{Hz} \lesssim \nu \lesssim 1 \times 10^{-2}$ Hz, corresponding to time scales of 2 minutes $\lesssim t_1 \lesssim 2$ hours. The longer records produced by tying passes together permit the investigation of time scales of up to 3-6 hours, while 10-second data extend the time scale down to 20 seconds ($\nu = 5 \times 10^{-2}$ Hz).

For some purposes, near-simultaneous ranging or the error of making a downlink-only measurement, the change of the columnar content on various time scales is of most interest. In other cases, two-station tracking or tracking of two separated spacecraft, the change of the SW density on various scale sizes is more important. The latter can be obtained from the former if the SW velocity is known. A typical SW velocity is 350-450 $\text{km}\cdot\text{s}^{-1}$. Since our data have no direct measurement of the velocity, scale sizes inferred using 400 $\text{km}\cdot\text{s}^{-1}$ could be in error by up to 50 percent. The results here are in terms of frequency.

The results below were obtained through the following steps:

(1) The columnar content change records from each pass where autocorrelated to 60 lags (~1 hour). The 10-second data were summed to ~30-second intervals and autocorrelated to 80 lags (~45 minutes).

(2) The cosine transform of the autocorrelation, smoothed with the Hanning window, was used to give the power spectrum.

(3) The individual power spectra were averaged in groups of 6 to 12. The data were grouped by the distance of the ray path's closest approach to the sun, Q. The lowest value of all the averaged points was subtracted to remove the noise.

(4) The slopes of the averaged spectra were obtained by hand. A number of estimates were made for each spectrum to determine the possible range. It is typically ±0.2.

The Viking S-X data and the Mariner DRVID were all treated in the same way except that the maximum lag for the DRVID data was ~45 minutes. None of the data have been corrected for the change in ionospheric columnar content. This change is generally $\lesssim 1.5$ meters over a pass and so is much less ($\lesssim 10$ percent) than the observed changes, except for some passes in August and September. Neglect of this correction is not thought to significantly affect any of the results.

In addition to the power spectrum analysis, the individual and long records were examined for rms variation about the

mean, peak-to-peak change, maximum rate of change, and character (slope, single or multiple "humps," and time scale of significant change) of the change. The former indices are all closely related to the power spectrum. The latter observation allows some investigation of changes on longer time scales than can be done formally with the power spectrum.

IV. Results and Discussion

From the general character of the columnar content changes, especially those seen on the long (tied) passes, one can see that the power spectra extend to low enough frequencies to pick up most of the important changes. Occasionally, there are slopes or "humps" with time scales of 8-12 hours, but these occur only about once per month. Thus, the data from the power spectra provide a fairly complete and realistic description of the columnar content changes for time scales from 30 seconds to several hours.

Table 1 summarizes the results of this investigation and gives the overall average results from Mariners 1969 and 1971. The volume of Viking data is obvious.

Table 1 suggests that the average spectral index is steeper for the Viking data (~3.0) near SSC minimum than for the Mariner data (~2.6-2.8) near maximum. This result, if confirmed, could be very important for understanding the SSC modulation of the SW and could affect estimates of navigation accuracy. The result is somewhat uncertain for two reasons. First, since the spectra are only approximately power laws, there is an uncertainty of 0.2-0.3 in fitting a straight line to them. Second, because the Mariner records were shorter, the spectral resolution is less, and the low-frequency points upon which the slope relies are more uncertain. This interesting, and potentially very important, suggestion that the slope decreases near SSC maxima needs to be followed up with more data from all parts of the SSC.

Figure 1 shows the power density at 3×10^{-4} Hz ($t \sim 1$ hour) from the Mariners (each divided into four groups) plotted with the Viking data as a function of Q, the distance of the ray path's closest approach to the sun (Q[AU] = sin [SEP angle]). No corrections for possible SSC changes (see below) have been made. Again, the data are variable, but a line of slope 2.6 (log-log) or a little more provides a reasonable representation of the data. The ionosphere may bias the points at large Q upward, reducing the slope. This slope implies that the density fluctuations in the SW, Δn, decline as $r^{-1.8}$. A similar plot of the Viking power densities at 6×10^{-4} Hz shows slopes of 2.4-2.6. More data at smaller values of Q are needed to better determine these slopes. From these data one concludes that $\Delta n \propto r^{-1.8 \pm 0.2}$. This slope agrees with that found empirically by Berman et al. (Ref. 2) for doppler noise data. This is because doppler noise is a measure of the same quantity as the power spectrum, the mean *squared* density integrated along the signal path.

The data of Table 1 and Fig. 1 suggest that the power density at 3×10^{-4} Hz may be a factor 2 less near SSC minimum than at maximum. The natural variability of the data makes this difficult to establish, but the Viking values lie systematically below the Mariner ones. More Viking post-conjunction data will make this determination more definite.

In an effort to study the time variations of the Viking data, shorter groups (3-5) of spectra were averaged and scaled by Q^3 to remove the radial dependence. These data were compared by eye to averaged (3 days running) sunspot numbers. No impressive correlation emerged. A similar attempt was made with the Mariner 9 data (Ref. 1). It produced possible, but not overwhelming, correlations at the expected rotational lags (~5-7 days). The lack of correlation may lie in the fact that the sunspot number is a very crude and large scale (a hemisphere) indicator of solar activity. Other measurements with better spatial (i.e., heliographic longitude) resolution such as white light coronagraph pictures and x-ray measurements will be used in further investigations.

The Viking data summarized in Table 1 can be used to estimate the errors which may be encountered in advanced navigation techniques such as alternate ranging. The power spectrum of the columnar content data can be fairly well represented by

$$P(\nu, Q) = 5.0 \times 10^{30} \left(\frac{Q}{0.1\ \text{AU}}\right)^{-2.6} \times \left(\frac{\nu}{3 \times 10^{-4}\ \text{Hz}}\right)^{-3.0} \text{cm}^{-4}\text{Hz}^{-1} \tag{2}$$

where Q is the distance of the ray path's closest approach to the sun, and ν is the frequency of the fluctuations in the columnar content, for $1 \times 10^{-4} \lesssim \nu \lesssim 1 \times 10^{-2}$ Hz, $0.03 \lesssim Q \lesssim 0.6$ AU. By using Eq. (1), one may easily deduce the rms change in columnar content from Eq. (2). The result in one-way meters of S-band range change is

$$\Delta I_{\text{rms}}\ (\nu, Q) = 3.4 \left(\frac{Q}{0.1\ \text{AU}}\right)^{-1.3} \left(\frac{\nu}{3 \times 10^{-4}}\right)^{-1.0} \text{meters} \tag{3}$$

Values of this expression for several values of ν and Q are given in Table 2. From the rms change, one gets the peak-to-peak

change, that is, the expected run, by multiplying by 3, so $\Delta I_{pp} \cong 3\Delta I_{rms}$. The solar wind fluctuates strongly on all time scales by a factor of 2 to 3, so $\Delta I_{pp_{max}} \cong 9\Delta I_{rms}$. Finally, it was estimated above that the average power spectrum may be higher by a factor of 2 around sunspot maximum than at minimum, so for Voyager around the coming sunspot maximum one might have $\Delta I_{max} \cong 9\sqrt{2} \cdot \Delta I_{rms} = 12.6\Delta I_{rms}$. Values of this quantity, but increased by 20 percent to account for the suspected flattening of the spectrum around SSC maximum, for several values of ν and Q are given in Table 3. The values of range change given in Table 3 are large enough to be of interest to navigators. One can place the following rough interpretation upon these numbers: one would expect 2 range points taken with the specified SEP and Δt to differ by this amount once in several hundred points. If the sun is reasonably active at the coming maximum, one would expect alternate range points to differ fairly frequently (1 in 3 or 5) by amounts a factor of 3 less than those in Table 3 (i.e., ~5 times those in Table 2). Note that in any case the errors increase directly with Δt so that the usefulness of alternate ranging depends critically upon its smooth implementation. In this connection it should be noted that Wu (Ref. 3) has shown that errors of up to several (2-3) meters in range calibrations can be made because of the one-way nature of the S-X data.

The main findings of this preliminary investigation are:

(1) $\Delta n\,(r) \propto r^{-1.8\pm0.2}$.

(2) The power density at 3×10^{-4} Hz may be a factor of 2 less near SSC minimum than at maximum.

(3) The spectrum appears to be steeper (~3.0 vs ~2.6-2.8) near SSC minimum.

(4) The time variations are not well-correlated with sunspot number.

(5) Columnar content changes, which could be important to Voyager navigation, are shown to be likely.

References

1. Callahan, P.S., "Columnar Content Measurements of the Solar Wind Turbulence," *Astrophys. J.*, Vol. 199, p. 227, 1975.

2. Berman, A. L., Wackley, J. A., Rockwell, S. T., and Kwan, M., "Viking Doppler Noise Used to Determine the Radial Dependence of Electron Density in the Extended Corona," in *The Deep Space Network Progress Report 42-38*, pp. 167-171, Jet Propulsion Laboratory, Pasadena, Calif., Apr. 15, 1977.

3. Wu, S. C., *A Demonstration of Uplink Charged-Particle Range Calibration Technique–Viking Radiometric Data*, JPL Engineering Memorandum 315-13, Jan. 31, 1977 (JPL internal document).

Table 1. Parameters of averaged spectra of single pass data

Time period	Number averaged	Avg Q, AU	Spectral index	$P(3\times10^{-4})$, $cm^{-4}Hz^{-1}$[a]	$P(6\times10^{-4})$, $cm^{-4}Hz^{-1}$[a]
Mariner '69; 1970					
May 21-July 2	17	0.185	2.2-2.8	4.8E30	4.8E29
Mariner '71, 1972					
Aug 10-Oct 25	33	0.132	2.6-2.9	7.8E30	1.6E30
Viking, 1976					
B, Aug 3-Aug 12	17	0.566	3.0	1.0E29	1.0E28
B, Aug 13-Aug 20	12	0.527	3.0	1.1E29	1.0E28
B, Aug 21-Aug 26	10	0.487	3.0	1.4E29	1.2E28
B, Aug 27-Sept 1	11	0.459	3.1	7.9E28	7.2E27
B, Sept 1-Sept 6	10	0.430	3.0	1.6E29	1.8E28
B, Sept 7-Sept 10	6	0.407	3.0	1.4E29	1.2E28
A, Sept 9-Sept 15	12	0.383	3.1	6.9E28	6.5E27
A, Sept 17-Sept 21	11	0.350	3.3	4.5E29	4.5E28
A, Oct 20-Nov 7	15	0.133	3.0-3.2	2.5E30	2.4E29
B, Oct 18-Nov 13	17	0.140	3.1-3.2	2.8E30	3.5E29
A&B[b] Nov 26-Dec 2	−7 (A11)	0.0286	2.8	1.1E32	1 3E31
	4	0.0185	2.6	3.7E32	5.3E31
	3	0.0359	2.7	6.6E31	5.3E30
A&B[c] Dec 8-Dec 15	8	0.0908	3.1	1.9E31	6.8E29

[a]One meter of one-way S-band range change = 1.15×10^{-13} cm^{-2} or 1 m^2 = 1.32×10^{26} cm^{-4}.
[b]These data were divided into 2 groups to help determine the radial dependence.
[c]These are 10-second data treated to give comparable spectral resolution.

Table 2. Rms columnar content change for Viking S-X doppler data (one-way, S-Band meters)

Q, AU	SEP, deg	ν, 10^{-3} Hz					
		16.7	3.33	1.67	1.11	0 833	0.556
		Δt, min					
		1	5	10	15	20	30
0.05	2.87	0.149	0.746	1.49	2.24	2.98	4.48
0.10	5.74	0.0606	0.303	0.606	0.909	1.21	1.82
0.15	8.63	0.0359	0.179	0.359	0.537	0.716	1.07
0.20	11.5	0.0246	0.123	0.246	0.369	0.493	0.738
0.25	14.5	0.0184	0.0922	0.184	0.276	0.368	0.552
0.30	17.5	0.0146	0.0728	0.146	0.218	0.291	0.436
0.40	23.6	0 0100	0.0500	0.100	0.150	0.200	0.300
0.50	30.0	0.00748	0.0374	0.0748	0.112	0.150	0.224
0.60	36.9	0.00590	0.0295	0.0590	0.0885	0.118	0.177

Table 3. Predicted peak-to-peak columnar content change for Voyager sunspot maximum (one-way, S-band meters)

Q, AU	SEP, deg	ν, 10^{-3} Hz					
		16.7	3.33	1.67	1.11	0.833	0.556
		Δt, min					
		1	5	10	15	20	30
0.05	2.87	2.32	11.6	23.2	34.9	46.5	69.8
0.10	5.74	0.945	4.72	9.45	14.2	18.9	28.4
0.15	8.63	0.560	2.80	5.60	8.37	11.2	16.7
0.20	11.5	0.384	1.92	3.84	5.75	7.67	11.5
0.25	14.5	0.287	1.43	2.87	4.30	5.74	8.61
0.30	17.5	0.228	1.14	2.28	3.40	4.55	6.80
0.40	23.6	0.156	0.78	1.56	2.34	3.12	4.68
0.50	30.0	0.117	0.58	1.17	1.75	2.33	3.50
0.60	36.9	0.0920	0.46	0.92	1.38	1.84	2.76

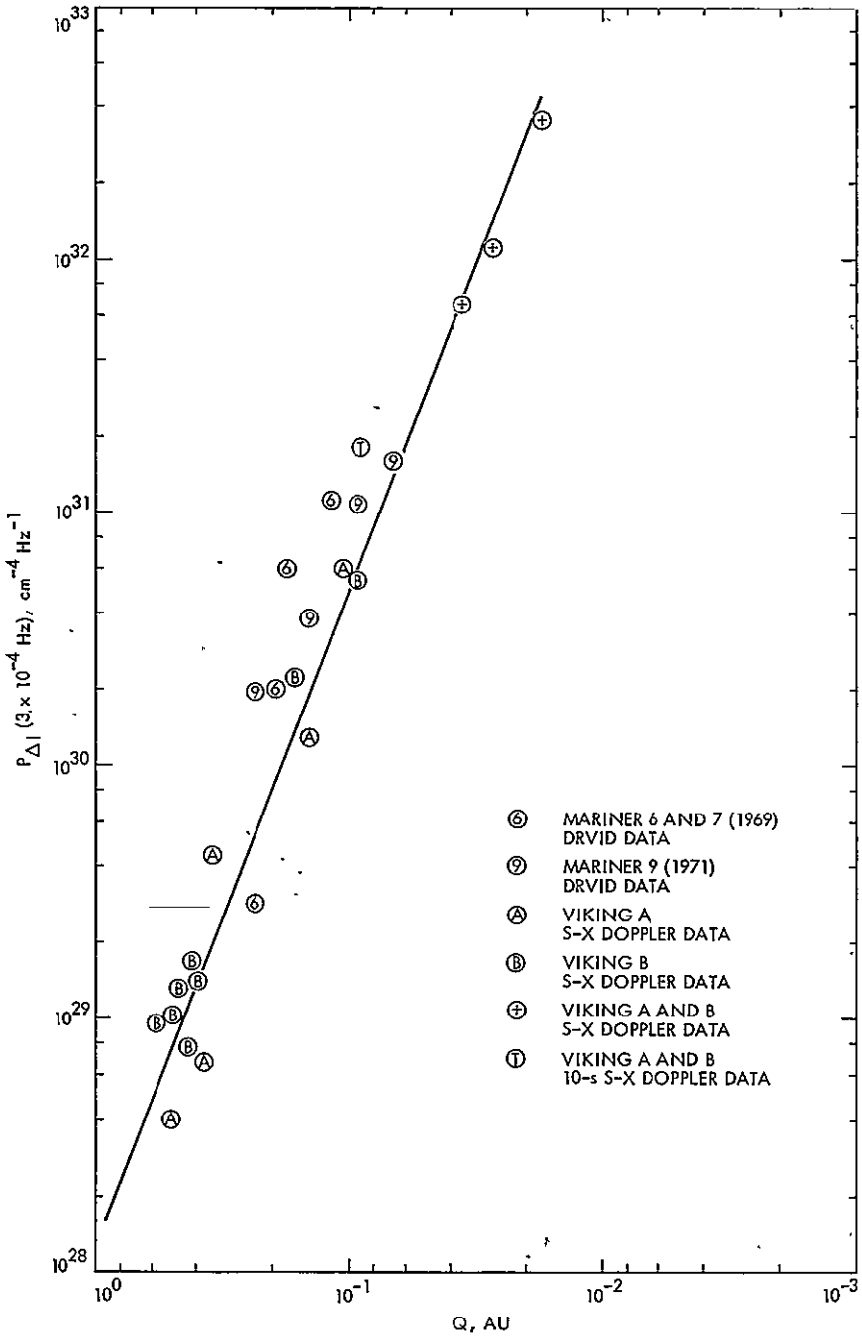

Fig. 1. Averaged power density at 3×10^{-4} Hz plotted against Q, the distance of the ray path's closest approach to the sun. The line through the points has slope 2.6. Note that the Mariner points generally lie above the Viking points. The points at large Q may be biased upward by the ionosphere.

D/6

N78-15073

An Asymptotic Analysis of a General Class of Signal Detection Algorithms

R. J. McEliece and E. R. Rodemich
Communications Systems Research Section

For applications to the problem of radio frequency interference identification, or in the search for extraterrestrial intelligence, it is important to have a basic understanding of signal detection algorithms. In this article we give a general technique for assessing the asymptotic sensitivity of a broad class of signal detection algorithms. In these algorithms, the decision is based on the value of $X_1 + X_2 + \cdots + X_n$, where the X_i's are obtained by sampling and preliminary processing of a physical process.

I. Introduction

Consider the following class of signal-detection rules. A physical process, which is either pure noise or contains a weak signal, is under observation. By sampling and preliminary calculation, n real numbers $X_1, X_2, \cdots, X_n$ are obtained from the process. We suppose that the X's can be modeled as independent, identically distributed random variables, and that their common distribution depends on a nonnegative real parameter ϵ, which we may think of as the "signal-to-noise ratio" of the process. If $\epsilon = 0$, no signal is present, but if one is, ϵ is positive.

The decision as to whether a signal is present or not is made by comparing $S_n/n = (X_1 + \cdots + X_n)/n$ to a threshold t_n:

$$\left.\begin{array}{ll} S_n/n \leqslant t_n & \text{report signal absent} \\ S_n/n > t_n: & \text{report signal present} \end{array}\right\} \quad (1)$$

Such a threshold test can fail in two distinct ways: it can report a signal present when it is not, or it can report no signal present when one actually is. These error events are commonly called *false alarm* and *miss*, and their respective probabilities are denoted by P_F and P_M. In different applications these two kinds of errors might not be equally severe, so let us choose arbitrary but fixed numbers α and β between 0 and 1 and try to design a detection system for which $P_F \leqslant \alpha$, $P_M \leqslant \beta$. For a given value of n, it will in general be possible to design such a system only if the signal-to-noise ratio ϵ is sufficiently large. In Section II we will prove a theorem giving an asymptotic expression for ϵ_n, the smallest such ϵ, as a function of n. This expression is typically of the form

$$\epsilon_n \sim \frac{K}{\sqrt{n}}\left[Q^{-1}(\alpha) + Q^{-1}(\beta)\right] \quad (2)$$

where Q^{-1} denotes the inverse to the complementary Gaussian distribution function

$$Q(x) = \frac{1}{\sqrt{2\pi}}\int_x^\infty e^{-t^2/2}\,dt \quad (3)$$

and K is a constant which depends on the common distribution of the X's.

In Section III we apply our general theorem to several special cases, in which the random variables X are derived from the real and imaginary components of a complex Gaussian signal. By computing the constants K in the asymptotic expansions (cf. Eq. (2)), we are able to compare their sensitivities. For example, we will show that binary quantization of the data prior to the computation of S_n/n costs about 0.94 dB in signal sensitivity.

II. Main Theorem

The following theorem will yield the asymptotic expansion of Eq. (2) above. In it the distribution function $F_\epsilon(x)$ is the common distribution of the random variables X when the signal-to-noise ratio is ϵ. Thus, in particular, $F_0(x)$ is the distribution when no signal is present.

THEOREM. For $0 \leqslant \epsilon \leqslant \epsilon_0$, let $F_\epsilon(x)$ be a distribution function with mean $\mu(\epsilon)$, variance $\sigma^2(\epsilon)$, and third moment $\tau(\epsilon) = \int |x - \mu(\epsilon)|^3 \, dF_\epsilon(x)$, such that

$$\mu(\epsilon) \text{ is continuous, and } \mu(\epsilon) > \mu(0) \text{ for } \epsilon > 0 \tag{4}$$

$$\sigma(\epsilon) \text{ is continuous and } \sigma(0) > 0 \tag{5}$$

$$\tau(\epsilon) \text{ is bounded for } 0 \leqslant \epsilon \leqslant \epsilon_0 \colon \tau(\epsilon) \leqslant T \tag{6}$$

For a given value of ϵ, and $n \geqslant 1$, let $X_1, \cdots, X_n$ be independent random variables with the distribution function $F_\epsilon(x)$, and put $S_n = X_1 + \cdots + X_n$. Define

$$p_+(a, \epsilon) = P\{S_n > na\}$$

$$p_-(a, \epsilon) = P\{S_n \leqslant na\}$$

Let α, β be positive with $\alpha + \beta < 1$. For $n \geqslant 1$, take

$$a_n = \inf\{a \colon p_+(a, 0) \leqslant \alpha\}$$

Since $p_+(a, 0)$ is a monotonic function of a, it follows that

$$p_+(a_n, 0) = \alpha$$

If n is sufficiently large, there are values of ϵ on $(0, \epsilon_0)$ for which $p_-(a_n, \epsilon) \leqslant \beta$. If we define

$$\epsilon_n = \inf\{\epsilon \colon p_-(a_n, \epsilon) \leqslant \beta\} \tag{7}$$

then

$$\mu(\epsilon_n) - \mu(0) = \frac{1}{\sqrt{n}} \sigma(0) \left[Q^{-1}(\alpha) + Q^{-1}(\beta)\right] + o(n^{-1/2}) \tag{8}$$

as $n \to \infty$, where $Q(x)$ is given by Eq. (3), above. In particular, if $\mu'(0)$ exists and is positive,

$$\epsilon_n = \frac{1}{\sqrt{n}} \frac{\sigma(0)}{\mu'(0)} \left[Q^{-1}(\alpha) + Q^{-1}(\beta)\right] + o(n^{-1/2}) \tag{9}$$

PROOF. We apply the Berry-Esseen refinements of the central limit theorem. By Theorem 1 on p. 542 of Ref. 1, Vol. 2,

$$\left| p_+(a, \epsilon) - Q\left[\sqrt{n} \frac{a - \mu(\epsilon)}{\sigma(\epsilon)}\right] \right| \leqslant \frac{3T}{\sigma(\epsilon)^3 \sqrt{n}}$$

By the continuity of $\sigma(\epsilon)$ at 0, $\sigma(\epsilon)$ is bounded away from 0 in some interval $0 \leqslant \epsilon \leqslant \epsilon_0'$. Suppose hereafter that $\epsilon \leqslant \epsilon_0'$. Then $3T/\sigma(\epsilon)^3 < B$, some positive constant, and

$$\left| p_+(a, \epsilon) - Q\left[\sqrt{n} \frac{a - \mu(\epsilon)}{\sigma(\epsilon)}\right] \right| \leqslant \frac{B}{\sqrt{n}}, \quad 0 \leqslant \epsilon \leqslant \epsilon_0' \tag{10}$$

In terms of the distribution function $P(x) = 1 - Q(x)$, this becomes

$$\left| p_-(a, \epsilon) - P\left[\sqrt{n} \frac{a - \mu(\epsilon)}{\sigma(\epsilon)}\right] \right| \leqslant \frac{B}{\sqrt{n}}, \quad 0 \leqslant \epsilon \leqslant \epsilon_0' \tag{11}$$

It follows from Eq. (10) and the fact that $p_+(a_n, 0) = \alpha$, that

$$Q\left[\sqrt{n} \frac{a_n - \mu(0)}{\sigma(0)}\right] = \alpha + \frac{\theta_1 B}{\sqrt{n}}$$

where $|\theta_1| \leqslant 1$. Let C be any constant such that $C > |Q^{-1\prime}(\alpha)|$. Then by the mean value theorem, for n sufficiently large,

$$\left| Q^{-1}\left(\alpha + \frac{\theta_1 B}{\sqrt{n}}\right) - Q^{-1}(\alpha) \right| \leqslant \frac{BC}{\sqrt{n}}$$

Hence

$$\sqrt{n} \frac{a_n - \mu(0)}{\sigma(0)} = Q^{-1}\left(\alpha + \frac{\theta_1 B}{\sqrt{n}}\right) = Q^{-1}(\alpha) + O\left(\frac{1}{\sqrt{n}}\right)$$

and so

$$a_n = \mu(0) + \frac{\sigma(0)\,Q^{-1}(\alpha)}{\sqrt{n}} + 0\left(\frac{1}{n}\right) \qquad (12)$$

The argument of the function P in Eq. (11) for $a = a_n$ is thus

$$\frac{\sqrt{n}}{\sigma(\epsilon)}\left[\mu(0) - \mu(\epsilon) + \frac{\sigma(0)\,Q^{-1}(\alpha)}{\sqrt{n}} + 0\left(\frac{1}{n}\right)\right]$$

$$= \frac{\sigma(0)}{\sigma(\epsilon)}\left[Q^{-1}(\alpha) - \frac{\sqrt{n}\,(\mu(\epsilon) - \mu(0))}{\sigma(0)} + 0\left(\frac{1}{\sqrt{n}}\right)\right]$$

By hypothesis (4), $\mu(\epsilon) - \mu(0) > 0$. Hence for fixed small $\epsilon > 0$ on $(0, \epsilon_0')$, the above expression approaches $-\infty$ as n increases. Thus the function P in Eq. (11) approaches 0 as $n \to \infty$, and so $p_-(a_n, \epsilon) \to 0$. This shows that for n sufficiently large, ϵ_n exists, and furthermore that $\epsilon_n \to 0$ as $n \to \infty$. By the definition (7) of ϵ_n, in every neighborhood of ϵ_n there are values of ϵ for which $p_-(a_n, \epsilon) \leqslant \beta$, and other values with $p_-(a_n, \epsilon) > \beta$. Thus there exists a sequence $\epsilon_{n,m}$ such that

$$\lim_{m\to\infty} \epsilon_{n,m} = \epsilon_n$$

$$\lim_{m\to\infty} p_-(a_n, \epsilon_{n,m}) = \beta$$

From Eq. (11),

$$\left| p_-(a_n, \epsilon_{n,m}) - P\left[\sqrt{n}\,\frac{a_n - \mu(\epsilon_{n,m})}{\sigma(\epsilon_{n,m})}\right] \right| \leqslant \frac{B}{\sqrt{n}}$$

Taking limits as $m \to \infty$, and using hypotheses (5) and (6) on the continuity of μ and σ, we conclude

$$P\left[\sqrt{n}\,\frac{a_n - \mu(\epsilon_n)}{\sigma(\epsilon_n)}\right] = \beta + \frac{\theta_2 B}{\sqrt{n}}$$

where $|\theta_2| \leqslant 1$. Arguing as above,

$$\sqrt{n}\,\frac{a_n - \mu(\epsilon_n)}{\sigma(\epsilon_n)} = P^{-1}(\beta) + 0(n^{-1/2})$$

and using the relationship $P^{-1}(x) = -Q^{-1}(x)$, we conclude

$$a_n = \mu(\epsilon_n) - \frac{\sigma(\epsilon_n)}{\sqrt{n}} Q^{-1}(\beta) + 0(n^{-1}) \qquad (13)$$

Combining Eqs. (12) and (13), we have

$$\mu(\epsilon_n) - \mu(0) = \frac{1}{\sqrt{n}}[\sigma(0)\,Q^{-1}(\alpha) + \sigma(\epsilon_n)\,Q^{-1}(\beta)] + 0(n^{-1})$$

Since by Eq. (5) σ is continuous at $\epsilon = 0$, and $\epsilon_n \to 0$, then $\sigma(\epsilon_n) = \sigma(0) + o(1)$, and Eq. (8) follows. Finally if $\mu'(0)$ exists, then $\mu(\epsilon_n) - \mu(0) = \epsilon_n \mu'(0) + o(\epsilon_n)$, and Eq. (9) follows. QED.

In Section III we will apply formula (9) to compare competing signal-detection algorithms. Since the term $[Q^{-1}(\alpha) + Q^{-1}(\beta)]$ does not depend on the distribution $F(x)$, it will only be necessary to compute the values of $\sigma(0)/\mu'(0)$. But it is instructive to see how the term $Q^{-1}(\alpha) + Q^{-1}(\beta)$ behaves as a function of α and β, so here is a short table of $Q^{-1}(\alpha)$:

α	$Q^{-1}(\alpha)$
0.1	1.28
0.01	2.33
10^{-3}	3.09
10^{-4}	3.72
10^{-5}	4.26
10^{-6}	4.75
10^{-8}	5.61
10^{-10}	6.36

From this table we can compute the price paid in sensitivity for stringent error requirements. For example, if we can tolerate $\alpha = 0.01$, $\beta = 0.001$, our test will be about 1-dB more sensitive than if $\alpha = 0.001$, $\beta = 0.0001$.

III. Examples

In each of the following examples the random variables X_i will be derived from samples of a complex Gaussian random process. We denote the real (in phase) components of these samples by $I_1, I_2, \cdots, I_n$, and the imaginary (quadrature) components by $Q_1, Q_2, \cdots, Q_n$. The I's and Q's are assumed to be independent, identically distributed normal random variables with mean zero and variance $1 + \epsilon$. This situation would occur if the observed process was the sum of a variance 1 normal process (noise with average power 1) and a variance ϵ normal process (a stochastic signal with average power ϵ).

In fact, all of our examples will be of detection algorithms based on the sample powers[1] $Z_i = I_i^2 + Q_i^2$. These random variables are distributed exponentially, and in fact for $\epsilon = 0$ we have

$$P\{Z \leqslant x\} = \int_0^{\sqrt{x}} re^{-r^2/2}\, dr = 1 - e^{-x/2} \qquad (14)$$

A. Case 1

Test based on the random variables $X_i = Z_i^a$, where $a > 0$. Here an easy manipulation of Eq. (14) yields, for any $a > 0$, and $\epsilon = 0$,

$$E(X^b) = 2^{ab} \int_0^{\infty} y^{ab} e^{-y}\, dy$$

$$= 2^{ab}\, \Gamma(ab + 1)$$

where Γ denotes the gamma function. Thus $\mu(\epsilon) = E((1+\epsilon)^a X) = 2^a(1+\epsilon)^a \Gamma(a+1)$, and so $\mu(0) = 2^a\Gamma(a+1)$, $\mu'(0) = a2^a\Gamma(a+1)$. To compute $\sigma^2(0)$, we use the formula $\sigma^2(0) = E(X^2) - (E(X))^2 = 2^{2a}\Gamma(2a+1) - (2^a\Gamma(a+1))^2$. Thus in the asymptotic expansion of Eq. (9) we have

$$K(a) = \frac{\sigma(0)}{\mu'(0)} = \frac{1}{a}\left\{\frac{\Gamma(2a+1)}{\Gamma(a+1)^2} - 1\right\}^{1/2}$$

A short table of $K(a)$ follows:

	$K(a)$	
a	Numerically	Exactly
0^+	1.283	$\pi/\sqrt{6}$
1/2	1.045	$2((4-\pi)/\pi)^{1/2}$
1	1.000	
2	1.118	$\sqrt{5}/2$
3	1.453	$\sqrt{19}/3$

From this we see that the best test of this kind is for $a = 1$ (a fact which follows from the Neyman-Pearson theorem); if the test is based on the amplitude $X = \sqrt{I^2 + Q^2}$, the loss is $10 \log_{10}(1.045) = 0.19$ dB. Notice also that in the limit as $a \to 0$, $X = Z^a = e^{a \log z} = 1 + a \log Z + 0(a^2)$, and so the performance must be the same as if we took $X = \log Z$. We conclude that the loss in this case is $10 \log_{10}(\pi/\sqrt{6}) = 1.08$ dB.

[1]There is no loss in considering the powers instead of the components separately, by the Neyman-Pearson criterion Ref. 2, Sec. 13.2.

B. Case 2 (Binary Quantization)

Here the test is based on the random variables

$$X_i = \begin{cases} 0 & \text{if } Z_i \leqslant T \\ 1 & \text{if } Z_i > T \end{cases}$$

where the threshold T is a fixed positive real number. According to Eq. (14), the distribution of the X's is given by

$$P\{X = 1\} = P\{Z \geqslant T\}$$

$$= \int_{\sqrt{T}}^{\infty} re^{-r^2/2}\, dr = e^{-T/2}$$

Hence, if the signal to noise ratio is ϵ,

$$\mu(\epsilon) = P\{(1+\epsilon)Z > T\}$$

$$= \exp\left[-\frac{T}{2(1+\epsilon)}\right]$$

Hence, $\mu(0) = e^{-T/2}$, $\mu'(0) = 1/2\ Te^{-T/2}$. Since X is a Bernoulli random variable, $\sigma(0) = (\mu(0)(1 - \mu(0)))^{1/2} = (e^{-T/2}(1 - e^{-T/2}))^{1/2}$. Hence in Eq. (9) the value of $\sigma(0)/\mu'(0)$ is

$$K = \frac{(e^x - 1)^{1/2}}{x}, \quad x = T/2 \qquad (15)$$

Of course one wishes to choose x so that K will be minimized. Numerically one calculates that the minimum of Eq. (15) occurs for $T = 3.18725$ and is $K_{min} = 1.24263$. Thus the loss in sensitivity due to binary quantization is $10 \log_{10}(1.24263) = 0.94$ dB.

C. Case 3

In this case we let b be a fixed positive integer, and assume that n is a large multiple of b, say $n = n_0 b$. The test is based on the random variables

$$X_i = \max(Z_{(i-1)b+1}, Z_{(i-1)b+2}, \cdots, Z_{ib}) \qquad (16)$$

i.e., X_i is the maximum of the i-th block of length b. Since by Eq. (14), the distribution function of Z for $\epsilon = 0$ is $F_1(x) = 1 - e^{-x/2}$, it follows (see Ref. 3, Sec. 13) that the distribution of each X_i is given by

$$F_b(x) = (F_1(x))^b = (1 - e^{-x/2})^b$$

Hence the density for the X's is

$$p_b(x) = \frac{d}{dx} F_b(x)$$

$$= \frac{b}{2} e^{-x/2} (1 - e^{-x/2})^{b-1}, \quad x \geqslant 0$$

The r-th moment of X is then given by

$$\mu_r(b) = \frac{b}{2} \int_0^\infty x^r e^{-x/2} (1 - e^{-x/2})^{b-1} dx \qquad (17)$$

After expanding the term $(1 - e^{-x/2})^{b-1}$ by the binomial theorem, integrating term-by-term, and summing, one obtains finally

$$\mu_r(b) = r!\, 2^r \sum_{k=1}^{b} (-1)^{k+1} \binom{b}{k} k^{-r} \qquad (18)$$

The sum in Eq. (18) was considered in Ref. 4; in particular it was shown there that

$$\mu_1(b) = 2\left(1 + \frac{1}{2} + \frac{1}{3} + \cdots + \frac{1}{b}\right)$$

$$\mu_2(b) = 4\left[\left(1 + \frac{1}{2} + \cdots + \frac{1}{b}\right)^2 + \left(1 + \frac{1}{2^2} + \cdots + \frac{1}{b^2}\right)\right]$$

Hence if $\epsilon = 0$, the mean of X is

$$\mu = 2\left(1 + \frac{1}{2} + \cdots + \frac{1}{b}\right)$$

and the variance is

$$\sigma^2 = 4\left(1 + \frac{1}{2^2} + \cdots + \frac{1}{b^2}\right)$$

For general ϵ, $\mu(\epsilon) = E[\max(1+\epsilon)\, Z_1, \cdots, (1+\epsilon) Z_n] = (1+\epsilon)\mu(0)$; and so $\mu'(0) = \mu(0)$. Thus in Eq. (9) the term $\sigma(0)/\mu'(0)$ is

$$\frac{\sigma(0)}{\mu'(0)} = \frac{\left(1 + \frac{1}{2^2} + \cdots + \frac{1}{b^2}\right)^{1/2}}{\left(1 + \frac{1}{2} + \cdots + \frac{1}{b}\right)}$$

However in Eq. (9) the number n should be replaced by $n_0 = n/b$, and so the formula for ϵ_n becomes

$$\epsilon_n \sim \frac{1}{\sqrt{n}} \left[\sqrt{b}\, \frac{\left(1 + \frac{1}{2^2} + \cdots + \frac{1}{b^2}\right)^{1/2}}{\left(1 + \frac{1}{2} + \cdots + \frac{1}{b}\right)}\right]$$

$$\cdot \left(Q^{-1}(\alpha) + Q^{-1}(\beta)\right)$$

and so the sensitivity is measured by the quantity

$$K_b = \sqrt{b}\, \frac{\left(1 + \frac{1}{2^2} + \cdots + \frac{1}{b^2}\right)^{1/2}}{\left(1 + \frac{1}{2} + \cdots + \frac{1}{b}\right)}.$$

A table of this quantity follows:

b	K_b	Loss in dB
1	1.000	0
2	1.054	0.23
3	1.102	0.42
4	1.145	0.59
5	1.185	0.74
6	1.221	0.87
7	1.255	0.99
8	1.286	1.09
16	1.489	1.73
32	1.771	2.48
64	2.153	3.33
128	2.664	4.26
256	3.348	5.25
512	4.256	6.29
1024	5.464	7.38

Acknowledgment

The authors wish to thank Dr. Barry K. Levitt for his helpful criticism of this manuscript, especially in the proof of the main theorem.

References

1. Feller, William, *An Introduction to Probability Theory and its Applications*, 2 vols. New York: John Wiley and Sons, 1971.
2. Wilks, Samuel, *Mathematical Statistics*. New York: John Wiley and Sons, 1962.
3. Lamperti, John, *Probability*. New York: W. A. Benjamin, 1966.
4. McEliece, Robert, "A Combinatorial Identity in Order Statistics", Jet Propulsion Laboratory *Space Program Summaries* Vol. 37-39, (1966), pp. 230-231.

D7

N78-15074

On the Existence of Binary Simplex Codes

H. Taylor
Communications Systems Research Section

Using a very simple combinatorial construction, we prove the existence of a binary simplex code with m codewords for all $m \geq 1$. The problem of the shortest possible length is left open.

I. Introduction

In a variety of communications problems it is necessary to have a set of digital sequences, i.e., codewords, where mutual correlations are as small as possible. In Ref. 1, Theorem 4.1, it is shown that if $\{x_1, x_2, \cdots, x_m\}$ is any set of m binary (components ± 1) codewords of length n, and if the correlation between $x_i = (x_{i1}, \cdots, x_{iN})$ and $x_j = (x_{j1}, \cdots, x_{jN})$ is defined as $\rho(x_i, x_j) = (\Sigma_{k=1}^{N} x_{ik}x_{jk})/n$, then

$$\max_{i \neq j} \rho(x_i, x_j) \geq \begin{cases} \dfrac{-1}{m-1}, & \text{if } m \text{ is even} \\ -\dfrac{1}{m}, & \text{if } m \text{ is odd} \end{cases} \tag{1}$$

A set of m binary codewords achieving the bound (1) is called a *simplex* code. In Ref. 1 it is shown that simplex codes exist for an infinite number of values of m. In this article we will show that simplex codes exist for *all* m, using a very simple combinatorial construction, which bypasses the question of making the codewords as short as possible.

II. Construction

First we note that if $x_1, \cdots, x_m$ is a simplex code with $m = 2n$ then $\{x_1, \cdots, x_{m-1}\}$ is a simplex code with $m = 2n - 1$, so we focus our attention on even values of m.

Form the incidence matrix of all the n-subsets of a $2n$-set. It will be a matrix of 0's and 1's having $2n$ rows and $\binom{2n}{n}$ columns. Each row corresponds to an element of the $2n$-set, and in each column the n 1's mark the elements of the corresponding n-subset. A good definition for the binomial coefficient $\binom{b}{a}$ for nonnegative integers a, b is that $\binom{b}{a}$ is the number of a-subsets of a b-set. For example, when $n = 3$, the

incidence matrix, easily written in binary lexicographic order, will be:

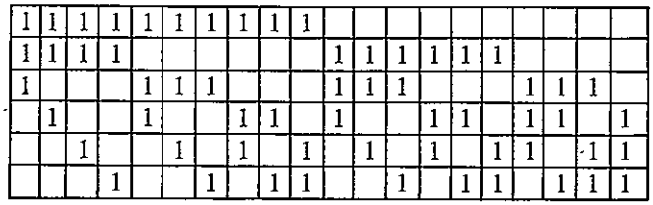

In this example, with $m = 6$, we can calculate, for any two rows:

$$A = \text{number of agreements} = 8$$

$$D = \text{number of disagreements} = 12$$

Thus, $(A - D)/(A + D) = -1/5$.

In general each element will belong to $\binom{2n-1}{n-1}$ of the n-sets. Thus, each codeword will have weight $\binom{2n-1}{n-1}$. Each pair of elements will be a 2-subset of $\binom{2n-2}{n-2}$ of the n-sets. Any two distinct codewords will overlap (*both* have 1's) in $\binom{2n-2}{n-2}$ of the columns. The interpretation in terms of sets has made it easy to evaluate:

$$D = 2\binom{2n-1}{n-1} - 2\binom{2n-2}{n-2}$$

$$A = \binom{2n}{n} - D$$

By straightforward calculation:

$$\frac{A-D}{A+D} = \frac{\binom{2n}{n} - 4\binom{2n-1}{n-1} + 4\binom{2n-2}{n-2}}{\binom{2n}{n}}$$

$$= \frac{\frac{2n(2n-1)}{n(n-1)} - 4\frac{(2n-1)}{(n-1)} + 4}{\frac{2n(2n-1)}{n(n-1)}}$$

$$= \frac{2n(2n-1) - 4n(2n-1) + 4n(n-1)}{2n(2n-1)}$$

$$= \frac{(2n-1) - 2(2n-1) + 2(n-1)}{(2n-1)}$$

$$= \frac{-1}{2n-1} = \frac{-1}{m-1}$$

III. Comments

These codewords are at least twice as long as they need to be – making them shorter will be the subject of a later article. Meanwhile, this is a good place to observe that these matrices have complete symmetry with respect to incidence. The codewords all have the same weight. Any two of them overlap in the same number of places. Any three of them overlap in the same number of places. And so on. And all those overlap numbers are easy to calculate.

Reference

1. Golumb, S. W., Baumert, L. D., Easterling, M. F., Stiffler, J. J., and Viterbi, A. J., *Digital Communication with Space Applications*, Prentice-Hall, Inc., Englewood Cliffs, N. J., 1964.

Modcomp Version of Tutorial Input

K. I. Moyd
Communications Systems Research Section

The version of Tutorial Input implemented on the Modcomp used for antenna control at DSS 13 is described. Emphasis is on the use of the Tutorial Input; program operation is described to the extent that it makes the use more understandable. Flow charts are provided.

I. Introduction

Tutorial Input, a standardized man/computer interface developed by A. I. Zygielbaum (Ref. 1) and modified by K. I. Moyd (Ref. 2), has been implemented on the Modcomp II computer used for antenna control at DSS 13. It is implemented as a set of FORTRAN subroutines that communicate with the user program by means of tables in common. Several features have been added to the version used in the DSS 13 automation project (Refs. 3 and 4).

II. Operation

Tutorial Input is divided into commands and parameters associated with the commands. Once the operator starts entering a command, he must enter values for all parameters associated with that command in a specified order. By doing a carriage return before all parameters are entered, the operator can request prompting of the next parameter to be entered.

The commands and parameters are defined in the program by means of tables set up by the user. A command definition includes the name of the command, the number of associated parameters and an index telling where the parameter definitions for the command start A parameter definition includes the name of the parameter, a code indicating the type of the parameter, and an index telling where the parameter value is to be stored. Because of the difference in the number of words required to store floating point and integer numbers, there are actually two separate parameter buffers. However, for purposes of knowing how to use the program, it is acceptable to consider that there is a single parameter buffer. There is also a flag table that indicates to the user program whether a particular command has been entered. The flag table allows commands having no parameters to be used for program control. The command and parameter definition tables, the flag table, and the parameter buffer can be accessed by both the user program and the Tutorial Input routine. To prevent premature transfer of flags and parameter values, an internal flag table and parameter buffer are established within the Tutorial Input routine. The internal values are transferred to the user only upon normal termination of the Tutorial Input routine. This allows the operator to verify or cancel entries before transferring them to the user. Several "internal" commands have been implemented to allow for verification and cancellation.

The Tutorial Input routine is activated by the operator entering a line of input on the Terminet. Upon activation, the values in the user parameter buffer are transferred to the internal parameter buffer and the internal flag table is zeroed.

Input lines are interpreted from left to right by field. A field consists of the characters from the first nonblank character following the previous delimiter to the trailing delimiter, which may be a slash, blank, comma, or carriage return.

There are two kinds of fields, i.e., command and parameter. A command field is alphanumeric The first four characters are used for comparison with the user-defined and internal command names. These four characters must match exactly, including blanks (trailing blanks will be added automatically if fewer than four characters are entered). If the user-defined command name has fewer than four nonblank characters, only that many characters may be entered by the operator. However, if the user-defined command name has four characters, the operator may enter as many characters as he wishes, as long as the first four agree. This difference is caused by the fact that blanks serve as delimiters.

A parameter field is interpreted according to the type specified by the user-defined code. There are four types: integer, double precision floating point, two-character alphanumeric, and six-character alphanumeric. An integer field, i.e., a field to be interpreted as an integer, may contain a decimal integer with sign (plus is optional) of magnitude less than or equal to 32767 or a four-digit hexadecimal number preceded by a #. A floating point field may contain an integer as described above, in which case the decimal point is assumed to be at the end, or it may contain a decimal number with an included decimal point. The field may not exceed eight characters. Any violation of these rules will cause an error message to be printed.

In the case of the alphanumeric fields, the number of allowed characters is not limited; however, only the first two or six characters will be transferred to the user. The same limitations may occur as for command fields if the user compares the parameter with a value containing fewer than the allowed number of characters.

The routine interprets all fields as command fields except when it is in the process of accepting the parameters for the previously entered command. When interpreting a command field, its first four characters are compared with the internal and then user-defined command names. If no match is found, an error message is typed, the remainder of the line is ignored, and the routine waits for a new line. If it matches with a user command name, the routine will then look for the parameters, if any. The operator may have the routine prompt him with the name of the first parameter to be entered by doing a carriage return after the command name. If he ends the line before all parameters are in, he will be prompted with the name of the next one to be entered. If the operator enters an * in place of a parameter value, the value in the internal buffer is left unchanged. Parameters will be converted to the format specified by the user code and stored in the internal buffer. Once all the parameters for a command have been found, an internal flag is set indicating that the command has been entered. The routine then checks whether there is additional input on the line. If so, it continues processing the line interpreting the next field as a command. If there is no additional input on the line, the user flags corresponding to the set internal flags are set, and the parameter values for the entered commands are transferred from the internal parameter buffer to the user parameter buffer. The routine is then deactivated until a new line is entered.

The internal commands are acted upon as soon as they are found. The EXIT command causes a normal termination to occur whether or not there is subsequent input on the line. All flags and parameters for commands preceding the EXIT are transferred to the user. The NOEX command prevents normal termination until another line has been entered. Anything on the same line following the NOEX is ignored. 'ENTER INPUT' will be typed to remind the operator. The LIST command causes all command names to be typed out with the associated parameter names and parameter values from the internal parameter buffer in a format corresponding to the user-specified type. If no input follows the LIST command, a normal termination will be made. Both the TYPE command and the DELE command require a user command name as a parameter. If the TYPE or DELE is not followed by any input, a normal termination will be made. The DELE command causes the internal flag for the command following the DELE to be set to a specific value different from the set or reset condition. Upon normal termination the corresponding user flag is reset. This allows a previously entered command to be deleted if it has not already been acted upon. It should be noted, however, that the values in the user parameter buffer will not be changed. If no additional input follows the command name, a normal termination will be made. The TYPE command causes the parameter values associated with the following command to be typed out from the internal buffer. Even if no additional input follows the command name, the routine will not be terminated. In this case 'ENTER INPUT' will be typed out. This feature allows the operator to verify the correctness of parameter entry before the values are transferred to the user. He may correct the values by repeating the command. The * may be used for any parameters that had been entered correctly. If the parameters were entered correctly to begin with, the EXIT command may be used to cause normal termination.

III. Additional Features

There are some additional editing features. The Terminet backspace (BS) and delete (DEL) keys may be used to delete a

character or a line, respectively. If a < is entered in place of any command name or parameter, the routine will be terminated immediately upon its interpretation without transferring any values to the user.

Error messages indicate the position and kind of error. An ! is typed out directly below the first character of the command or parameter in error. (Output caused by a preceding LIST or TYPE command may intervene.) There are two different error messages – UNRECOGNIZED COMMAND and ILLEGAL PARAMETER. In the first case, the routine expects a new command name to be entered; in the second case, the operator is prompted with the name of the parameter in error. In both cases all input preceding the error has been accepted; all input following the error will be ignored.

As an example, the commands and parameters being used in the DSS 13 antenna control program are presented in Appendix A. Because of the way Tutorial Input is set up, new commands may be implemented easily. It is expected that CONSCAN and three-day fit modes will be added in the near future.

Tutorial Input, as it is implemented here, could be used on any Modcomp with FORTRAN programming. Implementation details and flow charts are presented in Appendix B. Listings and additional material can be obtained from the author.

References

1. Zygielbaum, A. I., " 'Tutorial Input' – Standardizing the Computer/Human Interface", in *The Deep Space Network Progress Report* 42-23, pp. 78-86, Jet Propulsion Laboratory, Pasadena, California, October 15, 1974.
2. Moyd, K., "Fortran Implementation of Tutorial Input", in *The Deep Space Network Progress Report* 42-24, pp. 88-99, Jet Propulsion Laboratory, Pasadena, California, December 15, 1974.
3. Moyd, K. I. "Automatic Control of DSS-13", in *The Deep Space Network Progress Report* 42-29, pp. 107-114, Jet Propulsion Laboratory, Pasadena, California, October 15, 1975.
4. Moyd, K. I., "Remote Automatic Control of DSS-13", *The Deep Space Network Progress Report* 42-30, pp. 174-183, Jet Propulsion Laboratory, Pasadena, California, December 15, 1975.

Appendix A

Tutorial Input Commands for the DSS 13 Antenna Control Program

The first name is the command name; the indented names are the parameter names. b = blank (may be omitted but not replaced by nondelimiter).

Command	Parameter	Description
SIDb		Track a source at the sidereal rate. When acted on, RA and DEC will be typed in decimal degrees.
	ID	Up to 6 alphanumeric character identification.
	RA	Right ascension in form HHMMSST where HH = hours, MM = minutes, SS = seconds, T = tenths of seconds. Interpreted as double precision floating point.
	DEC	Declination in form ±DDMMSS where DD = degrees, MM = minutes, SS = seconds and the + is optional. Interpreted as double precision floating point.
AZEL		Move the antenna to a specified AZ and EL
	AZ	Azimuth in decimal degrees 0.000 to 359.999 (decimal point to be included).
	EL	Elevation in decimal degrees. 0.000 to 90.000 (decimal point to be included).
	REG	Lb = left wrap-up region. Rb = right wrap-up region. other = center region.
OFFb		Change variable offsets (default values are zeroes).
	AZOF	Azimuth offset in decimal degrees.
	ELOF	Elevation offset in decimal degrees Note: In SID mode, the azimuth offset will be divided by COS(EL) to get the specified number of degrees on the sky. In AZEL mode, the azimuth offset will be applied directly.
CLRO		Clear both variable offsets.
STOP		Safely decelerate antenna and apply brakes.

Appendix B

Implementation and Flow Charts

The implementation of Tutorial Input on the Modcomp was made easier by the fact that several string handling and conversion services are provided by the operating system (as REX services). Although some of these services have FORTRAN-callable versions, the assembly language versions had to be used to allow enough significant figures for the numerical parameters. FORTRAN-callable subroutines were therefore written to use these services. Several of the services are set up such that the output from one is in the form of the expected input of another. Details of these services can be found in the Modcomp computer manuals.

The main Tutorial Input routine is called TUTOR (Fig. B-1). It may be set up as a separate task or as a subroutine called by a user task. The remaining subroutines used to implement Tutorial Input are called only by the Tutorial Input routines, not by the user.

TUTIN (LFIRST) (Fig. B-2) provides one line of Terminet input to the calling program. If LFIRST is false, the input is accepted from the Terminet. If LFIRST is true, it is assumed that the input has already been accepted. This procedure is used so that the first line of input can be accepted by the user program before TUTOR is called.

TYPOUT (I, param buffers) (Fig. B-3) types out the internal values of the parameters for the I^{th} command in the formats specified by their type codes except that double precision floating point numbers are typed out both in double precision form with exponent, and in fixed point with three decimal places. The latter is easier to read, but may not contain enough significant figures.

COLLECT (IERR, LNUM) (Fig. B-4) uses the REX service COLLECT to pick out the next field in a character string. Delimiters are trailing blanks, slashes, commas, equal signs, and trailing plus or minus signs. If the field contains only characters allowed in numbers (decimal or hexidecimal if preceded by a #), LNUM is set to TRUE; otherwise it is FALSE. If a numerical parameter field exceeds 8 characters, IERR is set to -1; if there is no nonblank character before the end of the string, it is set to 1; otherwise, it is set to 0. The field is stored in A2 format in an array in COMMON.

ALTOBN (LINT, LDEC) (Fig. B-5) converts a field in the form stored by COLLECT to a binary double precision integer with scale factor using the REX service ATN. LINT is set to TRUE if the absolute value of the number is less than 32768 (i.e., if it can be contained in a single precision integer); LDEC is set to TRUE if a decimal point occurred in the number. The resulting number is placed in the same array as the input field.

INTFP (Fig. B-6) converts a number in the form stored by ALTOBN to a Modcomp double precision floating point number.

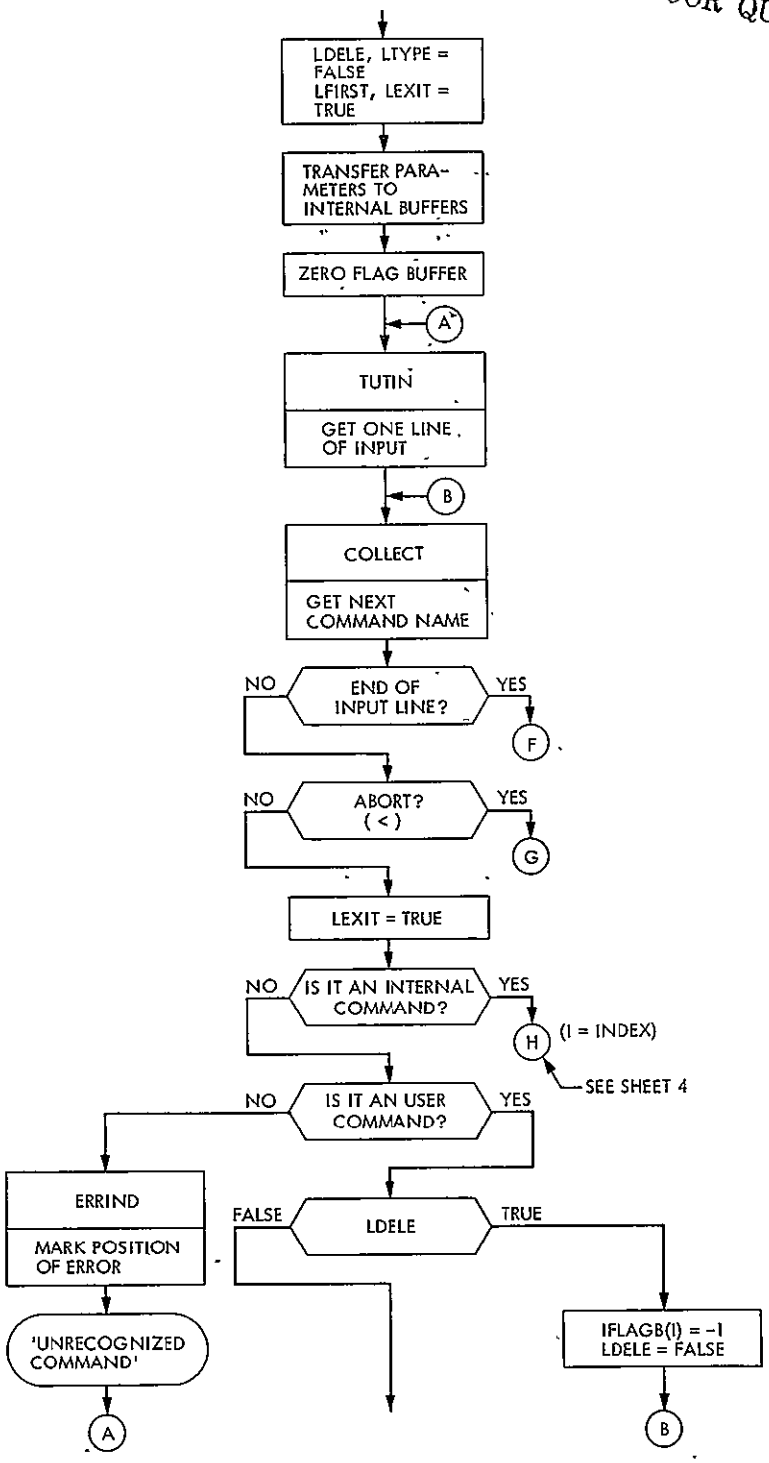

Fig. B-1. TUTOR

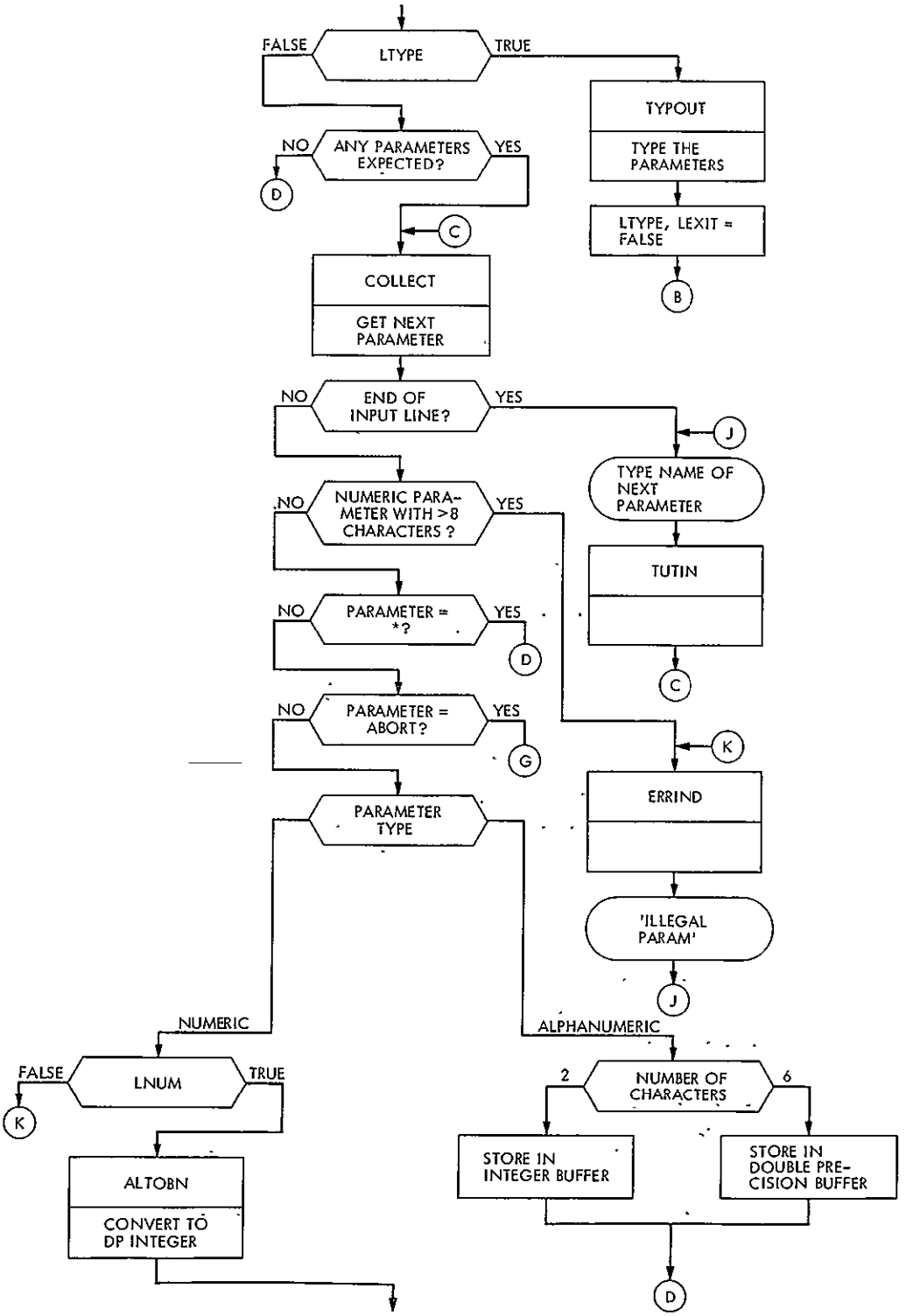

Fig. B-1 (contd)

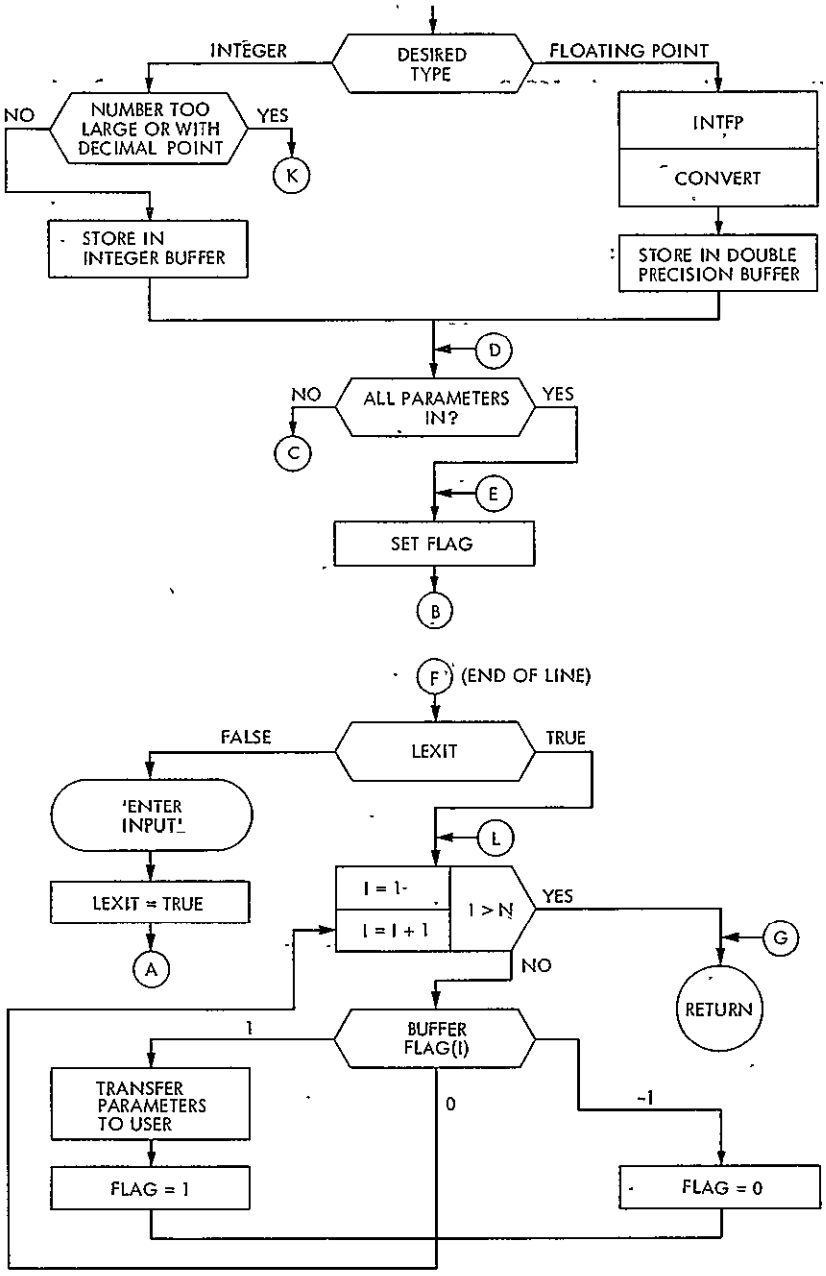

Fig. B-1 (contd)

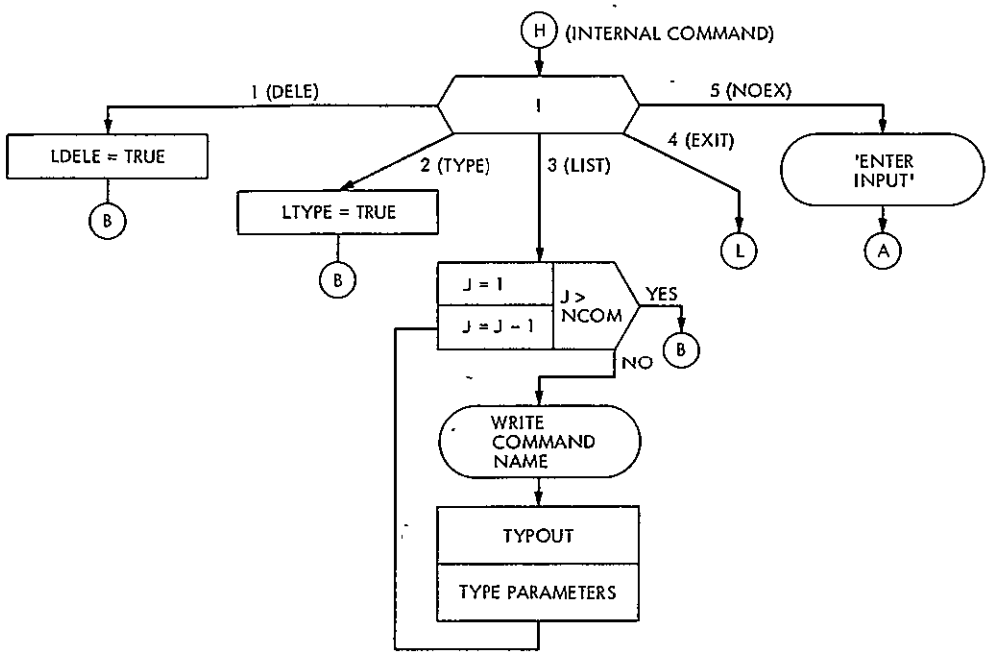

Fig. B-1 (contd)

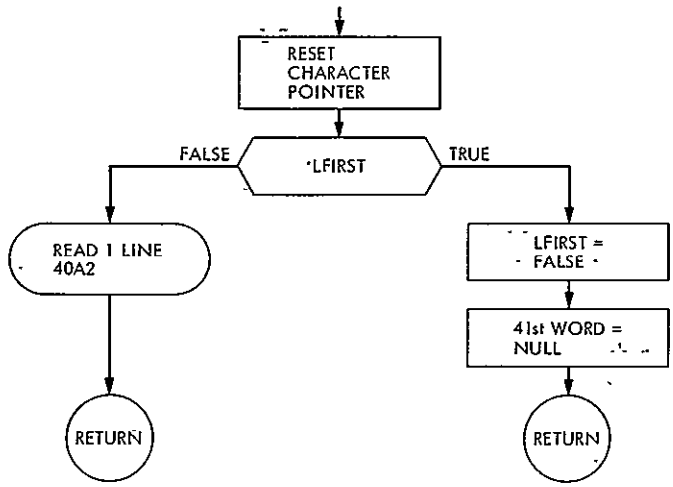

Fig. B-2. TUTIN (LFIRST)

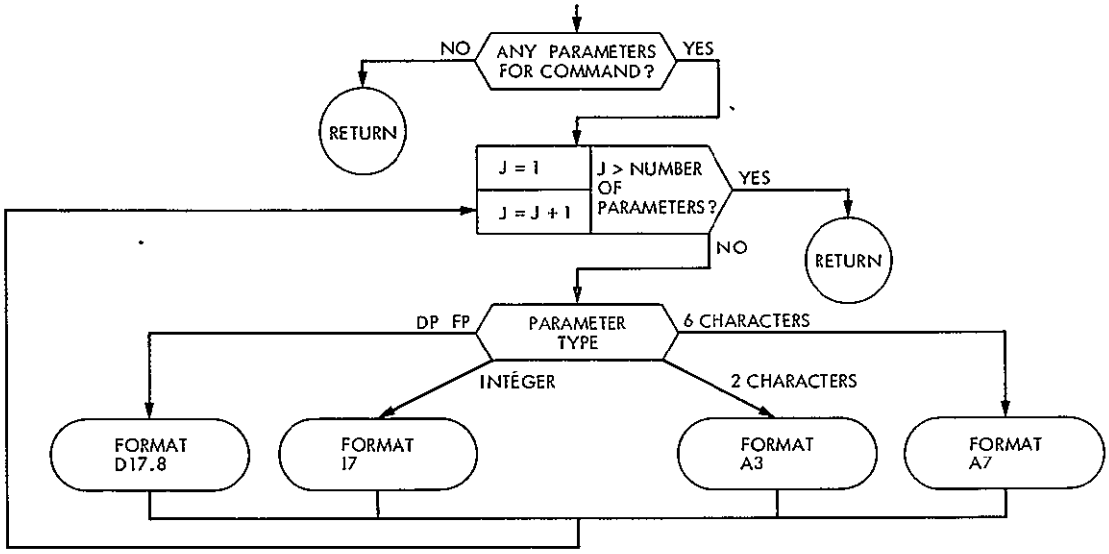

Fig. B-3. TYPOUT (I, parameter buffers)

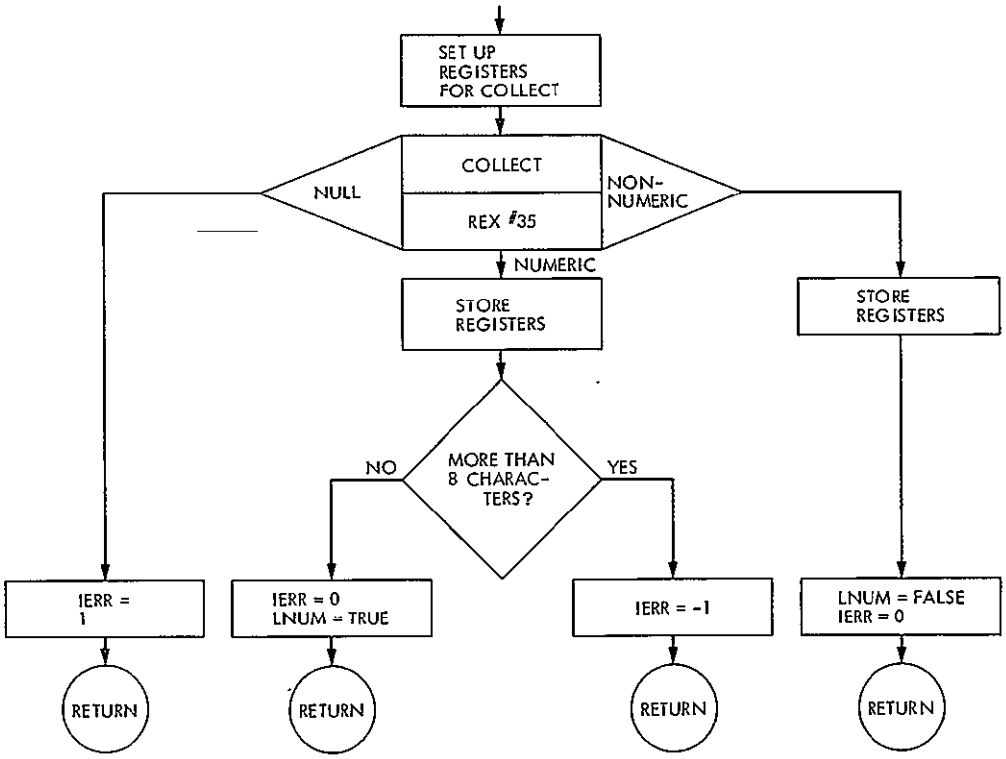

Fig. B-4. COLLECT (IERR, LNUM)

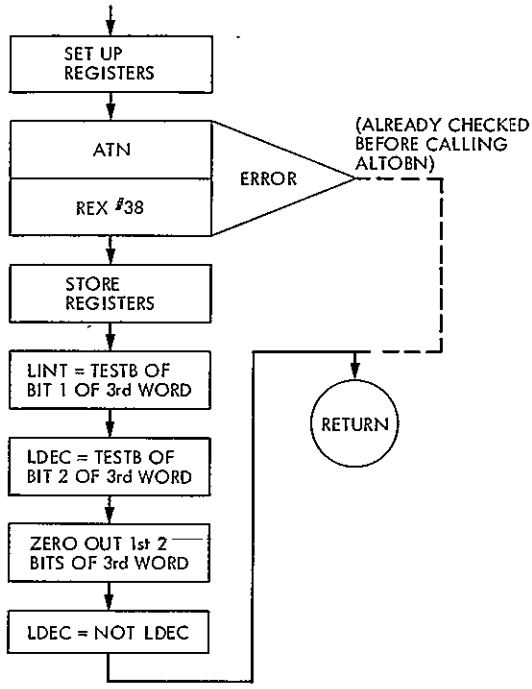

Fig. B-5. ALTOBN (LINT, LDEC)

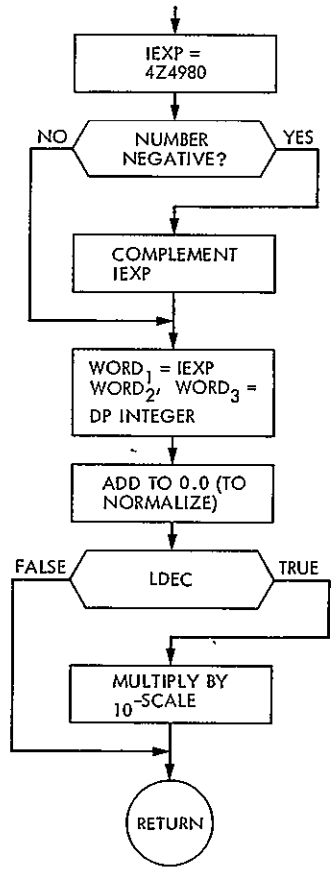

Fig. B-6. INTFP

Discovery and Repair of Software Anomalies

R. C. Tausworthe
DSN Data Systems Section

This article presents a simple model which explains anomaly discovery and repair phenomena when applied to variations in work load and multiple-stage testing. The theory shows that estimates of anomaly levels and team capability can be predicted after a significant fraction of the anomalies has been found, and indicates procedures for applying these figures to schedule estimation and work-load assignment. Of particular interest is the demonstration that end-to-end testing of programs in other than the operational environment is not generally cost effective.

I. Introduction

Almost every software project enters a phase where it is "90 percent complete," in which it seemingly remains for a very disproportionate length of time before true completion. Much of this time, as it turns out, is spent discovering and repairing anomalies in the program, operations manuals, or program requirements. The number and kinds of anomalies in a software package are matters of *fact* and not matters of probability; however, since only a relatively small portion of a large program's documentation and response can ever be verified in a practical sense, the process of discovering anomalies appears to be a random process.

Repairing an anomaly requires study, software alteration, and then reverification. Because the differing kinds of anomalies exhibit a range of difficulty, and because human interaction is always required, the repair rate also appears to be a random quantity.

This article evaluates the average time required to discover and repair anomalies which appear randomly in testing. "Testing" here refers to the end-to-end tests performed after the programming is complete. Anomalies are assumed few enough that their discovery is not so rapid as to swamp out the efforts of the test team. The work bases its evaluations on a Markov model (Ref. 1) with time-independent parameters. The assumptions made about the discovery and repair process are: (1) the probability that a test will find a new anomaly is proportional to the number of undiscovered anomalies yet in the system, and (2) the probability that an anomaly remains unfixed decreases exponentially in the time since its discovery. Both of these assumptions are intuitively based, but appear to be supported well by empirical data (Refs. 2, 3, and 4).

The goal of this evaluation is not so much to model or characterize precisely the way anomalies are detected and removed, but to provide a schedule prediction tool and status

monitor for software project managers. Although statistical, the method does allow extrapolations to be made early in testing so that resource reallocations, if necessary, can be made to align completion dates with committed capabilities.

The method accommodates variations in work loads and multistage testing in different sub-operational environments.

II. Discovery of Anomalies

Let us suppose that a system possesses A (number unknown *a priori*) anomalies, and that a constant effort is being applied toward the discovery of these. Having found n of these (define this as state E_n), let us further suppose that the probability of finding the next (moving to state E_{n+1}) is proportional to the number yet remaining, that is, we shall assume that a transition from state E_n to E_{n+1} in the time interval $(t, t + \Delta t)$ will take place with probability $\lambda_n \Delta t = (A - n)\ \alpha \Delta t$ for some appropriate constant α. Feller (Ref. 1) gives the general form for the state probabilities $P_n(t)$ as a function of time:

$$\begin{aligned} P_0'(t) &= -\lambda_0 P_0(t) \\ P_n'(t) &= -\lambda_n P_n(t) + \lambda_{n-1} P_{n-1}(t) \end{aligned} \tag{1}$$

The latter equation serves for $n = 1, \cdots, A$. The general solution may be found by straightforward application of the generating-function method, in which

$$\Phi(x, t) \triangleq \sum_{n=0}^{A} P_n(t) x^n \tag{2}$$

yields a partial differential equation

$$\frac{\partial \Phi}{\partial t} = \alpha (x - 1)\left(A \Phi - x \frac{\partial \Phi}{\partial x}\right) \tag{3}$$

whose solution (Ref. 4) is

$$P_n(t) = \binom{A}{n} e^{-\alpha A t} (e^{\alpha t} - 1)^n \tag{4}$$

Having this expression, we may proceed to compute the mean time to discovery of the nth anomaly: The probability (density) that the nth anomaly is discovered at time T_n is the probability that $n - 1$ anomalies had been found by $T_n - \Delta t$; times the probability, $\lambda_{n-1} \Delta t$, that the transition $E_{n-1} \rightarrow E_n$ occurs during the last Δt interval. As $\Delta t \rightarrow 0$, we reach the limiting equation

$$p_n(T) = \lambda_{n-1} P_{n-1}(T) \tag{5}$$

The generalized moments of this density are then

$$\begin{aligned} \text{avg}\,(T_n^m) &= \int_0^\infty T^m p_n(T)\, dt \\ &= \left(\frac{m!}{\alpha^m}\right)(A + 1 - n) \binom{A}{n - 1} \\ &\quad \times \sum_{k=0}^{n-1} \binom{n - 1}{k} \frac{(-1)^k}{(A_0 + 1 - n + 1)^{m+1}} \end{aligned} \tag{6}$$

The first two of these moments can be evaluated directly to produce mean and variance values

$$\overline{T}_n = \frac{1}{\alpha} \sum_{k=0}^{n-1} \frac{1}{A - k} = \frac{1}{\alpha} [\psi(A + 1) - \psi(A + 1 - n)]$$

$$\text{var}\,(T_n) = \frac{1}{\alpha^2} \sum_{k=0}^{n-1} \frac{1}{(A - k)^2} \tag{7}$$

The ψ-function is the "digamma" function, Γ'/Γ, in Ref. 5. The mean-to-deviation ratio is thus

$$\frac{\text{var}\,(T_n)}{\overline{T}_n^2} = \frac{\displaystyle\sum_{k=0}^{n-1} \frac{1}{(A - k)^2}}{\left(\displaystyle\sum_{k=0}^{n-1} \frac{1}{A - k}\right)^2} \tag{8}$$

The behavior of this ratio is shown in Fig. 1, and the normalized mean time to reach the nth anomaly is displayed in Fig. 2. The normalization in Fig. 2 is set to make the initial rates of anomaly discovery equal.

The first figure shows that the relative time variance to reach the nth anomaly decreases approximately as $1/n$, except

at values where n becomes appreciable to A, whereupon it rises, ultimately reaching the value

$$\frac{\text{var}\,(T_A)}{\overline{T}_A^2} \approx \frac{1.645}{(0.57721 + \ln A)^2} \tag{9}$$

The minimum relative variance appears to occur at an n of about 80 to 85 percent of the total anomalies, and its value is about $1.5/A$.

This behavior infers that the discovery of anomalies up to about 85 percent of the total proceeds quite normally; the relative variance decreases inversely proportionally to the number found, as would be expected of a random process. The remaining 15 percent of the anomalies, however, not only require longer and longer times each to discover, but the variations in discovery times begin to grow disproportionately, as well.

The ratio $\overline{T}_n/\overline{T}_A$ represents the average relative completion status during anomaly discovery. Note in the graph of this ratio (Fig. 3), for example, that if there are 100 anomalies, then when 90 percent of them have been found, only about 44 percent of the total required time has elapsed. Therefore, if one could estimate the number of total anomalies by some figure A, he could then also estimate the time which would probably be needed to complete testing.

An approximate value for $\overline{T}_n$ is given by

$$\alpha\overline{T}_n \approx \ln x + \frac{x-1}{2(A+1)} + \frac{x^2-1}{12(A+1)^2} - \frac{x^4-1}{120(A+1)^4} + \frac{x^7-1}{252(A+1)^6}$$

$$x \triangleq \frac{A+1}{A+1-n} \tag{10}$$

A. Estimating the Unknown Parameters α and A

Upon differencing the average times to discover successive anomalies, one finds

$$\overline{t}_{n+1} \triangleq \overline{T}_{n+1} - \overline{T}_n = \frac{1}{\alpha(A-n)} = \frac{1}{\lambda_n} \tag{11}$$

The expected time to uncover the final anomaly is $1/\alpha$, or A times as long as the discovery of the first.

By assuming a Markov process, we have thereby also assumed that the time increments t_n between discoveries are independent random variables. Given that $n-1$ anomalies have so far been uncovered, the probability function for the time required to find the nth follows (5), but may be solved in terms of t_n rather than T_n by moving the time origin to $T = T_n$ and redefining $A' = A - n$, $\lambda_0' = \lambda_{n-1}$, in order that (1) may be used to find the new $P_0(t)$. Ultimately, we then find

$$p_n(t_n) = \lambda_{n-1} \exp\left[-\lambda_{n-1} t_n\right] \tag{12}$$

Because of independence, the probability density for observing the values $t_1, t_2, \cdots, t_n$ is merely the product of the corresponding densities (12), or

$$p(t_1, \cdots, t_n) = (\lambda_1 \cdots \lambda_{n-1}) \exp\left[-(\lambda_0 t_1 + \cdots + \lambda_{n-1} t_n)\right] \tag{13}$$

Equating the derivatives of (12) with respect to α and A to zero produces the maximum likelihood estimators $\hat{\alpha}$ and $\hat{A}$. These satisfy

$$\hat{A} - n = \left[\sum_{k=0}^{n-1} \frac{1}{\hat{A}-k}\right]^{-1} = \frac{\sum_{k=1}^{n} (k-1)\, t_k}{\sum_{k=1}^{n} t_k}$$

$$\hat{\alpha} = \frac{\sum_{k=0}^{n-1} \frac{1}{\hat{A}-K}}{\sum_{k=1}^{n} t_k} \tag{14}$$

The solutions for $\hat{A}$ at several given values of n are displayed in Fig. 4 as a function of computations based on observed values t_k. Use of this $\hat{A}$ and the observed data yields $\hat{\alpha}$. These estimators were previously evaluated by Jelinski and Moranda (Ref. 6).

Note from the curves that when $\hat{A} \gg n$ there is very little precision in estimating $\hat{A}$; small variations in the computed ratio yield very large uncertainty regions in $\hat{A}$. Thus, the predictors $\hat{\alpha}$ and $\hat{A}$ are not very accurate unless A is fairly large and n is appreciable to A.

Wolverton and Schick (Ref. 3) report the amazing fidelity with which these estimators predicted failures in an actual application. After $n = 26$ anomalies had been discovered, they computed via (14) the estimates $\hat{A} = 31$, $\hat{\alpha} = 0.007$/day. They thus estimated that there were 5 errors remaining and that the time to discover the next would be about $1/5\hat{\alpha} = 24$ days. They record the fact that 5 errors were then found in later testing and that, after these, the estimates became $\hat{A} = 31.6$ and $\hat{\alpha} = 0.006$/day. They concluded with the projection that another error may yet remain in the system, but, if so, it would probably require $1/0.006 = 167$ days at the same level of effort to detect. They do not record, however, whether this error was ever actually found or not.

III. Repair-Only Model

Before going into a concurrent find-and-fix model, let us first address the repair-process statistics for a simplified situation in which the number of anomalies discovered is fixed. That is, we presume that there are n initially known anomalies. The rate at which anomalies are repaired is presumed to be constant and independent of the number yet open, as long as there are anomalies left to work on; more precisely, we assume that a transition from state E_{m-1} (i.e., $m - 1$ have been repaired) at time $t - \Delta t$ to state E_m (i.e., m repaired) at time t will take place with probability $\mu\Delta t$ for some appropriately chosen constant μ, so long as $m \leqslant n$. Feller (Ref. 1) gives the governing equation for the state probabilities as a function of time:

$$P'_m(t) = -\mu P_m(t) + \mu P_{m-1}(t) \quad \text{for } m = 0, \cdots, n-1$$

$$P'_n(t) = \mu P_{n-1}(t) \tag{15}$$

The solution of these is

$$P_m(t) = (\mu t)^m e^{-\mu t}/m! \quad \text{for } m = 0, \cdots, n-1$$

$$P_n(t) = e^{-\mu t} \sum_{k=n}^{\infty} (\mu t)^k/k! \tag{16}$$

The equation for the probability (density) that the nth anomaly will be repaired at time t is similar to (5):

$$p_m(T) = \mu P_{m-1}(t) \tag{17}$$

The mean time $\overline{T}_m$ to repair m anomalies and the variance about this value are straightforwardly found by integration similar to (6), yielding

$$\overline{T}_m = m/\mu$$

$$\text{var}(T_m) = m/\mu^2$$

$$\frac{\text{var}(T_m)}{(\overline{T}_m)^2} = 1/m \tag{18}$$

This model thus predicts that all n of the known anomalies will be repaired uniformly in time with growing absolute, but decreasing relative, uncertainty. Each anomaly requires an average time $1/\mu$ to repair, with variance $1/\mu^2$.

We may argue that this model has validity for a certain span of time. Whenever the initial find-rate (λ_0 in Section II) exceeds μ, the constant fix-rate, this span of time extends from time zero until such time as there is a significant likelihood that all anomalies so far discovered will have been cleared. That is, as long as there are anomalies to work on, the rate remains unaffected by their number.

A. Estimation of the μ Parameter

The μ parameter is, of course, generally unknown *a priori*, and therefore must be estimated to be of practical utility. We expect, subject to the assumptions above, that the times t_k between repairs will take the cumulative form $\mu\overline{T}_m = m$. Having measured

$$T_m = \sum_{k=1}^{m} t_k \quad \text{for } m = 0, \cdots, M$$

we may evaluate parameters $\hat{\mu}$ and b for the line $\hat{T}_m = m/\hat{\mu} + b$ with least mean-square error from the observed values:

$$\hat{\mu}^{-1} = \frac{6}{m(m+1)(m+2)} \sum_{j=1}^{n} (m+1-j)\, t_j$$

$$b = \frac{1}{(m+1)(m+2)} \sum_{j=1}^{m} (m+1-j)(m+2-3j)\, t_j \tag{19}$$

These estimators are unbiased (i.e., $E(b) = E(1/\hat{\mu}) = 0$) and the variation in $1/\hat{\mu}$ is reflected by

$$\text{var}\,(\mu/\hat{\mu}) = (6/5)\frac{m^3 + 4m^2 + 6m + 4}{m\,(m+1)\,(m+2)^2} \qquad (20)$$

$$\sim \frac{6}{5m} \text{ for large } m$$

B. Zero-Defects Estimation

The condition in which all known anomalies have been fixed is known as "zero defects." Its more precise characterization when discovery and repair are concurrent will be addressed a little later; for the moment, however, we may estimate when the first zero-defects condition will occur, on the average, using the models of this and the preceding sections. It will occur for $n < A$ when the repair time for n anomalies equals the discovery time for these anomalies plus the extra time needed to fix the last-discovered anomaly, so long as this extra time is not long enough to discover the next anomaly. This situation is described by

$$\frac{A}{(n-1)} \sum_{k=0}^{n-1} \frac{1}{A-k} = \frac{A\alpha}{\mu} < \frac{A}{A-n} \qquad (21)$$

Estimated values for $\hat{\alpha}$, $\hat{A}$, and $\hat{\mu}$ thus provide a means for predicting the first zero-defects time. The prediction is perhaps most easily determined graphically, as indicated in Fig. 5. On reaching zero defects, there remain $A - n$ anomalies yet to be found. The ratio $r \triangleq (A-n)/A = 1 - n/A$, i.e., the fraction of the anomalies undiscovered at the time of zero defects, is a function of the initial find-fix-rate ratio $\lambda_0/\mu = A\,\alpha/\mu$, governed by (21). The behavior of r vs λ_0/μ is shown in Fig. 6.

IV. Concurrent Discovery and Repair

This section formulates the equations which govern discovery and concurrent repair of anomalies; however, closed-form solutions for such things as the average number of open anomalies at any time, the average time to a zero-defect condition, etc., are not yet known. The equations which describe the probability $P_{n,m}(t)$ that n of A anomalies have been discovered by time t, and m have been fixed, are a generalization of (1) and (15):

$$\begin{aligned}
P'_{0,0} &= -\lambda_0 P_{0,0} \\
P'_{n,0} &= -(\lambda_0 + \mu - \alpha n) P_{n,0} + [\lambda_0 - \alpha(n-1)] P_{n-1,0} \\
&\quad \text{for } n > 0 \\
P'_{n,m} &= -(\lambda_0 + \mu - \alpha n) P_{n,m} + [\lambda_0 - \alpha(n-1)] P_{n-1,m} \\
&\quad + \mu P_{n,m-1} \text{ for } 0 < m < n < A \\
P'_{n,n} &= -(\lambda_0 - \alpha n) P_{n,n} + \mu P_{n,n-1} \text{ for } n > 0
\end{aligned} \qquad (22)$$

Of course, these equations can be solved recursively as, for example,

$$\begin{aligned}
P_{0,0}(t) &= e^{-\lambda_0 t} \\
P_{1,0}(t) &= \lambda_0 e^{-\lambda_0 t}\,[1 - e^{-(\mu-\alpha)t}]/(\mu - \alpha)
\end{aligned} \qquad (23)$$

and so on.

By extending the generating functions described by (2) to accommodate the present case,

$$\begin{aligned}
\Phi(x,y,t) &\triangleq \sum_{n=0}^{A} \sum_{m=0}^{n} P_{n,m}(t) x^n y^m \\
\Delta(x,y,t) &\triangleq \sum_{n=0}^{A} P_{n,n}(t) x^n y^n
\end{aligned} \qquad (24)$$

Then the system displayed in (22) can be written in the partial differential equation form

$$\frac{\partial \Phi}{\partial t} = \alpha(x-1)\left[A\Phi - x\frac{\partial \Phi}{\partial x}\right] + \mu(y-1)(\Phi - \Delta) \qquad (25)$$

As may be noted, the case with $y = 1$ is identical to Eq. (3), since

$$P_n = \sum_{m=0}^{n} P_{n,m}$$

However, a direct solution to (25) has not been forthcoming since Δ is unknown until Φ is found and vice versa. Thus,

further work is needed to solve or approximate the statistics of this more general case.

V. Effects of Variation in Effort

The models so far described have assumed that constant levels of effort were being applied to finding and fixing of anomalies. This assumption is tantamount to equating time and expended effort in the equations previously derived. In actuality, the effort profile may be variable for a number of reasons, among which are manpower phasing, availability of computer resources, and availability of software resources.

It is typical that effort during the early testing is at a rather lower level than later on, because "things are getting up to speed." Effort is being put into planning, coordination, and resource acquisition rather than actual testing. Toward the end, effort may also drop again, to the level supported by sustaining personnel. This phenomenon is illustrated in Fig. 7. In this figure, one person is applied for 7 days, 7 for 25, 4 for 22, and 2 for 30 days.

These efforts tend to distort the anomaly vs time curves shown previously. However, we may compensate for these by replacing the time variable t in previous calculations by the integral of the work-level profile, $\int w(t)\,dt$. An illustration of this principle appears in Fig. 8.

Conversely, one may compensate in reverse; that is, the anomaly vs effort behavior may be plotted and analyzed using the previous estimators, then translated via the projected work-level profile to produce estimates of anomaly status at future dates.

VI. Cascaded Testing

Even when work profile effects are factored in, it is frequently the case that the discovery of anomalies takes place in varying environments for supposed economic reasons. Certain anomalies may not be discoverable in one environment, but perhaps in another, due to the differing software or hardware configurations.

For example, if a set of real-time programs are first tested outside the real-time environment, those anomalies which are due to the real-time interaction among programs are perhaps undiscoverable until the programs are integrated into their true operational environment.

In such situations, only a portion A_1 of the total anomalies will be found during the first testing, no matter how long testing goes on. If the second stage takes place in the operational environment, then $A - n$ become discoverable during this stage ($n \leqslant A_1$ being the number discovered in stage 1). Typical projects generally find only about half of the total anomalies in this first state.

This phenomenon is illustrated in Fig. 9, assuming the same constant level of effort α, 100 total anomalies, and $A_1 = 50$ findable during the first stage. Switching to the operational environment takes place at 45 errors, or 90 percent of those that can be found. As may be seen, multistage testing may take a significantly longer time (31 percent in the illustrated case) to find all anomalies.

Moreover, the test time requirements on usage of the operational facility are about the same (52 vs 46 days) in either case; that is, there is probably no significant savings in the use of the more expensive facility! Therefore, unless there are other overriding constraints which mandate multistage testing, this form of "bottom-up" anomaly discovery plan cannot be cost effective.

VII. Conclusions

Although a general solution to the discovery and concurrent repair model may not be known at this time, solutions to the simpler underlying component models are given, valid when discovery and repair processes are non-interacting. These solutions permit the estimation of model parameters and the subsequent forecast of project completion dates. The accuracy of forecasting is also obtainable, to evaluate the need for contingency planning.

Inasmuch as the models studied here probably represent a fairly optimistic view of anomaly data, the results of this article tend to point out those things which *cannot* be gleaned from such data, perhaps more than revealing what things can accurately be deduced.

For example, the curves in Fig. 4 allow predictions of the total number of anomalies to be made. The fundamental truth contained in that figure is that an accurate estimation of the total number of anomalies requires testing a system which has many anomalies to begin with, of which a significant fraction must already have been found. Figure 2 echoes this fact.

Having estimated that a certain significant fraction, say, 90 percent, of the anomalies have already been found, Fig. 3 permits one to estimate how much time is yet required to find the remaining 10 percent. If there are 1000 estimated in all, the remaining 100 will require more than twice as much time to uncover as has already been spent! But the lesson here is that, although disproportionate, that time requirement is not unnatural or unreasonable.

Figure 1 shows that once 80 to 85 percent of the anomalies have been found, the expected discovery rate is subject to wider and wider variations; if schedules are being set or forecasts being made requiring contingencies or reapportionment of resources, such variances need to be taken into account in order to avert disasters. The lesson from this figure is that it is not realistic to believe the last 15 percent of anomalies will even progress as smoothly as the first 85 percent, in addition to requiring a disproportionate time.

This article has shown how the effects of a variable work profile can be used to influence the rate of discovery or repair. Also, it has shown that cascaded-stage testing is probably more expensive than single-stage end-to-end tests in the final operational environment.

Figure 10 is an actual anomaly history; unfortunately, the work profile is not available, so a detailed comparison with the theory presented here is not possible. However, the reader will note that all of the predicted elements are present: the effects of low-level effort during the start of testing, the decreasing rate of anomaly discovery in the sub-operational testing prior to transfer, the increased rate thereafter, and the ultimate leveling off as the testing continued.

References

1. Feller, W., *An Introduction to Probability and Statistics,* John Wiley & Sons, Inc., New York, 1957.
2. Craig, G. R., *et al.,* "Software Reliability Study," TRW Systems Group Report AD-787-784 for Rome Air Development Ctr, Griffiss AFB, N.Y., Oct. 1974.
3. Wolverton, G., and Schick, R., "Assessment of Software Reliability," Proc. 11th Meeting, German Operations Research Society, Hamburg, Sept. 1972.
4. Musa, J. D., "A Theory of Software Reliability and Its Application," *IEEE Trans. Software Eng.*, Vol. SE-1, No. 3, pp. 312-327, Sept. 1975.
5. Abramowitz, M. (ed.), *Handbook of Mathematical Functions,* National Bureau of Standards, U.S. Dept. of Commerce, Applied Math Series 55, June 1964.
6. Jelinski, Z., and Moranda, P. B., "Software Reliability Research," Conf. on Statistical Methods for the Evaluation of Computer Systems, Brown University, Providence, R.I., Nov. 1971.

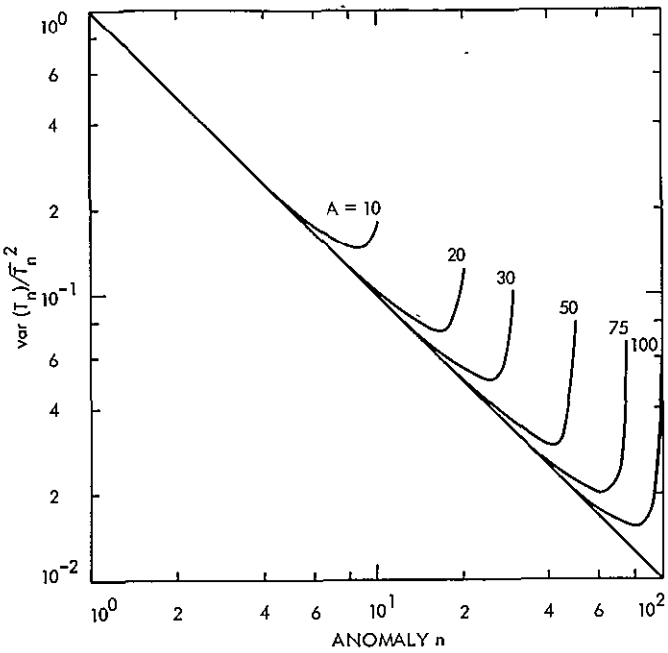

Fig. 1. Normalized variance in time to detect *n*th anomaly

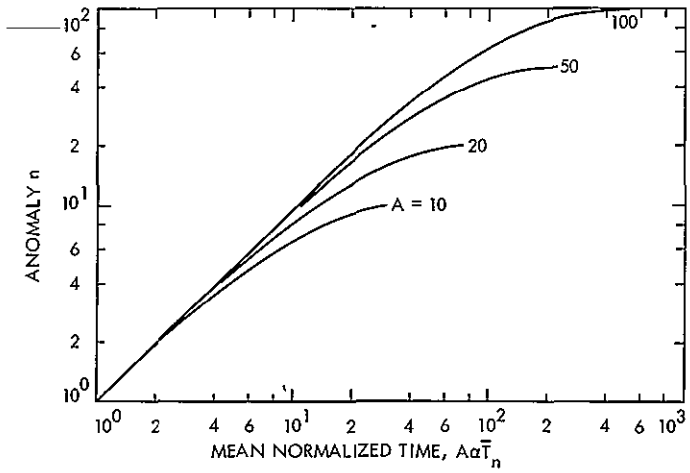

Fig. 2. Normalized mean time to reach *n*th anomaly

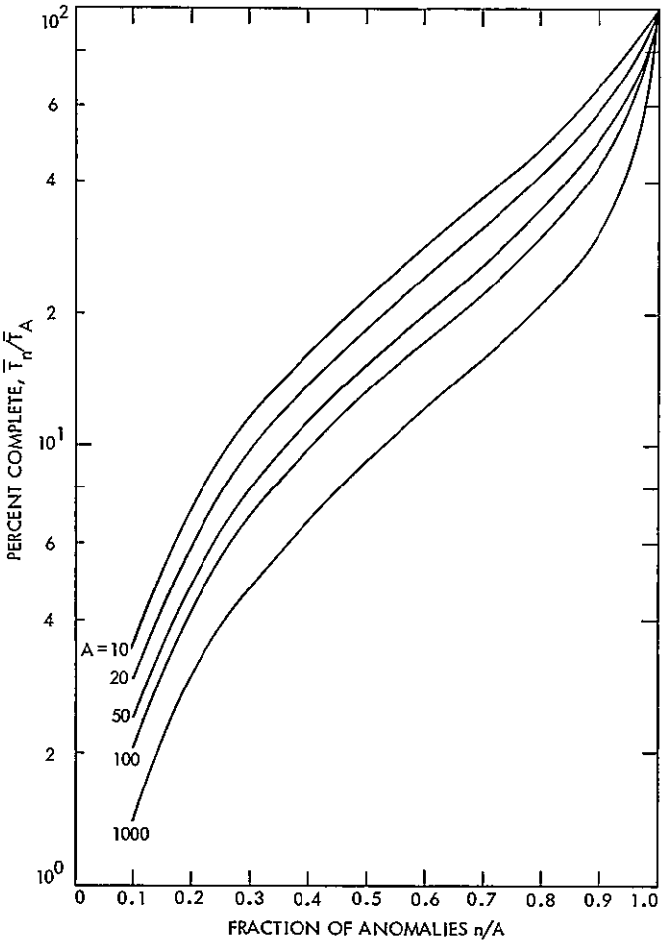

Fig. 3. Normalized expected completion ratio vs fraction of anomalies discovered

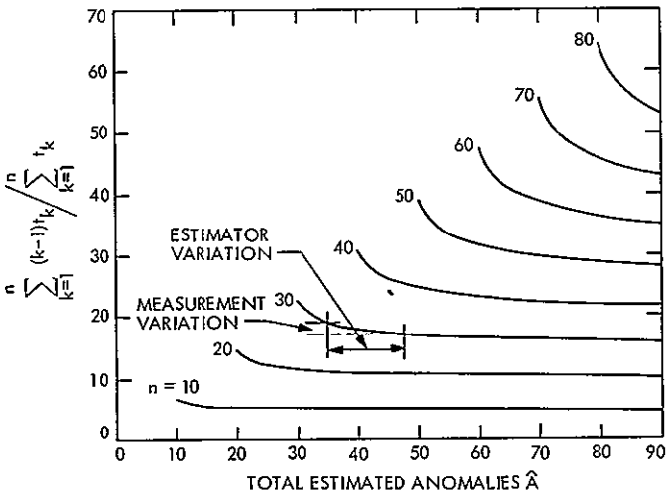

Fig. 4. Measurement ratio vs maximum likelihood estimator for number of anomalies, given the number *n* of anomalies discovered so far

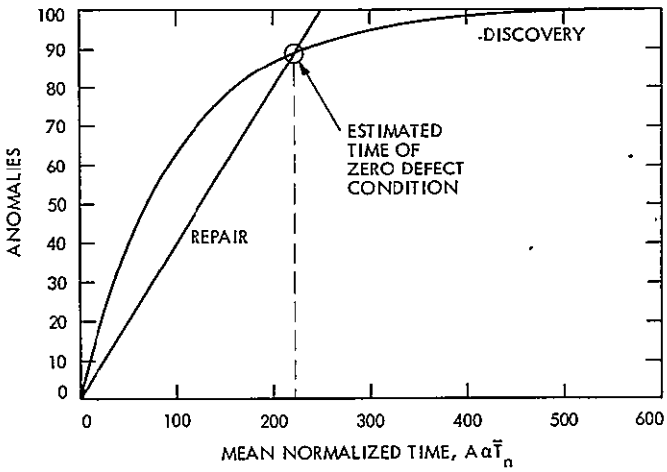

Fig. 5. Plot of Eq. (7) for $A = 100$ and Eq. (18) to estimate time of zero defects for $\lambda_0/\mu = 2.5$

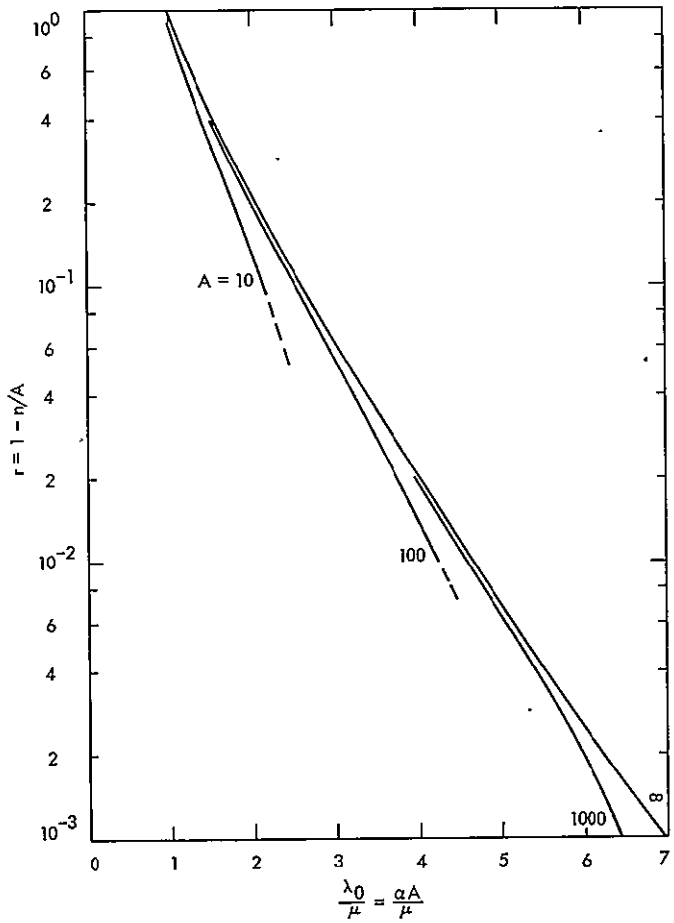

Fig. 6. Mean time intersection approximation to fraction of anomalies remaining at time of first zero-defect condition

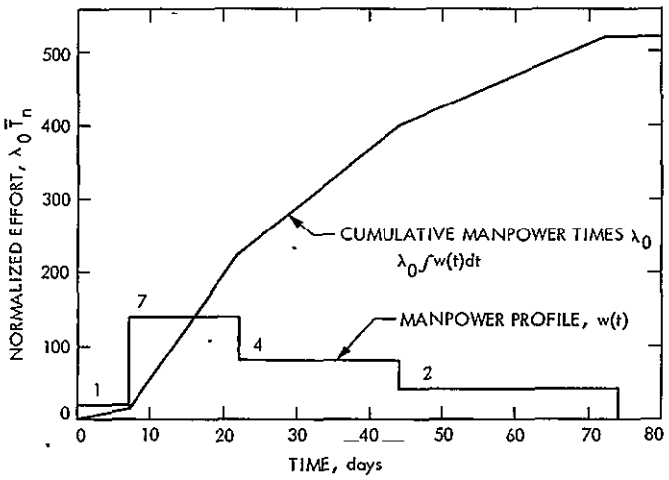

Fig. 7. Work-level profile and cumulative effort normalized by initial discovery rate of $\lambda_0 = 2$ anomalies per man-day

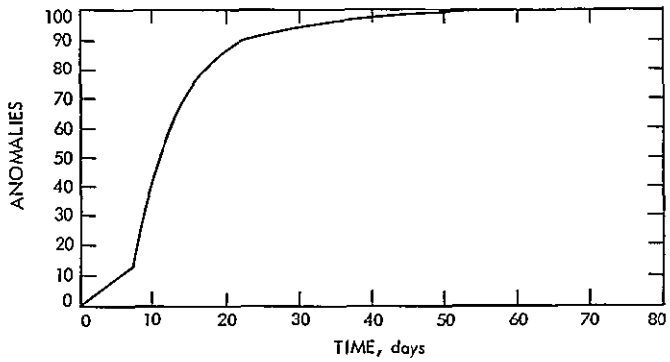

Fig. 8. Effect of work-level profile on discovery of anomalies for in Fig. 7 and $\lambda_0 = 2$ anomalies per man-day

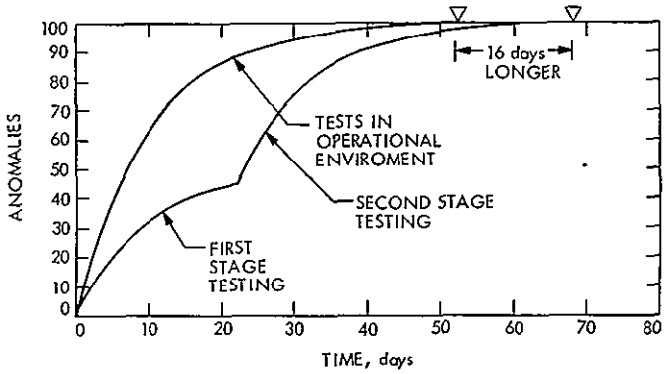

Fig. 9. Cascaded discovery of 100 anomalies in 2 stages where 50 anomalies only were visible during first stage for same $\alpha = 0.1$

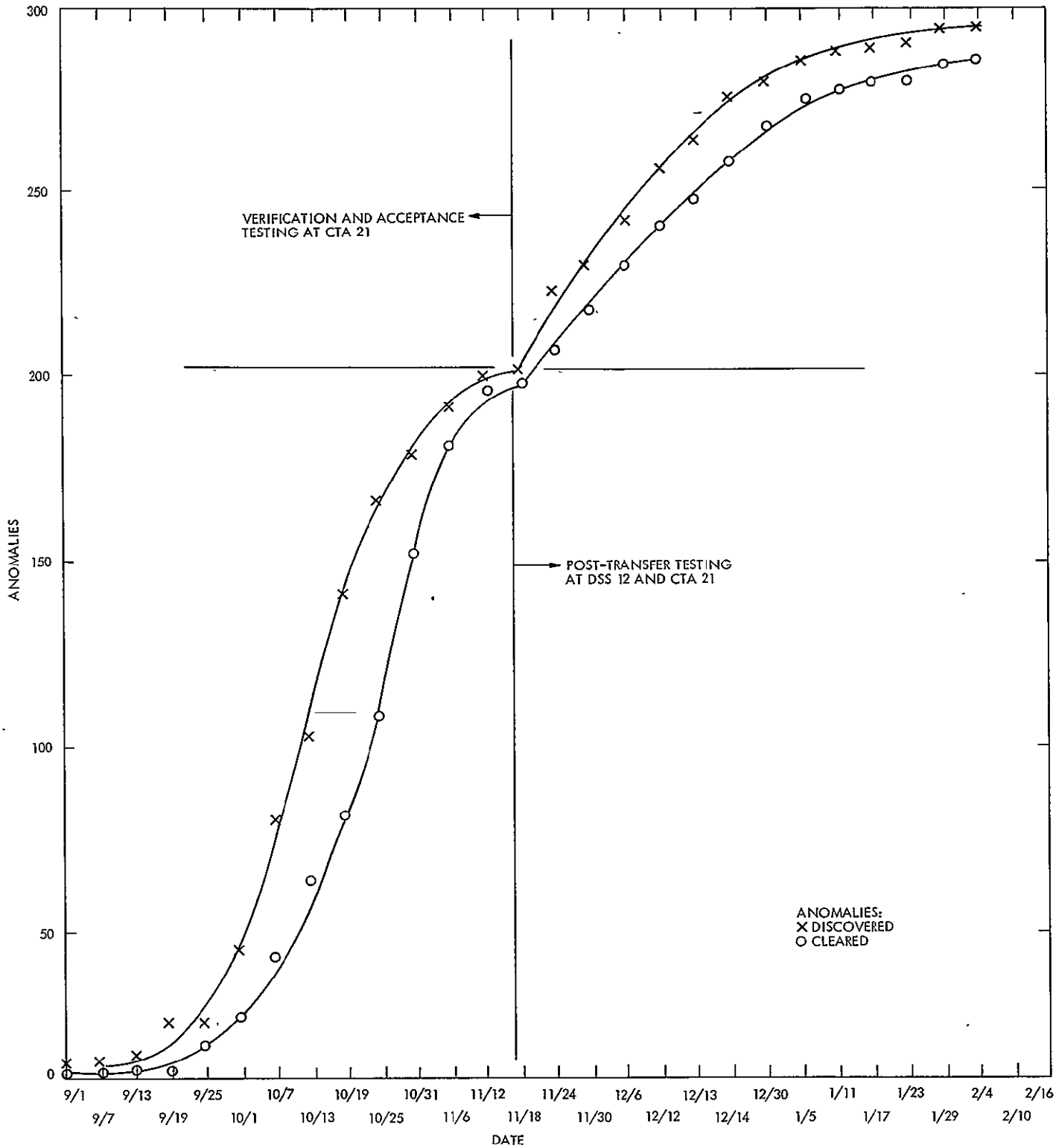

Fig. 10. Mark III Data System software anomaly history

D/10

N78-15077

A Life Cycle Cost Economics Model for Projects With Uniformly Varying Operating Costs

D. S. Remer
Communications Systems Research Section/Harvey Mudd College

A mathematical model is developed for calculating the life cycle costs for a project where the operating costs increase or decrease in a linear manner with time. The life cycle cost is shown to be a function of the (1) investment costs, (2) initial operating costs, (3) operating cost gradient, (4) project life time, (5) interest rate for capital, and (6) salvage value. The results show that the life cycle cost for a project can be grossly underestimated (or overestimated) if the operating costs increase (or decrease) uniformly over time rather than being constant as is often assumed in project economic evaluations. The following range of variables is examined: (1) project life from 2 to 30 years, (2) interest rate from 0 to 15 percent per year, and (3) operating cost gradient from 5 to 90 percent of the initial operating cost. A numerical example plus tables and graphs is given to help the reader calculate project life cycle costs over a wide range of variables.

I. Introduction

In the last two years, OTDA-TDA program reviews have emphasized DSN Cost Effectiveness. Thus DSN Cost Effectiveness is defined as end users station hours per dollars of DSN funding. DSN funding can be divided into two areas:

(1) Investment costs for new projects.

(2) Operations and maintenance costs[1] over the life of the project.

Future operating costs for a project are often more difficult to estimate than the initial project investment cost.

[1] For brevity, operations and maintenance costs (O&M) will be called operating costs in this article.

With relatively constant OTDA budgets and the growth in annual operating costs, there have been less funds available for new project implementation. The same phenomenon is occurring in other government installations. For example, the Air Force Systems Command. (Ref. 1) has seen operating costs grow from 45 percent of their budget in 1962 to 60 percent in 1975. At the same time, new project investment dropped from 55 percent of their budget in 1962 to 40 percent in 1975. This situation is depicted qualitatively in Fig. 1.

How did this situation arise where operating costs are continually consuming a larger share of the budget? There are two major reasons: (1) budget growth rates have been below inflation rates, and (2) past economic methodologies used for project evaluations accentuated the problem by trying to minimize initial investment at the expense of future operating

costs. For example, one of the most popular economic methodologies in the defense industry used to be "Design-to-Cost". This method essentially selected the project based on an initial cost criteria without considering the implications of future operating costs over the life of the project.

A relatively new economic methodology called life cycle costing (LCC) attempts to overcome these difficulties. This method incorporates into the project evaluation procedure not only the initial project costs but also the total operating costs over the project life cycle. Hopefully, the use of LCC concepts will improve the budget balance between operating costs and investments as shown by the dashed lines in Fig. 1. The purpose of this article is to propose a LCC model for use in evaluating projects that have uniformly increasing or decreasing operating costs during the life of a project.

II. Advantages and Disadvantages of Life Cycle Cost Analysis

Life cycle costs are defined as the sum of the initial investment cost plus the total operating costs over the life of the project. The goal of LCC analysis is to minimize the total cost of a project over its life time. There are several advantages and disadvantages of LCC analysis.

A. Advantages

There are three important advantages of LCC calculations. First, LCC analysis is a management tool used to select the best project among several alternatives. Second, LCC analysis is used to evaluate a specific project by doing tradeoff studies between initial investment costs and future operating costs in order to minimize total costs during a project's life cycle. There is a third less obvious advantage. The additional analysis required to estimate life cycle operating costs yields insight into reducing initial investment costs and insight into designing equipment to minimize operating costs. Let's look at an example where life cycle costing was the key to energy conservation.

A recent LCC analysis (Ref. 2) for the new 38-story Federal Reserve Bank of Boston not only resulted in reducing operating costs by $4,000 per year but also in reducing initial investment by $46,000. During the LCC evaluation of this project, it became apparent that energy costs for air conditioning this building were high. One of the design engineers proposed using aluminum shades to save energy by reducing the load on the air conditioning system. The annual operating cost savings were $4,000. In addition, the reduced air conditioning load resulted in a $180,000 investment saving because a smaller air conditioning system could now be used. This $180,000 saving was partially offset by the cost of $134,000 for the aluminum shades. The LCC analysis showed a net investment savings of $46,000 in addition to the annual operating cost savings of $4,000.

For the above building example, LCC analysis actually reduced initial investment and future operating costs; however, this is the exception rather than the rule. Usually LCC analysis results in a trade off between larger initial investment versus lower future operating costs.

B. Disadvantages

The advantages of LCC are more apparent than the disadvantages. There are two major disadvantages. First, if the estimated project life is too long, which often happens because of new technology replacing obsolete technology, then more is probably invested in the original project than is justified. For example, if LCC analysis is used to evaluate a hardware computer project, then the project life must be estimated very carefully because of rapidly changing technology. An arbitrary standard project life, 10 years is usually used for LCC in the DSN, can be very misleading for projects that wind up with a shorter life.

A second major disadvantage with LCC is developing a model to describe the operating costs over a project life time. Since the available data bases and predictive tools for estimating operating costs are usually inadequate, LCC is often very difficult, if not impossible, to apply to a real problem.

Many standard reference books on engineering economics (Refs. 3 and 4) indicate that operating costs often increase or decrease in a uniform manner with time. The goal of this article is to introduce a useful methodology to calculate LCC assuming a uniform increase (or decrease) each year in operating costs. This means that the proposed model will incorporate a uniform increasing (or decreasing) gradient function to approximate the unknown operating cost function.

III. Development of the Life Cycle Cost (LCC) Model

The following discussion of the LCC model is divided into four parts: (1) propose a model for the LCC of a project with uniformly increasing or decreasing operating costs, (2) solve the resulting analytical expression, (3) provide tables and graphs so that others can use the results, and (4) give an example to illustrate how to use the results.

A. Life Cycle Cost Model

Life cycle costs are defined as the initial costs, P, plus the sum of the operating costs, U, over the project life, n. Thus,

$$LCC = P + \sum_{j=1}^{n} U_j \qquad (1)$$

Let's assume the operating cost function, U, is a uniformly increasing function of time (later we will consider the case where it is a decreasing uniform function of time). For the purposes of this development, we will consider discrete step increases in costs rather than a continuous function because the discrete approach more closely matches our actual budgeting and forecasting system.

We will define uniformly increasing operating costs as shown in Table 1 and as illustrated in Fig. 2. The initial operating cost in year number 1 is designated by U_I^0 and the operating cost increases an amount R each year.

We now need to introduce the time value of money for these future operating cost cash flows. There is some discussion at the present time as to whether DSN should (1) discount future cash flows, (2) use a negative discount rate, or (3) ignore discounting and use no time value of money. The following LCC model will be able to accommodate all three cases and we leave it to the reader to select his preferred method. However, we prefer discounting future cash flows as shown below.

The present value, P, of a future amount of money, F, is

$$P = F(1+i)^{-n} .$$

where i is the time value of money (interest rate) per year and n is the number of years between P and F. The factor $(1+i)^{-n}$ is referred to as the discounting factor and accounts for the time value of capital. For the no discounting case we discussed earlier, i is zero. Throughout the rest of this article when we refer to LCC, we mean the present value of the LCC.

B. Analytical Solution for the Life Cycle Cost Model

The operating cost term

$$\sum_{j=1}^{n} U_j,$$

can be divided into two parts.

$$\sum_{j=1}^{n} U_j = U_c(n, i) + U_I(n, i) \qquad (2)$$

The first part, $U_c(n, i)$, represents the operating costs at any interest rate, i, and any project life, n, when the operating costs are constant throughout the project life. The second term, $U_I(n, i)$, represents the additional operating costs for any i and n assuming that operating costs increase in a uniform manner over time.

The present value of $U_c(n,i)$ is given by

$$U_c(n, i) = \frac{U_I^0}{1+i} + \frac{U_I^0}{(1+i)^2} + \cdots + \frac{U_I^0}{(1+i)^{n-1}} + \frac{U_I^0}{(1+i)^n}$$

or

$$U_c(n, i) = U_I^0 \sum_{j=1}^{n} \frac{1}{(1+i)^j}$$

and the present value of $U_I(n, i)$ is given by

$$U_I(n, i) = \frac{R}{(1+i)^2} + \frac{2R}{(1+i)^3} + \cdots + \frac{(n-2)R}{(1+i)^{n-1}} + \frac{(n-1)R}{(1+i)^n}$$

or

$$U_I(n, i) = R \sum_{j=2}^{n} \frac{j-1}{(1+i)^j}$$

It is relatively easy to show that

$$U_c(n, i) = U_I^0 \frac{(1+i)^n - 1}{i(1+i)^n}, \qquad i \neq 0 \qquad (3)$$

and

$$U_I(n, i) = R \frac{(1+i)^n - (1+ni)}{i^2(1+i)^n}, \qquad i \neq 0 \qquad (4)$$

For the case of $i = 0$, $U_I(n, 0) = Rn(n - 1)/2$ and $U_c(n, 0) = nU_I^0$.

The total present value of the LCC for a project with a life of n years and a time value of money, i, is obtained by combining Eqs. (1) and (2) to get

$$LCC = P + U_c(n, i) + U_I(n, i) \tag{5}$$

Now, by substituting Eqs. (3) and (4) into Eq. (5), we obtain

$$LCC = P + U_I^0 \frac{(1 + i)^n - 1}{i(1 + i)^n} + R \frac{(1 + i)^n - (1 + ni)}{i^2(1 + i)^n} \tag{6}$$

Equation (5) is the general analytical expression for LCC when the operating costs increase uniformly each year during the project life. The expression

$$\frac{(1 + i)^n - 1}{i(1 + i)^n}$$

is usually called the annuity present worth factor and the expression

$$\frac{(1 + i)^n - (1 + ni)}{i^2(1 + i)^n} \tag{7}$$

is usually called the gradient present with factor (Ref. 3).

For the case of uniformly decreasing operating costs, the total LCC for a project is given by Eq. (6) if we change the positive sign to a negative sign for the R term in the equation.

There are two additional things one may want to consider when calculating the total LCC of a project. First, there is the possibility that the project equipment may have a salvage value, and second, the project investment cost may be spread over several years.

A project's facilities may have some residual or salvage value at the end of the project's life. The salvage value, SV, is defined as the net realizable value after any dismantling or removal costs have been deducted from the actual cash value. The salvage value may be either positive or negative. The present value of this cash flow received n years from now with a time value of money, i, is

$$\pm SV(1 + i)^{-n} \tag{8}$$

In addition to the salvage value consideration, the project investment cost, P, may be spread over several years before startup. The total project investment is

$$P = P_0 + P_{-1} + P_{-2} + P_{-3} + \cdots$$

where the subscripts refer to the number of years prior to project startup. We have arbitrarily chosen $n = 1$ to be the first year of operation. As a result, we must compound these investment costs to calculate the total present value of these individual investments. Thus,

$$P = P_0 + P_{-1}(1 + i) + P_{-2}(1 + i)^2 + P_{-3}(1 + i)^3 + \cdots$$

or

$$P = \sum_{j=0}^{k} P_{-j}(1 + i)^j \tag{9}$$

where k is the number of years prior to project startup.

Occasionally a project will have investment costs after start-up; for this case, the investment cash flows are discounted back to $n = 0$, just like the treatment of the salvage value. Now if we incorporate the salvage value from Eq. (8) and the project investment costs from Eq. (9) into the LCC cost Eq. (6), we obtain the following general equation for the total present value of the LCC of a project.

$$LCC = \sum_{j=0}^{k} P_{-j}(1 + i)^j + U_I^0 \frac{(1 + i)^n - 1}{i(1 + i)^n} \pm R \frac{(1 + i)^n - (1 + ni)}{i^2(1 + i)^n} \pm SV(1 + i)^{-n} \tag{10}$$

C. Results from the Life Cycle Cost Model

To help calculate LCC for a project, the functions $U_I(n, i)/R$ and $U_c(n, i)/U_I^0$ are tabulated in Tables 2 and 3 for $i = 0$,

0.05, 0.10, and 0.15 and n of 2 to 30 years. A summary of this data is also shown in Fig. 3 and 4. The ratio of

$$\frac{U_I(n, i)/R}{U_c(n, i)/U_I^0}$$

indicates the large difference in LCC for a uniform increase in operating costs versus operating costs that are assumed constant over time. For example, in the DSN we often use a project life of $n = 10$ years, and lets assume $i = 0.10$, as does the Department of Defense (Ref. 5), then.

$$\frac{U_I(n, i)/R}{U_c(n, i)/U_I^0} \text{ is } 3.7$$

For most projects R/U_I^0 will be between 0.01 and 0.9. A typical value for R/U_I^0 is 0.1. Therefore, the ratio of $U_I(n, i)/U_c(n, i)$ is 0.37. If the project has uniformly increasing operating costs and one had assumed that the operating costs were constant over time, then the operating cost portion of LCC would be off by 37 percent, which is a very significant error in calculating operating costs.

The percent error in calculating DSN operating costs is summarized in Table 4 for the entire range of R/U_I^0 from 0.01 to 0.9 for $i = 10\%$ and a 10-year life.

Figure 5 shows the ratio of uniformly increasing operating costs to uniform operating costs for $i = 0.10$ and $n = 2$ to 30 years in the range of R/U_I^0 from 0.05 to 0.9. This data is shown for $i = 0.10$ because this is the interest rate most often used by government agencies such as the Department of Defense (Ref. 5).

In Fig. 6, the ratio of $U_I(n, i)/U_c(n, i)$ is shown for a typical value of $R/U_I^0 = 0.1$ and an interest rate in the range of 0 to 15 percent and project life of 2 to 30 years.

From Figs. 5 and 6, we see that the ratio of $U_I(n, i)/U_c(n, i)$, (1) increases with increasing project life, (2) decreases with increasing interest rate, and (3) increases with the ratio R/U_I^0.

D. Life Cycle Cost Example

Here is a simplified example to show how the analytical solution and accompanying tables can be used to calculate the LCC for a project.

1. **Problem Statement.** We want to calculate the LCC for a project that has an initial investment cost of \$1,000,000. The forecast for the initial operating cost is \$100,000 and these operating costs will increase \$10,000 per year. In the DSN, we usually use a project life of 10 years for LCC. Also, let's use a cost of capital of 10 percent (Ref. 5). In addition, we will assume the equipment has no salvage value. These six input variables are summarized in Table 5.

2. **Problem Solution.** The problem can be solved by using Eq. (10) or Tables 2 and 3, and Figs. 3 through 6. From Table 2, $U_I(10, 0.1)/R = 22.891$ and from Table 3, $U_c(10, 0.1)/U_I^0 = 6.145$. Therefore, $U_I(10, 0.1) = \$228{,}910$ and $U_c(10, 0.1) = \$614{,}500$. The total LCC for this project is \$1,843,410. Notice that the total LCC for this project is almost double the initial investment cost of \$1,000,000. Also, notice that if the operating costs were assumed to be constant over the project life rather than increasing a modest \$10,000/year, then the LCC would have been underestimated by \$228,910. The LCC example solution is summarized in the bottom half of Table 5. Note that the ratio of the increasing operating cost term to the uniform operating cost term is \$228,910/\$614,500 = 0.37. This ratio is summarized in Table 4 for $i = 0.10$ and $n = 10$ years, in Fig. 5 for $i = 0.10$ and n from 2 to 30 years, and in Fig. 6 for $R/U_I^0 = 0.1$ and n from 2 to 30 years.

IV. Summary

We have shown that operating costs are continuing to chew up a larger percentage of the total budget for a high technology government agency like the Air Force Systems Command. As operating costs continue to take a larger piece of the budget, investment in new projects must be reduced. As new projects are deferred or eliminated because of lack of budget funds, the present operating system becomes obsolete. The key question is this: how can this trend be turned around in an environment with a relatively constant total budget? One potential answer is to introduce a new economic evaluation procedure that will predict the total life cycle cost of a system rather than just the initial investment cost. In the past, many high technology projects have been evaluated on a design-to-cost basis, where minimizing the initial project investment was the key optimization variable rather than minimizing the total LCC.

LCC evaluation has several advantages and also several disadvantages. The advantages are: (1) to compare alternate projects, (2) to minimize the total project cost over the project life time, and (3) to give insight into reducing initial investment costs as well as insight into designing equipment to reduce operating costs. Before LCC can be calculated, penetrating cost and design questions need to be asked and

answered. This process may be as valuable as the LCC methodology itself.

One of the disadvantages of LCC is that the estimate of project life is critical in the economic calculation. If the project life estimate is incorrect, then the wrong project may be selected.

The second major obstacle to using LCC is developing a model to predict the operating costs over a project's life. This disadvantage has kept LCC analysis from being more widely used.

In this article, a simple model was proposed for predicting the operating cost function over time. This model assumed that operating costs increase (or decrease) uniformly over time. The resulting analytical solution for LCC was solved as shown below:

$$LCC = \underbrace{\sum_{j=0}^{k} P_{-j}(1+i)^{j}}_{\text{initial investments}} + \underbrace{U_I^0 \frac{(1+i)^n - 1}{i(1+i)^n}}_{\text{uniform annual operating costs}}$$

$$\underbrace{\pm R \frac{(1+i)^n - (1+ni)}{i^2(1+i)^n}}_{\text{uniformly increasing or decreasing operating costs}} \underbrace{\pm SV(1+i)^{-n}}_{\text{salvage value}}$$

The present value of the LCC is a function of the project life, n, the cost of capital, i, the increase (or decrease) of operating costs each year, $\pm R$, and the salvage value, $\pm SV$. The results of this model are shown in Figs. 3 through 6 and Tables 2 through 4. The difference between assuming a uniform operating cost function vs a uniformly increasing (or decreasing) operating cost function becomes more important as the project life increases and the cost of capital decreases. An example was given illustrating how one would apply these results to calculate LCC for a project. In this typical example, the operating costs turned out to be almost half of the total LCC for the project.

With most projects the operating costs at first decrease with experience, then level off, and finally start to increase as the equipment begins to wearout. The model described above could be used to calculate the LCC for this type of project by assuming that initially the operating costs decreased uniformly ($-R$), then leveled off during the midlife of the project ($R = 0$), and finally increased uniformly (R) as the project reaches the end of its life cycle.

V. Future Work

A. Operating Cost Function

The key unknown variable, namely, how does the operating cost function vary with time for a system or subsystem, needs to be examined in more detail by using historical data. Is the operating cost function linear as used in the model herein, or is the operating cost function some other simple or complicated function, or is the cost function the same for similar subsystems? These questions need to be tackled and answered before LCC can be applied universally.

B. Probability or Risk Analysis

The future cash flows that are used to calculate the LCC for a project have some probability or range associated with them. In other words, these estimates may not be close to the final outcome, and, in fact, rarely are. As a result, the calculation of LCC could be improved by superimposing risk or sensitivity analysis on the future cash flows. This might give a more accurate range for the LCC of a project.

C. Learning Curve

The learning curve concept has long been recognized and used in manufacturing industries. It is well known that the time to perform repetitive operations declines in a negative exponential curve. It seems reasonable then to take account of the learning curve in our LCC economic model. Preliminary work is now underway to apply the learning curve to the operating cost function.

Acknowledgment

The author wants to thank I. Eisenberger for his help in the preparation of this paper.

References

1. Gregory, W. H., "Life Cycle Cost Concept Pushed by AFSC", *Aviation Week and Space Technology,* McGraw-Hill, July 19, 1976, pp. 22-24.
2. "Life Cycle Costing Is Key to Conservation", *Engineering News-Record*, McGraw-Hill, November 13, 1975, p. 48.
3. Tarquin, A. J., and Blank, L. T., *Engineering Economy*, McGraw Hill, 1976.
4. Neuman, D. G., *Engineering Economic Analysis*, Engineering Press, 1976.
5. Schultz, G. P., *Cost Benefit Factors*, U.S. Government, Office of Management and Budget, Circular No. A-94.

Table 1. Uniformly increasing operating costs

Uniformly increasing operating costs, U_I	Time, years
U_I^0	1
$U_I^0 + R$	2
$U_I^0 + 2R$	3
$U_I^0 + 3R$	4
⋮	⋮
$U_I^0 + (n-2)R$	$n-1$
$U_I^0 + (n-1)R$	n

Table 2. Uniformly increasing annual operating costs as a function of interest rate and time, $U_I(n, i)/R$

n	$i = 0$	$i = 0.5$	$i = 0.10$	$i = 0.15$
2	1	0 907	0.826	0.756
3	3	2.635	2.329	2 071
4	6	5 103	4.378	3.786
5	10	8.237	6.862	5.775
6	15	11.968	9 684	7.937
7	21	16.232	12.763	10.192
8	28	20.970	16 029	12.481
9	36	26.126	19 422	14.755
10	45	31.652	22.891	16.980
11	55	37.499	26.396	19.129
12	66	43.624	29.901	21 185
13	78	49.988	33.377	23.135
14	91	56.554	36.801	24.973
15	105	63 288	40 152	26 693
20	190	98.488	55.407	33.582
25	300	134.23	67 696	38.031
30	435	168.62	77 077	40.753

Table 3. Uniform annual operating costs as a function of interest rate and time, $U_c(n, i)/U_I^0$

n	$i = 0$	$i = 0\,5$	$i = 0.10$	$i = 0.15$
2	2	1.859	1.736	1.626
3	3	2 723	2 487	2 283
4	4	3.546	3.170	2.855
5	5	4.330	3.791	3.352
6	6	5.076	4.355	3.785
7	7	5.786	4.868	4.160
8	8	6.463	5.335	4.487
9	9	7.108	5.759	4.772
10	10	7.722	6.145	5.019
11	11	8.306	6.495	5.234
12	12	8.863	6.814	5.421
13	13	9.394	7.103	5.583
14	14	9.899	7.367	5.725
15	15	10.380	7.606	5.847
20	20	12.462	8.514	6 259
25	25	14.094	9.077	6.464
30	30	15.373	9.427	6.566

Table 4. Ratio of uniformly increasing operating costs to uniform annual operating costs for $i = 10$ percent and $n = 10$ years

R/U_I^0	$\frac{U_I(10, 0.10)}{U_c(10, 0.10)} \times 100\%$
0.01	4
0.05	19
0.1	37
0.3	112
0.5	186
0.7	261
0.9	335

Table 5. LCC example summary

Input		
Variable	Symbol	Amount
Initial investment	P	$1,000,000
Initial operating cost	U_I^0	$100,000
Annual operating cost increase	R	$10,000/year
Time value of money	i	10%
Project life	n	10 years
Salvage value	SV	0
Output		
Increasing operating cost factor	$U_I(n, i)/R$	22.891 (from Table 2 using $n = 10$ and $i = 0$ 1)
Uniform operating cost factor	$U_c(n, i)/U_I^0$	6 145 (from Table 3 using $n = 10$ and $i = 0.1$)
Increasing operating cost term	$U_I(n, i)$	$228,910
Uniform operating cost term	$U_c(n, i)$	$614;500
Total Life Cycle Cost	LCC	$1,843,410

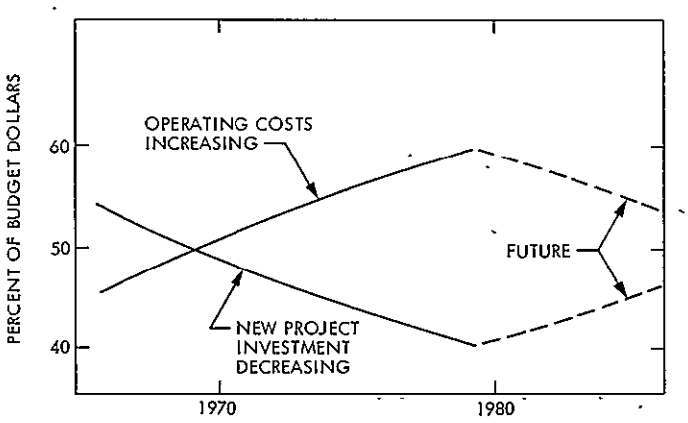

Fig. 1. Dollar allocation between new project investments and operating costs

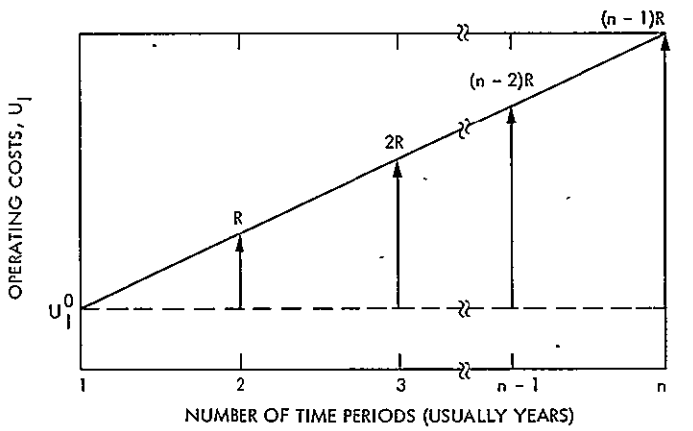

Fig. 2. Uniformly increasing operating costs

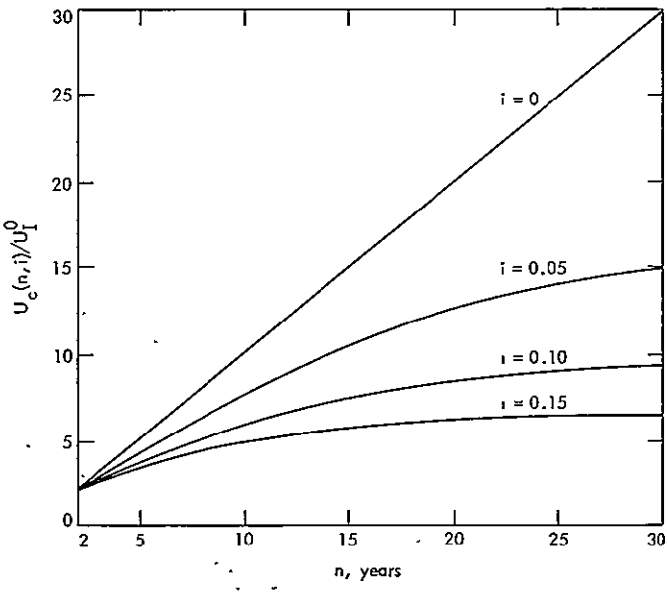

Fig. 3. Uniform operating costs as a function of interest rate and time

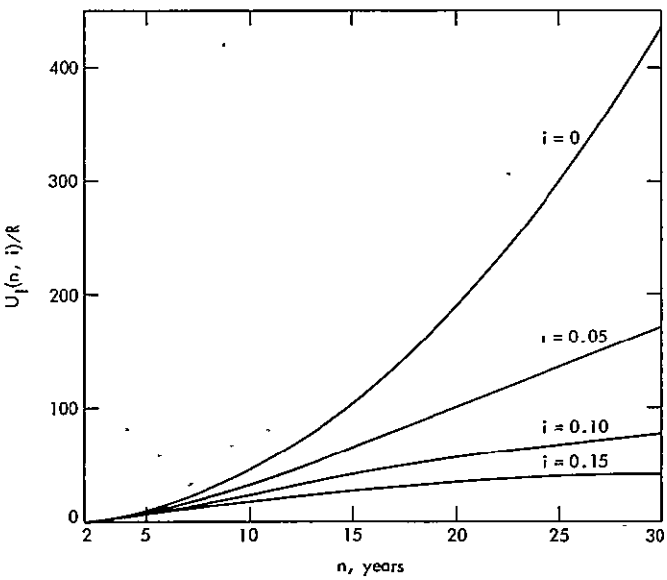

Fig. 4. Uniformly increasing operating costs as a function of interest rate and time

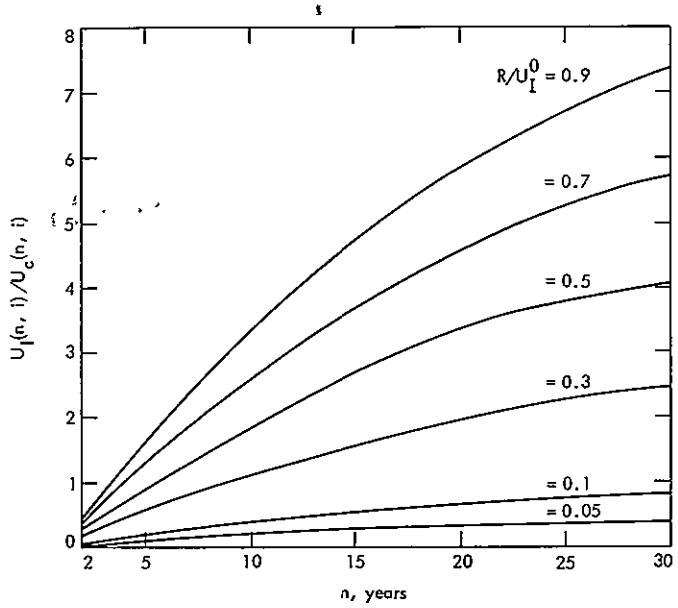

Fig. 5. Ratio of uniformly increasing operating costs to uniform operating costs as a function of time and R/U_I^0 at an interest rate of 10 percent

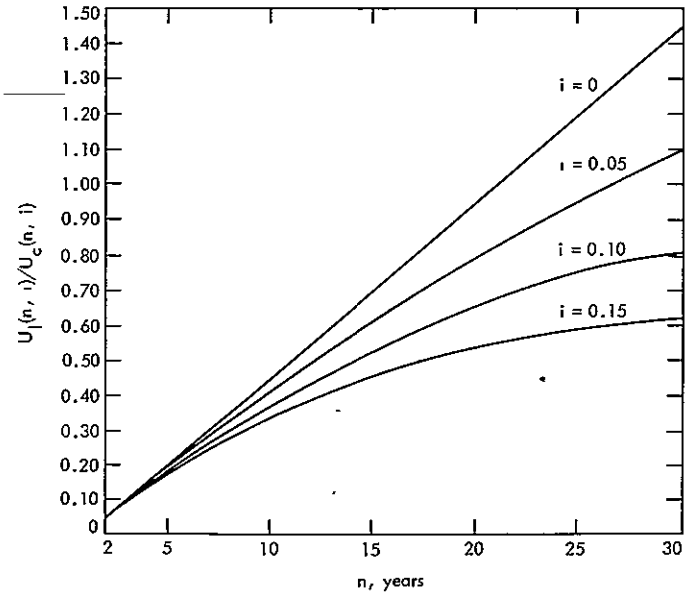

Fig. 6. Ratio of uniformly increasing operating costs to uniform operating costs as a function of time and interest rate for R/U_I^0 = 0.1

D11

N78-15078

A New Fast Algorithm for Computing a Complex Number — Theoretic Transforms

I. S. Reed and K. Y. Liu
University of Southern California

T. K. Truong
TDA Engineering Office

A high-radix FFT algorithm for computing transforms over $GF(q^2)$, where q is a Mersenne prime, is developed to implement fast circular convolutions. This new algorithm requires substantially fewer multiplications than the conventional FFT.

I. Introduction

Several authors (Refs. 1 through 3) have proposed the use of the fast Fourier transform (FFT) over finite fields or rings. Such transforms can be used to compute circular convolutions of real or complex integer sequences without round-off error (Refs. 4 through 11).

Recently, Winograd (Ref. 12) developed a new class of algorithms for computing the conventional discrete Fourier transform (DFT). This algorithm requires substantially fewer multiplications than the best FFT algorithm previously known.

Reed and Truong (Ref. 5) extended the integer transforms of Rader by defining a complex number-theoretic transform (CNT) over the Galois field $GF(q^2)$, where $q = 2^p - 1$ is a Mersenne prime. An FFT algorithm of length $d = 2^k$, where $1 \leqslant k \leqslant p + 1$, can be carried out in $GF(q^2)$ with $d \log_2 d$ multiplications. In this paper a mixed high-radix transform of $GF(q^2)$ is developed that requires only dm multiplications where m is a fractional number, depending on the factors of d, where d is an integer of form $2^k \cdot p (0 \leqslant k \leqslant p + 1)$. This algorithm for $GF(q^2)$ appears comparable in speed with that given by S. Winograd.

II. Transforms Over $GF(q^2)$

Let $GF(q^2)$ be a Galios field, where q is a Mersenne prime, and let the integer $d | q^2 - 1$. Also let the element $\gamma \in GF(q^2)$ generate the cyclic subgroup of d elements $G_d = (\gamma, \gamma^2, \cdots,$

γ^{d-1}, 1) in the multiplicative group of $GF(q^2)$. Then a transform over this subgroup G_d can be defined by the following (Ref. 5):

$$A(f) = \sum_{t=0}^{d-1} a(t)\,\gamma^{ft} \qquad \text{for } 0 \leqslant f \leqslant d-1 \qquad (1)$$

where

$$a(t) \epsilon GF(q^2) \qquad \text{for } 0 \leqslant t \leqslant d-1$$

By Fermat's theorem $2^{p-1} \equiv 1 \bmod p$. Hence $p | 2^{p-1} - 1$. Thus, $t = 2^{p+1}(2^{p-1} - 1)$ has the factor $d = 2^{p+1} \cdot p$. A mixed-radix FFT algorithm will be developed now to calculate transforms of $d = 2^k \cdot p$ points, where $0 \leqslant k \leqslant p+1$.

To perform the transform over $GF(q^2)$, where $d | 2^{p+1} \cdot p$, it is necessary to find primitive elements in the d-element cyclic subgroup G_d in $GF(q^2)$. To do this, let α be a primitive element of $GF(q^2)$. Using a computer program, one can choose an element $\alpha = a + \hat{i}b$, where $a \neq 0$ and $b \neq 0$, such that

$$\alpha^{2^{p+1}(2^{p-1}-1)/2} \equiv -1 \bmod q \qquad (2)$$

If $\alpha = a + \hat{i}b$ satisfies Eq. (2), then, by Theorem 1 of Ref. 5, $\alpha = a + \hat{i}b$ is an element of order $2^{p+1}(2^{p-1} - 1)$ in $GF(q^2)$. If $d = p \cdot 2^k$, where $1 \leqslant k \leqslant p+1$, then the generator of G_d, a multiplicative subgroup of order d, is evidently

$$\gamma = 2^{2^{p-1-k}(2^{p-1}-1)/p}$$

Also, γ^j is a primitive element in G_d for $j = 1, 3, 5, \cdots, d-1$.

Brigham (Ref. 13) shows that a mixed-radix transform of length $d = r_1 r_2 \cdots r_n$, where r_i are the n radices, requires $d(r_1 + r_2 + \cdots + r_n)$ complex additions and $d(r_1 + r_2 + \cdots + r_n)$ complex multiplications to perform a conventional mixed-radix FFT. To develop a similar mixed-radix FFT over $GF(q^2)$, it is desirable that multiplications, involving the r_i^{th} roots of unity for $i = 1, 2, \cdots, n$ in $GF(q^2)$, be accomplished by circular shifts. As we shall see, this is made possible if one chooses $d = r_1 r_2 \cdots r_n = 2^k \cdot p$, where $r_i = 2$ or 4 or 8 for $i = 1, 2, \cdots, n-1$ and $r_n = 8p$, where $0 \leqslant k \leqslant p+1$. It will next be shown that each r_i^{th} root of unity is a power of 2 modulo q for $i = 1, 2, \cdots, n$.

To see this, suppose γ is a generator of the multiplicative subgroup G_d of order d, where $d = 2^k \cdot p$ for $0 \leqslant k \leqslant p+1$. Then by Theorem 1 of Ref. 5, γ satisfies

$$\gamma^{d/2} \equiv -1 \bmod q \qquad (3)$$

But also,

$$(1 + \hat{i})^{4p} \equiv (-4)^p \equiv -1 \bmod q \qquad (4)$$

where q is the Mersenne prime $2^p - 1$ so that again by Theorem 1 of Ref. 5 $(1 + \hat{i})$ is an element of order $8p$. This result has also been given in Ref. 7. Thus, combining Eqs. (3) and (4), a generator γ of G_d satisfies

$$\gamma^{d/8p} \equiv (1 + \hat{i}) \bmod q \qquad (5)$$

By Eq. (5), a computer program can be used to find primitive element γ of G_d that satisfies Eqs. (3) and (5). Note that the powers of $\gamma^{d/8p}$ are powers of 2 modulo q, i.e., $\gamma^{d/4p} \equiv 2 \bmod q$, $\gamma^{d/2p} \equiv 2^2 \bmod q$, $\gamma^{d/p} \equiv 2^4 \bmod q$, etc.

In $GF(q^2)$, the equation $X^2 \equiv -1 \bmod q$ has the unique solutions $X \equiv \pm \hat{i} \bmod q$. Hence, $\gamma^{d/4} \equiv \hat{i}$ or $-\hat{i} \bmod q$. The powers of $\gamma^{d/4}$ are thus $\hat{i}$, $-\hat{i}$, 1, or -1.

The following theorem given in Ref. 14 is stated now without proof. It is useful for finding the eighth roots of unity in $GF(q^2)$.

Theorem 1. If $q = 2^p - 1$ is a mersenne prime, then the only solutions of $X^2 \equiv \pm\hat{i} \bmod q$ over $GF(q^2)$ are

$$X \equiv \pm 2^{(p-1)/2}(1 \pm \hat{i}) \bmod q$$

By Theorem 1, $(\gamma)^{d/8}$ is one of the forms $\pm 2^{(p-1)/2}(1 \pm \hat{i})$ mod q.

If one combines the results of the above three paragraphs, one has shown that complex multiplications by γ^{d/r_i} or its powers for $r_i = 2, 4, 8, 8p$ can be accomplished simply by circular shifts instead of multiplications. Hence, if one applies a mixed-radix FFT algorithm (Ref. 13) to a transform over $GF(q^2)$, the set of r_i-point DFT's can be evaluated without complex integer multiplications before referencing by the so-called twiddle factors. As a consequence, the maximum number of modulo $-q$ complex integer multiplications by γ^j $(j = 0, 1, 2, \cdots, d-1)$ needed for an FFT over $GF(q^2)$ is

$d(n-1)$ where $d = 2^k p$, n is the number of FFT stages, and $0 \leq k \leq p+1$. Consider now a simple example: Let

$$q = 2^3 - 1 \; ; d = r_1 r_2 = (2^3 p) \cdot 2 = 24 \times 2, \quad p = 3$$

A mixed-radix, decimation-in-frequency, twiddle factor, FFT algorithm over $GF(7^2)$ is described as follows for this example.

Let f and t in Eq. (1) be expressed in two ways as:

$$f = f_1 \cdot 24 + f_0 \equiv (f_1 f_0) \tag{6}$$

$$t = t_1 \cdot 2 + t_0 \equiv (t_1 t_0) \tag{7}$$

where

$$0 \leq f_1 \leq 1 \qquad 0 \leq f_0 \leq 23$$

$$0 \leq t_1 \leq 23 \qquad 0 \leq t_0 \leq 1$$

Substituting Eqs. (6) and (7) into Eq. (1) yields

$$A(f_1 f_0) = \sum_{t_0=0}^{r_2-1} \sum_{t_1=0}^{r_1-1} a(t_1 t_0) \gamma^{(f_1 \cdot 24 + f_0)(t_1 \cdot 2 + t_0)}$$

The mixed-radix FFT algorithm over $GF(7^2)$ for $d = 48$ points is composed of the following two successive stages of computation:

Stage 1:

$$A^{(1)}(f_0 t_1) = \left[\sum_{t_1=0}^{23} a(t_1 t_0) \gamma^{f_0 t_1 \cdot 2} \right] \gamma^{f_0 t_0} \tag{8}$$

Stage 2:

$$A^{(2)}(f_1 t_0) = \left[\sum_{t_0=0}^{1} A^{(1)}(f_0 t_1) \gamma^{f_1 t_0 \cdot 24} \right] \tag{9}$$

Since $(4 + \hat{i})^{24} \equiv -1 \bmod 7$, $\gamma = 4 + \hat{i}$ is a primitive element in $GF(7^2)$. By Eq. (5), this choice of γ yields $\gamma^2 \equiv (1 + \hat{i}) \bmod 7$. Hence, using this and the fact that $\gamma^{48} \equiv 1 \bmod 7$ and $\gamma^{24} \equiv -1 \bmod 7$, it is clear that the term $\gamma^{f_0 t_1 \cdot 2}$ in Eq. (8) can assume only the values ± 1 or plus or minus a power of $(1 + \hat{i})$.

Since multiplications involving ± 1 do not involve a multiplication, and since multiplications involving powers of $(1 + \hat{i})$ mod 7 can be achieved by circular shifts, the 24-point discrete Fourier transform in the brackets of Eq. (8) can be evaluated without a multiplier unit. The results of Eq. (8) are referenced now by multiplying the twiddle factor $\gamma^{f_0 t_0}$. This requires a total of 12 complex integer multiplications modulo 7 for evaluating Eq. (8). Since $\gamma^{24} \equiv -1 \bmod 7$, by an argument similar to that used in Eq. (8), it is clear that Eq. (9) can also be evaluated without multiplications.

The number of complex integer multiplications used to perform a mixed-radix FFT over $GF(q^2)$ of $d = r_1 r_2$ points, where $r_1 = 2^3 p$, $r_2 = 2$ or 4 or 8, and $q = 2^{31} - 1$, is given in Table 1. The present algorithm, Winograd's new algorithm (Ref. 12) and the standard FFT (Ref. 15) are compared in Table 1 by giving the number of real multiplications needed to perform these algorithms. The results for Winograd's algorithm were obtained from Ref. 11, Table 2. In Table 1, one can see that the transforms over $GF(q^2)$ of $d = 31$, 62, 124, 248 points can be evaluated without multiplications. For $d > 248$, the transforms over $GF(q^2)$ appear comparable in speed with that given by Winograd (Ref. 12).

Acknowledgment

The authors wish to thank the members of the Advanced Engineering Group in the Deep Space Network of the Jet Propulsion Laboratory for their early support, suggestions, and encouragement of the research that led to this paper. Special thanks are due to Dr. B. Benjauthrit for his attentive review of the paper.

References

1. J. M. Pollard, "The Fast Fourier Transform in a Finite Field," *Math. Comput.*, Vol. 25, No. 114, April, 1971.
2. A. Schonhage, and V. Strassen, "Schnelle Multiplikation Grosser Zahlem," *Computing 7,* 1971, pp. 281-292.
3. C. M. Rader, "Discrete Convolution via Mersenne Transforms," *IEEE Trans. on Computers,* Vol. C-21, No. 12, December, 1972.
4. R. C. Agarwal and C. S. Burrus, "Number Theoretic Transforms to Implement Fast Digital Convolution," *Proceedings of the IEEE,* Vol. 63, No. 4 April, 1975.
5. I. S. Reed and T. K. Truong, "The Use of Finite Fields to Compute Convolutions," *IEEE Trans. Inf. Theory,* Vol. IT-21, No. 2, March 1975, pp. 208-212.
6. I. S. Reed and T. K. Truong, "Complex Integer Convolutions Over a Direct Sum of Galois Fields," *IEEE Trans Info. Theory,* Vol. IT-21, November 1975.
7. E. Vegh and L. M. Leibow, "Fast Complex Convolution in Finite Rings," *IEEE Trans. on Acoustics, Speed, and Signal Processing,* Vol. Assp-24, No. 4, August 1976, pp. 343-344.
8. S. W. Golomb, I. S. Reed, and T. K. Truong, "Integer Convolutions over the Finite Field $GF(3 \cdot 2^n + 1)$," to be published in *SIAM Journal on Applied Mathematics,* March 1977.
9. I. S. Reed and T. K. Truong, "Convolutionals Over Residue Classes of Quadratic Integers," *IEEE Trans. Inf. Theory,* July 1976.
10. J. M. Pollard, "Implementation of Number Theoretic Transforms," *Electron Lett.,* 1976, Vol. 12, pp. 378-379.
11. K. Y. Liu, I. S. Reed, and T. K. Truong, "Fast Number Theoretic Transforms for Digital Filtering," *Electron Lett.,* Vol. 12, No. 24, pp. 644-646, 25 November 1976.
12. S. Winograd, "On Computing the Discrete Fourier Transform," *Proc. Nat. Acad. Math. U.S.A.*, Vol. 73, No. 4, pp. 1005-1006, April 1976.
13. E. O. Brigham, *The Fast Fourier Transform,* Prentice-Hall, Inc., 1974.
14. H. Murakami and I. S. Reed, "Recursive Realization of Finite Impulse Filters Using Finite Field Arithmetic," to be published in *IEEE Trans. Inf. Theory,* March 1977.
15. J. W. Cooley and J. W. Tukey, "An Algorithm for the Machine Calculation of Complex Fourier-Series," *Math of Comp., 19,* pp. 297-301. 1965.

Table 1. The complexity of the transform over $GF(q^2)$, where $q = 2^{31} - 1$

d	No. of real integer multiplications of transform over $GF(q^2)$ of complex data	No. of real multiplications of Winograd's new algorithm for complex data	$2d\log_2 d$ real multiplications for conventional FFT (d is a power of 2)
31	0		
30		72	295
62	0		
60		144	709
124	0		
120		288	1658
248	0		
240		648	3796
496	496		
504		1872	9050
992	1984		
1008		4212	20115
1984	5456		
2520		11232	56949

X-Band Antenna Gain and System Noise Temperature of 64-Meter Deep Space Stations

B. Benjauthrit and B. D. L. Mulhall
TDA Engineering Office

This report presents a new set of measured data on the X-band performance of the three 64-meter Deep Space Stations. These data will be useful for future mission telecommunication design and predictions. The test configuration and measurement procedure is described. A method of modelling attenuation due to the atmosphere is given. A short review of radio source brightness temperature and flux density is also included.

I. Introduction

The telecommunication design for future missions, specifically in planning for the use of a 64-meter DSS, requires precise knowledge of the system performance of each of the three Deep Space Stations.[1] Only DSS 14 performance had been measured by the Communications Elements Research Section during the X-band cassegrain experimental feedcone development stages; also, by using a noise adding radiometer, data were taken both before (January 1973) and after (May 1973) the antenna modifications (Ref. 1). Additional measurements were made in November 1974 (Ref. 2). Since the other two 64-meter antennas (DSS 43 and DSS 63) are identical in design and construction to DSS 14 before its modifications, their performance specified in the Deep Space Network/Flight Project Interface Design Handbook has been assumed to be approximately the same as that of DSS 14 before antenna modifications.

With the installation of X-band capability at DSS 43 and DSS 63, a measurement program was undertaken to determine their actual X-band performance as part of the continuing effort to upgrade the above mentioned design handbook.

This article describes the test and measurement procedure, the evaluation process, and the data obtained.

II. Test Plan and Radio Sources

Though antenna gain and system noise temperature (T_{OP}) performance curves of DSS 14 are available, in order to verify the previous results and test procedure with the Y-factor technique, the test plan called for new X-band measurements on all three 64-meter stations.

[1] Located at Goldstone, California (DSS 14), Tidbinbilla, Australia (DSS 43) and Madrid, Spain (DSS 63).

To ease the system setup and obtain accurate focussing, strong radio sources were desired. The three chosen non-thermal radio sources were 3C274 (Virgo A), 3C218 (Hydra A), and 3C123. The strength and characteristics of these radio sources at 8415 MHz are given, along with some antenna characteristics, in Table 1 (Refs. 1 and 3). The source 3C274 was the strongest and was used primarily.

III. Test Procedure

The basic principles of the test are as follows: The RF System is calibrated with the antenna at zenith. With the maser on the ambient load, variations in maser gain are recorded on the strip chart as the antenna position is changed. Having completed the maser gain measurements and focussing procedures, the measurement of the RF System parameters by "radio source tracking (by Y-factor)" is started.

A. Measurement of Receiving System Noise Temperature

A simplified X-band receiving system is block-diagrammed in Fig. 1, where:

T_A = effective antenna noise temperature

T_F = effective noise temperature of the components following the maser

T_M = effective travelling wave maser (TWM) noise temperature

T_R = effective receiver noise temperature

= $T_M + T_F$

These effective noise temperatures are all referred to the input to the maser. At stations which have no masers, they are referred to the input to the preamp. Also, all the temperatures are in Kelvins (K) [K = °C + 273.16].

The receiving system may be calibrated by using a noise diode or gas tube (hot load), T_H, a nitrogen cryogenic load, T_N, or a physical ambient load, T_P. The last approach is currently employed.

In the Y-factor technique, the Y-factor is defined by the relationship between the ambient load and the antenna as:

$$Y = \frac{T_P + T_R}{T_A + T_R} \tag{1}$$

Here, T_R is the effective receiver noise temperature and T_A defines the temperature obtained when the receiver is connected to the antenna.

From Fig. 1, the operating system temperature is given by:

$$T_{OP} = T_A + T_R \tag{2}$$

Substituting T_A from Eq. 1 in Eq. 2, and rearranging, yields

$$T_{OP} = \frac{T_P + T_R}{Y} \tag{3}$$

Thus, with T_R known and Y and T_P measured, T_{OP} can be calculated from Eq. (3).

By switching between ambient and cryogenic loads, T_R, if not known, may be determined from the relation:

$$Y_n = \frac{T_P + T_R}{T_N + T_R}$$

where T_N designates the temperature corresponding to cryogenic loads and Y_n designates the corresponding 'y' factor measurement. Note that T_R is usually constant enough that T_M and T_F need not be measured every time it is desired to measure T_{OP}.

A typical noise temperature measurement configuration is shown in Fig. 2. Measurement of the system noise temperature requires the establishment of a noise output level while the receiver input is on the ambient load. The receiver input is then switched to the antenna and the difference in attenuation required to return the receiver to the noise output reference level is then measured, yielding

$$Y = 10^{(A_P - P_A)/10} = ALOG\left(\frac{A_P - A_A}{10}\right)$$

where

A_P = attenuation reading in dB with TWM input connected to the ambient load

A_A = attenuation reading in dB with TWM input connected to the antenna

and $ALOG\,(X)$ denotes the antilog of X.

The Y-factor, together with the other system parameters, is then used in calculating the system noise temperature.

B. Radiometric Technique for Measuring System Efficiency

The radiometric technique for observing radio sources using the *Y*-factor technique is as follows:

(1) Update, if necessary, the focal adjustment setting according to a precalibrated curve. (See Fig. 3 for example.)

(2) Boresight the antenna by using the half-power point method.

(3) Steer the antenna off source (one degree in azimuth if below 45 degrees elevation, one degree in elevation if above 45 degrees elevation). Take attenuation reading (reference).

(4) Steer the antenna on source. Take attenuation reading.

(5) Repeat Step 3.

(6) Repeat Steps 3 through 5 two additional times, alternating the direction of the off-source steering.

Since the system noise temperature varies with time due to elevation angle, as roughly demonstrated in Fig. 4, the procedure described above provides a short and accurate estimate of the performance. This way the operating system temperature for each set of measurements is calculated from:

$$T_{OP}(\text{off source}) = \frac{\bar{T}_{P1} + T_R}{ALOG\left(\frac{A_{P1} - A_{A1}}{10}\right)} \qquad (4)$$

The actual source temperature of the first reading is

$$\Delta T_{A1} = T_{OP}(\text{on source}) - T_{OP}(\text{off source})$$

$$= (T_{P1} + T_R)\left[\frac{1}{ALOG\left(\frac{A_{P1} - \bar{A}_{A1}}{10}\right)} - \frac{1}{ALOG\left(\frac{A_{P1} - A_{A1}}{10}\right)}\right] \qquad (5)$$

Where $\bar{A}_{A1} = (A'_{A2} + A'_{A1})/2$ is the average of the on-source attenuation's first reading. ΔT_{A2} and ΔT_{A3} can be calculated analogously, noting that $\bar{A}_{A2} = (A'_{A3} + A'_{A2})/2$. The actual source temperature, ΔT_A, is then the average of ΔT_{A1}, ΔT_{A2}, and ΔT_{A3}.

Once the actual antenna system noise temperature is determined, the operating antenna gain can be computed from the relationships:

$$\text{Antenna efficiency} = \eta = \frac{\Delta T_A \cdot C_R}{T_A\ 100\%} \qquad (6)$$

$$\text{Antenna gain} = \eta \cdot G_{100\%} = \eta \cdot \frac{4\pi}{\lambda^2} A_p$$

$$= \eta \cdot \left(\frac{\pi D}{\lambda}\right)^2$$

or

$$\text{Antenna gain dB} = 10 \log_{10}\left(\frac{\pi D}{\lambda}\right)^2 + 10 \log_{10} \eta \qquad (7)$$

where

$T_A\ 100\%$ = ideal source temperature

A_p = physical antenna aperture area

D = physical diameter of antenna aperture

λ = wavelength of received signal

C_R = resolution correction

$G_{100\%}$ = antenna gain with 100% antenna efficiency

Determination of ideal source temperature is a subject by itself and will not be discussed here. A discussion of the subject may be found in technical description 1008B – "Radio Sources for Antenna Calibrations." The T_A 100% and C_R for 3C123, 3C218, and 3C274 were given in Table 1.

As an example, consider the set of measurements given in Table 2. From this table and Eq. (4), we have

$$T_{OP1}(\text{off source}) = \frac{12.60 + 273.16 + 8 + 1.32}{ALOG\left(\frac{52.6 - (44.5 + 44.5)/2}{10}\right)} = 45.702\ \text{K}$$

$$T_{OP1}(\text{on source}) = \frac{12.60 + 273.16 + 8 + 1.32}{ALOG\left(\frac{52.6 - 45.94}{10}\right)} = 63.670\ \text{K}$$

$$\therefore \Delta T_{A1} = T_{OP1} \text{ (on source)} - T_{OP1} \text{ (off source)} = 17.968 \text{ K}$$

Similarly, ΔT_{A2} and ΔT_{A3} can be calculated to be 17.980 and 18.366 K, respectively. Thus, the average ΔT_A is 18.108 K and

$$\text{Antenna efficiency} = \frac{18.108}{54.05} \cdot 1.13 = 0.379$$

$$\therefore \text{Antenna gain} = 10 \log \left[\frac{\pi \left(\frac{210}{2} \text{ft} \right)^2 \left(0.305 \frac{\text{m}}{\text{ft}} \right)^2}{(0.0357 \text{ m})^2} \right]$$

$$\begin{aligned} &-10 \log_{10} (0.379) \\ &= 10 \log_{10} (3.177 \times 10^7) \\ &-10 \log_{10} (0.379) \\ &= 75.02 - 4.21 = 70.81 \text{ dB} \end{aligned}$$

where $C/f = 3.0 \times 10^8 / 8415 \times 10^6 = 0.0357$ m, and C is the speed of light.

IV. Test Results and Discussion

The work to collect data on X-band antenna system noise temperature and gain to verify the data for DSS 14 and to provide actual data for DSS 43 and DSS 63 was undertaken in early September 1976. However, due to bad weather conditions and some anomalies, considerable amounts of early data were discarded. Data considered valid are provided in Figs. 5 through 7.

Figure 3 depicts a precalibrated curve for the antenna focus setting at DSS 14. This curve was obtained by a separate calibration method, which was believed to provide an accurate calibration. This may be observed from the three measured points, obtained during the test on DOY 024 (77).

With the precalibrated focus setting curve in Fig. 3, the system noise temperature vs elevation angle data for DOY 024 (77) and 052 (77) were obtained as shown in Fig. 5a. The solid curve in Fig. 5 and in some later figures was derived from a mathematical model for clear dry weather, with a constant ground temperature. It is used to reflect local ground effects of each station, as well as a reference. (To be discussed further in Section V). The zenith T_{OP} for both days is 27 K. The cloudy condition did not appear to effect the T_{OP} here significantly.

The T_{OP} data from DSS 43 for DOY 024, 040, 045, and 046 (77) are given in Fig. 5b. The lowest T_{OP} is 32 K. The overall T_{OP} is relatively high compared to that of DSS 14 and DSS 63. The discrepancies have not been identified. One possible speculation is that this may be due to ambient load noise causing receiver saturation, making the difference $A_P - A_A$ in Eq. (4) smaller, which results in apparent high measured system temperature. A slight adverse effect of heavy clouds is noticeable in the T_{OP} taken at DSS 63 on DOY 026 and 029 (77), as shown in Fig. 5c. Heavy rain data for DOY 026 (77) are shown in Fig. 5d. The rain started to subside before the data for DOY 026 (77) in Fig. 5c were taken, from 52 deg down. Figure 5e shows the T_{OP} of DSS 63 taken on DOY 037 (77). The lowest T_{OP} for DSS 63 is about 26 K.

Using the derivation described in the last section, the corresponding antenna gain curve for all three stations is given in Fig. 6. Figures 6a and 6b describe the data taken from DSS 14 on DOY 286 (76), 024 (77), and 052 (77). The data are highly packed at elevation angles above 30 deg. The peak gain is about 71.5 dB at 55 deg. Data taken below 30 deg are more scattered, especially at around 8 to 9 deg for DOY 052 (77). This data dispersion is believed to be due to scattering effects at low elevation and the lack of time for precise measurements due to quick rise of the source. Observe that with the same elevation, data from 3C218 appear to scatter more than that from 3C274, a stronger source.

The solid curves A and B are the data from Ref. 1, taken at DSS 14 before and after the antenna modifications, respectively, using the noise adding radiometer technique. They are used here as references.

The new measured data seem to indicate an improvement in gain up to 0.2 dB, compared to the May 1973 curve. No obvious interpretation was noted for this gain improvement, but it is speculated that it was due to the uncertainty of the Y-factor technique.

Figures 6c and 6d depict the gain data obtained from DSS 43 on DOY 321 (76), 024 (77) and DOY 040, 045, 046 (77), respectively. In spite of some dispersion, the majority of the data provides a definite performance pattern. The dispersion is believed to be due to the measurement process. An estimate peak gain is 72 dB at 52 deg. Note that the overall gain curve of the measured data shows an improvement of up to 0.4 dB over the January 1973 curve.

The gain data from DSS 63 are given in Figs. 6e through 6i covering test dates 301, 303, 307 (76) and 026, 029, 037 (77). The data seem to follow the May 1973 curve closely at high elevation angles. It tapers off to the January 1973 curve at low elevation angles. The peak gain is about 71.8 dB at 49 deg.

Note again, that 3C218 offered lower gain and more scattered data than 3C274. A gain performance obtained during a heavy rain is shown in Fig. 6i.

The corresponding curves of antenna efficiency versus elevation angles for all three stations of various test dates are given in Fig. 7.

An estimate of the performance of all three 64-m antenna at X-band are summarized in Table 3.

V. Antenna Performance in the Absence of Atmospheric Losses

The data presented in the previous section include attenuations due to atmosphere, ground, etc. To provide the isolated (in a vacuum) antenna performance, certain attenuation components must be removed from the measured data. To accomplish this, let us first examine the various components of the antenna operating system temperatures. It may be roughly expressed as (see Eq. 2):

$$T_{OP} = T_R + T_A, \text{K}$$

where

$T_R = T_M + T_F$

$T_A = T_{gnd} + T_{gal} + T_{atm} + T_{\text{hot body}} + T_{ar}$

T_M = effective maser temperature

T_F = effective temperature of components following the maser

T_{gnd} = effective temperature due to spillover and scattering on the ground

T_{gal} = effective galactic temperature

T_{atm} = effective atmospheric temperature

$T_{\text{hot body}}$ = effective temperature of hot body or radio source

T_{ar} = effective temperature of transmission line (coaxial line or waveguide) between antenna and receiver. It is usually small (3.88 K).

The components which give rise to T_{atm} are (see Appendix):

$$T_{atm} = \left[\frac{L_{ox} - 1}{L_{ox}}\right] T_{pox} + \left[\frac{L_{wv} - 1}{L_{wv}}\right] T_{pwv} + \left[\frac{L_{c\ell} - 1}{L_{c\ell}}\right] T_{pc\ell} + \left[\frac{L_{ra} - 1}{L_{ra}}\right] T_{pra}$$

where

$L_{ox}, L_{wv}, L_{c\ell}, L_{ra}$ = losses (in ratio) at a given elevation angle due to oxygen, water vapor, clouds, and rain, respectively.

$T_{pox}, T_{pwr}, T_{pc\ell}, T_{pra}$ = physical temperatures of the respective components

Thus, the total atmospheric attenuation at angle θ, ℓ_θ, is

$$\ell_\theta \text{ (dB)} = (\ell_{ox} + \ell_{wv} + \ell_{c\ell} + \ell_{ra}) \cdot D/a$$

where (for a uniform atmosphere, see Fig. 8)

$D = D_f = a/\sin\theta$, for a flat earth model

$D = D_r = |r \sin\theta \pm \sqrt{(r\sin\theta)^2 + 2ar + a^2}|$, for a round earth model

a = tropospheric thickness, km

r = radio earth radius = 8500 km

$= \frac{4}{3} r_e$, r_e = 6375 km, earth's radius at DSS 14

θ = elevation angle in degrees

$L_{ij} = 10^{\ell_{ij}/10}$, ℓ_{ij} in dB

The flat earth model does not hold at $\theta = 0$ deg, but otherwise provides less than 5.06% error at $\theta \geqslant 6$ deg (See Table 4)[1]. Thus, the loss in ratio at elevation angle θ, L_θ, is

$$L_\theta = 10^{\ell_z \cdot D/10a}$$

[1]The assumption $r \simeq 4/3(r_e)$ gives a negligibly small error over a more accurate model that is derived from the concept of refractive index, local elevation angles, and a variable absorption coefficient. This model was derived separately by Dr. C. A. Greenhall.

where ℓ_z is the atmospheric loss (in dB) at zenith, and is assumed to be 0.043 dB for clear dry weather.

Most of the parameters given above have been mentioned in previous sections or described in the Appendix. One possible mathematical model is given in Fig. 9,[2] for clear, dry weather (see Appendix). A plot of this mathematical model is given in Fig. 10. Curve 4 was used as a referenced curve in the last section with a constant ground temperature. The value of a is considered to be 10 km here. This is based on the assumption observed from the International Standard Atmosphere (Ref. 4) that air temperature, pressure, and water vapor do not vary appreciably in the region above 10 km, i.e., the influence of the atmosphere above 10 km to T_{OP} is small (see Fig. 11).

There are two possible ways to exclude atmospheric losses from the gain curves given in Section IV. One way is to calculate the losses directly from the recorded weather condition. Another way is to use the clear weather model (Fig. 9) as a basis and then use the difference in the operating system temperatures due to bad weather to calculate the losses due to bad weather. To employ the latter approach, one starts from the equation

$$T_{\theta B} = T_{\theta C} + \Delta T_\theta = \frac{(L_{\theta B} - 1)}{L_{\theta B}} T \tag{8a}$$

or

$$L_{\theta B} = \frac{T}{T - (T_{\theta C} + \Delta T_\theta)} \tag{8b}$$

$$T_{\theta C} = \frac{(L_{\theta C} - 1)}{L_\theta} T \tag{8c}$$

$$L_{\theta C} = 10^{0.0043D} \tag{8d}$$

where

$T_{\theta B}$ = bad weather T_A, K

$T_{\theta C}$ = clear weather T_A, K

$L_{\theta B}$ = bad weather L_θ

$L_{\theta C}$ = clear weather L_θ

ΔT_θ = T_{OP} (bad weather) $- T_{OP}$ (clear weather)

[2]Partly proposed by R. Riggs of the Telecommunication Systems Section.

T = weighted average physical temperature of troposphere and r, a, and D were defined previously (see Appendix).

Now let a_{zB} be the loss in dB due to bad weather. Then

$$L_{\theta B} = 10^{a_{zB} D/10a}$$

so that

$$a_{zB} = \frac{10a}{D} \log_{10} L_{\theta B}$$

$$= \frac{10a}{D} \log_{10} \left[\frac{T}{T - (T_{\theta C} + \Delta T_\theta)} \right] \tag{9}$$

Thus, the gain (in vacuum) performance is obtained by adding the measured gain with the loss $a_{\theta B}$ due to atmosphere. The gain performance plots with atmospheric losses removed for all three stations are given in Fig. 12, a through c.

As an example, consider T_{OP} (bad weather) = 26.83 K, T_{OP} (clear weather) = 26.5 K, $\theta = 90°$, $T = 265$ K. From Eq. (8),

$$L_{\theta C} = 1.00995, \quad T_{\theta C} = 2.61 \text{ K}, \quad \Delta T_\theta = 0.33 \text{ K}$$

so that $L_{\theta B} = 1.011$ and $a_{zB} = 0.048$ dB.

Thus, the atmospheric losses in dB at zenith due to weather is 0.048. Consequently, the loss at elevation angle θ is

$$0.0048 \, | \, r \sin\theta \pm \sqrt{(r \sin\theta)^2 + 2ra + a^2} \, | / a$$

for the round earth model. Specifically, at $\theta = 30$, the loss is 0.096 dB where $a = 10$ km and $r = 8500$ km.

Figure 13 plots the values of a_{zB} (dB) as a function of $T(K)$ and of $\Delta T_\theta(K)$, using Eq. 9. From the figure, a_{zB} varies only 0.008 dB over 50 kelvins of T, but it changes 0.344 dB over 20 kelvins of ΔT_θ. This establishes that ΔT_θ has more influence on a_{zB} than T, and that the actual value of T is not very critical in determining the atmospheric losses.

VI. Conclusions

Using the Y-factor technique, the new X-band 64-m antenna performance data appear to substantiate the past performance data taken using the noise adding radiometer

technique, but with some increase in gain for all three stations. The increase in the gain has not been identified but could easily be due to the uncertainty of the Y-factor technique. Further, heavy rains, clouds, and the strength of radio sources were observed to have strong influences on the measurement of performance of the antenna at X-band. Lastly, the overall antenna gain of DSS 14 is observed to be 0.2 to 0.5 dB lower than that of DSS 43 and DSS 63.

Acknowledgment

The authors wish to express their sincere thanks to all parties concerned from the various JPL Engineering Sections and all three 64-m Deep Space Stations in organizing and carrying this effort to a completion. Special thanks are due to R. Caswell who indefatigably collected, analyzed, and turned the data into a useable form. Appreciations are also due to D. Bathker, J. Allen, N. Fanelli, S. Slobin, and A. Caticchio for their special efforts in this regard. In addition, appreciation and acknowledgment are due to A. Freiley for transfer of R&D techniques and experience to operations environment, including major software capabilities.

Table 1. Radio source and 64-m antenna characteristics at 8415 MHz

(a) Radio source characteristics

Characteristic	Radio source		
	3C123	3C218 (Hydra A)	3C274 (Virgo A)
Type	Galaxy	Galaxy	Galaxy
Source shape	Two-dimensional gaussian	Core halo	One-dimensional gaussian
Size, arcsec	20	15 X 45, 200	1 X 45
8415-MHz flux, Janskys[a]	10	8.64	46.3
Spectral index	−0.86	−0 91	−1.02
Position (1950.0)			
Right ascension	$04^h\ 33^m\ 56^s$	$04^h\ 15^m\ 41.5^s$	$12^h\ 28^m\ 18^s$
Declination	29°34′	−11°53′ 06″	12°40′

(b) 64-m antenna characteristics

Characteristic	Radio source		
	3C123	3C218 (Hydra A)	3C274 (Virgo A)
Antenna polarization	RCP[b]	RCP	RCP
Resolution correction[c], C_R	1.006	1.06	1.13
Antenna temperature[d], T_A, 100%, Kelvins	11.67	10.09	54.05

[a] 1 Jansky = 10^{-26} W m^{-2} Hz^{-1}.

[b] Right circular polarization.

[c] 137 arcsec, half-power beam width selected.

[d] T_A 100% = 1.1674 · source flux (see Eq. A-9).

Table 2. Calculation of antenna performance (An edited version of the computer printout)

Station	14				
Feedcone	Type XRO; serial number 001; modification 00; polarization 0				
Maser	Serial number XR014				
Receiver	BLK IV, RCV 4				
I.F. attenuator	Serial number lab				
Operator	JE M				
Date (GMT)	Day number 024, year 77, HHMM 545				
Outside weather	Humidity 37 per cent; temperature 8.3°C				
Weather conditions	Clear Clear weather Sun not in beam No R.F. spur No water on horn, answer given. yes				
Radio source	3C-274				
Frequency	8415.0 MHz				
Comments					
Zero ambient load specified for maser ref./gain					
Maser off-on on ambient load	off 28.5 dB; on 52.0 dB				
Maser gain on ambient load	Ref./gain 0.0 dB; maser/gain 45.0 dB				
Ambient load temperature	12.50°C				
Maser gain	45.00 dB; follow on temp. 0.132 ± 01 K				
Maser table constants .. XR014	8395.00	8435.00	8.00	.00	.00
Antenna boresight	Dec or el 0.001 HA or az −0.010				
Block 1					
Offsets, deg	(IF reboresighted)				
Time (GMT), hour: min	06:12				
Antenna elevation angle	9.3 deg				
T_P = Ambient load temperature	12.60°C				
	Y-factor attenuator readings, dB:				
A_A = Antenna off source	44.500	44.500	44.310	44.360	
A'_A = Antenna on source	45.940	45.870	45.850		
A_P = Ambient load	52.600	52.590	52.600		
$T_R = T_M + T_F$ = 8 K + 1.32 K = 9.32 K	T_A 100% = 54.05 K				
Final				Initial average	sigma
Mean sigma antenna system temp.	45.702	44.816	43.998	44.834	.852
Source temp.	17.968	17.980	18.366	18.108	.226
Comments	3C-274				

Table 3. Measured 64-m antenna performance at X-band

64-m DSS	Zenith T_{OP} K (at 86° el)		Peak gain, dB
	Clear dry	Average	
14	26.5	27	71.5 at 55°C
43	27.5	28	72.0 at 52°C
63	24.0	25	71.8 at 49°C

Table 4. Comparison of round and flat earth models for a = 10 km and r = 8500 km

El angle, deg	D_r, km	D_f, km	% error
0	412.43	∞	∞
1	289 95	572.99	97.62
6	91.06	95.67	5.06
30	19.96	20.00	0.20
90	10	10	0

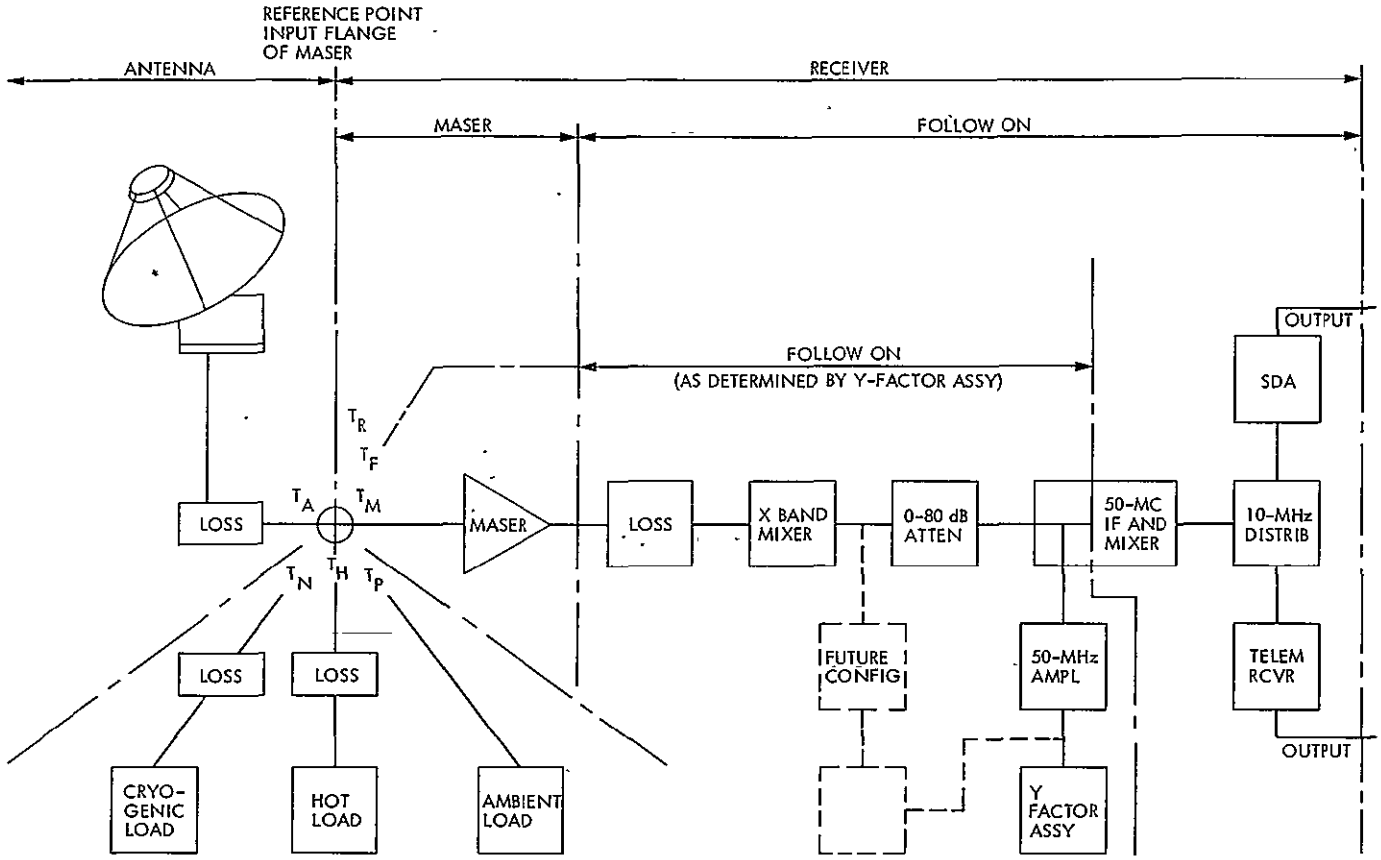

NOTE: CRYOGENIC LOAD AND HOT LOAD ARE NOT GENERALLY AVAILABLE

Fig. 1. Simplified receiving system block diagram

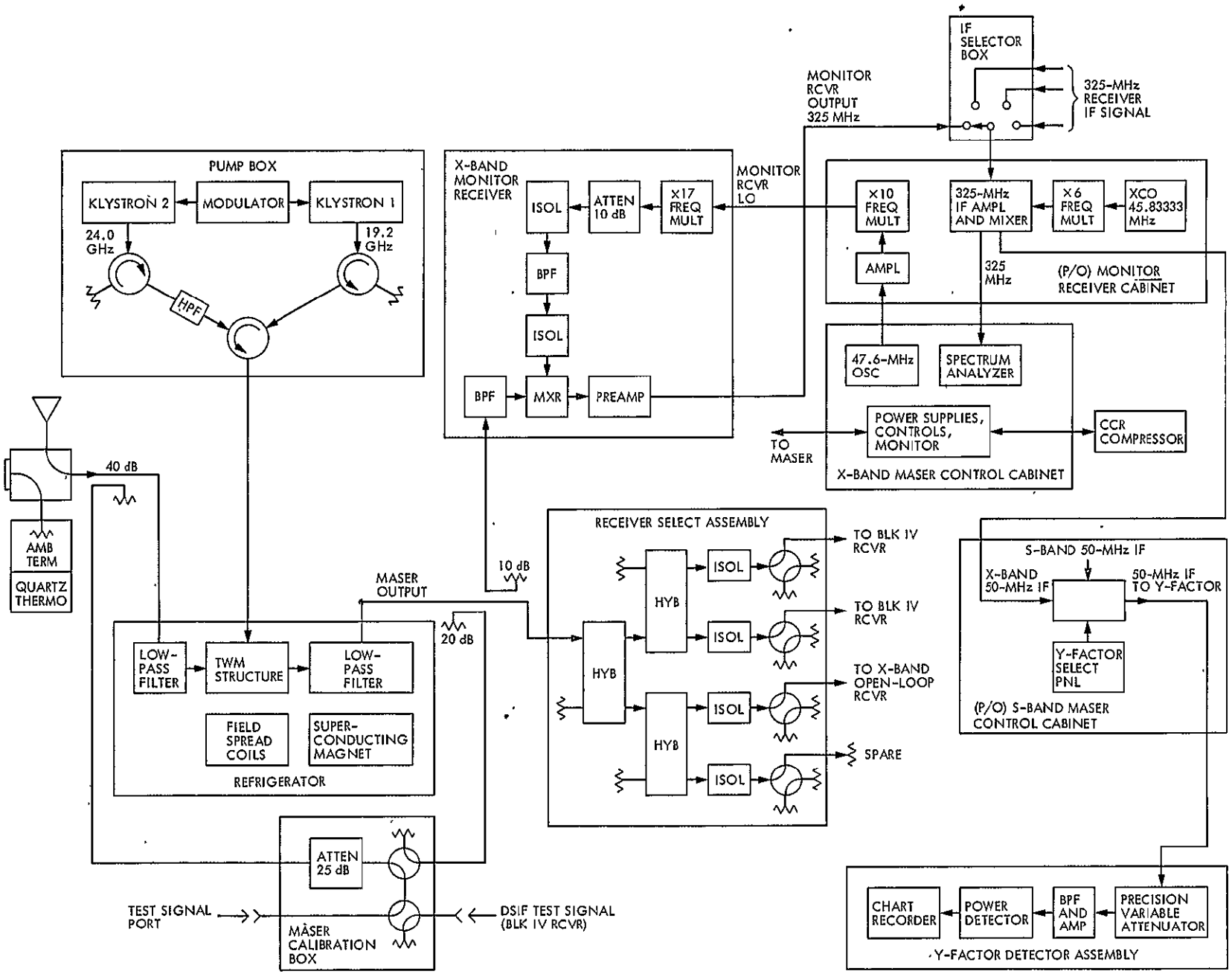

Fig. 2. X-band TWM system noise temperature configuration

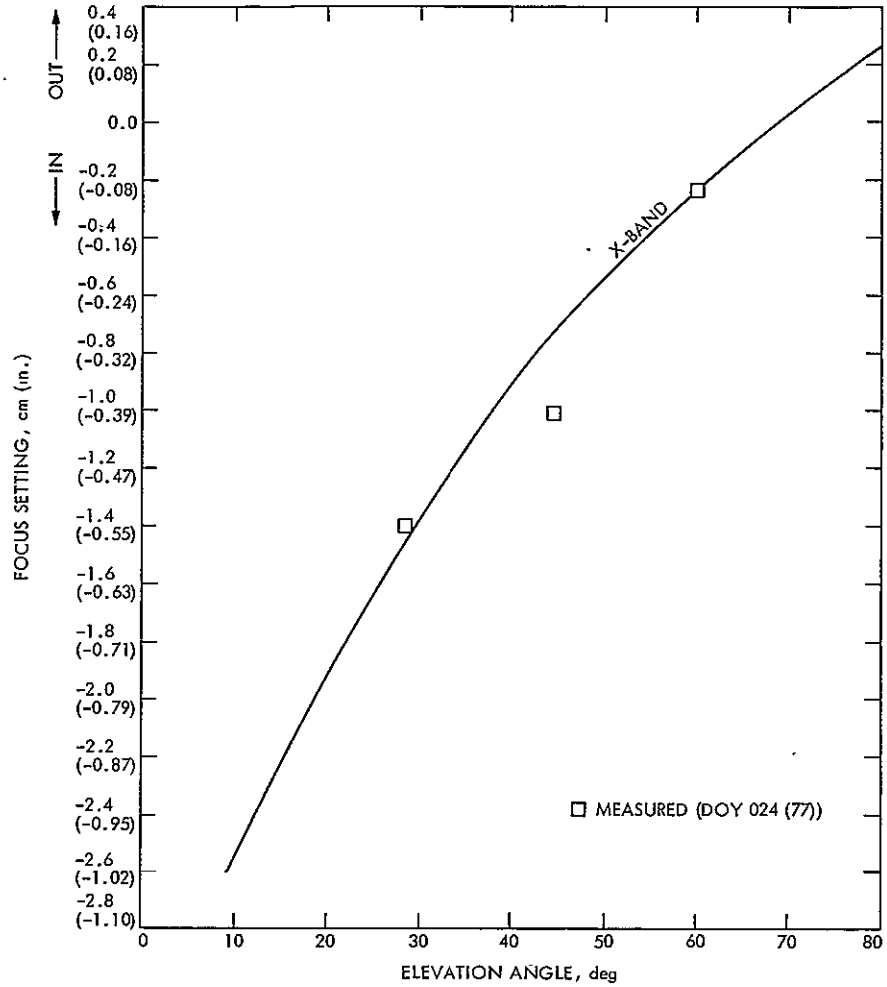

Fig. 3. DSS 14 subreflector axial position at X-band

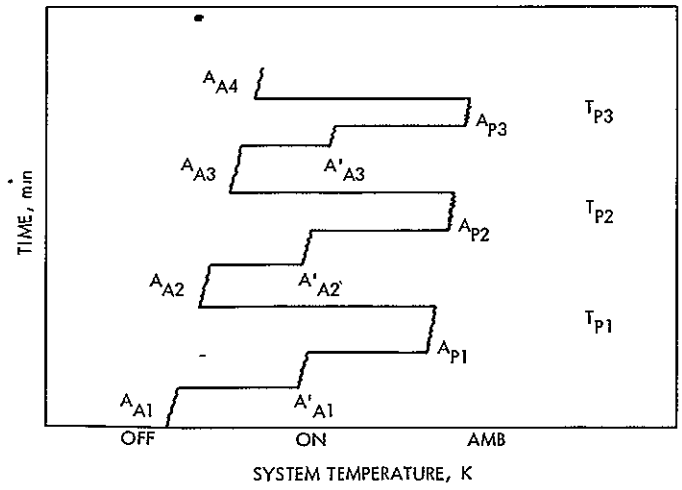

Fig. 4. System temperature varies with time due to elevation angle change

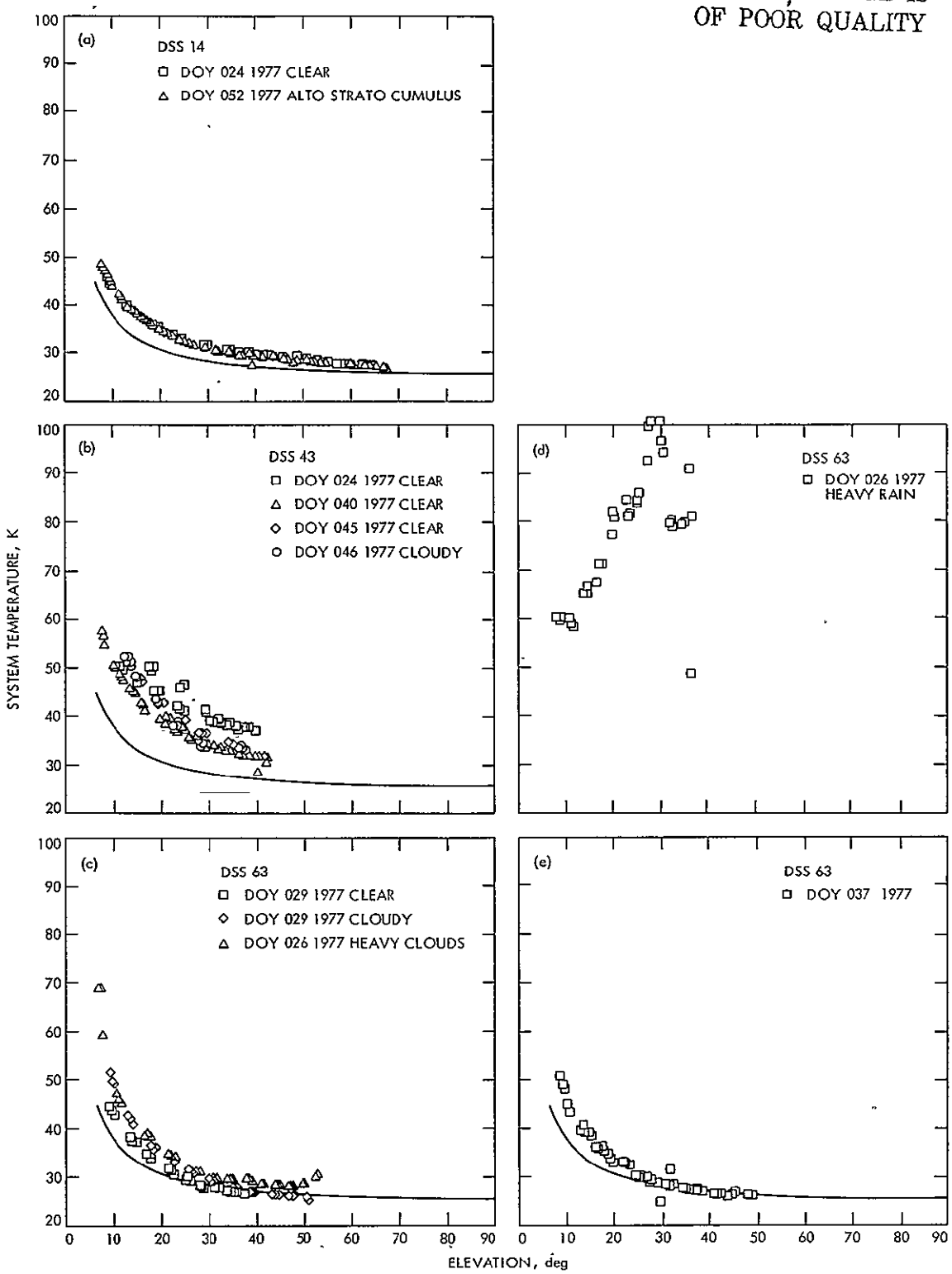

Fig. 5. System noise temperature vs elevation angle at X-band (8415 MHz): (a) DSS 14; (b) DSS 43; (c), (d), and (e) DSS 63

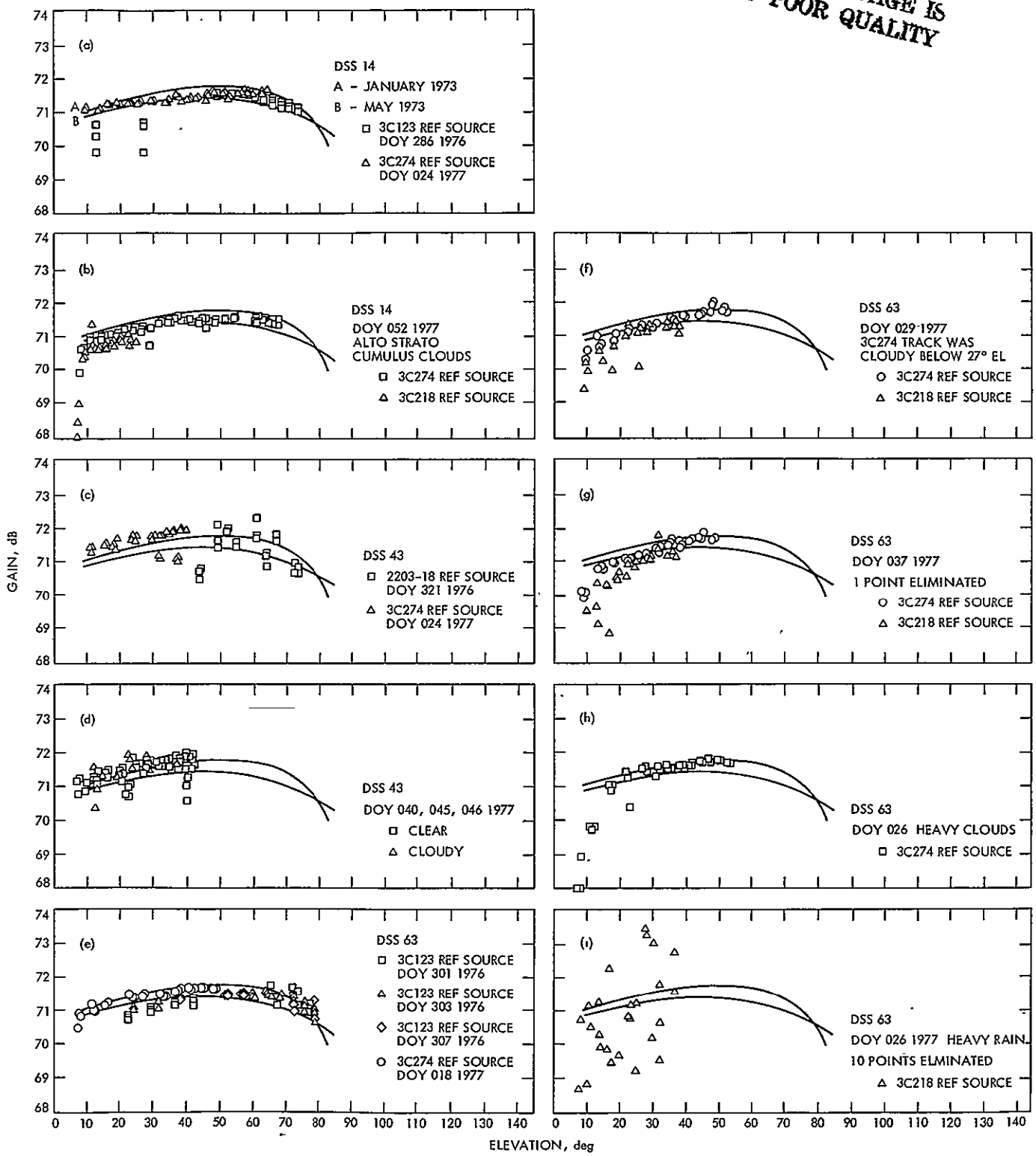

Fig. 6. Antenna gain vs elevation angle at X-band (8415 MHz): (a) and (b) DSS 14; (c) and (d) DSS 43; (e) through (i) DSS 63

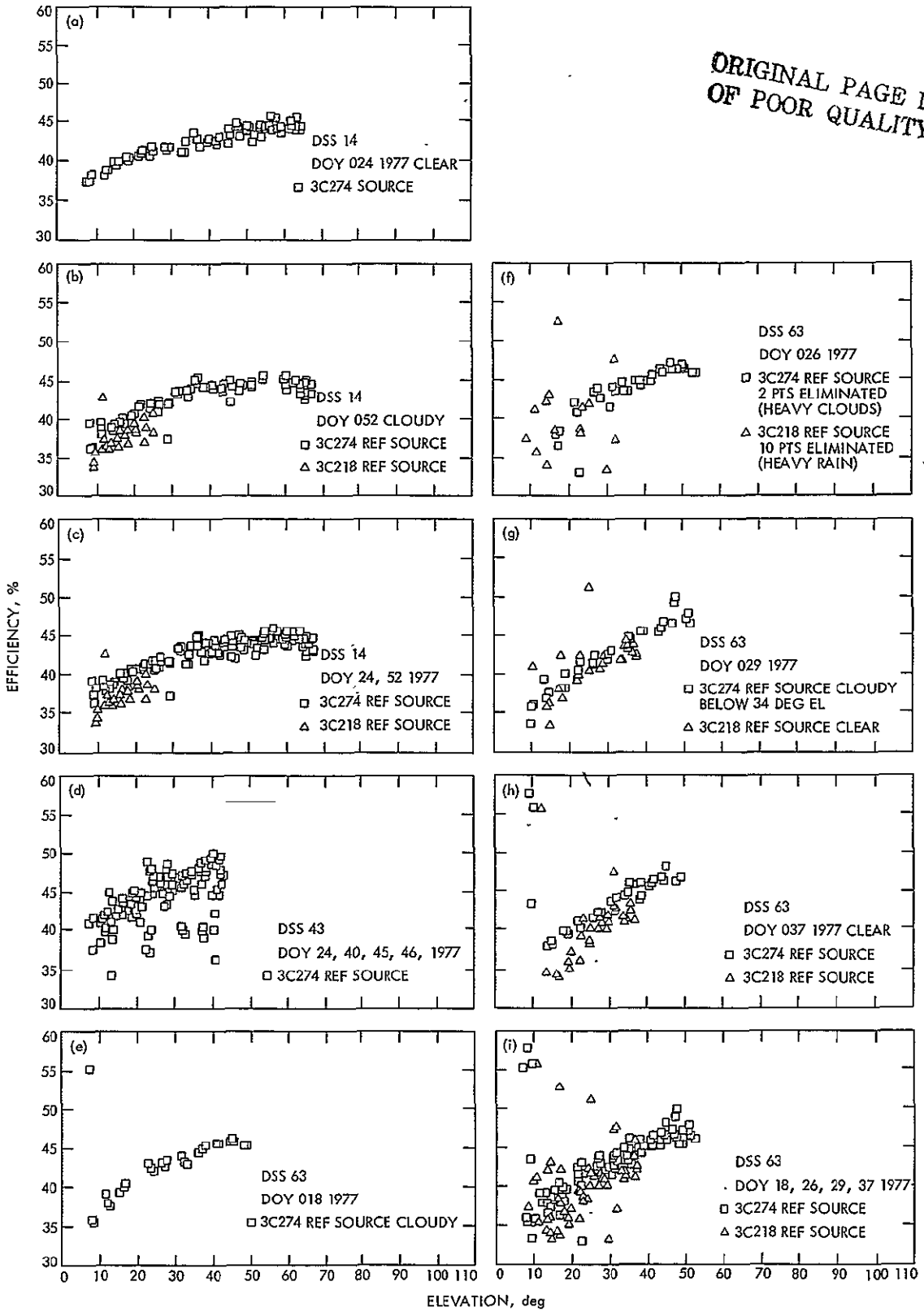

Fig. 7. Efficiency vs elevation at X-band (8415 MHz): (a) through (c) DSS 14; (d) DSS 43; (e) through (i) DSS 63

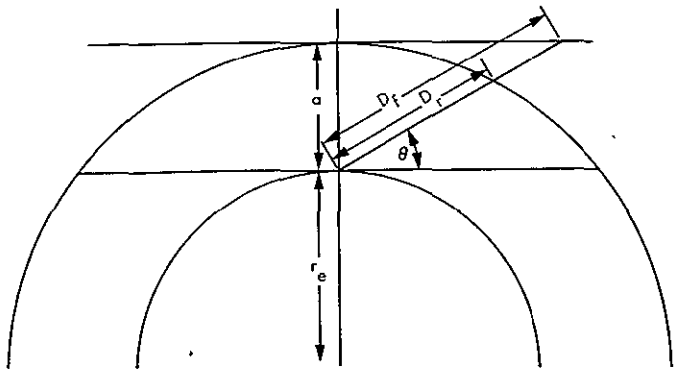

Fig. 8. Earth models

$$T_{OP} = T_R + T_{gnd} + T_{gal} + T_{atm} + T_{ar}$$

$T_R = T_M + T_F$, $T_M = 8\ K$, T_F = 1.32 K for DSS 14,
0.493 K for DSS 43,
0.936 K for DSS 63

$$T_{ar} = 3.88\ \text{K}$$

$$T_{gnd}{}^{a} = 29.1034\,\theta^{(-0.3673)}\ \text{K for DSS 14}$$

$$T_{gal} = 2.7/L_\theta\ \text{K}$$

$$T_{atm} = \frac{(L_\theta - 1)}{L_\theta} \cdot 265\ \text{K}$$

$$L_\theta = 10^{\ell_z D/10a},\ \ell_z = 0.043\ \text{dB for clear dry weather}$$

$$D = \left| r \sin\theta \pm \sqrt{(r\sin\theta)^2 + 2ar + a^2} \right| \text{ for round earth}$$

$r = a/\sin\theta$ for flat earth

θ = elevation angle in degrees

R = radio earth radio = 8500 km

a = 10 km

[a]Obtained by curvefitting measured data.

Fig. 9. A mathematical model of T_{OP}

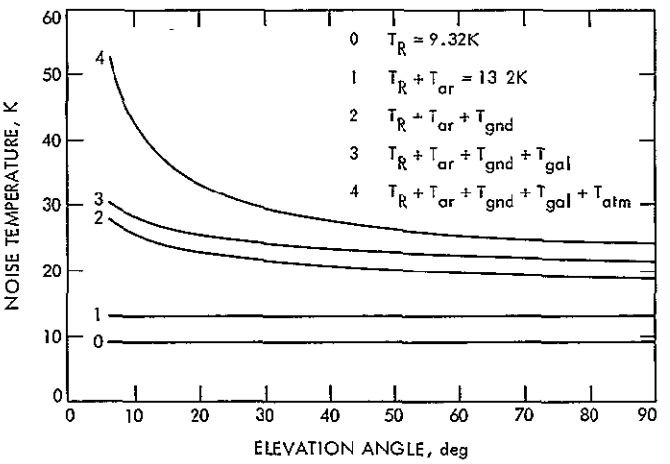

Fig. 10. Plots of the mathematical model of T_{OP} given in Fig. 8, round earth, DSS 14

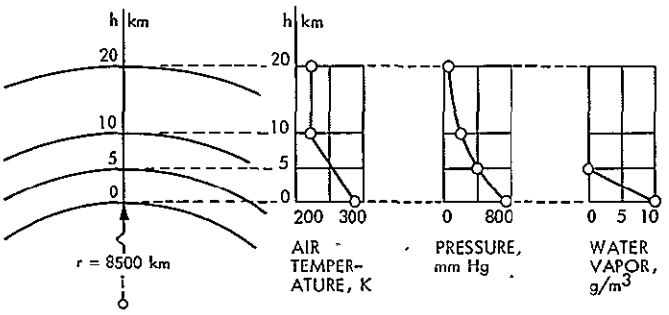

Fig. 11. Air temperature, pressure, and water vapor distribution over the earth troposphere

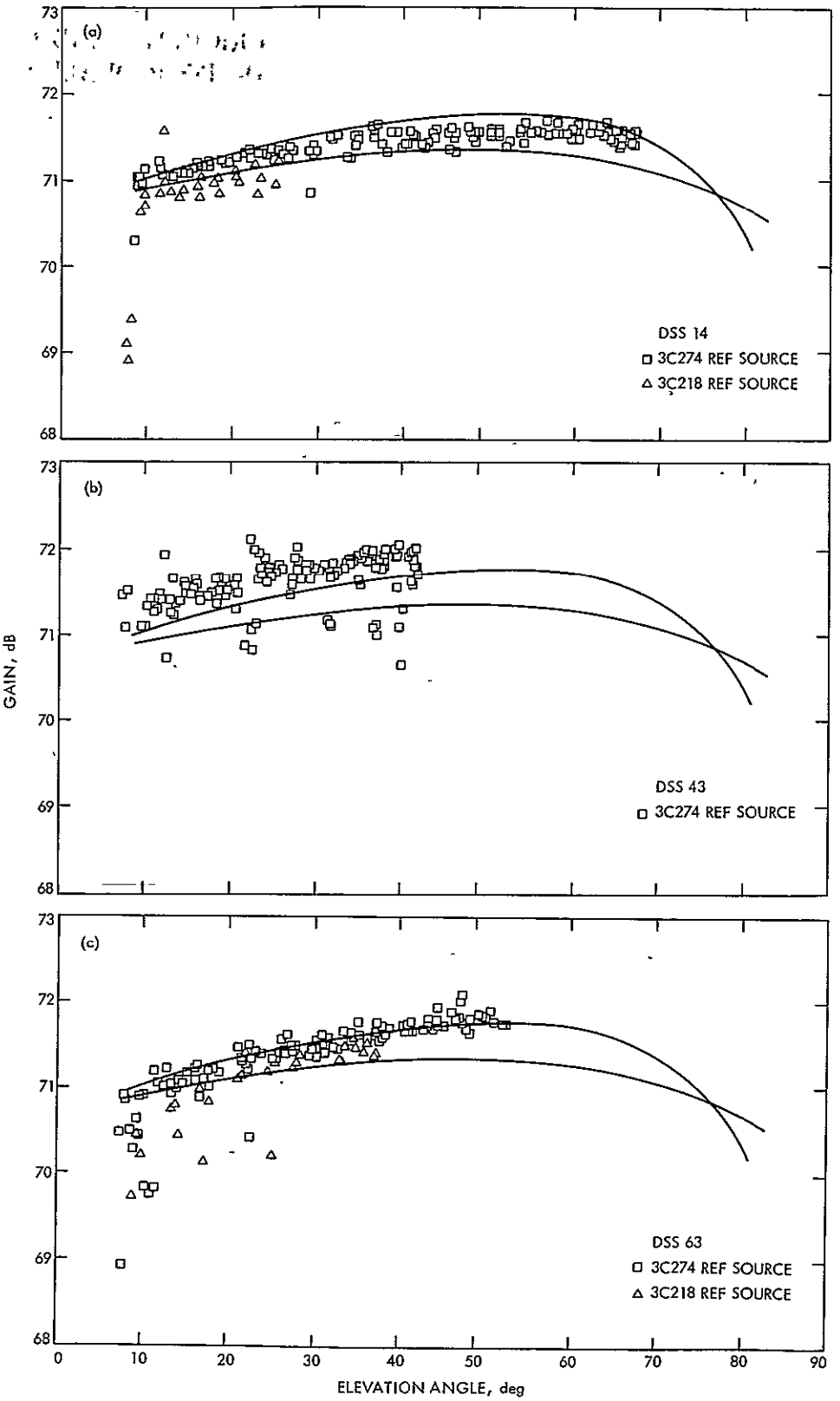

Fig. 12. Antenna gain vs elevation angle at 8415 MHz with atmospheric losses removed: (a) DSS14; (b) DSS 43; (c) DSS 63

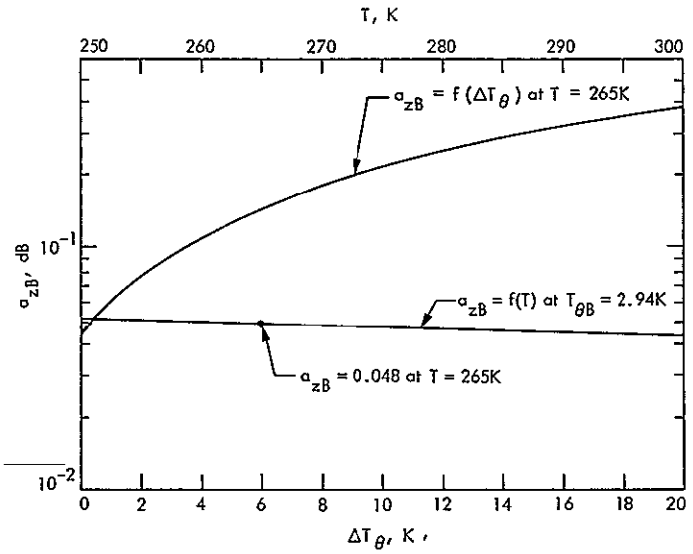

Fig 13. a_{zB} vs ΔT_θ and a_{zB} vs T

Appendix

Derivation of Observed Brightness Temperature and Star Source Flux Density

By using the concept of brightness change in an elemental volume dv (see Fig. A-1) due to emission and absorption of electromagnetic energy, the observed brightness of a radio source may be derived to be (Ref. 5):

$$B = B_s e^{-\tau} + \int_0^{\tau} e^{-(\tau - \tau')} B(T) d\tau' \qquad \text{(A-1)}$$

where

B = observed brightness, watts m^{-2} Hz^{-1} rad^{-2}

B_s = brightness of source

τ = optical depth of the medium, dimensionless

$= \tau(r) = \int_0^r \alpha(r')\, dr'$, dependent on the medium thickness, α ( ) is the absorption coefficient

T = temperature, K

For $B(T) = B_i$ = intrinsic brightness = constant, and denoting τ by τ_m for τ of a medium, Eq. (A-1) yields

$$B = B_s e^{-\tau_m} + B_i (1 - e^{-\tau_m}) \qquad \text{(A-2)}$$

With $h\nu \ll kT$ and using Maclaurin's expansion, Planck's black body radiation law

$$B(T) = 2\frac{h\nu^3}{C^2} \frac{1}{e^{h\nu/kt} - 1}$$

can be reduced to give an approximate relationship between brightness and temperature (known as the Rayleigh–Jeans law) as:

$$B(T) = 2kT/\lambda, \quad \nu = c/\lambda \qquad \text{(A-3)}$$

where

k = Boltzmann's constant (= 1.38×10^{-23} joules K^{-1})

λ = wavelength, m

ν = frequency, Hz

C = speed of light, $msec^{-1}$

h = Planck's constant (= 6.63×10^{-34} joules sec)

Thus in terms of brightness temperature, Eq. (A-2) gives (See Fig. A-1)

$$T_b = T_s e^{-\tau_m} + T_m (1 - e^{-\tau_m}) \qquad \text{(A-4)}^3$$

where

T_b = observed brightness temperature, K

T_s = source temperature, K

T_m = medium temperature, K

τ_m = optical depth of medium, dimensionless

Figure A-2 depicts a plot of Eq. (A-4) for the case $T_s > T_m$. At the optical depth of 1, T_b receives only about 67% from T_m and about 37% from T_s. A similar plot may also be obtained for the case $T_m > T_s$. When the source and medium temperatures are identical, $T_b = T_s = T_m$ and is independent of τ_m. In all cases,

$$\lim_{\tau_m \to \infty} T_b \simeq T_m$$

[3] The validity of this relationship at X-band is justifiable. For a typical $T = 298$ Kelvins, $\nu = 6.2 \times 10^{12}$ Hz (0 05-mm wave), which is 737 times larger than $8\,4 \times 10^9$ Hz (3.57-cm wave) at X-band and thus the relation $h\nu \ll kT$ holds.

which states that the observed brightness temperature of an atmosphere with a very thick medium is the temperature of the medium itself.

When the temperature of the medium is not constant, we have from Eqs. (A-1) and (A-3):

$$T_b = \frac{T_s}{L} + \int_1^L \frac{T_m}{L} e^{\tau'} d\tau'$$

$$= \frac{1}{L}\left(T_s + \int_1^{L} T_m \, dL'\right)$$

where $L' = e^{\tau'}$ and $dL' = e^{\tau'} d\tau'$.

By defining

$$\overline{T}_m = \frac{1}{L-1} \int_1^L T_m \, dL'$$

as a weighted average temperature from $L' = 1$ to $L' = L$, we then have

$$T_b = \frac{T_s}{L} + \frac{(L-1)}{L} \overline{T}_m \qquad \text{(A-5)}$$

The first term on the right of Eq. (A-5) is the brightness temperature due to source. The second term is the brightness temperature due to medium, often referred to as the effective atmospheric temperature.

With a similar approach as the above, the galactic temperature effects may also be derived to be of the form

$$T_{gal} = T/L$$

Where T is the galactic temperature measured at zenith which has a nominal value of 2.7 K.

The observed flux density of a radio source can also be determined. The spectral power P or power per unit bandwidth radiated from a solid angle Ω of the sky on to an antenna of effective aperture area A_p is

$$P = (1/2) A_p \int\int B(\theta, \phi) P_n(\theta, \phi) \, d\Omega \qquad \text{(A-6)}$$

where

P = received spectral power, watts Hz^{-1}

A_p = effective aperture area of antenna, m^2

$B(\theta, \phi)$ = brightness of sky, watts m^{-2} Hz^{-1} rad^{-2}

$P_n(\theta, \phi)$ = normalized power pattern of antenna, dimensionless

$d\Omega$ = $\sin\theta \, d\theta d\phi$ = element of solid angle, rad^2

ϕ = the azimuthal angle

If the antenna is placed inside of a blackbody enclosure at a temperature T, then the brightness will be constant in all directions. According to the Rayleigh–Jeans law, its value is (see Eq. A-3):

$$B(\theta, \phi) = \frac{2kT}{\lambda^2} \qquad \text{(A-7)}$$

Since the beam area of the antenna is

$$\Omega_A = \int\int_{4\pi} P_n(\theta, \phi) \, d\Omega$$

with Eq. (A-7), Eq. (A-6) yields

$$P = \frac{kT}{\lambda^2} \cdot A_p \Omega_A = kT, \; A_p \Omega_A = \lambda^2$$

Furthermore, if the source of temperature T does not extend over the entire antenna beam area, the measured or antenna temperature T_A will be less so that

$$P = (1/2) A_p \int\int_{\Omega} B(\theta, \phi) P_n(\theta, \phi) \, d\Omega = kT_A \qquad \text{(A-8)}$$

Now when the source is observed with an antenna of power pattern $P_n(\theta_1 \phi)$, a flux density S_0 is observed to be

$$S_0 = \int\int_{\text{source}} B(\theta, \phi) P_n(\theta, \phi) \, d\Omega$$

Hence, the observed flux density of a radio source can be determined from the measured antenna temperature and its effective aperture area through the relation

$$S_0 \doteq \frac{2kT_A}{A_p} \qquad \text{(A-9)}$$

where

S_0 = observed flux density of source, watts m^{-2} Hz^{-1}

T_A = (maximum) antenna temperature due to source, K

A_p = effective aperture area of antenna, m^2

k = Boltzmann's constant (= 1.38×10^{-23} joules K^{-1})

References

1. Freiley, A. J., "Radio Frequency Performance of DSS 14 64-m Antenna at 3.56 and 1.96 cm Wavelengths" in the *DSN Progress Report,* Technical Report 32-1526, Vol. XIX, pp. 110-115, JPL, Pasadena, California, February 15, 1974.
2. Neff, D. E., and Bathker, D. A., "DSS 14 X-Band Radar Feed Cone," *DSN Progress Report* 42-30, pp. 119-131, JPL, Pasadena, Calif., December 15, 1975.
3. Janssen, M. A., et al., "Extension of the Absolute Flux Density Scale to 22.285 GHz," *Astronomy & Astrophysics*, Vol. 33, 373-377 (1974).
4. Hogg, D. C., "Effective Antenna Temperature Due to Oxygen and Water Vapor in the Atmosphere," *J. Appl. Phys.*, Vol. 30, No. 9, September 1959.
5. Kraus, J. D., *Radio Astronomy*, McGraw-Hill, 1966.

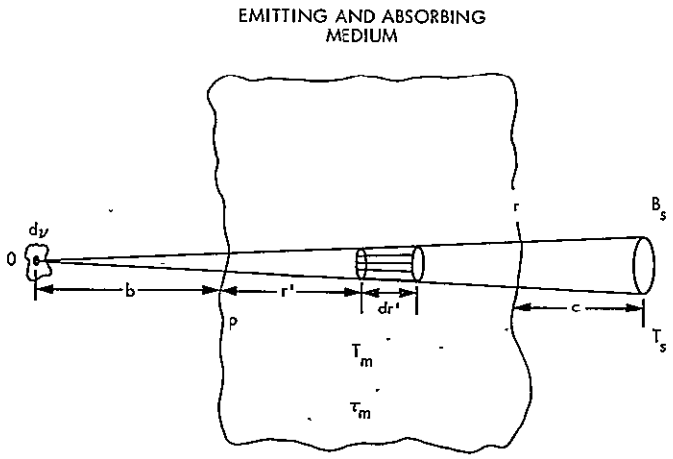

Fig. A-1. Source of brightness B_s (or brightness temperature T_s) observed through an intervening medium of temperature T_m and optical depth τ_m

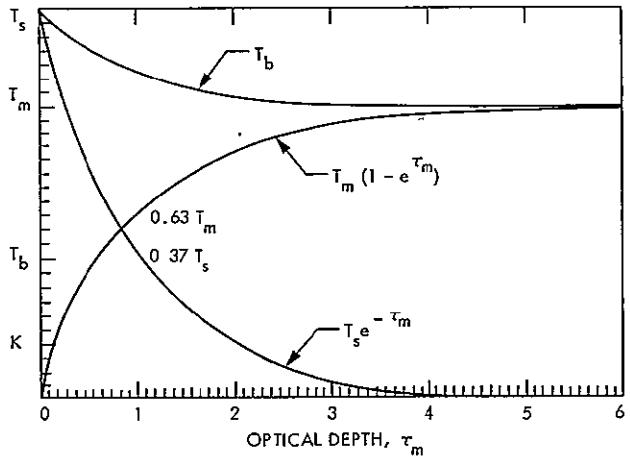

Fig. A-2. Variation of brightness temperature due to emission, absorption, and both as a function of optical depth, τ_m; $T_s > T_m$

D13

N78-15080

Modification of Simulation Conversion Assembly for Support of Voyager Project and Pioneer-Venus 1978 Project

S. H. Yee

DSN Data Systems Section

The Simulation Conversion Assembly (SCA) has been upgraded to provide the additional capabilities of simulating Voyager and Pioneer-Venus 1978 telemetry data streams for verifying the integrity of the Deep Space Stations while continuing to fulfill the DSN test and training support requirements. A summary of the requirements and the implementations are presented in this article.

I. Introduction

The Simulation Conversion Assembly (SCA), as part of the DSS Test and Training Subsystem, has been upgraded to provide the additional hardware and software capabilities listed below to support Voyager and Pioneer-Venus 1978 (PV-78) Projects:

(1) Voyager short constraint length convolutional coding.

(2) PV long constraint length convolutional coding.

(3) Voyager project data patterns.

(4) Pioneer-Venus 1978 project data patterns.

The SCA consists of two levels of capability to support the respective telemetry data processing equipment at each of the deep space stations.

(1) SCA provides four telemetry data channels, required at the 26-m stations.

(2) SCA provides six telemetry data channels, required at the 64-m stations.

The SCA described in this article is the six-channel configuration for the 64-m stations.

II. New Hardware Capabilities

A. Voyager Short Constraint Length Convolutional Coder

The SCA is required to provide nonsystematic convolutional coding with constraint length of 7 bits at the computer-controlled code format of 1/2 and 1/3 on three data channels

for symbol rates up to 230,400 bits/second. The Voyager coding connection vector will be as shown in Figs. 1 and 2.

B. PV-78 Long Constraint Length Convolutional Coder

The SCA is required to provide nonsystematic convolutional coding with constraint length of 32 bits at the computer-controlled code format of 1/2 on three data channels for symbol rates up to 2048 bits/second. The PV-78 coding connection vectors will be as shown in Fig. 3. Thirty-two bits of tail code are inserted, and the register is reset at the end of each frame in both the manual and computer modes of operation.

III. New Software Capabilities

A. Voyager Project Data Patterns

Software-generated, framed-synchronized data patterns are provided to simulate the Voyager formats and frame sizes. An incrementing data pattern of nine different frame sizes as shown in Fig. 4 is required for data rates up to 115.2 kbits/second, in addition to the incrementing pattern. Fixed, static data of seven different frame sizes is required for data rates up to 7200 bits/second as shown in Fig. 5.

B. PV-78 Data Pattern

Software-generated, frame synchronized data patterns representing Pioneer-Venus formats are provided for each of the SCA channels having long constraint length convolutional coding capability. All Pioneer-Venus frames are 512 bits in length; each frame corresponds to an encoding cycle. The frame count in the orbiter and bus data patterns are incremented one count per frame as shown in Fig. 6. The probe patterns are static as shown in Fig. 7.

Provision is made for operator-entry changes to the format identification (ID) in bus and orbiter patterns, the probe ID in probe pattern, the data rate ID in any type pattern, and any computer word in the data-generating table.

C. High-Speed and Wideband Input and Output

The SCA processes a 56-kbit/second (kbs) wideband input of 4800-bit block size, with output data rate up to 44.8 kbs on one channel, and simultaneously processes a 7.2-kbs high-speed input of 1200-bit block size with an output rate up to 40 bits/second on a second channel.

IV. Hardware Implementation

To provide for the additional convolutional coding function, the SCA required the addition of the new convolutional coder drawer (CCD). The new CCD contains all necessary hardware to enable the SCA to provide the capabilities defined in Paragraph II. The CCD consists of four major functions. See Fig. 8 for block diagram of CCD.

A. Convolutional Coding Section

There are four modes of convolutional coding:

(1) Systematic 1/2 (S 1/2).

(2) Nonsystematic 1/2 ($\overline{S}$ 1/2).

(3) Systematic 1/3 (S 1/3)

(4) Nonsystematic 1/3 ($\overline{S}$ 1/3)

When S 1/2 or $\overline{S}$ 1/2 is selected, the output consists of two symbols for each data bit. The coders are also able to operate in an uncoded mode. The modes of operation are described below:

(1) S 1/2: In the S 1/2 mode, the first output symbol is the true data bit, and the other is parity symbol. Example:

$$P_{1N}D_N \cdots P_{12}D_2P_{11}D_1$$

where D_N is the first data bit and P_{1N} is the first parity bit.

(2) $\overline{S}$ 1/2: In the $\overline{S}$ 1/2 mode, the two output symbols are both parity symbols. Example:

$$P_{2N}P_{1N} \cdots P_{22}P_{12}P_{21}P_{11}$$

where P_{2N} and P_{1N} are parity bits.

(3) S 1/3: In the S 1/3 mode, the first output symbol is the true data bit; the other two symbols are parity symbols. Example:

$$P_{2N}P_{1N}D_N \cdots P_{22}P_{12}D_2P_{21}P_{11}D_1$$

where D_N is the first data bit, P_{1N} is the first parity bit and P_{2N} is the second parity bit.

(4) $\overline{S}$ 1/3: In the $\overline{S}$ 1/3 mode, all three output symbols are parity symbols. Example:

$$P_{3N}P_{2N}P_{1N}\cdots P_{32}P_{22}P_{12}P_{31}P_{21}P_{11}$$

B. Timing Section

This section provides the control to synchronize the data generated from the computer and resets the register at the end of each frame. It also provides the clock signals to the data generator to code the data at the rates of 1/2 or 1/3 format.

C. Computer Control

The computer control section provides the means for the computer to control and monitor the coder.

D. Selection Matrix

The CCD is required to have manual control of the convolutional error rate (CER) selection and routing for assemblies in the DSS.

V. Software Implementation

The new program is a modification of the current program. The code that pertains only to the Viking mission has been deleted from the current program to make core space available for the new code to meet the requirements defined in Paragraph III. All of the required mission-independent functions of the current program have been retained. The additions to the program provide SCA capabilities to support the DSS test and training activities for the Voyager and PV-78 missions. The program will support both stand-alone and long-loop operations at all stations. Stand-alone data streams with incrementing counters will be output at selected rates up to 115,200 bits/second. Long-loop data will be received on both wideband and high-speed lines and routed to selected output channels. The program allows for the altering of fixed and incrementing data tables, provides for controlling the new convolutional coders, and for the selecting of fixed data patterns.

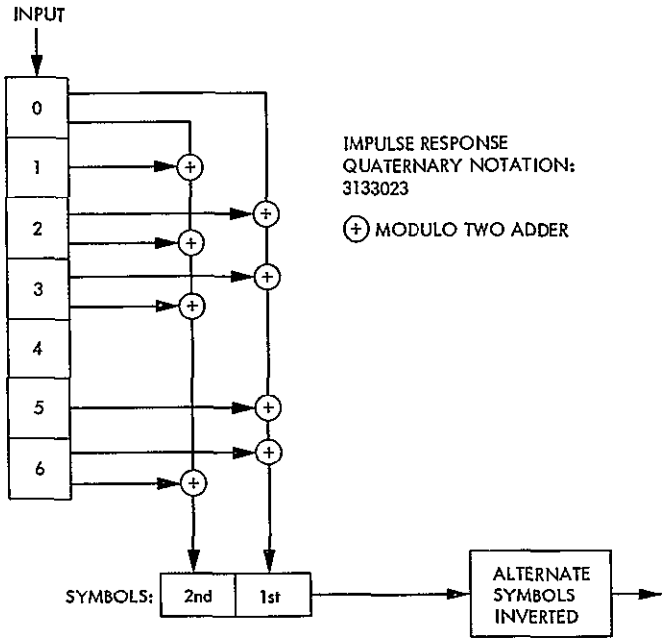

Fig. 1. Schematic of Voyager connection vector, constraint length = 7, rate = ½

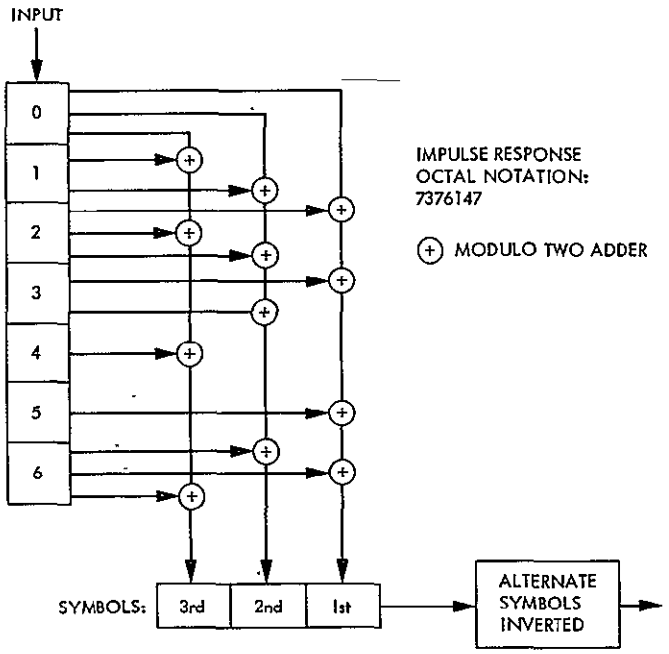

Fig. 2. Schematic of connection vector, constraint length = 7, rate = ⅓

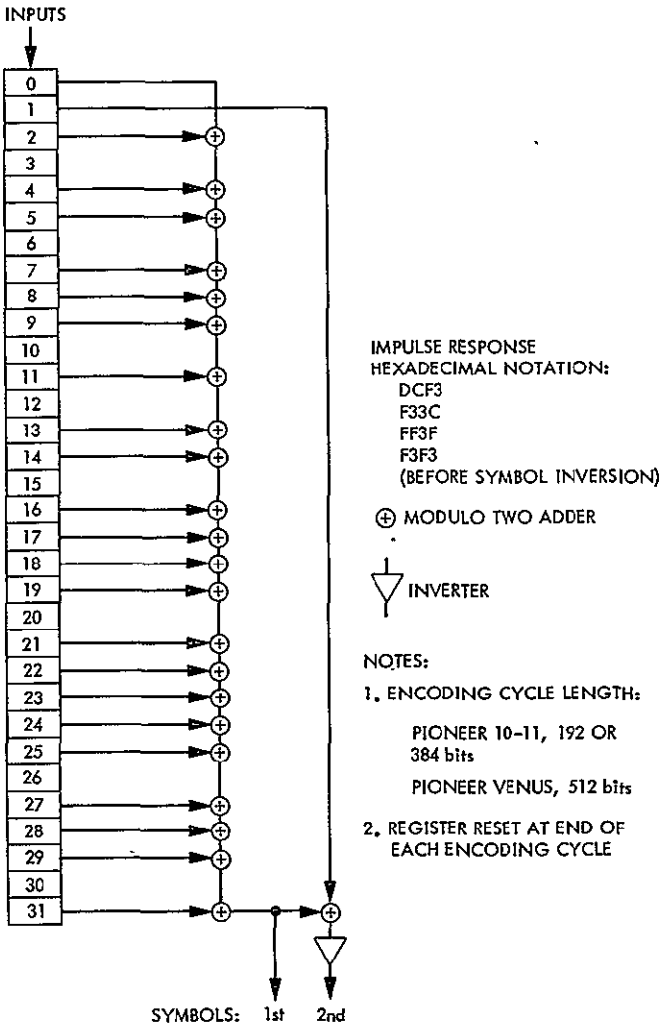

Fig. 3. Schematic of PV-78 connection vector, constraint length = 32, rate = ½

VOYAGER INCREMENTING DATA PATTERN (288 WORDS)

Generator Word No.	Times Output	Buffer Word No.	Format	0 1 2 3 4 - - - - - Binary Contents - - - - - - - 20 21 22 23	Octal	Hex
1	1	1	[Level 119 Pixel (1)][Frame SYNC]	[0 1 1 1 0 1 1 1][0 0 0 0 0 0 1 1 1 0 0 1 0 0 0 1	35601621	770391
2	1	2	[Format ID]	0 1 0 1 1 1 1 0 1 1 0 1 0 0 1 1][X X X X X X X X]	27551400	5ED300
3, 19	1	3	Time Subcom[Picture Count][Line Count]	0 0 0 0 1 1 1 1][PICTURE COUNT][LINE COUNT]	03600001	0F0001
4	18	4-21	Golay Field (432 Bits)	0 1 0 1 0 1 0 1 0 1 0 1 0 1 0 1 0 1 0 1 0 1 0 1	25252525	555555
5	15	22-36	Level 170 Pixels (46)	1 0 1 0 1 0 1 0 1 0 1 0 1 0 1 0 1 0 1 0 1 0 1 0	52525252	AAAAAA
6	1	37		1 0 1 0 1 0 1 0][0 1 1 1 0 1 1 1 0 1 1 1 0 1 1 1	52473567	AA7777
7	35	38-72	Level 119 Pixels (108)	0 1 1 1 0 1 1 1 0 1 1 1 0 1 1 1 0 1 1 1 0 1 1 1	35673567	777777
8	1	73		0 1 1 1 0 1 1 1][0 0 0 1 0 0 0 1 0 0 0 1 0 0 0 1	35610421	771111
9	35	74-108	Level 17 Pixels (106)	0 0 0 1 0 0 0 1 0 0 0 1 0 0 0 1 0 0 0 1 0 0 0 1	04210421	111111
10	1	109	Level 119 Pixels (11)	0 0 0 1 0 0 0 1][0 1 1 1 0 1 1 1 0 1 1 1 0 1 1 1	04273567	117777
11	3	110-112		0 1 1 1 0 1 1 1 0 1 1 1 0 1 1 1 0 1 1 1 0 1 1 1	35673567	777777
12	12	113-144	Level 204 Pixels (97)	1 1 0 0 1 1 0 0 1 1 0 0 1 1 0 0 1 1 0 0 1 1 0 0	63146314	CCCCCC
13	1	145		1 1 0 0 1 1 0 0][0 1 1 1 0 1 1 1 0 1 1 1 0 1 1 1	63073567	CC7777
14	35	146-180	Level 119 Pixels (107)	0 1 1 1 0 1 1 1 0 1 1 1 0 1 1 1 0 1 1 1 0 1 1 1	35673567	777777
15	36	181-216	Level 68 Pixels (108)	0 1 0 0 0 1 0 0 0 1 0 0 0 1 0 0 0 1 0 0 0 1 0 0	21042104	444444
16	8	217-224	Level 119 Pixels (24)	0 1 1 1 0 1 1 1 0 1 1 1 0 1 1 1 0 1 1 1 0 1 1 1	35673567	777777
17	36	225-260	Level 238 Pixels (108)	1 1 1 0 1 1 1 0 1 1 1 0 1 1 1 0 1 1 1 0 1 1 1 0	73567356	EEEEEE
18	28	261-288	Level 119 Pixels (84)	0 1 1 1 0 1 1 1 0 1 1 1 0 1 1 1 0 1 1 1 0 1 1 1	35673567	777777

Notes

1) Format ID Set by mnemonic input.

2) Frame sizes (20, 48, 64, 112, 120 168, 180, 224, and 288 words) set by mnemonic input

3) See SOM-DYS-5128, Section 5.7 for Voyager mnemonic codes.

4) Picture Count Increments from 0 to 59 at a rate of one count per 800 Line Counts.

5) Line Count increments from 1 to 800 at a rate of one count per frame.

6) Generator word No. 19 provides recycle of word No. 3 picture and line count

7) Applicable to SCA output channels as follows

Convolutional coded: Channels 1, 2, or 5.
Uncoded: Channels 1, 6 and 2 or 5.

Fig. 4. Voyager incrementing data format

VOYAGER FIXED DATA PATTERN (180 WORDS)

Generator Word No.	Times Output	Buffer Word No.	Format	0 1 2 3 - - - - - - - - Binary Contents - - - - - - - - 20 21 22 23	Octal	Hex
1	1	1	[Frame Sync	[0 0 0 0 0 0 1 1 1 0 0 1 0 0 0 1 0 1 0 1 1 1 1 0	00710536	03915E
2	1	2	] Format ID] Time Subcom]	1 1 0 1 0 0 1 1] X X X X X X X X] 0 0 0 0 1 1 1 1]	64600017	D3000F
3	1	3	Mod 60 Count] Mod 800 Count]	0 1 0 1 0 1] 0 0 0 0 0 0 0 0 1] 0 1 0 1 0 1 0 1	25000525	540155
4	33	4-36		0 1 0 1 0 1 0 1 0 1 0 1 0 1 0 1 0 1 0 1 0 1 0 1	25252525	555555
5	36	37-72	DATA	1 0 1 0 1 0 1 0 1 0 1 0 1 0 1 0 1 0 1 0 1 0 1 0	52525252	AAAAAA
6	36	73-108	(177 24-Bit Words)	1 1 0 0 1 1 0 0 1 1 0 0 1 1 0 0 1 1 0 0 1 1 0 0	63146314	CCCCCC
7	36	109-144		0 0 1 1 0 0 1 1 0 0 1 1 0 0 1 1 0 0 1 1 0 0 1 1	14631463	333333
8	36	145-180	]	0 1 0 1 0 1 0 1 0 1 0 1 0 1 0 1 0 1 0 1 0 1 0 1]	25252525	555555

Notes:

1) Format ID = Set by mnemonic input.

2) Frame Sizes (20, 48, 64, 112, 120, 168, 180 words) set by mnemonic input.

3) See SOM-DYS-5128, section 5.7 for Voyager mnemonic codes.

4) Applicable to SCA output channels as follows:

   Convolutional coded: Channels 1, 2, and 5.
   Uncoded: Channels 1, 2, 5, and 6.

Fig. 5. Voyager fixed data format

PIONEER - VENUS '78 BUS AND ORBITER INCREMENTING PATTERN (64 WORDS)

Generator Word No.	Times Output	Buffer Word No	Format	Binary Contents (0 1 2 3 4 - - - - - 20 21 22 23)	BUS Octal	BUS Hex	ORBITER Octal	ORBITER Hex
1	1	1	[Format ID] Rate ID] DAS Mode ID] SID] Frame Count]	[X X X X] X X X X] 1 0 1 0 1 0 1 0] X X] Frame Count]	00125000	00AA00	00125200	00AA80
2	1	2	Subcom Data] ———	0 0 0 1 0 0 0 1] 0 1 1 1 0 0 0 1 1 1 0 0 0 1 1 1	04270707	1171C7		
3	18	3-20	—Data ———	0 0 0 1 1 1 0 0 0 1 1 1 0 0 0 1 1 1 0 0 0 1 1 1	07070707	1C71C7		
4	1	21	—] Tail Code Sync ———	0 0 0 1 1 1 0 0] 1 1 1 1 1 0 0 0 1 1 0 0 0 1 0 1	07174305	1CF8C5		
5	1	22	—] Format ID] Rate ID] DAS Mode ID]	0 1 0 0 1 0 0 1] X X X X] X X X X] 1 0 1 0 1 0 1 0]	22200252	4900AA		
6	1	23	SID] Frame Count] Subcom Data] ———	X X] Frame Count] 1 0 0 0 1 0 0 0] 0 1 1 1 0 0 0 1	00304161	018871	40304161	818871
7	18	24-41	—Data ———	1 1 0 0 0 1 1 1 0 0 0 1 1 1 0 0 0 1 1 1 0 0 0 1	61616161	C71C71		
8	1	42	—] Tail Code Sync—	1 1 0 0 0 1 1 1 0 0 0 1 1 1 0 0] 1 1 1 1 1 0 0 0	61616370	C71CF8		
9	1	43	—] Format ID] Rate ID]	1 1 0 0 0 1 0 1 0 1 0 0 1 0 0 1] X X X X] X X X X]	61244400	C54900		
10	1	44	DAS Mode ID] SID] Frame Count] Subcom Data]	1 0 1 0 1 0 1 0] X X] Frame Count] 1 1 1 1 1 1 1 1]	52401377	AA02FF	52501377	AA62FF
11	19	45-63	Data ———]	0 1 1 1 0 0 0 1 1 1 0 0 0 1 1 1 0 0 0 1 1 1 0 0]	34343434	71C71C		
12	1	64	Tail Code Sync ———]	1 1 1 1 1 0 0 0 1 1 0 0 0 1 0 1 0 1 0 0 1 0 0 1]	76142511	F8C549		

Notes

1) Format and Rate IDs set by mnemonic input, See SOM-DYS-5128, section 5.7 for PVB and PVS mnemonic codes.

2) SID = Spacecraft ID. Bus (PVB) = 00_2, Orbiter (RVS) = 10_2.

3) Orbiter and Bus patterns can run simultaneously at different data rates.

4) Frame Count increments from 0 to 63 at a rate of one increment per 512-bit frame.

5) Applicable to SCA output channels as follows:

Convolutional coded: Channels 1 and 2 or 5.
Uncoded: Channels 1 and 2, or 5 and 6.

Fig. 6. PVB and PVS incrementing data format

PIONEER - VENUS '78 PROBE FIXED DATA PATTERN (64 WORDS)

Generator Word No.	Times Output	Buffer Word No.	Format	0 1 2 3 4 - - - - - Binary Contents - - - - - 20 21 22 23	Octal	Hex
1	1	1	[M][REF][PID][F/R ID][Frame Count]	[1][0 0][X X][X X X][0 0 0 0 0 0 0 0][1 1 0 0 0 1 1 1]	40000307	8000C7
2	8	2-9	Data	0 0 0 1 1 1 0 0 0 1 1 1 0 0 0 1 1 1 0 0 0 1 1 1	07070707	1C71C7
3	1	10	Subcom Data	0 0 0 1 1 1 0 0 0 1 1 1 0 0 0 1 [0 0 0 0 0 0 0 1]	07070401	1C7101
4	1	11	[	0 0 0 0 0 0 1 0 0 0 0 0 0 0 1 1 0 0 0 0 0 1 0 0]	00401404	020304
5	9	12-20	Data	1 1 1 0 0 0 1 1 1 0 0 0 1 1 1 0 0 0 1 1 1 0 0 0	70707070	E38E38
6	1	21	Frame Sync	1 1 1 0 0 0 1 1 [1 1 1 1 1 0 0 0 1 1 0 0 0 1 0 1]	70774305	E3F8C5
7	1	22	[M][REF][PID][F/R ID][Frame Count]	0 1 0 0 1 0 0 1 [1][0 0][X X][X X X][0 0 0 0 0 0 0 1]	22300001	498001
8	9	23-31	Data	1 1 0 0 0 1 1 1 0 0 0 1 1 1 0 0 0 1 1 1 0 0 0 1]	61616161	C71C71
9	1	32	Subcom Data	0 0 0 1 0 0 0 1 0 0 0 1 0 0 1 0 0 0 1 0 0 0 1 1	04211043	111283
10	1	33	[	0 0 0 1 0 1 0 0 [1 1 1 0 0 0 1 1 1 0 0 0 1 1 1 0]	05161616	14E38E
11	8	34-41	Data	0 0 1 1 1 0 0 0 1 1 1 0 0 0 1 1 1 0 0 0 1 1 1 0	16161616	38E38E
12	1	42	Frame Sync	0 0 1 1 1 0 0 0 1 1 1 0 0 0 1 1 [1 1 1 1 1 0 0 0]	16161770	38E3F8
13	1	43	[M][REF][PID][F/R ID]	1 1 0 0 0 1 0 1 0 1 0 0 1 0 0 1 [1][0 0][X X][X X X]	61244600	C54980
14	1	44	Frame Count	0 0 0 0 0 0 1 0 [1 1 0 0 0 1 1 1 0 0 0 1 1 1 0 0]	00543434	02C71C
15	8	45-52	Data	0 1 1 1 0 0 0 1 1 1 0 0 0 1 1 1 0 0 0 1 1 1 0 0	34343434	71C71C
16	1	53	Subcom Data	0 1 1 1 0 0 0 1 [1 0 1 0 0 0 0 1 0 0 1 0 0 0 1 0]	34320442	71A122
17	1	54	Data	0 0 1 0 0 0 1 1 0 0 1 0 0 1 0 0 [1 1 1 0 0 0 1 1]	10622343	2324E3
18	9	55-63	[	1 0 0 0 1 1 1 0 0 0 1 1 1 0 0 0 1 1 1 0 0 0 1 1]	43434343	8E38E3
19	1	64	Frame Sync	1 1 1 1 1 0 0 0 1 1 0 0 0 1 0 1 0 1 0 0 1 0 0 1]	76142511	F8C549

Notes:

1) M = Memory on (1)/Off (0).
2) PID = Probe ID. Set by mnemonic input, Large probe = 11_2, Small probe = 00_2, 01_2, 10_2,
3) F/R ID = Format/Rate ID Set by mnemonic input.
4) See SDM-DYS-5128, section 5 7 for PVP mnemonic codes
5) Applicable to SCA output channels as follows.
   Convolutional coded: Channels 1, 2, and 5.
   Uncoded: Channels 1, 2, 5 and 6

Fig. 7. PVP fixed data format

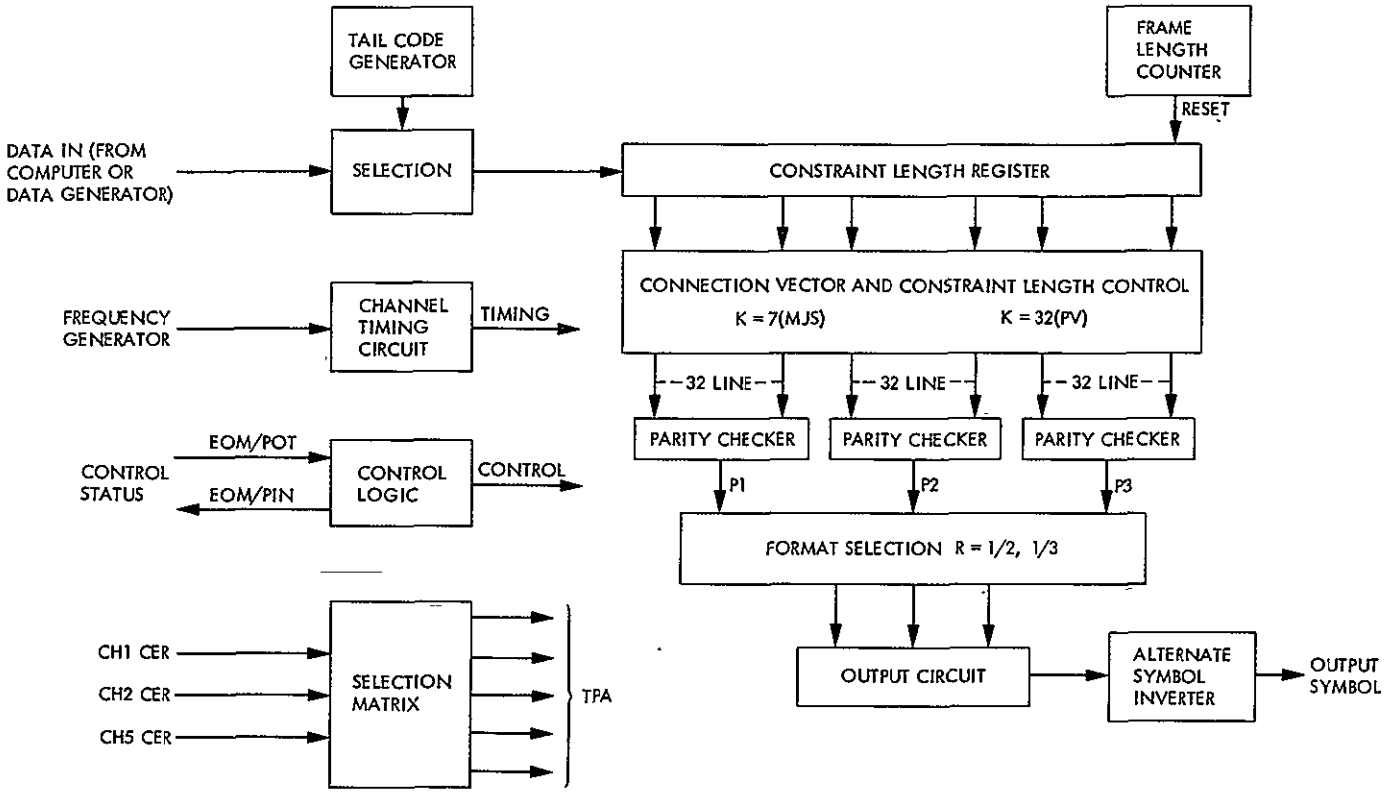

Fig. 8. Voyager/PV-78 DSS Simulation Conversion Assembly convolutional coder block diagram

D14

N78-15081

Range Validation Using Kalman Filter Techniques

G. A. Madrid
Navigation Systems Section

A method is presented whereby range pseudo-residuals may be improved to the level required for the purposes of data validation. Basically, the method proposed is a measurement updating process which utilizes Bierman's adaptation of the Kalman filter measurement updating algorithms together with process noise compensation to account for model errors. This algorithm involves combining the currently available range predictions and measurements to produce an updated range residual measurement whose accuracy is constrained by the range data quality and by the estimated error in the prediction. The algorithm is compact and fast, and is thus suitable for on-line applications in network control or at the station.

I. Introduction

The problem of near-real-time validation of ranging data has, to now, never been completely resolved mainly because the output of the ranging machine (Planetary Ranging Assembly, hereafter referred to as the PRA) is only a vernier measurement and not an absolute measure of distance or elapsed time. The problem is well described by Berman (Ref. 1) in an article which describes a technique for validating range within a pass by using the range and doppler data types to produce a "pseudo-DRVID" which can be used for this purpose. This approach proved fruitful for validating data within a pass but left the problem of validating range data after intervals when no radio metric data has been collected unresolved.

In general the problem occurs because the predicted observables are dependent on the probe ephemeris determined by the Orbit Determination Program (ODP) on the basis of fitting a model to past observations. Errors in the determination of this ephemeris show up as an error bias and an error drift rate in the predicted range observables. When these predictions are beat against the actual observables in near-realtime, the error growth eventually causes the residuals[1] to separate beyond the limits of the modulo and, in fact, if the data are sparse, there may be several modulos lost in the interval. Such conditions render the residuals almost useless for the purposes of data validation.

There are three basic ways by which this problem can be resolved:

(1) Place requirements on the flight project to maintain the predicted ephemeris at a specified level of accuracy.

[1] These residuals are usually termed pseudo-residuals to distinguish them from the actual ODP residuals.

(2) Develop a special purpose differential correction computer program for network control operations which would correct the orbital elements based on the incoming data so as to reduce the drift and bias errors in the predicted ephemeris.

(3) Develop statistical and/or numerical techniques using only the data types and information currently available to the DSN to compute improved range estimates from the predicted ephemeris.

The first method, although not requiring new software, would be costly and is contrary to the present mode of operation. The reason for this is that the Navigation Team updates the orbit in terms of weeks of data, and orbit predicts are produced for 8 days at a time based on orbits that may be updated once a month. To change this method of operation to meet the requirements would mean tracking and updating the probe ephemeris almost every other day. Considering the workload that current operations are placing on an already overburdened system, one must reject this first approach as being unrealistic.

The second approach, though seemingly reasonable, nevertheless has its own drawbacks. A differential correction process to produce dynamically corrected orbital elements would result in a sizeable computer program which, because of the demand to be made upon it, would require that either a mini- or a midi-computer be dedicated to this purpose alone. Furthermore, such a computer program could not be operated with untrained personnel; a team of knowledgeable technicians would be required. There is currently no in-house expertise of this type within the DSN. Even if these problems were to be resolved, the cost and time of developing and checking out such a program could be considerable.

The third approach appears capable of performing the task within reasonable cost and effort bounds. Berman (Refs. 1 and 2) has achieved partial success by employing doppler data to validate range measurement within a tracking pass or within contiguous passes. The method presented here demonstrates how currently available range predictions and measurements can be sequentially processed in an on-line fashion, using a Kalman filter (Ref. 3) to permit validation of range even when there are substantial gaps in the data coverage. By modeling the errors on the predicted observables, the method has the potential of being able to maintain residuals of sufficient accuracy to detect system malfunctions for periods of up to a year with data taken every 20 days.

Previous numerical experiments documented in Ref. 4 have demonstrated the efficiency, stability, and reliability of the U-D factorized Kalman filter (cf Refs. 3 and 5). A U-D filter formulation was chosen because the ultimate goal is to develop a real-time algorithm that can function on a limited precision minicomputer.

The filter model described in Section III was tested with simulated data and with real data obtained from one of the Viking spacecraft. A simple linear stochastic filter was developed and applied to the Viking data, giving accurate range residual estimates for the four-month period of data available for our test. Although further tests and analysis remain to be performed, the initial results reported demonstrate the efficiency of the approach.

II. Problem Formulation

The major cause for divergence of the predicted spacecraft range is the effect of unmodeled velocity and acceleration errors. The basis of the approach is to assume that the systematic components of these errors along the line-of-sight from the earth to the spacecraft can be modeled locally with a low order polynomial. This assumption is consistent with past analyses of spacecraft tracking errors (Ref. 6), and is evidenced in the characteristics of our test data (Section IV). Figure 1 illustrates the typical localized behavior of this error process when the spacecraft trajectory is not affected by any gravitational forces other than those due to the sun.

The actual signal traversal time between the observing station and the spacecraft is designated T_a, while the traversal time predicted from the spacecraft ephemeris is designated T_e. The time difference measured as an observable, T_M, may then be represented as

$$T_M = T_a + \nu(t) - n(t)M \tag{1}$$

where

$\nu(t)$ = noise on the data including errors due to medium effects

M = modulo as determined by frequency and hardware characteristics

$n(t)$ = integral number of modulos inherent in the round-trip delay

= $[(T_a + \nu(t))/M]_{\text{int}}$ (see footnote 2)

[2] $[a]_{\text{int}}$ indicates the integral part of a.

A residual is produced by differencing the observed measurement from a nominal estimate obtained from the spacecraft ephemeris. Thus,

$$\Delta T_M = T_M - \hat{T}_M \tag{2}$$

where

$$\hat{T}_M = T_e - \hat{n}(t) M$$

$\hat{n}$ = integral number of modulos that enter into T_e, i.e., $\hat{n} = [T_e/M]_{\text{int}}$

Assume that the difference between the actual and observed measurements may be expressed as

$$\Delta T_e = T_a - T_e \cong \epsilon_0(t) + \dot{\epsilon}_0 t + \frac{1}{2}\ddot{\epsilon}_0 t^2 \tag{3}$$

Then the observable difference, ΔT_M, may be written as

$$z(t) = [\mathrm{a}^{\mathrm{T}}(\Delta t_j)\, \epsilon(t_j) + \nu(t)] \text{ modulo } M \tag{4a}$$

or

$$z(t) = \mathrm{a}^{\mathrm{T}}(\Delta t_j)\, \epsilon(t_j) + \nu(t) - \Delta n(t) M \tag{4b}$$

where

$z(t) = \Delta T_M$

$\Delta n(t) = n(t) - \hat{n}(t)$

$\mathrm{a}^{\mathrm{T}}(\Delta t_j) = (1, \Delta t_j, (\Delta t_j)^2/2)$

$\Delta t_j = t - t_j$

$\epsilon^{\mathrm{T}}(t_j) = (\epsilon(t_j), \dot{\epsilon}(t_j), \ddot{\epsilon}(t_j))$

The role of t_j is to periodically introduce a time shift so that the expansion, Eq. (3), can better retain its validity. Mapping equations corresponding to this time update are

$$\epsilon(t_j) = \Phi(t_j)\, \epsilon(t_{j-1}) + \mathrm{B}\omega_j \tag{5}$$

where

$\epsilon(t_j)$ = 3-component state vector at time t_j

$\Phi(t_j)$ = state transition matrix from time t_{j-1} to t_j

ω_j = stochastic white noise

$\mathrm{B} = [0, 0, 1]^{\mathrm{T}}$

With the exception of the modulo M term in Eq. (4), the problem described is an ordinary parameter estimation or filtering problem (depending on whether the acceleration time constant, τ, of Eq. (7) is small or large). The structure of the Kalman filter is well suited to this type of problem. Its recursive structure allows one to perform the following functions:

(1) Recursively estimate (t_j) and produce an estimate of the innovations variance, $\mathrm{E}[z(t_j) - \mathrm{a}^{\mathrm{T}}(\Delta t_j)\, \epsilon(t_j|t_{j-1})]^2$ for use in data validation.

(2) Detect and pass outlier points; viz., points having an observation error greater than, say, 3σ, are flagged and omitted from the filtering process (σ is the innovations standard deviation).

(3) Maintain the condition $|z(t) < M|$, i.e., keep $\hat{T}_M$ close to T_M.

Maintaining the modulo constraint is of principal importance because it allows us to deal with an essentially linear problem. This can be seen clearly by referring to Eq. (4b) and noting that the differences between the observation z_j and the filter predicted estimate $\tilde{z}_j = z(t_j|t_{j-1})$ is given by

$$\begin{aligned} \Delta z_j &= z_j - \tilde{z}_j \\ &= \mathrm{a}^{\mathrm{T}}(\Delta t_j)\, (\epsilon(t_j) - \epsilon(t_j|t_{j-1})) + \nu(t_j) - \Delta n(t) M \end{aligned} \tag{6}$$

where

$$\Delta n(t) = n - \hat{n} = [(\Delta T_e + \nu)/M]_{\text{int}}$$

The validity of the rejection criterion depends on the assumption that $\Delta n = 0$. As long as this is true, the data can be processed in a conventional manner. Whenever $|\Delta z| > 3$, an additional test is made to determine whether $\Delta n \neq 0$. If it is, the datum can be corrected for the modulo rollover and the

standard rejection criterion can then be applied. The test is based on the assumption that

$$|\Delta z_j| \ll M/2$$

When $\Delta n > 0$, either our estimated function or the actual data must go through modulo rollovers at distinct times. When this happens, the anomaly can be detected because, then,

$$|\Delta z_j| > |M - 3\sigma|$$

Note how this rollover procedure introduces a major nonlinearity into the problem structure.

III. A Compact and Efficient Recursive Filter Solution

In this section a recursive filter algorithm is described that is well suited for on-line range calibration. Besides being compact and efficient, the mechanization (Refs. 3 and 5) is numerically accurate and stable. The specific form chosen for our dynamic model is

$$\begin{bmatrix} \dot{\epsilon} \\ \epsilon \\ \ddot{\epsilon} \end{bmatrix}_{j+1} = \begin{bmatrix} 1 & \Delta t & \Delta^2 t/2 \\ 0 & 1 & \Delta t \\ 0 & 0 & m \end{bmatrix} \begin{bmatrix} \dot{\epsilon} \\ \epsilon \\ \ddot{\epsilon} \end{bmatrix}_j + \begin{bmatrix} 0 \\ 0 \\ w_j \end{bmatrix} \tag{7}$$

where $\Delta t = t_{j+1} - t_j$, $m = \exp(-\Delta t/\tau)$, and $\{w_j\}$ is a white noise sequence with variance $(1 - m^2)\,\sigma_{\ddot{\epsilon}}(\infty)^2$.

This model is not completely general, but it seems to adequately compensate for model errors in space navigation problems (Refs. 6 and 7). Accelerations which might otherwise be modeled as constant parameters are allowed to have modest time variations. By acknowledging such variations, the pitfall of processing data over a large period of time is avoided, thus bypassing the computation of acceleration error uncertainties that are unacceptably small.[3] The inclusion of process noise prevents the filter from being restricted by the past behavior of the data. When process noise is not included, it often happens that the filter diverges when too much data is processed. Using the U-D factored form of the Kalman filter, we express the filter mechanization in the following sequential steps[4]:

(1) State propagation

$$\tilde{\epsilon} = \Phi \hat{\epsilon}$$

$$\hat{\epsilon} = \epsilon(t_j|t_{j-1}), \text{ and } \tilde{\epsilon} = \epsilon(t_{j+1}|t_j)$$

(2) Deterministic covariance update

$$\bar{P} = \bar{U}\bar{D}\bar{U}^T = (\Phi\hat{U})\,\hat{D}\,(\Phi\hat{U})^T$$

(3) Process noise covariance update

$$\tilde{P} = \tilde{U}\tilde{D}\tilde{U}^T = \bar{U}\bar{D}\bar{U}^T + \text{Diag}\,(0,0,\sigma_w^2)$$

$\tilde{U}$-$\tilde{D}$ are obtained using the Agee-Turner rank one update algorithm of Ref. 5. $\hat{U}$-$\hat{D}$ refers to filter values at time j, and $\tilde{U}$-$\tilde{D}$ refers to the predicted values at time $j+1$.

(4) Preliminary measurement update calculations

$$f = \tilde{U}^T a^T \;;\; a^T = (1, \Delta t, \Delta t^2/2)$$

$$g = \tilde{D} f$$

$$\alpha = \sigma_{\Delta z}^2 + f^T g \text{ (innovations variance)}$$

(5) Residual validation

$$\Delta z = z - a^T \tilde{\epsilon}$$

(6) Kalman gain computation

$$v = \tilde{U} g \text{ (normalized gain)}$$

(7) Measurement covariance update

$$\hat{P} = \hat{U}\hat{D}\hat{U}^T = \tilde{U}\left(\tilde{D} - \frac{1}{\alpha} g g^T\right)\tilde{U}^T$$

The U-D measurement update formulae of Ref. 3 simultaneously computes v, $\hat{U}$ and $\hat{D}$; $\hat{U}$-$\hat{D}$ represents $P(t_{j+1}|t_{j+1})$

[3] Smaller than experience would predict or smaller than is consistent with the observed residuals.

[4] Time subscripts are omitted. It is assumed that we start with "^" filter quantities at step j, perform a time update, steps (1) – (3), and obtain "~" predict quantities at step $j+1$; and complete the cycle by computing "^" filter quantities, steps (4) – (7), which refer to time $j+1$.

(8) State update

$\hat{\epsilon} = \tilde{\epsilon} + v\ (\Delta z/\alpha)$.

$\hat{\epsilon}$ now represents $\epsilon\,(t_{j+1}|t_{j+1})$

Figure 2 illustrates one way in which this algorithm could be configured for the Tracking Real-Time Monitor Computer. Conditioning or pre-processing would be required to properly calibrate the incoming data. A start-up module could optimally be included to compute the *a priori* statistic and initial values required for an initial start. These can be computed from one or two passes of range and doppler data. The other two functions contain the Kalman sequential filter and its concomitant logic. Steps (1) – (5) would be performed in the first functional unit, while Steps (6) – (8) would be performed in the remaining functional unit.

Consideration could also be given to placing the algorithm at each station since all data and parameters required are available at each site. Figure 3 points out how this algorithm could be utilized within the existing radiometric data collection and processing system.

IV. Results

The filter algorithm just described was coded and tested on the Univac 1108 computer using simulated data. The data were produced assuming that the trajectory divergency phenomenon could be represented by a second-order polynomial. The data were perturbed by adding noise from a Gaussian pseudo-random number generator. Several tests using simulated data were executed with unvarying success. The following test parameters represent one of the more significant:

Modulo number = 100 μs

Polynomial coefficients used to initialize the simulation estimate:

ϵ_0 = 98 μs $\approx$ 15-km position error

$\dot{\epsilon}_0$ = 10 μs/day $\approx$ 35-mm/s velocity error

$\ddot{\epsilon}_0$ = 0.05 μs/day^2 $\approx 2 \times 10^{-6}$-mm/s^2 acceleration error

Filter *a priori* uncertainties:

σ_ϵ = 0.2 μs $\approx$ 30 m

$\sigma_{\dot{\epsilon}}$ = 0.05 μs/day $\approx$ 0.17 mm/s

$\sigma_{\ddot{\epsilon}}$ = 0.001 μs/day^2 $\approx 4 \times 10^{-8}$ mm/s^2

Simulation parameters:

$\eta\,(t)$ = N (0, 100), 100 nanosecond (ns) gaussian white noise

Δt_1 = 0.08-day (2-h) sample interval used to generate data residuals

Δt_2 = 0.3 day (7.2 h), length of data span

Δt_3 = 20 days, time between data spans

Δt_m = $t_j - t_{j-1}$ = 1-yr interval between state estimate time updates.[5]

τ = 7 days

To compress the results for illustration purposes, the filter residuals were averaged on a pass-by-pass basis (i.e., over each data span) over the one year period of the test. The upper graph in Fig. 4 represents the residual output of the filter, Δz, while the lower graph represents the innovations variance, α.

The filter reacted well to the simulated data; the residuals remained within bounds, and the innovations variance converged to the level of noise impressed on the data. This is a bit surprising because the filter model does not quite match the simulated data model, and the nature of the rollover effects is highly nonlinear. One rather interesting feature of this simulation that led us to pursue more conclusive testing was the observation that here was a case (although admittedly fabricated) where the range residuals could be tracked over an entire one-year period without the need of a trajectory update. Note that the space between tracking periods was 20 days.

In order to further verify the filter formulation, data from several spacecraft were collected and processed. The results from processing range data from the Viking A mission are presented here.

In processing these data, it was found that there was a greater sensitivity to the *a priori* model statistics and filter parameters than in the simulated cases. Although the divergence model matched the long term behavior of the observable, there were local trends in the data that tended to weaken

[5] Using this large time step corresponds to using a constant parameter model; the value of τ in this case is immaterial.

the predictive capability of the filter, thus preventing accurate processing over more than two or three days. The general nature of this data is illustrated in Fig. 5 with the scale distorted to illustrate the local features.

At this point the stochastic update feature of the filter became extremely important. After some experimentation, it was found that accurate estimates could be obtained with the evidently mismatched model if appropriate filter parameter values were chosen, viz., the epoch or state mapping interval, Δt_m, and the time constant or correlation interval, τ. The following set of test parameters permitted us to validly process 4 months of randomly spaced data with some gaps of 1-1/2 to 2 weeks:

$$\text{Modulo number} = 1000\ \mu s$$

$$\epsilon_0 = 293\ \mu s$$

$$\dot{\epsilon}_0 = 0.0004\ \mu s/\text{day}$$

$$\ddot{\epsilon}_0 = 1\ \mu s/\text{day}^2$$

$$\sigma_\epsilon = 1.0\ \mu s$$

$$\sigma_{\dot{\epsilon}} = 1.0\ \mu s/\text{day}$$

$$\sigma_{\ddot{\epsilon}} = 1.0\ \mu s/\text{day}^2$$

$$\eta(t) = 50\ \text{ns}$$

$$\Delta t_m = 0.03\ \text{days (45 h)}$$

$$\tau = 14\ \text{days}$$

The adaptability of the filter to the data is demonstrated by the sample of the Viking A range data results. Figure 6 shows the filter results for 6 passes of data between 25 October and 4 December 1975. This data sequence began approximately 50 days after spacecraft launch and has data gaps of up to 18 days. The quality of the data fit is demonstrated by noting that in Fig. 5 the input data were on the order of microseconds (10^{-6} seconds), whereas the filter in this case has reduced the residuals to the nanosecond (10^{-9} second) level. The anomalous behavior of the data on 1 December 1975 which had not been previously detected in the original data is clearly in evidence. The anomalous behavior has not yet been verified because station logs are not detailed enough to reflect hardware malfunctions at this level. It is believed, however, that the anomaly is attributable to either hardware noise or a charged particle pulse in the transmission media. More analysis of this and other data phenomena remains. There is, however, no doubt that achieving the type of results would have been difficult if not impossible using the conventional least squares filter techniques that are commonly used for orbit determination.

V. Conclusions

The tests using both simulated and real data demonstrated that satisfactory real-time, automated estimation of our nonlinear ranging process is achievable. The factorization filter algorithm design is compact and efficient, and is suitable for use in a mini-computer or micro-processor where processing time and memory constraints are important considerations.

Further tests must be performed before this ranging residual estimation technique can be determined suitable for use during actual operations. Future studies are planned to investigate model modifications to account for a diurnal velocity term that is often encountered in the actual data and for the inclusion of doppler data to improve the filter predictive characteristics. A final filter design will be arrived at by tuning the filter parameters so that acceptable performance is achieved under the various conditions that the filter is expected to operate.

References

1. Berman, A. L., "Pseudo-DRVID: A New Technique for Near-Real-Time Validation of Ranging System Data," in *The Deep Space Network Progress Report 42-29*, pp. 180-187, Jet Propulsion Laboratory, Pasadena, Calif., Oct. 15, 1975.

2. Berman, A. L., "Differential Range Validation: A New Technique for Near-Real-Time Validation of Multistation Ranging System Data," in *The Deep Space Network Progress Report 42-36*, pp. 114-120, Jet Propulsion Laboratory, Pasadena, Calif., Dec. 15, 1976.

3. Bierman, G. J., "Measurement Updating Using the U-D Factorization," *Automatica*, Vol. 12, pp. 375-382, 1976.

4. Thornton, C. L., and Bierman, G. J., "A Numerical Comparison of Discrete Kalman Filtering Algorithms: An Orbit Determination Case Study," *Proc. 1976 Conference on Decision and Control, Key Sands, Florida*, pp. 859-872.

5. Thornton, C. L., and Bierman, G. J., "Gram-Schmidt Algorithms for Covariance Propagation," *Proc. 1975 Conference on Decision and Control, Houston, Texas*, pp. 489-498.

6. Curkendall, D. W., et al., "The Effects of Random Accelerations on Estimation Accuracy with Applications to the Mariner 1969 Relativity Experiment," *Proc. Conference on Experimental Tests of Gravitation Theories, California Institute of Technology, Pasadena, Calif., Nov. 11-13, 1970.*

7. Christensen, C. S., *Performance of the Square Root Information Filter for Navigation of the Mariner 10 Spacecraft,* Technical Memorandum 33-757, Jet Propulsion Laboratory, Pasadena, Calif., Jan. 15, 1976.

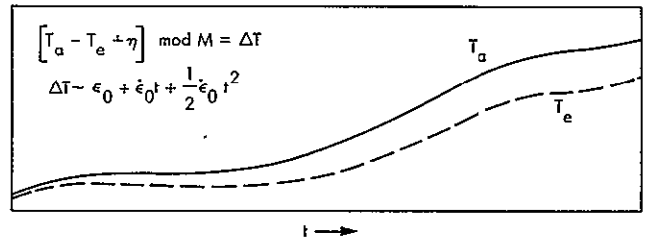

Fig. 1. Divergence of predicted line-of-sight range

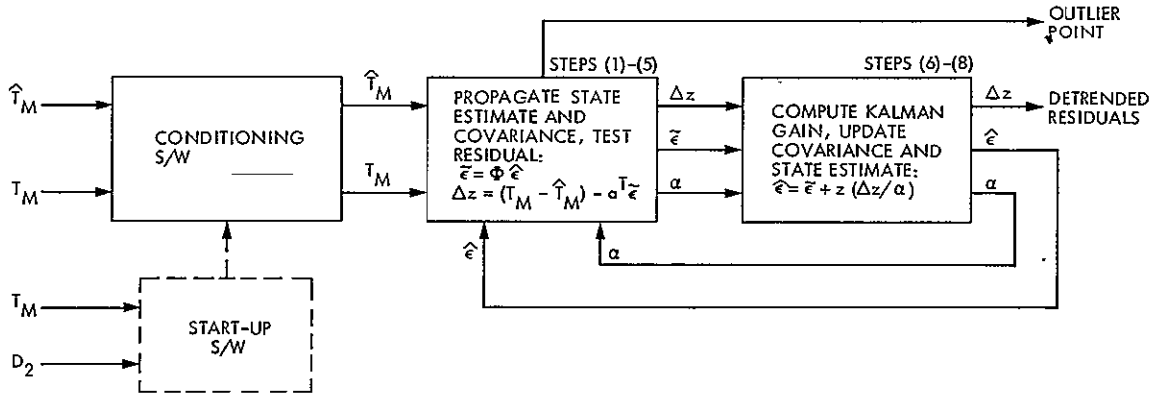

Fig. 2. Possible RTM mechanization of Kalman filter

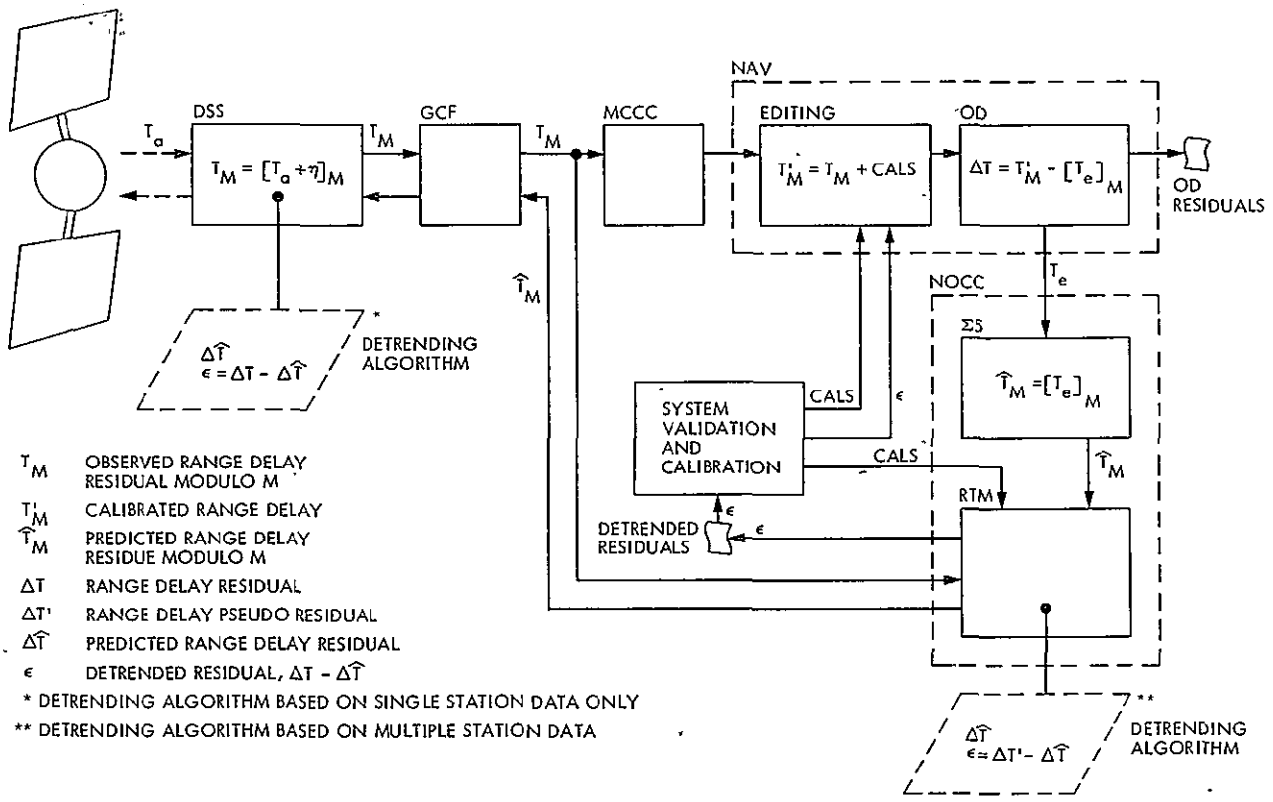

Fig. 3. Detrending algorithm location within radio metric data collection and processing system

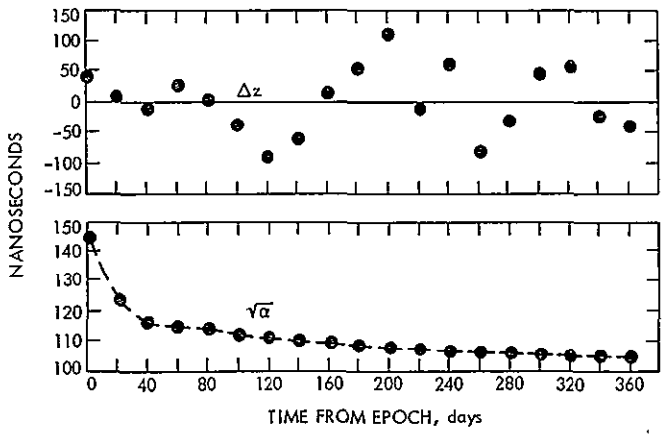

Fig. 4. Simulated case detrended residuals and statistics

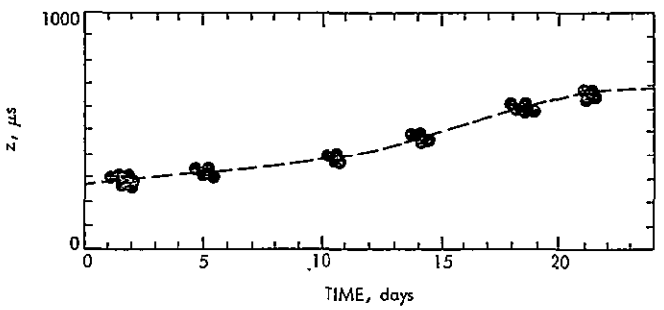

Fig. 5. Typical range residual trends in Viking spacecraft data

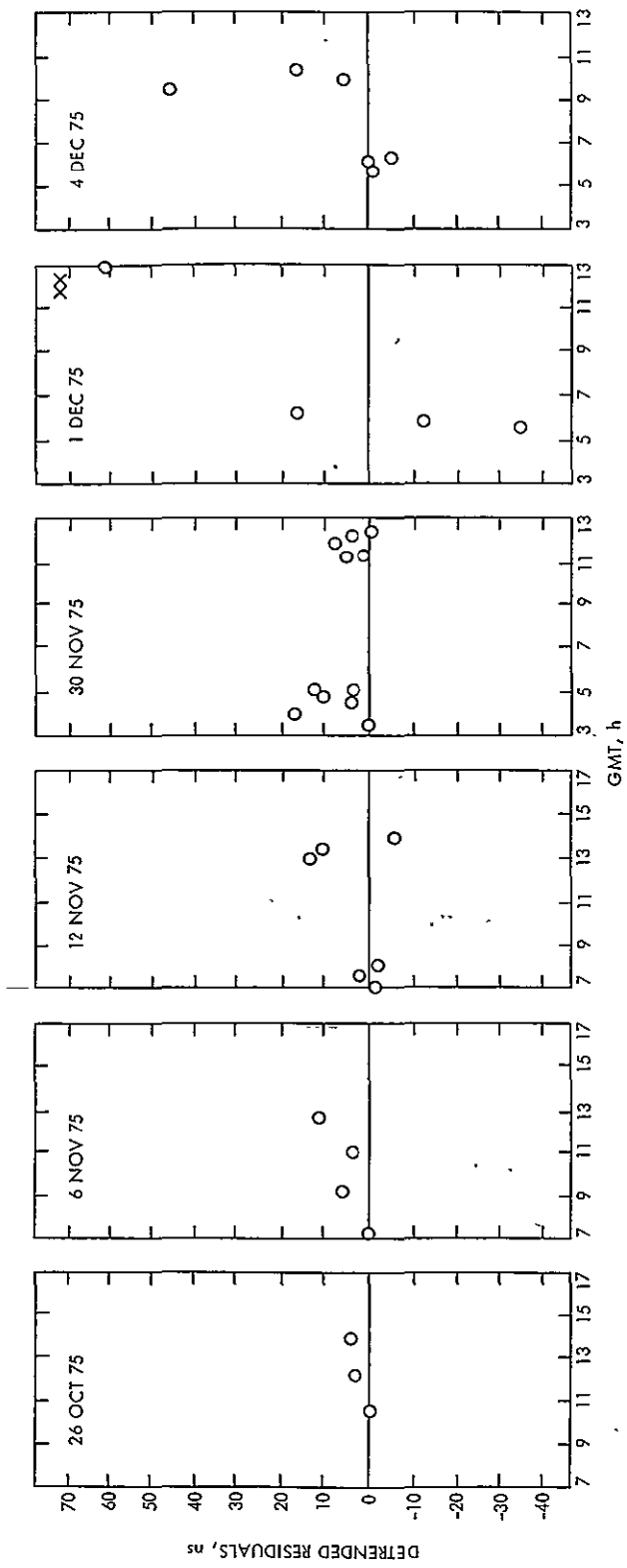

Fig. 6. Viking range residuals after Kalman filter detrending

D15

N78-15082

DSN Radio Science System Description and Requirements

B. D. L. Mulhall
TDA Engineering

A new DSN data system has been created to collect the functions performed by the DSN in support of spacecraft radio science experiments. The system is described and some of its major functions are delineated.

I. Introduction

Until recently the Deep Space Network was functionally organized into five data systems, i.e., Tracking, Telemetry, Command, Test and Training, and Monitor and Control. These systems produced the major data types provided to flight projects, and also embodied all the functions and the equipment, personnel, and resources required to accomplish the functions which collected, processed, and delivered the data to the end user as a service to the flight projects.

The DSN has accepted a new role which is the production of spacecraft radio science data to meet flight project requirements. In the past these data types consisted of the conventional, radio metric data supplied to flight projects for navigation purposes and the use of special, R&D equipment for recording occultation data at certain Deep Space Stations. The requirements for the Voyager and Pioneer Venus missions specify new accuracy requirements on the conventional radio metric data types which exceed the navigational requirements and consequently impose new system requirements on the DSN. Also, the use of operational equipment for the collection of occultation data and other radio science related measurements is being implemented in the Network and must be identified as a new, sixth data system, the DSN Radio Science System, so that the functions which are unique to this System can be identified, and their corresponding requirements developed.

To develop DSN radio science functional requirements, meetings were held with radio scientists from the Voyager and Pioneer Venus Projects. This effort culminated in a review of these requirements on February 4, 1977 for these two flight projects. This article describes the System itself and provides at least an overview of some of the major functional requirements presently being considered for the System.

II. System Description

The requirements review began with a series of definitions; the first was the term "radio science" itself. The area of radio science is usually considered to include the measuring of phenomenon associated with radio wave generation and propagation, which includes those radio signals that originate from natural sources and from spacecraft sources. In the case where natural sources are involved, the object of the experiment is usually to study either the generation process or the propagation, and can be referred to as radio astronomy. Also, natural radio sources are used for very long baseline interferometry (VLBI).

When the spacecraft is the source of the radio signal, the investigation is usually related to phenomenon that occur along the ray path and affect the propagation of the radio wave. Some of these experiments concern celestial mechanics, planetary atmospheres investigations, interplanetary charged particle media investigations, the solar corona, measurements of planetary wind such as those made during the Pioneer Venus entry mission, and investigation of the rings of Saturn by the Voyager occultation. The material presented dealt only with spacecraft radio science and did not include requirements for receiving natural radio source signals. In the future, a presentation on VLBI requirements is planned that will cover the requirements for that system.

The DSN Radio Science System, intended primarily for use with spacecraft radio signals, can be divided into two major areas or data types. The first is radio metric or closed-loop receiver data, which generate doppler and ranging as principal data types. The second area is open-loop received data. The review was further limited to discussing only open-loop requirements. The closed-loop or radio metric data requirements will be the subject of another review in the near future. The reason for concentrating on the open-loop requirements is that these requirements need to be understood rather quickly so that the implementation of the new equipment planned in the DSN, which is dedicated solely to open-loop functions, can proceed. This is not to say that there are not many important open questions in the closed-loop area. However, the issue of the open-loop requirements, as was well documented by the review, could more than occupy time available for discussion in one day.

Figure 1 defines the various bandwidths discussed in the remainder of the review meeting. The scale of the horizontal axis is frequency either in MHz or kHz. The widest bandwidth, titled "allocated bandwidth," is intended to show the deep-space communication band, either at S- or at X-band, and allocated by international agreement, within which deep-space communication is conducted. Noting the break lines on the axis to indicate that somewhere within this 10- to 40-MHz band is an input bandwidth for the DSN Radio Science System that has been assigned to a particular mission. Consequently, the equipment must be able to be tuned anywhere within the allocated bandwidth but needs only to provide the requirements for a particular mission within the "input bandwidth," the bandwidth that the front end of the system must be capable of handling.

Within the input bandwidth is a system "output bandwidth," which implies that the DSN has performed some kind of bandwidth reduction. This bandwidth reduction can either be performed in real time, after the fact in nonreal time, or conceivably both. No requirement has been recognized for both however. This output bandwidth must contain the signal bandwidth that is intended to describe the actual instantaneous bandwidth occupied by the spacecraft signal.

Figure 1 shows the instantaneous bandwidths. The output bandwidth and signal bandwidth may move anywhere within the input bandwidth due to doppler excursions that must not exceed the input bandwidth.

The material presented at the review has taken a fairly novel and unprecedented approach to specify requirements in the purest sense as opposed to design parameters. Frequently, experimenters have stated their needs in terms of an assumed design (e.g., sample rates and bits per sample). If design parameters are used as a starting point, the design is unnecessarily constrained, preventing life-cycle cost analysis, trades, and minimization. The constraints will also very likely inhibit a design that is multimission, since each experimenter is likely to conceive a different design and use somewhat different design parameters to specify his needs. Consequently, the presentation was intended to get back to basic, fundamental requirements and to deal with them further in a top-down approach.

The basic requirements are first, to acquire the radio signal; second, to maintain system linearity through the various steps in handling the signals, namely acquisition, recording, and reproduction; and third, a new commitment by the DSN, to perform bandwidth reduction consistent with the requirements for acquisition and linearity. The reason that the DSN has accepted requirements for bandwidth reduction, either real-time or nonreal-time, is that performing this first step in one facility removes the requirement on each flight project for this first data processing step and, consequently, does not have to be reinvented for each flight project. The reason for this was the overwhelming costs to the Pioneer Venus Orbiter occultation data reduction which, if performed in real time, could vastly reduce the overall agency cost for this experiment. It was recognized that this capability was really a multimission capability. Minimization of system life-cycle costs is also a first-level requirement.

Figures 2 and 3 show functions and major system interfaces at the Deep Space Stations, CTA-21, and the Network Operations Control Center (NOCC). The Transmitter and Frequency & Timing Subsystems form part of the system since, even though data is being received open loop, an uplink may still have been established in at least some cases. Consequently, system requirements need to be levied on these subsystems.

Two new subsystems, the DSS Radio Science Subsystem (DRS) and the CTA-21 Radio Science Subsystem (CRS) were proposed as a means of identifying the equipment at the stations, and at CTA-21, which is dedicated to radio science

data acquisition and processing. Functions of these subsystems are shown in Fig. 4.

Radio frequency requirements were then discussed (see Table 1). The need for signal presence indication by all projects was strongly voiced. The requirement is not only for an indicator for the station operator, but also for a signal presence indication within the radio science Mission Support Area. This latter requirement will require some study since a design that minimizes system life-cycle costs may not be feasible.

The signal power and system noise temperature measurements were also discussed. The data are required as calibrations of the system rather than experimental observational data.

Data handling requirements were presented for both real and nonreal-time bandwidth reduction. The requirement for backup recording was discussed at length. The first few occultations of an orbiter are extremely important since the uncertainty in the doppler signature for these first few events will limit the amount of real-time bandwidth reduction that can be performed until the signature is well enough in hand so that the remaining occultations can be performed with more bandwidth reduction to reduce nonreal-time processing costs.

Suitable backup recording will be provided for orbiters as well as flyby missions.

In the process of performing bandwidth reduction, linear ramps are used to sweep the local oscillator frequency to track out some of the doppler excursion. It is required that the history of the ramps used be provided to the experimenters. In addition, the deviation of the mixer frequency from the nominal model must be less than 0.005 Hz. The programmed oscillator will deliver this accuracy even for extremely high doppler rates, one kHz per second, which is greater than any anticipated.

Table 2 provides more detailed requirements; it addresses the subject of the characteristics of the spacecraft signal, the system requirements on the input bandwidth previously defined, and the requirements on the output bandwidth (after bandwidth reduction process).

By developing Table 2 and filling in the requirements, the most stringent requirement in each of the four cases can be identified. These four cases are the Pioneer Venus Entry and Orbiter radio science experiments, and the Jupiter and Saturn encounters by Voyager. When the most stringent requirement in any one line item is found, then a multimission system can be designed to meet that requirement and also satisfy the less stringent requirement at the same time. Missing from these charts are the requirements for the Pioneer 11 occultation of Saturn, which occurs in 1979. These requirements will be included prior to publication of the functional requirements document.

In Table 2 where an S is followed by a diagonal slant and an X, the corresponding numbers refer to the S-band or the X-band requirement.

In the input bandwidth requirements, constraints are listed that include the range over which the doppler can cause the input frequency to shift, the uncertainty in the doppler shift, and the spectral broadening of the carrier, which is fairly pronounced for the rings of Saturn occultation.

In Table 2 are two items titled "Linearity." The first one, under the phase response across the system input band, is for phase linearity and impacts the work required for data reduction since nonlinear phase requires more calibration. The other Linearity entry refers to harmonic distortions (which is not believed to be a problem) and allowable saturation. This latter item has not been developed fully enough to show the specific items of importance and the units or the quantities that need specification. However, it was included since it is the subject for further study and may or may not survive to be incorporated in the requirements documents.

The requirements of the bandwidth reduction process are also outlined in Table 2. The constraints on the real-time bandwidth reduction include Doppler shift uncertainty, spectral broadening, and time of onset of the doppler shift. Real-time bandwidth reduction is limited by the a priori knowledge of these parameters. These requirements will be extended to the Jupiter encounters since real-time bandwidth reduction for this event appears to be quite feasible.

Also in Table 2 nonreal-time reduction is discussed. Here the constraints are not as severe since the data has been recorded and more than one attempt can be made at bandwidth reduction. Nonreal-time bandwidth reduction will probably be required for the Saturn encounter since the real-time system will not be capable of accommodating the bandwidths for this event.

The general system requirements were also discussed and the requirement for minimal life-cycle cost was modified to show that for the temporary installations for the Pioneer Venus entry mission, the normal 10-year life cycle will not be used. Instead, the actual time that the equipment is maintained in the Network will be used for the life-cycle period.

Acknowledgment

The author wishes to acknowledge the assistance of Dr. J. I. Molinder in developing the material presented in this article.

Table 1. Radio frequency requirements

Parameter	Pioneer Venus 78		Voyager	
	Entry	Orbiter	Jupiter encounter	Saturn encounter
Frequency bands	S	S and X	S and X	S and X
Polarization	RCP	RCP	RCP or LCP	RCP and LCP
Signal presence indicator	Required	Required	Required	Required
Signal power measurement			Required	Required
System noise temperature measurement			Required	Required

Table 2. Open-loop requirements

Requirement	Pioneer Venus 78		Voyager	
	Entry	Orbiter	Jupiter encounter	Saturn encounter
Signal parameters				
Amplitude measurement				
Precision			0.1 dB over any 10-dB range 0.5 dB over any 40-dB range	
Calibration			1.5 dB	1.5 dB
Phase measurement				
Absolute phase at receiver input frequency, S/X			36 deg/132 deg	
Differential phase				
Across band, S/X	1 deg/not applicable (NA)			
Between S- and X-band (S-3/11 X)		To be supplied (TBS)	10 deg (1 deg design goal)	
Between receivers tuned to same frequency at one DSS				1 deg
System				
System input bandwidth, S/X	2 MHz/NA	TBS	600 kHz/2 MHz	600 kHz/2 MHz
Constraints				
Doppler shift range	TBS	TBS	TBS	TBS
Doppler uncertainty	TBS	TBS	TBS	TBS
Spectral broadening			1 kHz	20 kHz
Placement of system bandwidth within total allocated band	Adjustable within entire S- and X-band allocation			
Amplitude response across system input bandwidth				
Calibration			0.2 dB	0.2 dB
Stability (over 1 hour)			0.2 dB	0.2 dB
Uniformity			±3 dB (±1 dB desired)	
Phase response across system input bandwidth				
Calibration				
Real-time, S/X				
Nonreal-time, S/X	0.5 deg/NA		0.5 deg/0.5 deg	
Stability				
Real-time, S/X				
Nonreal-time, S/X	0.5 deg/NA		0.5 deg/0.5 deg	
Linearity				
System noise spectral density				
Calibration precision			1%	1%
Accuracy (1 sample/10 s)			2%	2%
Stability			10%	10%
Amplitude dynamic range				
Linearity				

Table 2 (contd)

Requirement	Pioneer Venus 78		Voyager	
	Entry	Orbiter	Jupiter encounter	Saturn encounter
Bandwidth reduction				
Real-time bandwidth reduction				
Input bandwidth, S/X	NA	80 kHz/300 kHz	TBS	NA
Constraints				
Doppler uncertainty				
Spectral broadening				
Time of onset				
Amplitude degradation	NA	< 0.5 dB	TBS	NA
Phase degradation				
Absolute, S/X	NA	< 5 deg/< 20 deg	TBS	NA
Differential				
Output bandwidth	NA	1 kHz to 40 kHz	TBS	NA
Nonreal-time bandwidth reduction				
Input bandwidth	2 MHz	NA	NA	TBS
Amplitude degradation	<2 dB	NA	NA	TBS
Phase degradation				
Absolute	< 2 deg	NA	NA	TBS
Differential between signals on one recording	< 5 deg	NA	NA	TBS
Output bandwidth	1 kHz to 10 kHz	NA	NA	TBS

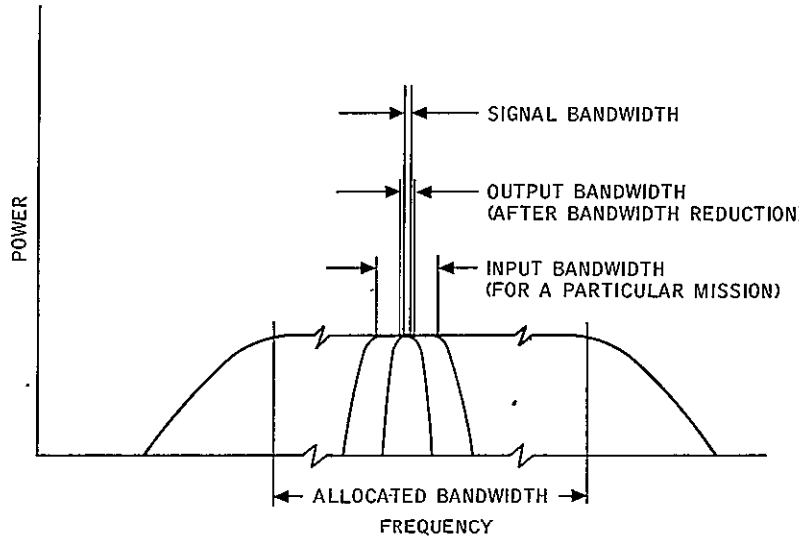

Fig. 1. Bandwidth definitions

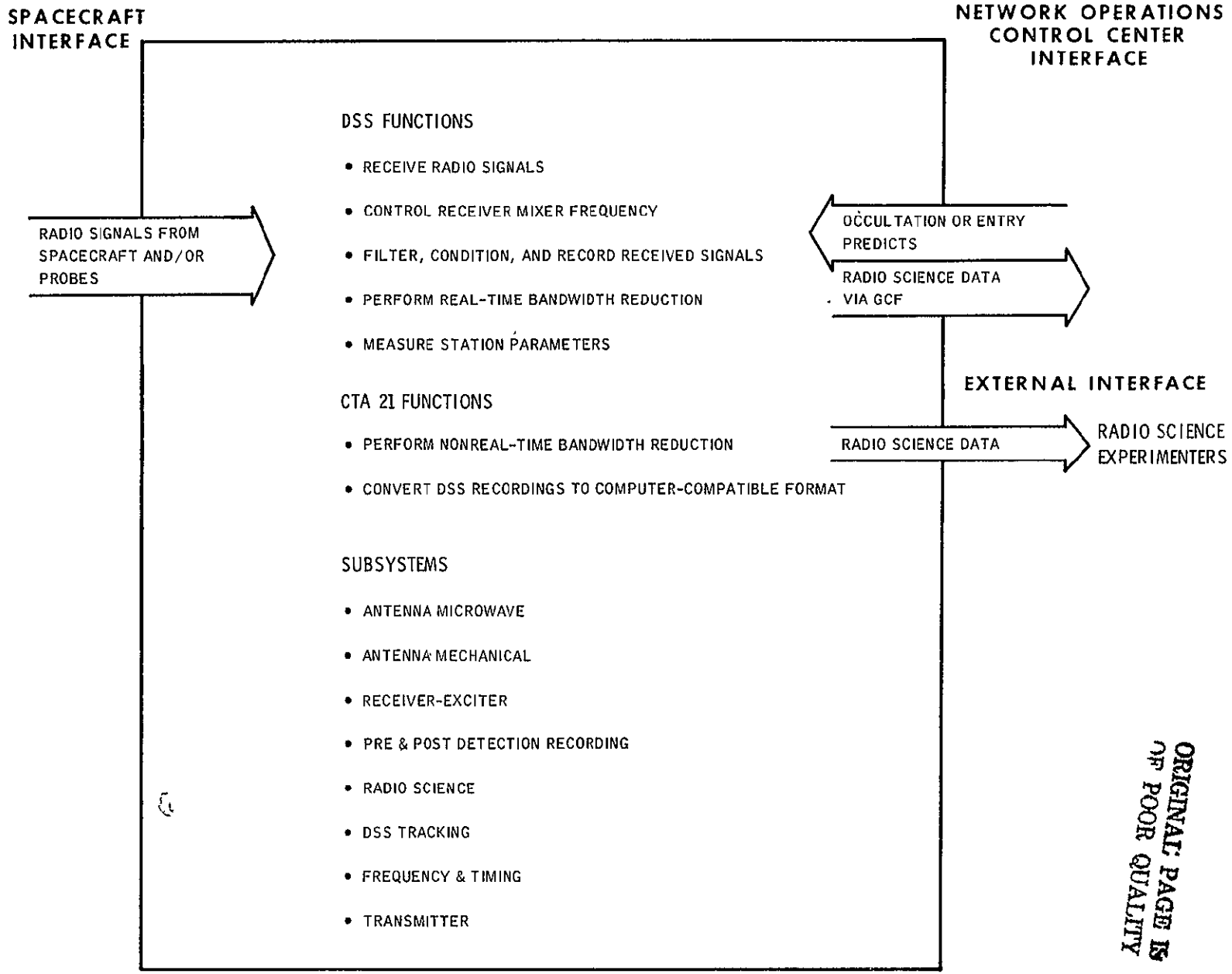

Fig. 2. DSS and CTA 21 open-loop functions and interfaces

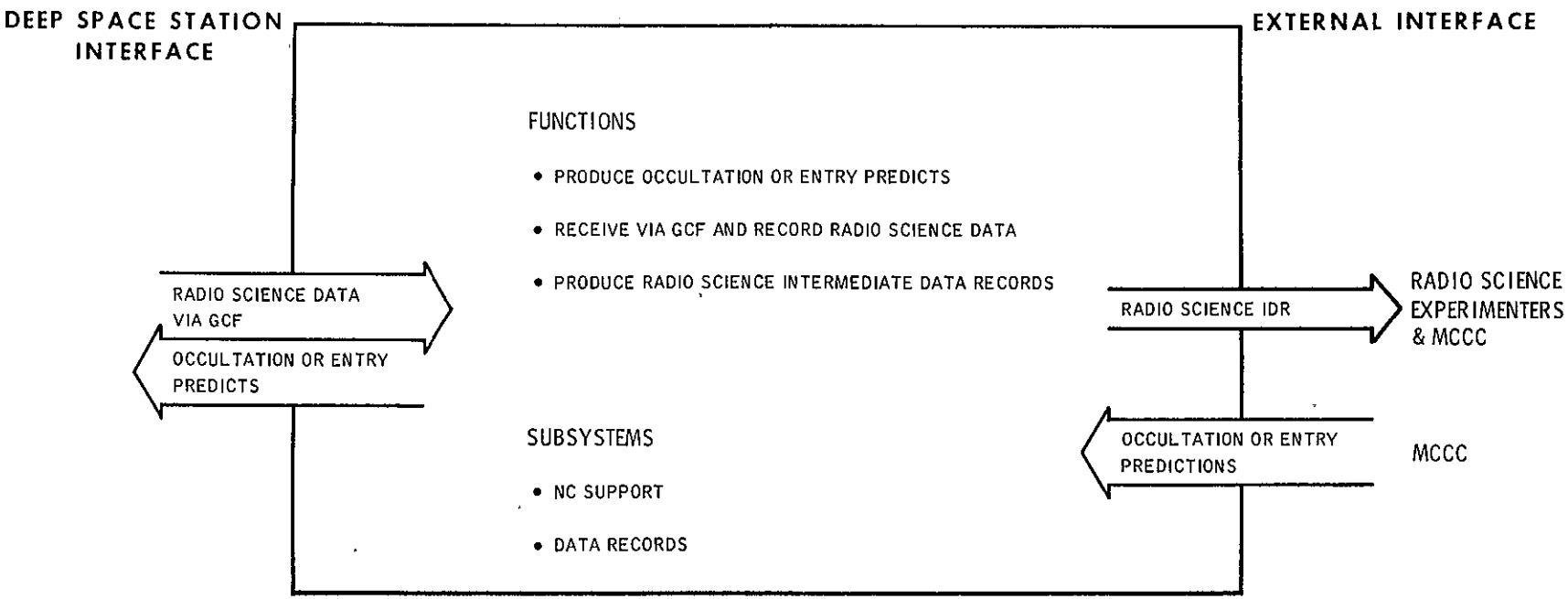

Fig. 3. NOCC functions and interfaces

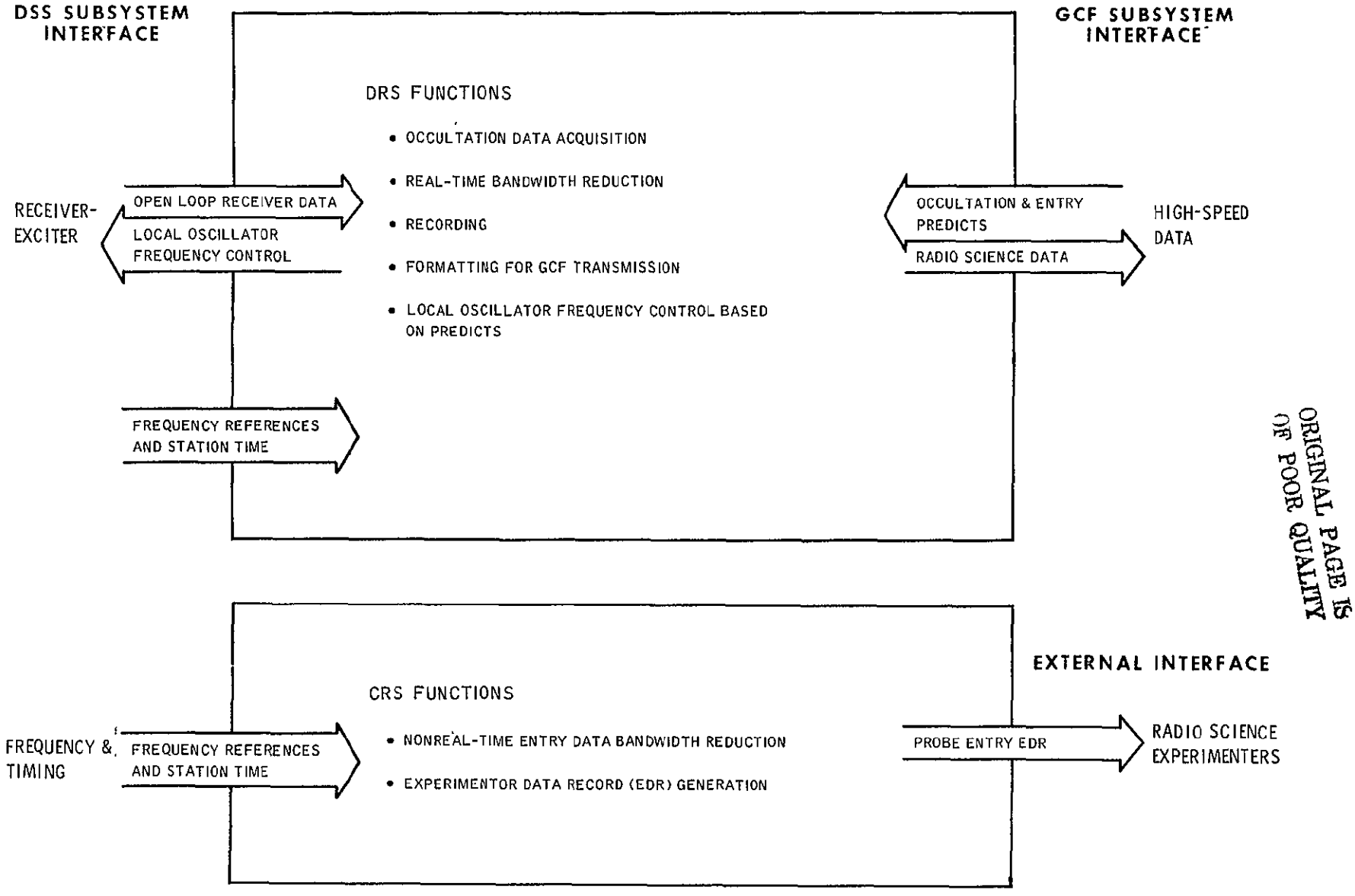

Fig. 4. Radio science subsystems functions and interfaces

Standard High-Reliability Integrated Circuit Logic Packaging

D. W. Slaughter
DSN Data Systems Section

A family of standard, high-reliability hardware used for packaging digital integrated circuits is described. The design transition from early prototypes to production hardware is covered and future plans are discussed. This article includes detail descriptions of the interconnection techniques, connectors and related hardware available, both at the microcircuit packaging and main-frame level; general applications information is also provided.

I. Introduction

Standardized modular hardware for the packaging of integrated circuit (IC) logic systems was described in Ref. 1, when development was in the early prototype stage. Since that time, a considerable quantity of hardware has been produced and installed in the DSN stations. This article will review the design transition from early prototypes to production hardware, deal with the production phase, and discuss some user application considerations, and future plans.

The modular packaging hardware, as reported in Ref. 1, evolved at two distinct levels. The first level is a plugable subchassis (Figs. 1 and 2), which packages and interconnects up to 144 ICs of the 14- or 16-pin dual-in-line package (DIP) type. This subchassis was designed to serve (by replacement at the subchassis level) as the first line of maintenance in the DSN stations, for the logic packaged therein. Approximately 1400 of these subchassis have been manufactured to date. Cost data are provided in Table 1. Interconnection of the ICs, which plug into special high-reliability (hi-rel) sockets, is by wirewrap, which can be accomplished on a fully automatic machine. The second packaging level is that of the main chassis, which provides the mating receptacles and interconnections for the several subchassis (usually but not necessarily more than one) required to implement a functional unit. Whereas the one subchassis design has been utilized as a standard for all applications, the main chassis design has been fully standardized only at the level of the subchassis mating receptacle (Fig. 3), because of variations in the number of subchassis per subsystem, presence of other digital hardware and display devices, the system of subsystem partitioning (i.e., breakdown into independent drawers, perhaps each with its own power supply), all related to the need for accessibility for testing, and the number of wires (cables) to be carried into the chassis.

This report will also describe three main chassis designs which have been used to package a majority of the subsystems implemented to date and will list the documentation available to the potential user.

II. Detail Description

Figure 2 shows the subchassis design adopted. Subchassis may carry part numbers 9457999-1 or -2 (the first lot of 175, now obsolete, carried part number 9457085-1). The -1 and -2 suffixes cover minor differences in manufacturing; all subchassis, including obsolete model 9457085-1, are fully interchangeable to the user. The subchassis holds 144 of the 14- or 16-pin plugable DIP ICs. A half-size subchassis has been documented but has not been fabricated to date.

The design is based on an aluminum base plate which serves as the ground plane. A power plane is laminated over the base plate, on the wirewrap side (Fig. 4). This arrangement provides excellent ground-plane and power distribution characteristics, suitable for 54S (Schottky-clamped) ICs. Plane noise is insignificant when compared with the noise margins of 54-series circuits (about 1 volt). Ground and power connections to the IC sockets are made by wirewrapped connections on posts press-fitted into the ground and power plane (see Fig. 5). The standard subchassis comes with one ground and one power post pre-installed at locations convenient to the power and ground pins of 14- and 16-pin ICs. Users of larger, high-speed LSI packages may install additional ground and power pins in spare holes provided for this purpose, if required to minimize lead length (ground and power connections should not exceed 1 in. (2.54 cm) for any 54-series circuit).

Strip sockets (Fig. 6) permit the use of LSI modules or any module whose pins are disciplined to multiples of 0.1-in. (2.54-mm) centers. Sockets are press-fitted into the base plate (ground plane). The tuning fork contact provides sufficient tension for a reliable contact, and, when formed from beryllium-copper alloy and heat-treated, is capable of expanding to accept larger diameter pins, and after withdrawal of these pins, recovering to grip the very thin pins used on many ICs. Broken contacts may be replaced individually.

The subchassis interface connector provides 204 pins, consisting of sixty-eight 3-pin modular connectors. These 3-pin connectors, shown in Fig. 7, are individually replaceable. Four additional 3-pin connectors, providing for ground connections, are made with tin-plated brass bodies.

The subchassis is mounted on the mating receptacle (in Fig. 3, both wirewrapable and wire-crimp terminations are shown) with two jack screws. In the interest of providing for maximum flexibility in overall chassis design (which varies widely according to system requirements), these jack screws are the sole method of subchassis mounting. This arrangement has been drop-tested to confirm handling and shipping survival.

Jack screws are assembled internal to the subchassis as shown in Fig. 8. The first lot of 175 subchassis did not use the lubricated thrust washer and had difficulty with galling of the jackshaft on the housing. As a result of this galling, and a tendency for personnel to apply more torque than necessary to fully seat the jack screw, roll pins were sheared off. The present model subchassis (9457999-1 or -2) uses a larger diameter roll pin, and replacement parts of the newer design are available for the older subchassis.

The mating receptacle uses tuning-fork contacts housed in insulating sleeves (aluminum sleeves for grounded contacts), which are press-fitted into holes drilled in the aluminum base plate. Contacts are individually replaceable and are rated at 5 amperes. The receptacles shown in Fig. 3 are available with either wirewrap terminations (which may also be soldered) or wire-crimp terminations.

III. Development Progress

The present design differs from the one pictured in Ref. 1 in the following details. The first prototype used an extruded aluminum section (Fig. 9) as the basic structure. Note that the new design (Fig. 2) uses a flat plate with attaching rails which serve to stiffen the plate and protect the wrap-posts from damage. Experience at the JPL machine shop indicated that the aluminum extrusion used in the original design would reduce costs by eliminating the machining costs of the separate rails. This experience was not sustained when commercial bids were received. The extrusion apparently raised fears of possible production difficulties and all bids contained a substantial hedge against these difficulties. Low bids were (for 200 parts) $200 for machining the extrusions, and $112 for machining the flat plate. The four rails and one connector retainer bar cost $25, for a total of $137 for the assembly. Other considerations include the cost of the raw extrusion which balances out with the cost of labor and screws required to assemble the rails. A decision was made to use the flat plate and separate rails.

Because of schedule commitments and because the modular connectors (Fig. 7) were the longest lead-time component, a cost plus incentive fee contract was let for these connectors prior to completing a thorough worst-case analysis of the connector mating; a problem area was noted when this analysis was performed. Referring to Fig. 10, note that the blades of the modular connector are recessed into a channel for protection during handling. The nylon sleeves (which form the

mating receptacle) must fit into this recess. In addition to protecting the blades, the initial contact between the subchassis channel and the receptacle sleeves serves to guide the subchassis connector blades into the receptacle "tuning fork" contacts as the jack screws are engaged. This feature is a desirable addition to the pair of guide pins which are also used for alignment, because the jack screws, used to apply the 200 pounds (890 newtons) of force required to mate 216 connector blades, deprive the operator of any feeling for misaligned, i.e., jammed blades. For this reason, the width of the subchassis recess was designed to barely accommodate the mating nylon sleeves. However, worst-case analysis showed that insufficient tolerance had been allowed for the small random mislocations of the nylon sleeves. It was then found necessary to increase the spacing by 0.005 in. (0.127 mm). Since it was undesirable to increase the height of the connector bodies due to the incentive fee contract, it was decided that 0.005 in. (0.127 mm) would be milled off the base plate, as shown in Fig. 10. When a contract was let for a second manufacturing source and second set of tooling, this milling operation was deleted and the connector height increased. The new connectors use a different body color.

The original prototype and the first 175 production subchassis also used power and ground pins with threaded sleeves, held in place with a No. 1 hex nut (Fig. 8 of Ref. 1), whereas present production uses a press-fit sleeve. These early subchassis carry part number 9457085-1. Subchassis using pins with press-fit sleeves (1188 have been manufactured to date) carry part numbers 9457999-1 or -2. The -1 suffix applies to subchassis manufactured by Masterite Industries, while the -2 suffix applies to Fabri-Tek production. They are fully interchangeable to the user. The original decision to use pins with threaded sleeves was based on ease of repair. The press-fit sleeves require special tooling to remove and replace, particularly after the subchassis has been wirewrapped. However, the pins with threaded sleeves and nuts presented the following problems:

(1) They were relatively costly, both in per item cost and installation labor. The savings using press-fit sleeves is $60 to $70 per subchassis, or 10 to 15 percent of the subchassis cost.

(2) They were sole-sourced.

(3) Quality control of the threads proved difficult, and some pins failed to tighten down properly. Inspection was difficult.

The strip sockets (Fig. 6) are derived from the Standard Hardware Program of the Naval Avionics Facility, Indianapolis. As used in the Navy program, these sockets mated with the 0.020-in. (0.5-mm) thick blades of a circuit board (IC flat packages were mounted on the circuit board). The tuning fork style of contact, using beryllium-copper alloy, was selected because it had the potential for accommodating the wide variety of pin sizes used on the various ICs and other commercial DIP circuit modules without damage, providing exceptionally good contact retention for all packages. However, to accommodate the 0.010-in. (0.25-mm) thick blades of the typical DIP packages, it was necessary to have the manufacturing tooling redesigned to provide an 0.006-in. (0.15-mm) maximum contact opening. In Ref. 1, it was stated that these sockets were commercially available. However, the material used by that vendor was phosphor-bronze alloy, a material which exhibits aging fatigue, and negotiations to substitute beryllium-copper alloy were never successfully completed. However, two other sources of the Navy contact (which used beryllium-copper alloy) were willing to re-tool as required to provide the JPL-specified contact opening.

IV. Documentation and Manufacturing

All component parts (including those used on the subchassis mating receptacles) are covered by JPL detail drawings or, in the case of commercial components, either by JPL specification control drawings or military/federal specifications.

Subchassis have been manufactured for JPL by two different companies. The first lot was built at a unit cost of $836 by Masterite Industries (the only bidder): a total of 429 subchassis were manufactured. The second source, the National Connector Division of Fabri-Tek, Inc., has produced 943 subchassis at an approximate cost of $550 each. The price reduction is thought to be due to:

(1) The additional competition available as evidence of JPL's intent to purchase significant quantities became available.

(2) Improved tooling design, more automation and better production controls used by the second source.

With the exception of the off-the-shelf commercial components, JPL owns the production tooling manufactured by both of the above companies. Two sets of tooling exist because the production contracts overlapped, and because of our desire to obtain two sources. The tooling produced by Masterite is now in storage in a federal warehouse, while the tooling produced by Fabri-Tek is now at that company or its subcontractors. The Fabri-Tek tooling represents an investment of approximately $55,000, or about $58 per subchassis produced to date (10 percent of the per unit price).

Major items of tooling include punch-press dies for the contacts of the modular connector and the IC strip socket, and injection molds for the connector bodies. There is also a punch-press die for the power plane, and drill jigs for the mounting rails. There are also fixtures which assist in the loading of contacts and wrap-posts, and which otherwise aid in assembly.

V. Quality Control

Contractor quality control is governed by JPL Specification ES509281, "Quality Control Requirements for Subchassis, IC Logic Packaging, Detail Specification for." This specification includes all applicable portions of GMO-50139-GEN, The General Specification of Quality Control Requirements for Operational Support Equipment, plus additional material specifically applicable to subchassis. Additional detail specifications have been written to cover the IC sockets and modular connectors. Workmanship is inspected to QAWS 200.60, a Quality Assurance Workmanship Standard written specifically for the subchassis. It has proven necessary to have a JPL inspector present at the contractor's facility for first article inspections at the component level, and for the final inspection of each subchassis. In this way, any necessary rework can be accomplished with assurance that it is properly performed. It has also proven highly desirable to utilize the same inspector for each successive production lot, because there is very substantial learning function. The location of defects or omissions among the thousands of contacts and wrap-posts (any one of which is costly to the ultimate user) requires several days of on-the-job training, during which time the new inspector learns from his oversights.

VI. Procurement Lead Times

Procurement lead times vary significantly according to the situation encountered when competitive bids are solicited. If the tooling is utilized by a past manufacturer, finished subchassis will be available 12 to 14 weeks after receipt of order. An additional 10 to 14 weeks should be allowed for procurement procedures required prior to placement of order. If the tooling is furnished to a vendor who has not utilized it before, an additional 4 to 12 weeks will be required for tooling adaptations, first article inspections, and production de-bugging.

Because of these lead times, a stock of about 100 to 250 subchassis is maintained. Delivery from stock is made on approval of the Section 338 manager. Table 1 lists the subchassis and accessory components available. Orders are not normally placed unless a requirement for at least 100 subchassis has been accumulated, to take advantage of the price break.

VII. Subchassis Application Guidelines and Conventions

A. Installing LSI Modules

The strip sockets permit the use of LSI modules having more than 16 pins. By installing additional strip sockets, as shown in Fig. 11, any pin row spacing based on integer multiples of 0.1 in. (2.5 mm) can be accommodated. Ground pins may be removed if necessary. Documentation should consist of a tabular list of the subchassis coordinates where strip sockets are to be added and ground pins removed (if any).

B. Pin Numbering System

The subchassis is divided into four identical sections. Referring to Fig. 12, which shows one of these sections, note that each section has 18 (9 pairs on 0.3-in. (7.6-mm) centers) strip sockets, with 35 pins per row. Allowing for one unused pin between ICs (required for package end overhang), each pair of rows accommodates four 16-pin DIP modules. The numbering system is also shown in Fig. 12. Note that pins are numbered 101 through 135, with the second section numbered 201 through 235, etc. Utilizing this numbering system, pin No. 1 of 14- or 16-pin DIPs are installed at contacts 1Y101, 1Y110, 1Y119, and 1Y128; and for the second row at 2Y101, etc. ICs in the second section are installed at 2Y101, etc. This numbering system was devised with the expectation that significant numbers of larger LSI modules would be used. Their location would be designated per the location of their pin No. 1. However, some engineers whose applications have been limited to 14- and 16-pin ICs have thought the above system too cumbersome, and have designated socket positions using a conventional socket numbering system. A useful technique for troubleshooting on the wirewrap side consists of colored plastic sleeving installed on the unused pins between "sockets," specifically pins 9, 18, and 27 in each row of 35.

C. Power Short Circuits

If a subchassis is found to have +5 volts shorted to ground, an instrument is available for locating the fault without removal of ICs or wirewrap: The IC Fault Locator Model CL-1 is manufactured by the Concept Electronics Corp.

D. IC Installation and Removal

Because of the high contact retention force, IC pins may tend to crumple unless installed with the aid of an insertion tool which supports the pins and holds the dual pin rows in alignment, 0.300 in. (7.6 mm) on center. Figure 13 shows vector tool P157. Some difficulty may be experienced because the sides are not 0.310 in. (7.874 mm) apart, as required to align leads to 0.300-in. (7.6-mm) centers. The tool shown was

modified by replacing the tool's rivets with machine screws, after which the sides were bent as required to provide 0.310 + 0.005 - 0.000-in. (7.87 + 0.127 - 0.000 mm) separation. It is also very difficult to remove an IC without bending the leads unless they are pulled with the aid of a special IC puller. Figure 13 shows an Augat T114-1 puller.

E. Power Supply Bypassing

The subchassis power plane is bypassed for high-frequencies with twenty-four 51,000 picofarad capacitors. However, the power supply leads may ring in the 100-kHz range in response to power loading which varies according to the logic states of the ICs, unless additional medium-frequency bypassing is used. Two 35-microfarad capacitors should be installed on the terminals provided on the front rail for this purpose, and connected to the nearest power plane power pin with short, direct leads. Other terminals are available for bypassing auxiliary power supplies. It may be necessary to install small low-inductance capacitors near the ICs which use these auxiliary supply voltages, in order to prevent noise spikes from coupling into other logic.

F. Line Terminations

The subchassis provides an excellent ground plane effect, which is carried through the mating receptacle by four ground connectors. Twisted pairs may be terminated outside the subchassis, on the ground bus (see Fig. 3), if the connection inside the subchassis (to the driver or terminating resistor) is limited to about 6 in. (15 cm).

G. Repair Tools and Maintenance Procedures

Figures 14 and 15 show the tool kits available for the repair and modification of subchassis and interface receptacles, including the replacement of broken pins and the installation of extra pins or sockets. Maintenance Procedure MP511469 governs the maintenance of subchassis, and MP511709 governs the maintenance of wirewrap interface receptacles.

H. Additional Information for Engineers and Contractor Users

In many instances, detail logic design and layout of the logic on the subchassis is accomplished by JPL subcontractors. It is necessary to provide these contractors with some applications information and restrictions. TRD-338-954107-01 was written as the mechanism for including these application standards in a recent contract. In order to facilitate the inclusion of this material in all applicable contracts, it will be published as a released JPL document. This document covers the use of special tools for installing and extracting ICs, the necessity for short (1 in. (2.54 cm) maximum) ground and power connectors to ICs, the permissible module pin sizes, power supply bypassing, the designation of JPL FS505770 as the specification covering wirewrapping and repair procedures.

VIII. Chassis Design

The subchassis receptacle design uses contacts and nylon sleeves which are press-fitted into an aluminum plate. It is thus possible to design a single large plate which will serve as the receptacle for several subchassis, as shown in Fig. 3 of Ref. 1 and reproduced here as Fig. 16. This procedure is customary in commercial or military products with substantial production runs. However, the DSN usually does not require enough copies of one functional unit to justify the design cost of a custom plate (even after subtracting the cost differential between a modular receptacle system and the large plate). In addition, the DSN design requirements for standardized packaging hardware emphasize the advantages of the off-the-shelf components available at the highest reasonable level of assembly. For these reasons, the modular connectors shown in Fig. 3 were designed. The following subsections describe three main chassis designs which have been utilized in the DSN and for which documentation exists.

A. Chassis With One or Two Subchassis

Figure 17 shows an assembly which holds one or two subchassis. The original design was developed by one of the DSN development engineers and has been adopted as a standardized assembly per drawing 9457952. This assembly is designed to pivot out of the drawer for service; Figs. 18 and 19 show the pivot assembly installed in a Star Switch Controller 9501300.

B. Chassis With Multiple Subchassis

Figure 20 shows a chassis drawer assembled out of modular components. Figures 21 and 22 show the Metric Data Assembly assembled using these components. Two typical assemblies are documented in JPL sample drawing 9468707. These modular components were developed to meet the following requirements:

(1) The drawer should be able to slide in and out of the cabinet while carrying several hundred system interface wires. The DSN standard interface cable design, with its stiff and heavy molded jacket, poses a severe problem if several of the larger cables must move in and out with the drawer slides.

(2) The design should be capable of packaging up to six or seven subchassis, or a lesser number of other digital

devices or a self-contained power supply, using a maximum number of off-the-shelf mechanical components. Space should be available for front panel displays, if necessary.

The first objective was met by a design which does not attempt to draw the DSN standard cables in and out with the drawer slides; they mate with a rigidly mounted connector panel as shown in Fig. 23. Woven cables (preferably flat) provide connections to the chassis assembly. They track in and out with the drawer slides, excess cable lying in a tray. The chassis connections are made through a connector designed to mate with a wirewrap receptacle using the same contacts and wrap-post as the subchassis receptacle (Fig. 24). Thus, the connections among the subchassis and with the interface cables can all be made with wirewrap (see Fig. 22). The first user of this design reports that jumpers between the DSN standard interface cables should be made by carrying the wires up to chassis wirewrap level where the advantages of wirewrap changes are available.

The second objective was met with the modular design in which the user installs subchassis receptacles only where necessary. Deep panel displays may be accommodated by leaving the first receptacle position behind the front panel vacant (Fig. 20). As many cable receptacles may be installed (at the rear) as necessary, at the sacrifice of subchassis slots. Blank panels should be used to fill any unused space; these blanks may also be used for coaxial fittings.

C. Chassis With Multiple Interface Cables

The chassis assembly shown in Fig. 25 was designed (in conjunction with M. Galitzen, cognizant engineer for the Timing and Frequency Assembly) to meet the need for an interface with up to sixteen 128-pin DSN cables. These cables form an exceptionally heavy and rigid mass. Access was necessary for in-system testing; however, the use of intermediary cables of the type shown in Fig. 22 was undesirable because of the large number of wires. A decision was made to mount the subchassis vertically as shown in the photograph. No slides are needed because the subchassis are accessible from the front. A hinged door closes on the assembly when access is not needed for service. The rack space required for vertical mounting of the subchassis was needed in any instance for the 16 large cable connectors and for cable routing.

D. Procurement of Chassis Hardware

All chassis hardware, with the exception of the receptacle mounting accessories listed in Table 1, must be procured by the user. The Cognizant Sustaining Engineer for hi-rel packaging maintains cognizance over the drawing sets for the Pivot Assembly 9457952 (Fig. 17, not including mounting drawer) and the Modular Drawer Assembly 9468707 (Fig. 20). While consulting assistance is available, the user is responsible for all other drawings.

E. Subchassis Extender

Access to the ICs or the wirewrap connectors in packaging systems utilizing two or more subchassis requires the use of a subchassis extender, JPL part 9458186, shown in Fig. 26.

IX. Current Design Efforts and Future Plans

A. Half-Size Subchassis

JPL drawings have been completed for a half-size subchassis (2 sections of the normal 4-section layout), and a model has been fabricated by cutting down a full-size subchassis. This half-sized subchassis will be included in our next subchassis procurement. The eventual quantity price is estimated at 65 percent of the full-size subchassis. The principal applications are expected to be found in subsystems which require only small numbers of microelectronic packages for which the cost or space savings are significant.

B. Accommodating LSI Components

Additional consideration is now being given to the use of large-scale integration (LSI) microcontroller-processor packages which have up to 40 pins (future packages may have up to 80 pins) arranged in two rows with 0.6-in. (1.5-cm) spacing between rows (present 14 and 16 pin packages use 0.3-in. (7.6-mm) spacing).

These larger packages can be accommodated by removing some of the ground posts (ground posts are visible in the z-rows; i.e., 1z, 2z, 3z, etc., of Fig. 12) and installing additional socket strips in these z-rows, as shown in Fig. 27. This procedure sometimes requires the removal of existing sockets and the installation of new ground posts, in order to keep ground lead lengths short. R. Winkelstein has suggested a design modification which would eliminate the need for extensive customizing by providing ground posts alternating with the power posts in the x-rows, as illustrated in Fig. 28. This modification can be implemented at modest expense. However, the DSN's continuing requirements for the existing model (if only to build additional copies of existing subsystems) would result in the stocking of two different subchassis versions. This arrangement would not be too painful, since subchassis could be converted from one version to the other simply by moving the ground posts. A decision has been made to make mechanical provisions for the new ground post location in the next units to be manufactured, but to install all

ground posts in the current z-row locations. However, the half-size subchassis will be provided with ground posts installed in the new location.

C. Development of Inspection Aids

Training inspectors to perform source inspection of subchassis has been difficult because of a lack of training aids. It has been recognized that photographs of manufacturing defects would be useful, and 15 photographs were taken during the last contract. Additional photographs should be taken during the next contract and descriptive material added. No decision has been made whether to publish these photographs in a formal document or simply to retain sets in the offices of the cognizant sustaining engineer and the QA Supervisor.

D. Other Mounting Techniques

Most chassis designs require the use of an extender if access is required to subchassis ICs or wirewrap during in-system testing. Some thought has been given to the possibility of a design similar to that of the standard minicomputer currently used in the DSN; wirewrap boards in these minicomputers fold out as the pages in a book. No plans for a full-scale development project have been formulated to date.

Reference

1. Slaughter D.W., "Hi-Rel Integrated Circuit Packaging Development," in *The Deep Space Network*, Technical Report 32-1526, Vol. VII, pp. 113-123, Jet Propulsion Laboratory, Pasadena, Calif., Feb. 15, 1972.

Table 1. Parts list of hi-rel standard packaging hardware

Part description	Note	Part No.	Reference figure	Cost,* $
Subchassis (full-size)	1	9457999**	1	800.00
Subchassis (half-size)		9458904-1		520.00
Receptacle, wirewrap		9459013-1	3	56.00
Receptacle, wire-crimp		9459014-1	3	60.00
Ground bus	2	9458877-1	3	3.00
Stiffening rail, ventilating	3	9459033-1	3	6.00
Stiffening rail, nonventilating	4	9460106-1	3	6.00
Ball catch	5	9501223-1	17	free
Subchassis extender		9458186**	26	480.00
IC modular socket	6	9457910-1	6	0.50
Wrap-post, ground	6	9457084-1	–	0.25

*Prices may vary depending on quantities (combined JPL requirements) ordered and the state of the commercial market.

**May be supplied as –1 or –2 versions. Dash numbers cover manufacturing differences only; parts are interchangeable to the user who should list part with both dash numbers, for example 9457999-1 or -2.

NOTES

1. Future procurement only; not in stock.
2. Mounts on receptacle; use to ground shields or twisted pairs.
3. Mounts receptacles on 2-in. (5.08-cm) centers and allows for air flow between receptacles.
4. Mounts receptacles on 1.8-in. (4.57-cm) centers.
5. Used on pivot assembly 9457952.
6. Install on subchassis as required to accommodate LSI packages.

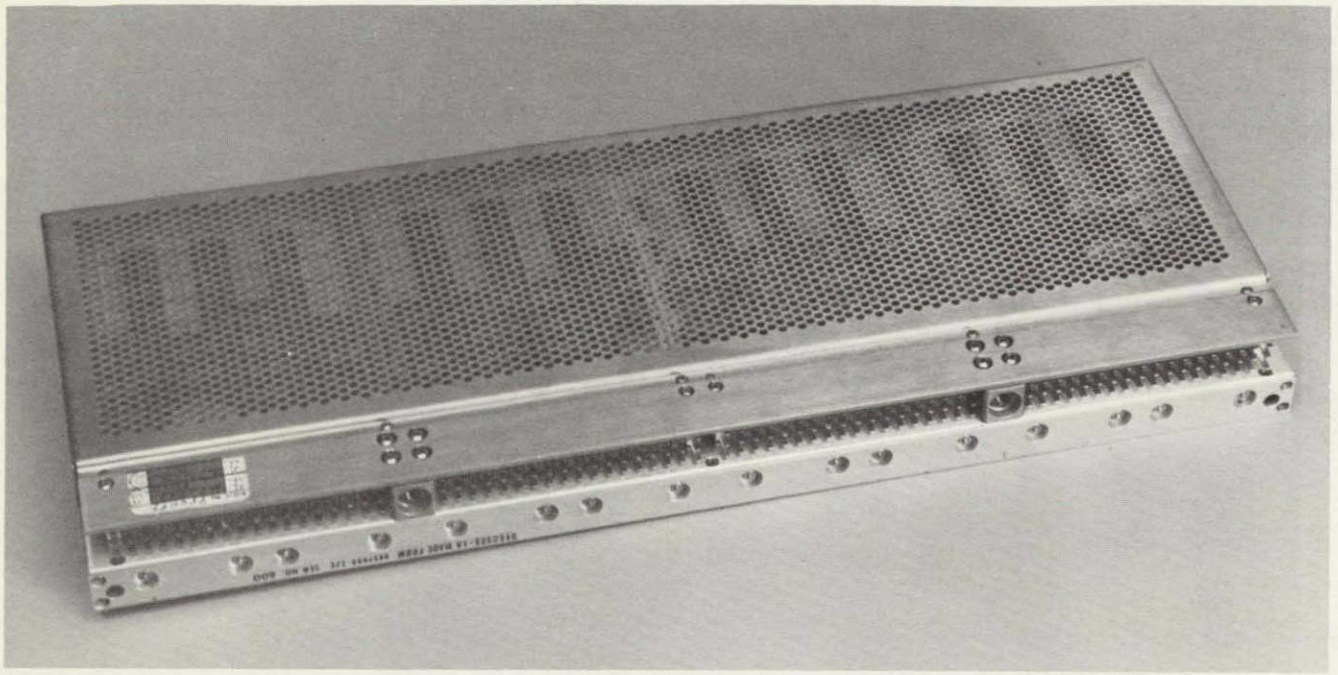

Fig. 1. Subchassis with cover installed

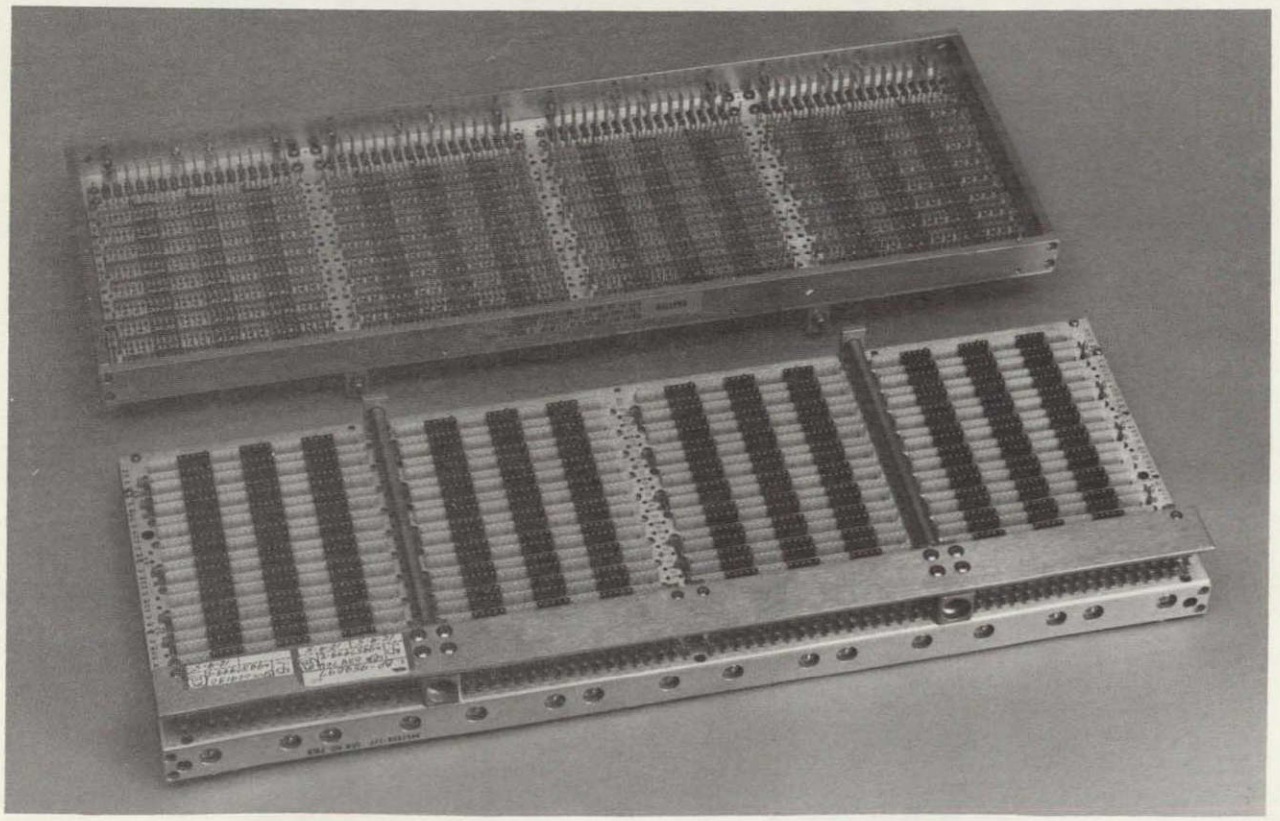

Fig. 2. Socket and wirewrap sides of subchassis

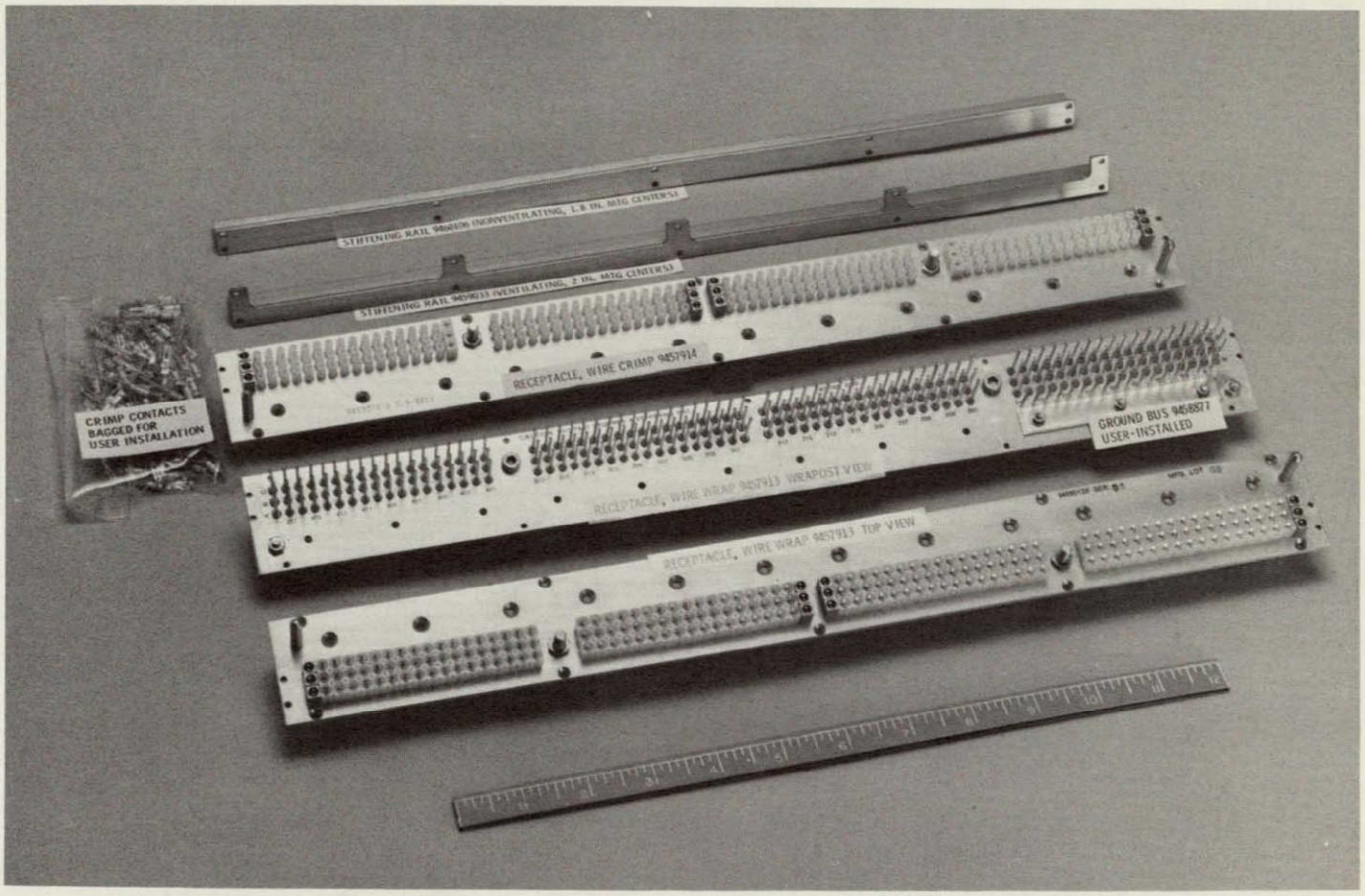

Fig. 3. Receptacles and stiffening rails

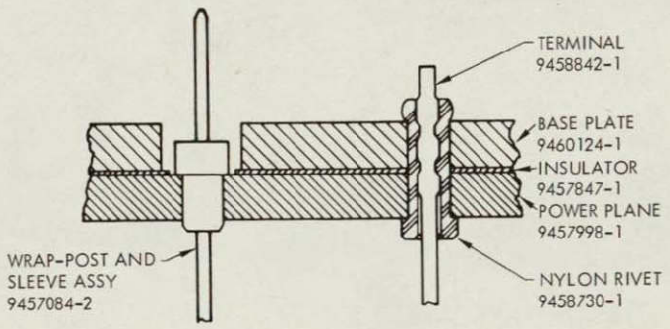

Fig. 4. Power plane with power pin and rivet

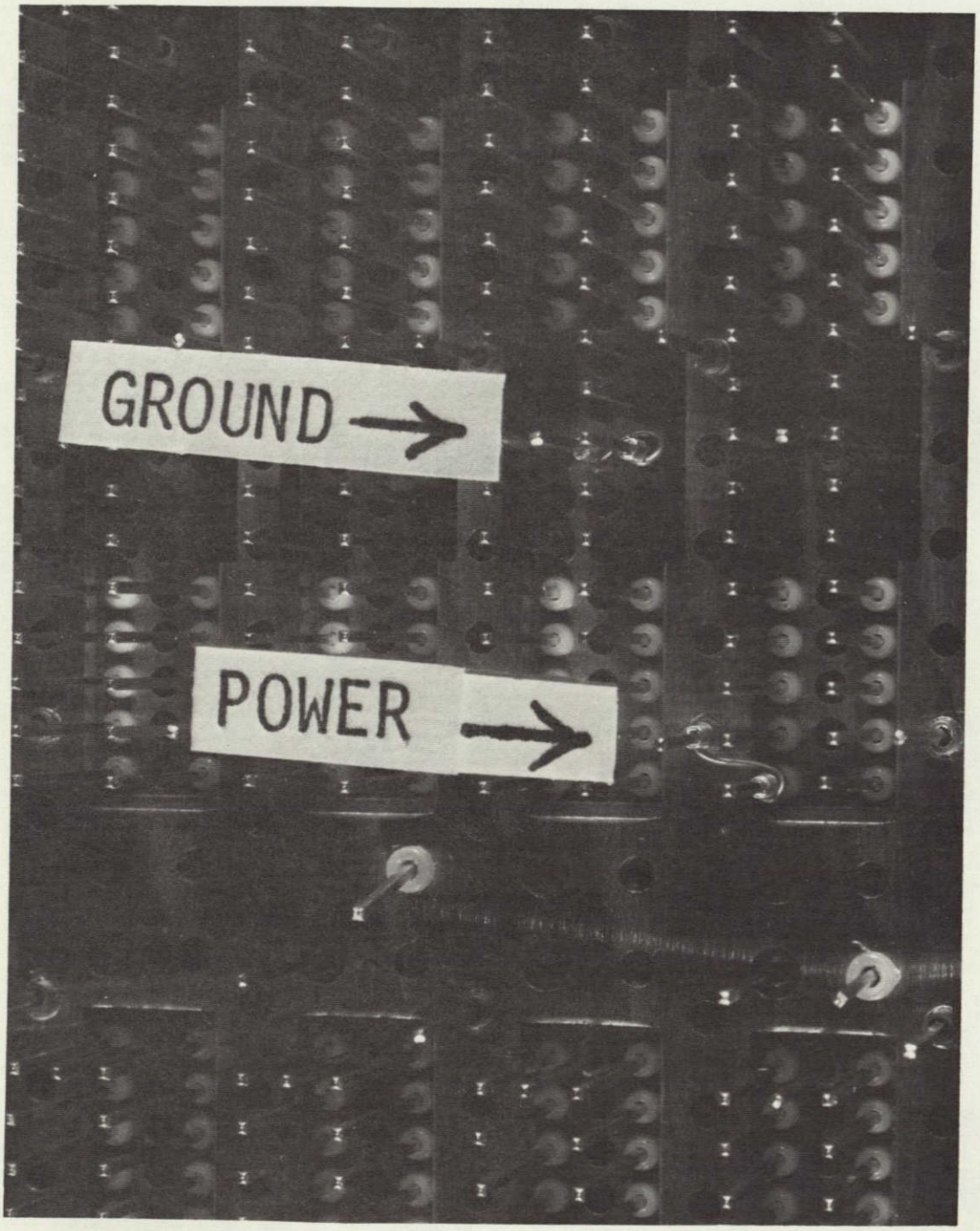

Fig. 5. Wirewrapped ground and power connections

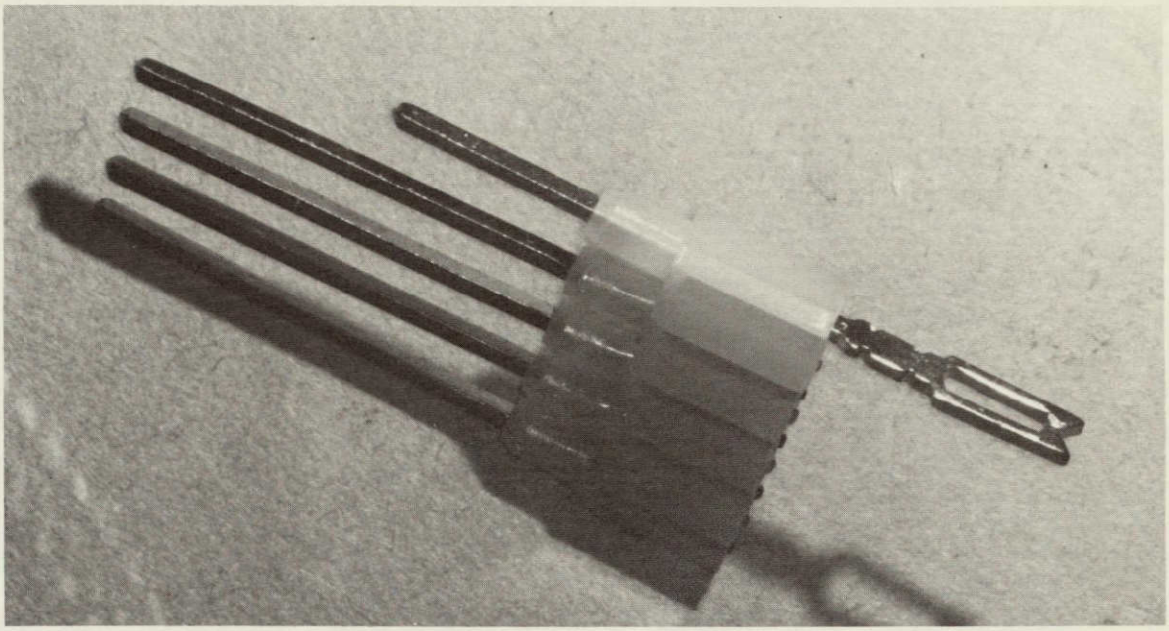

Fig. 6. IC strip socket

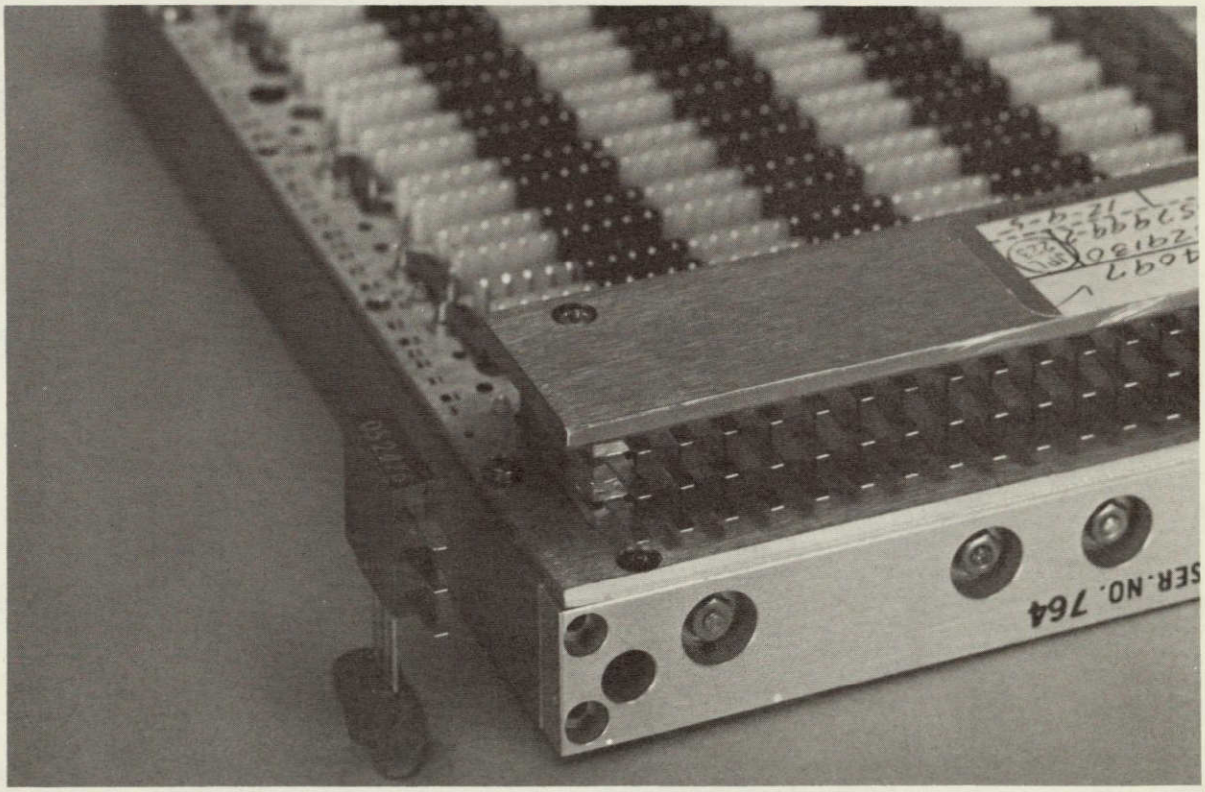

Fig. 7. Modular connector

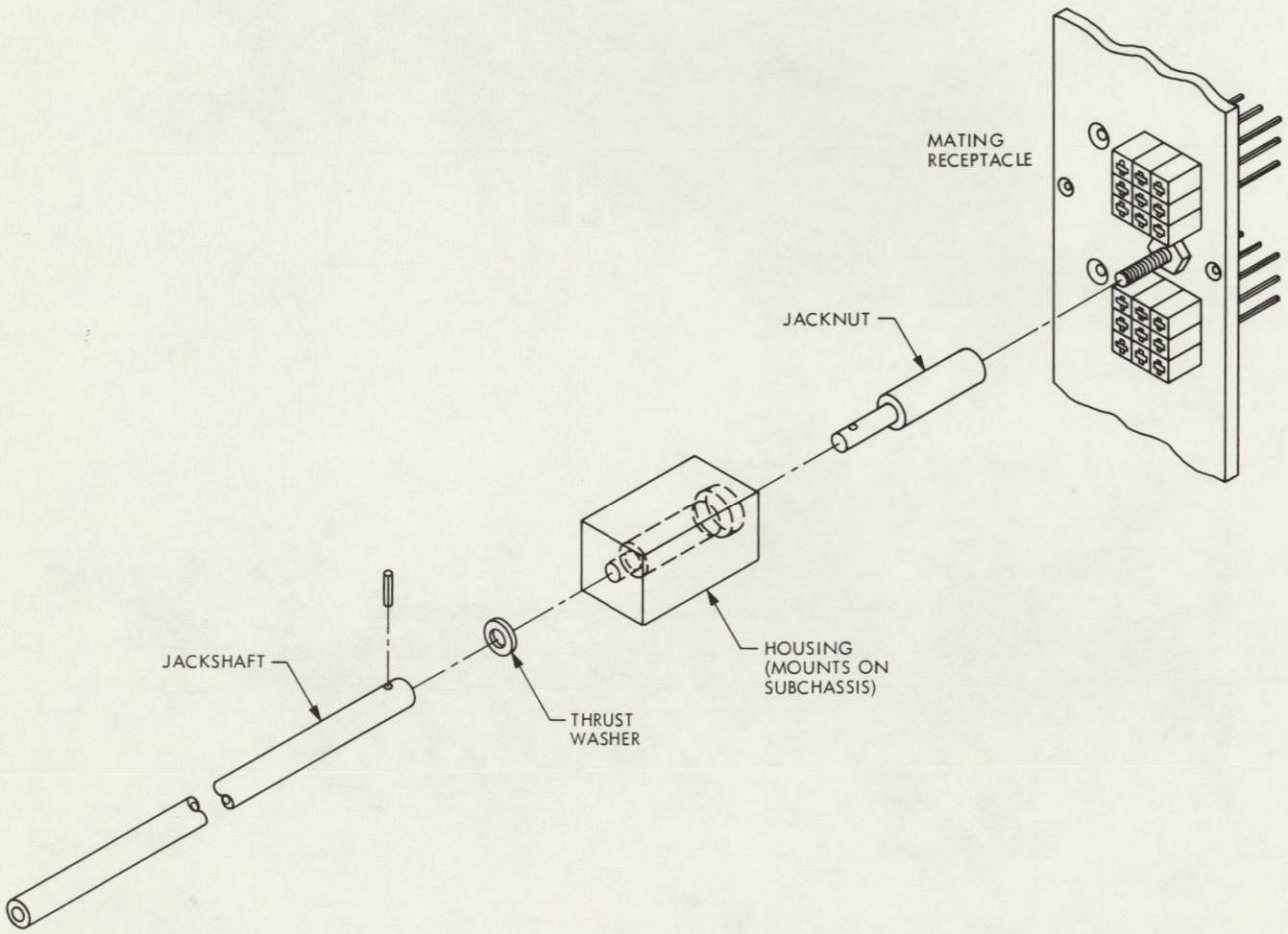

Fig. 8. Jackscrew assembly

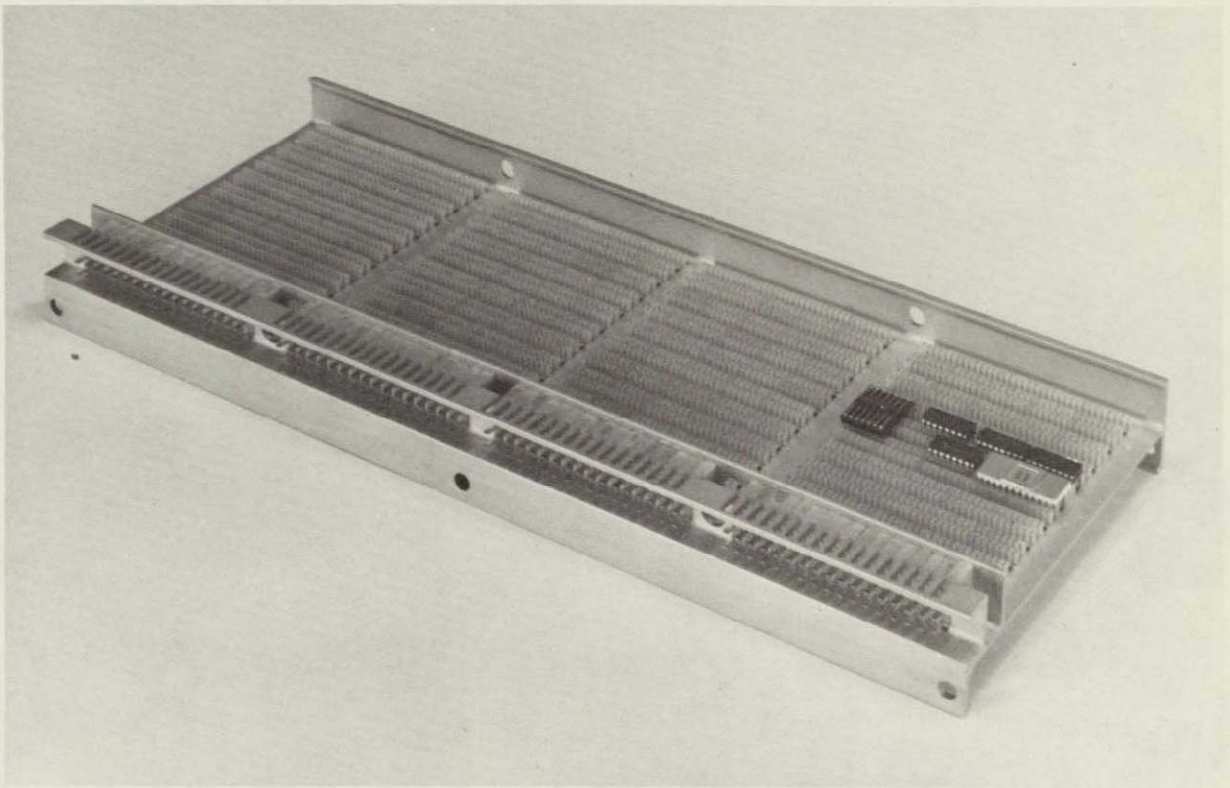

Fig. 9. Obsolete design of extruded subchassis

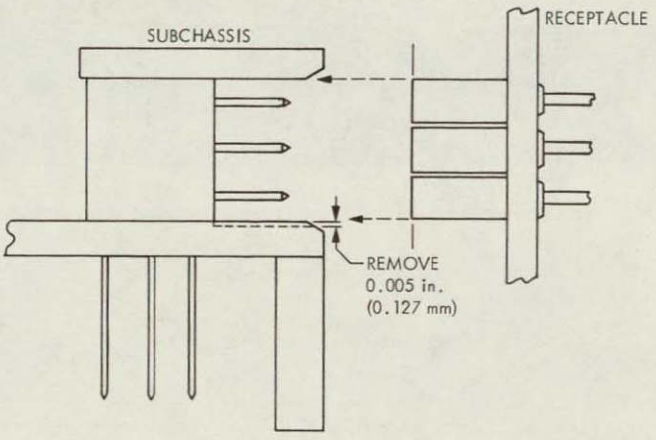

Fig. 10. Subchassis to receptacle mating

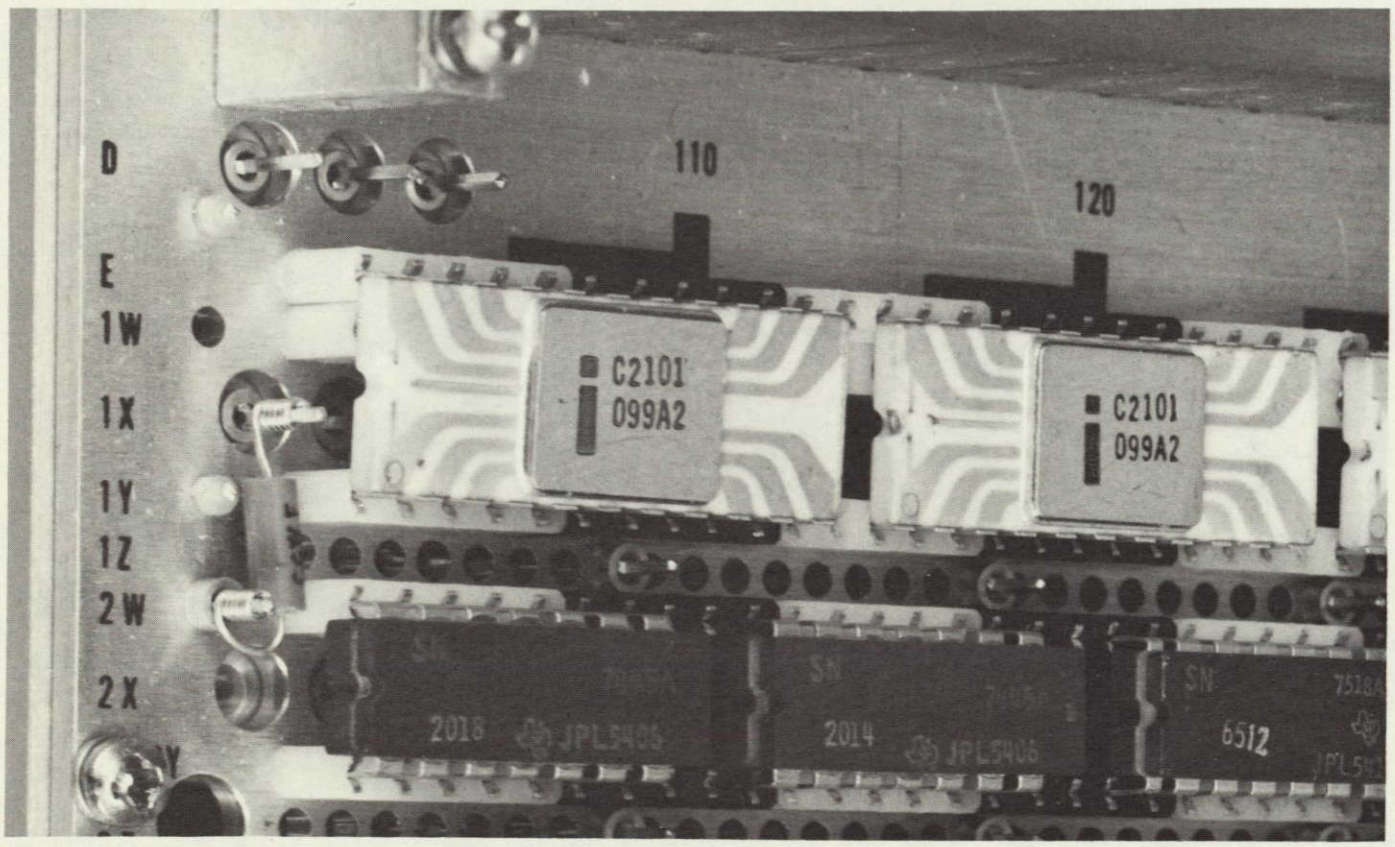

Fig. 11. LSI microcircuits mounted in user-installed strip sockets

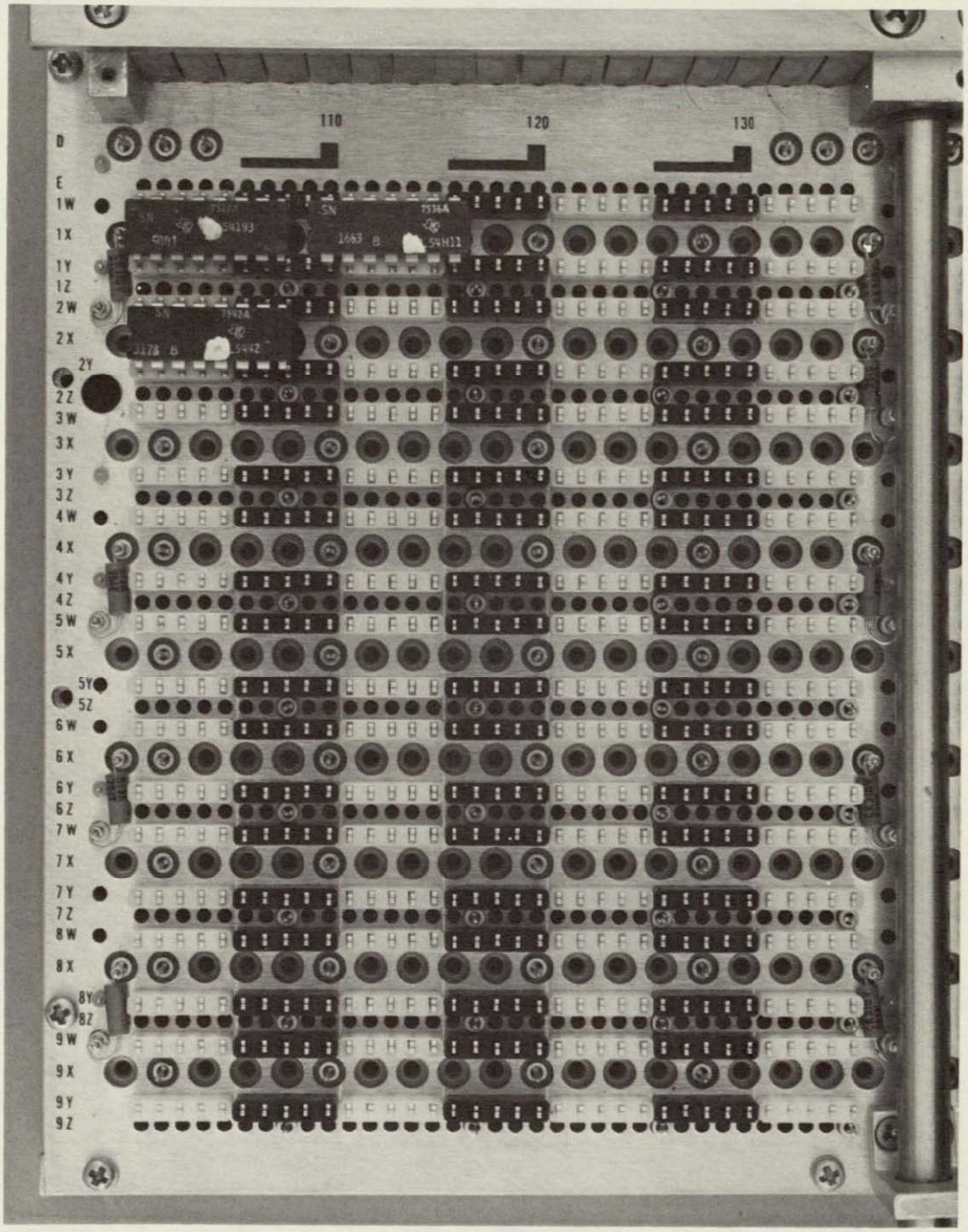

Fig. 12. One section of subchassis showing numbering system

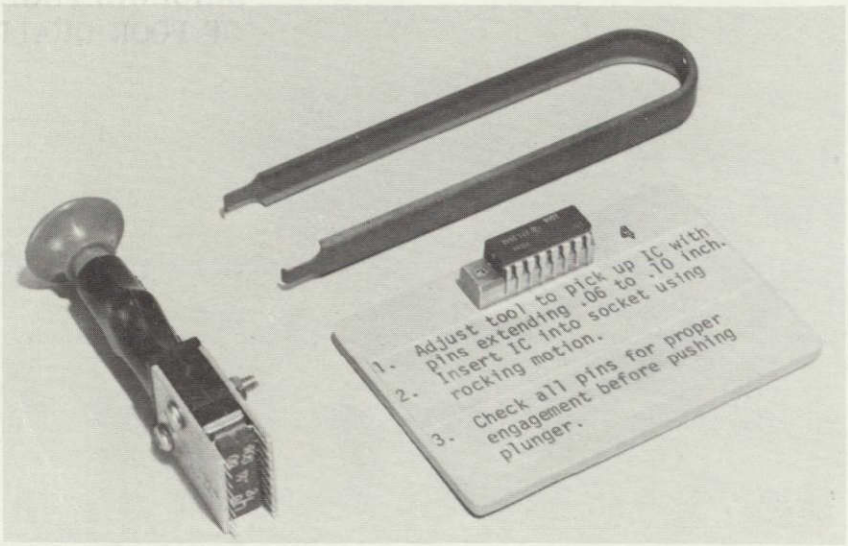

Fig. 13. IC insertion and removal aids

Fig. 14. Subchassis maintenance tool kit

Fig. 15. Wirewrap receptacle maintenance tool kit

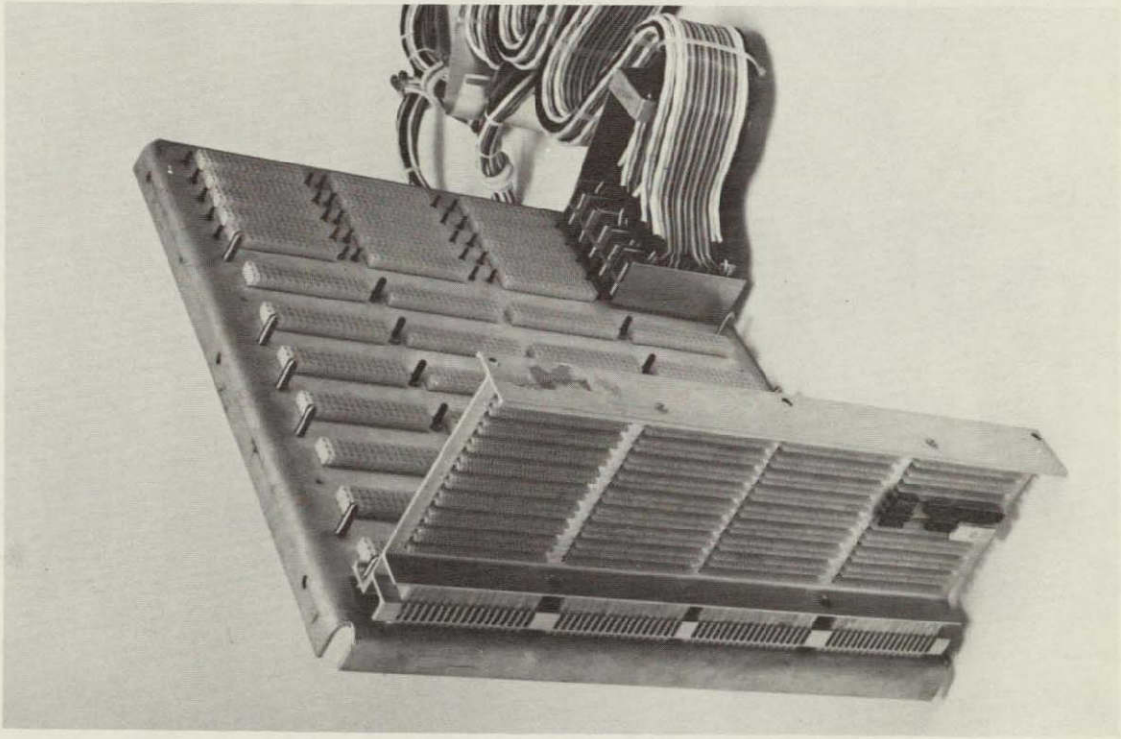

Fig. 16. Custom design of main chassis

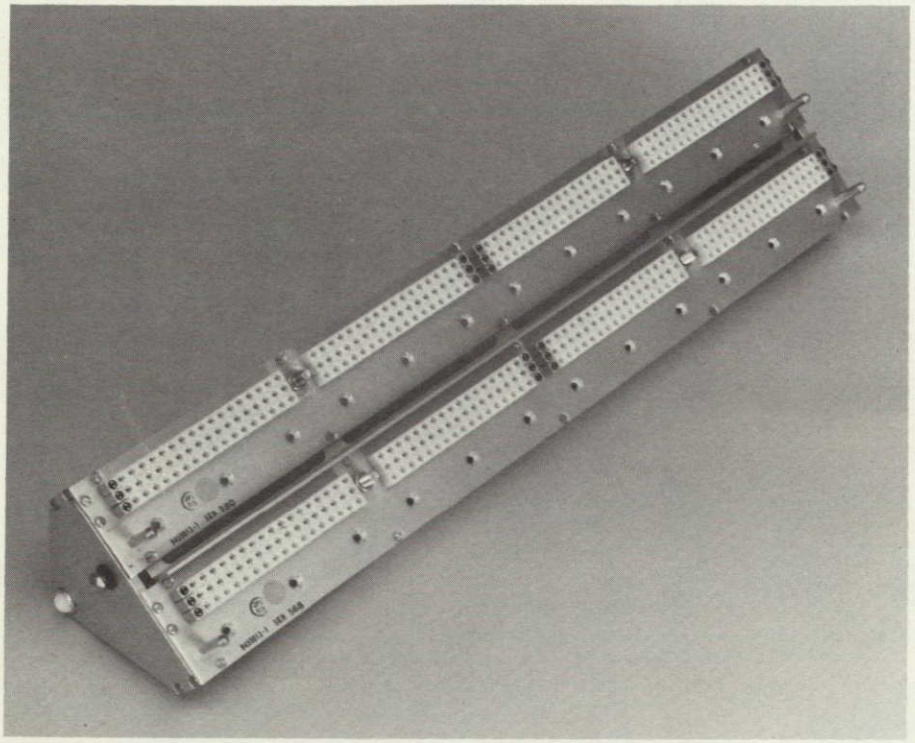

Fig. 17. Pivoting receptacle assembly

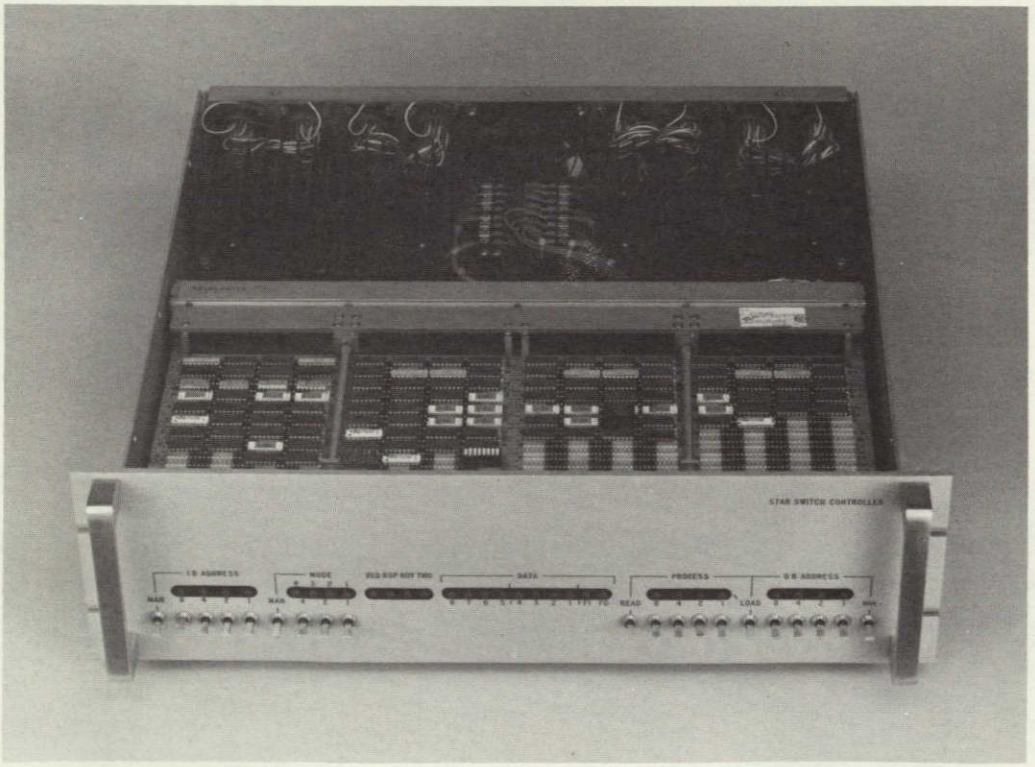

Fig. 18. Star switch controller

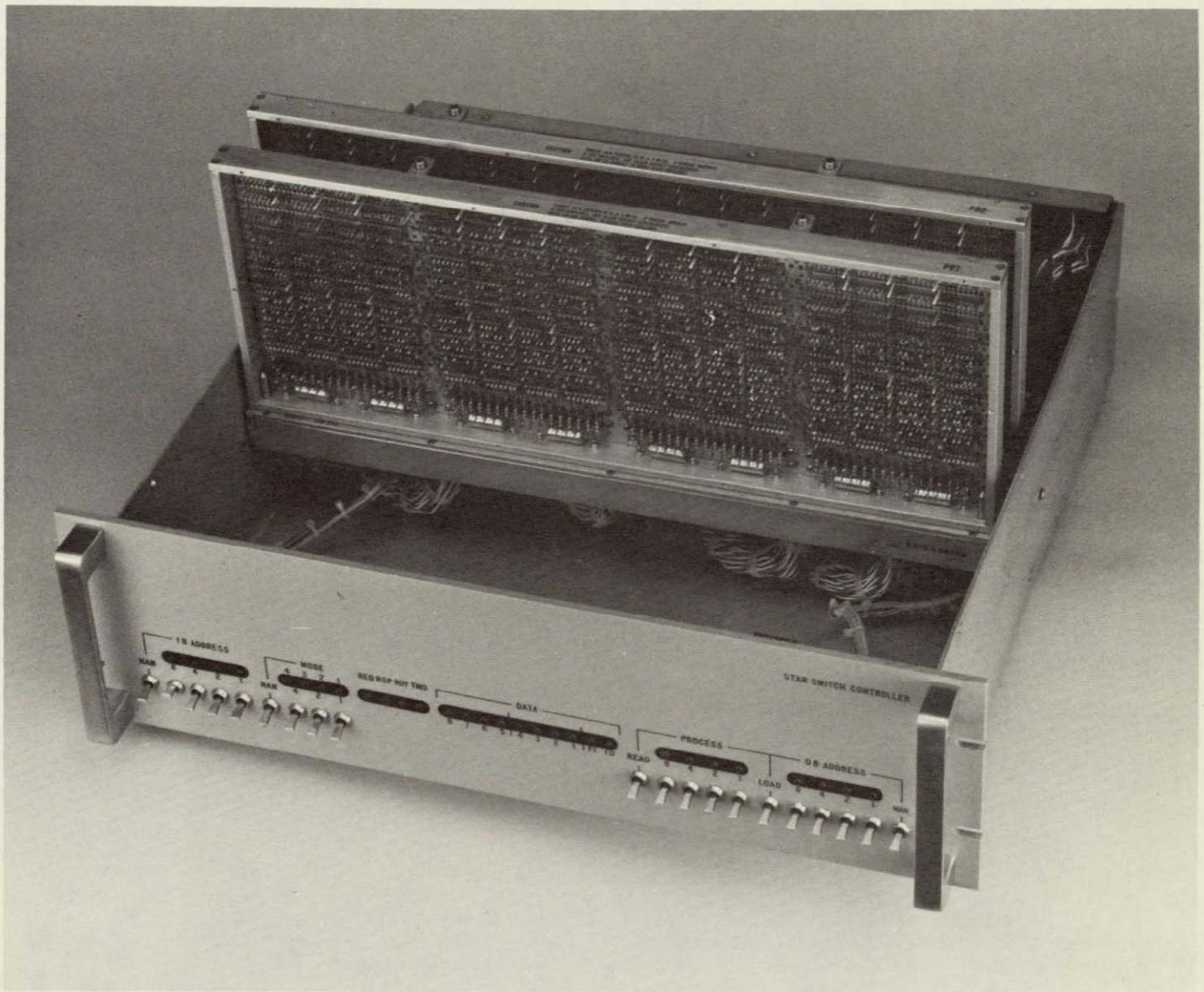

Fig. 19. Star switch in service position

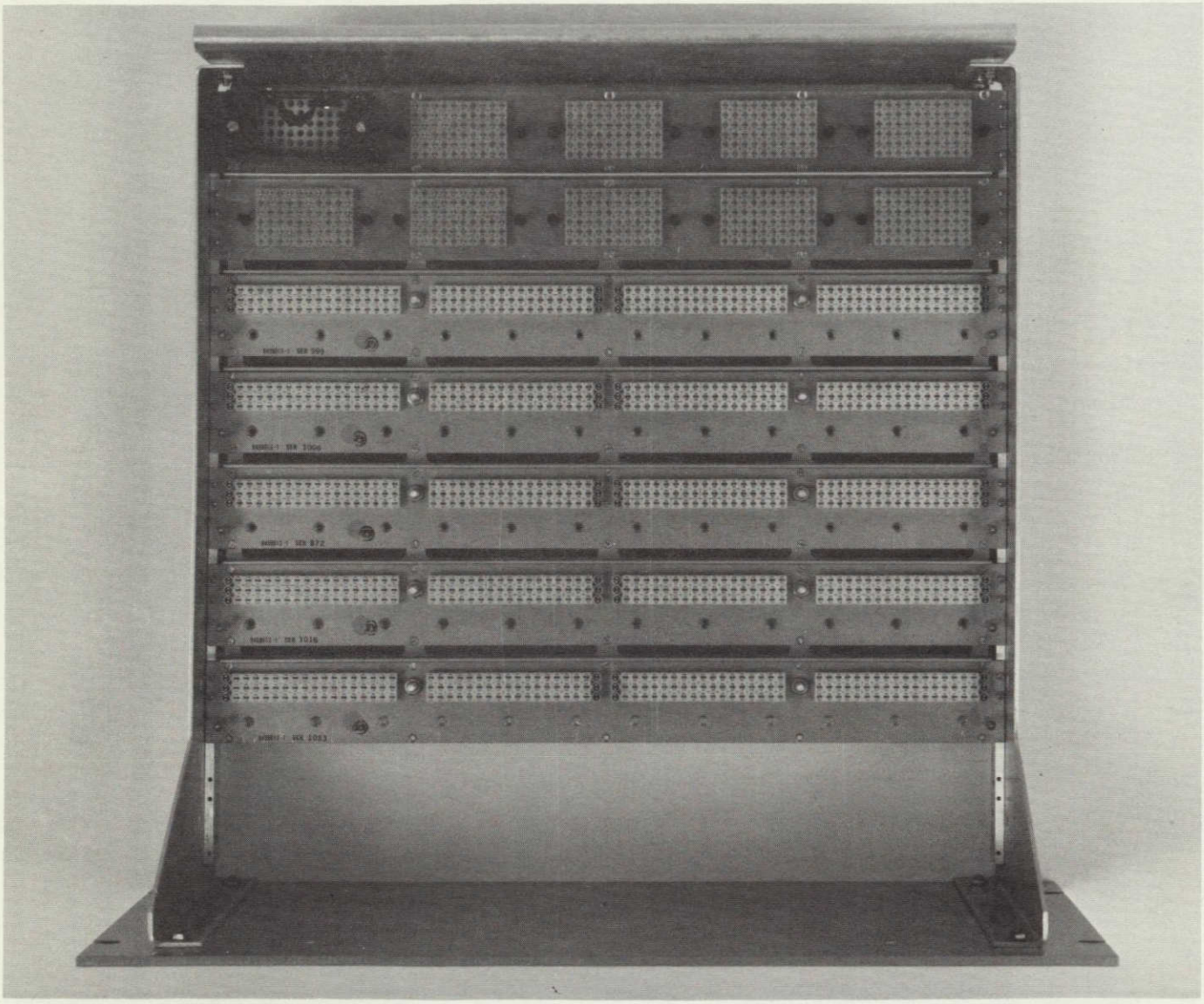

Fig. 20. Modular Drawer Assembly with one receptacle omitted to provide space for panel-mounted indicators

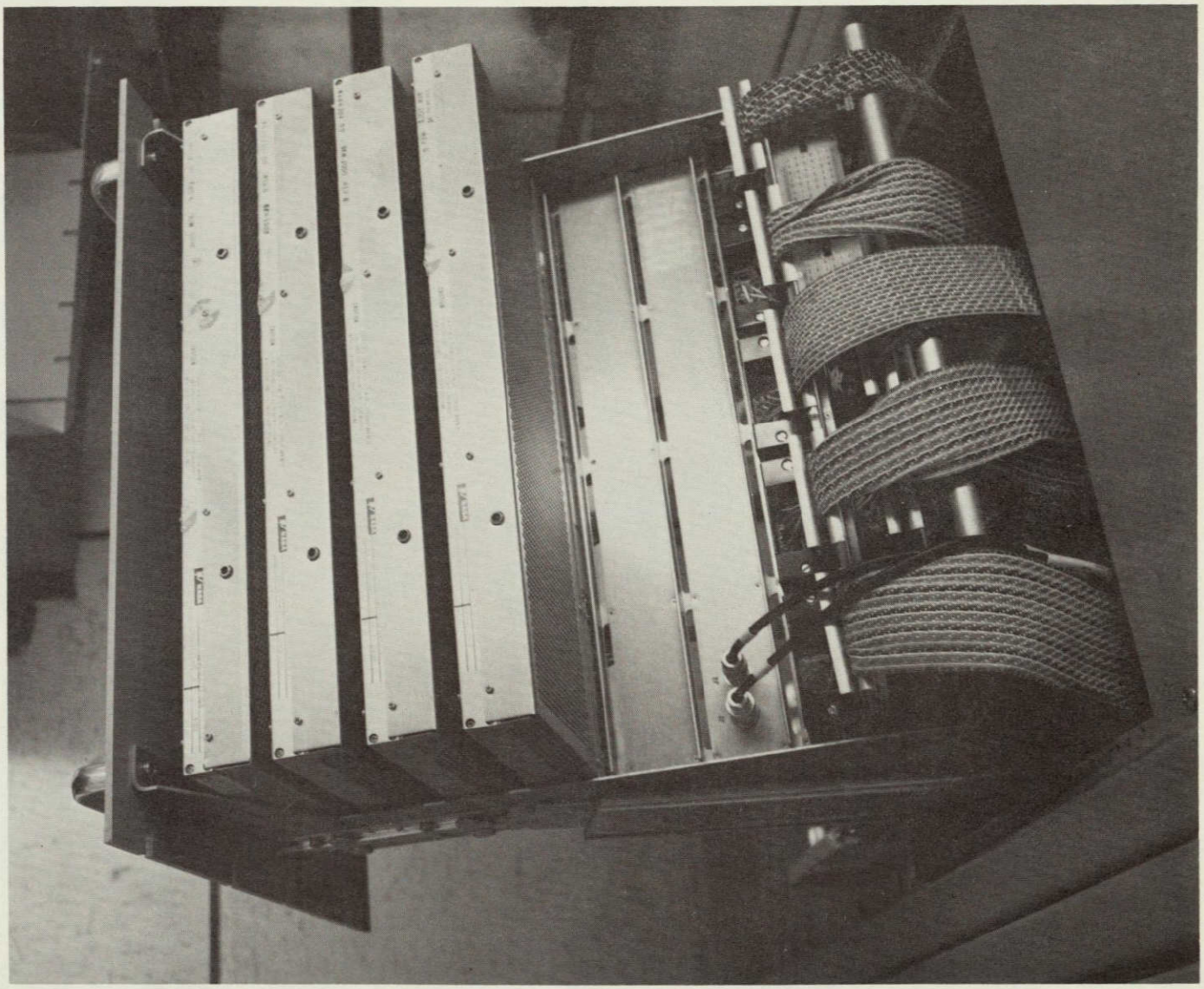

Fig. 21. Metric Data Assembly packaged with modular components

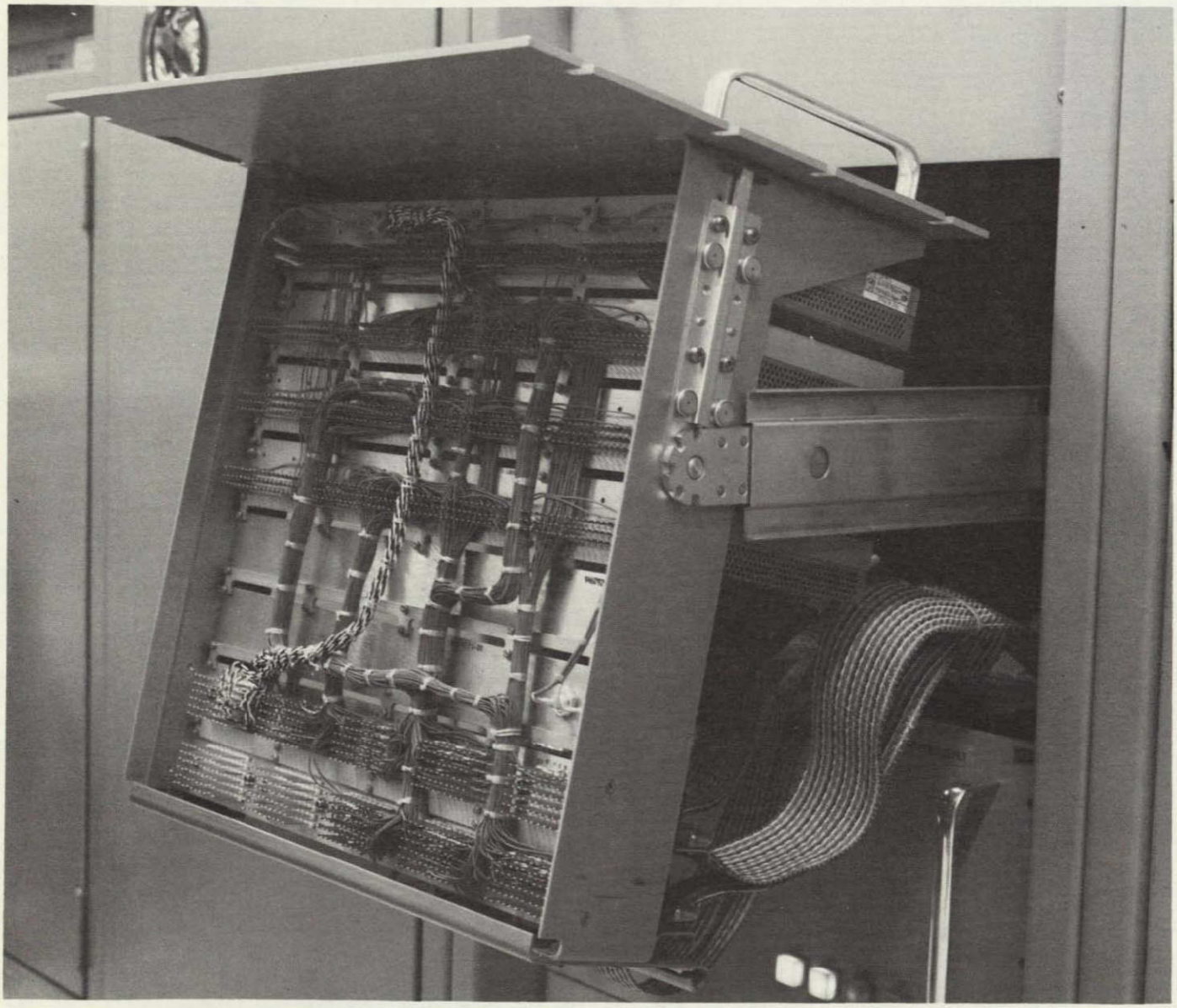

Fig. 22. Metric Data Assembly

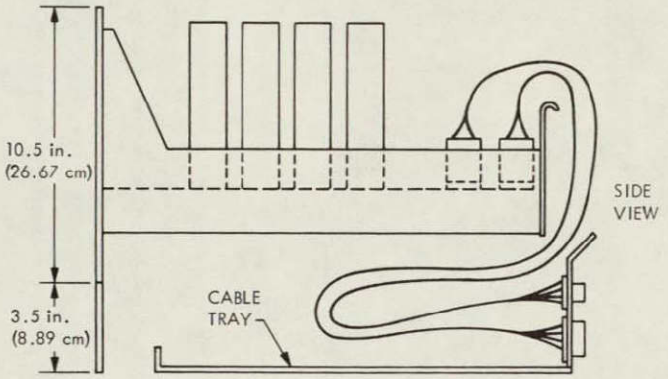

Fig. 23. Modular drawer with cable tray

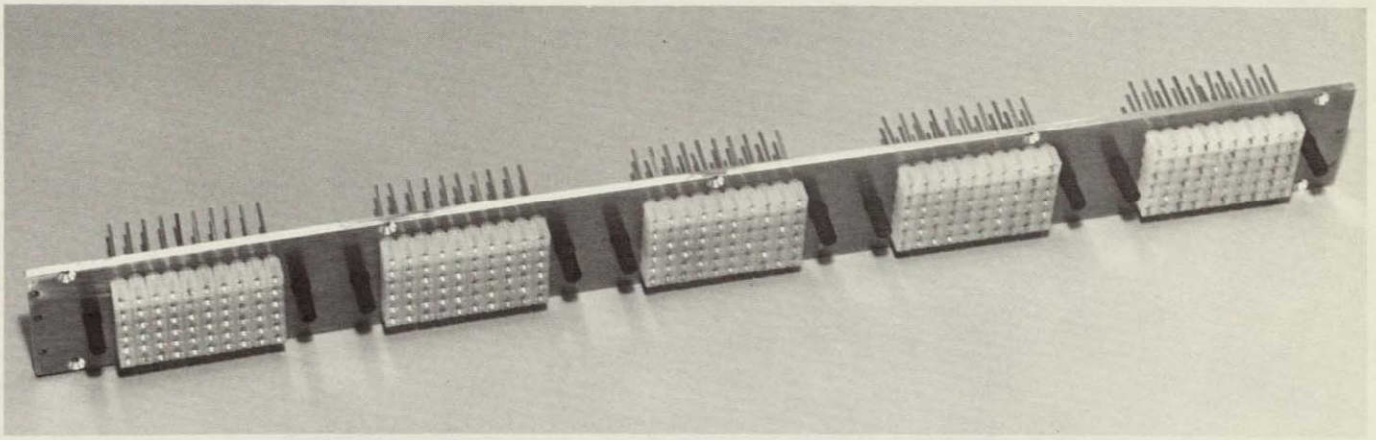

Fig. 24. Cable receptacle showing receptacle used in Modular Drawer Assembly of Fig. 20

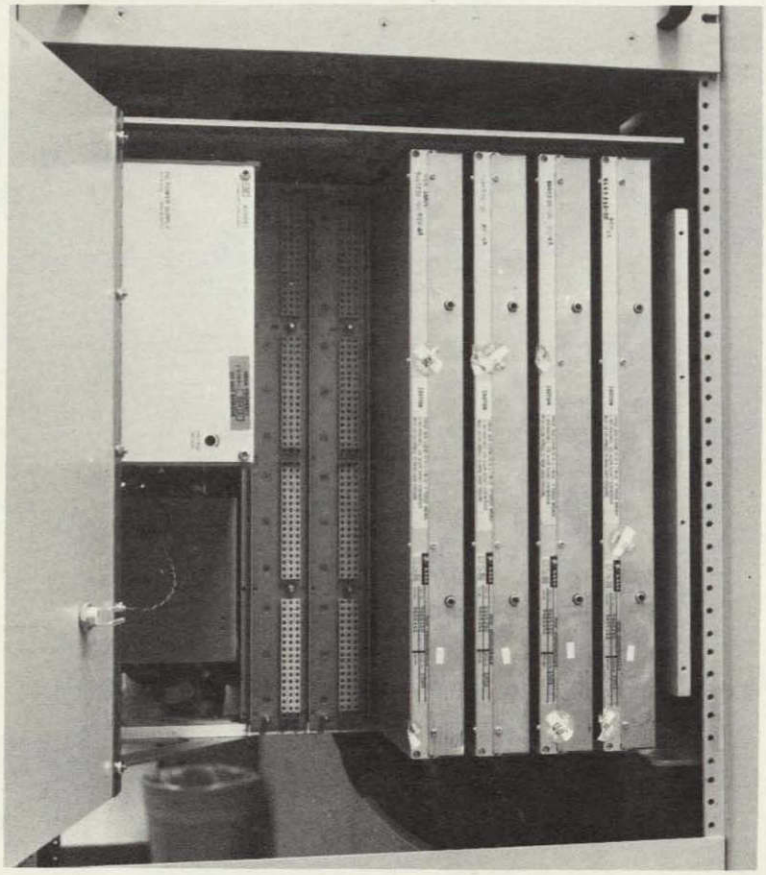

Fig. 25. Timing and Frequency Assembly

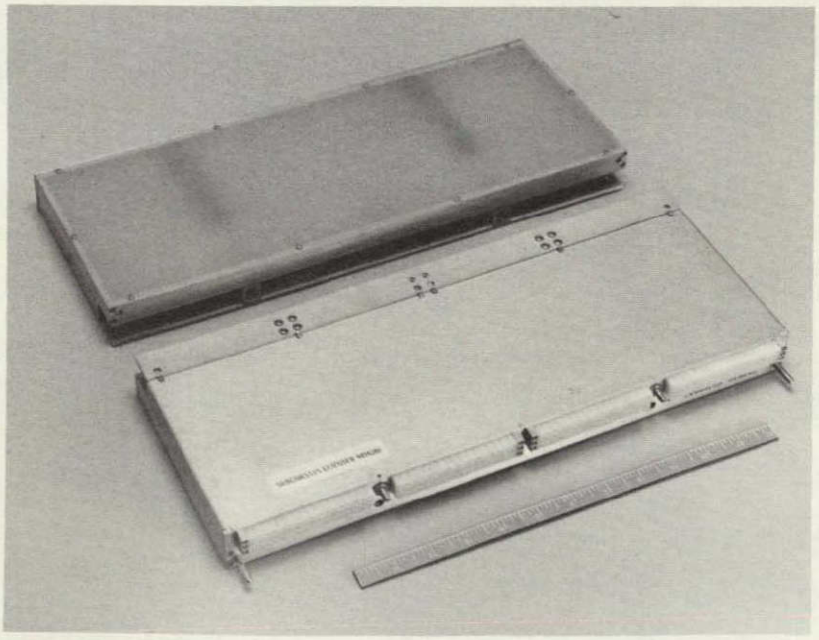

Fig. 26. Subchassis extender

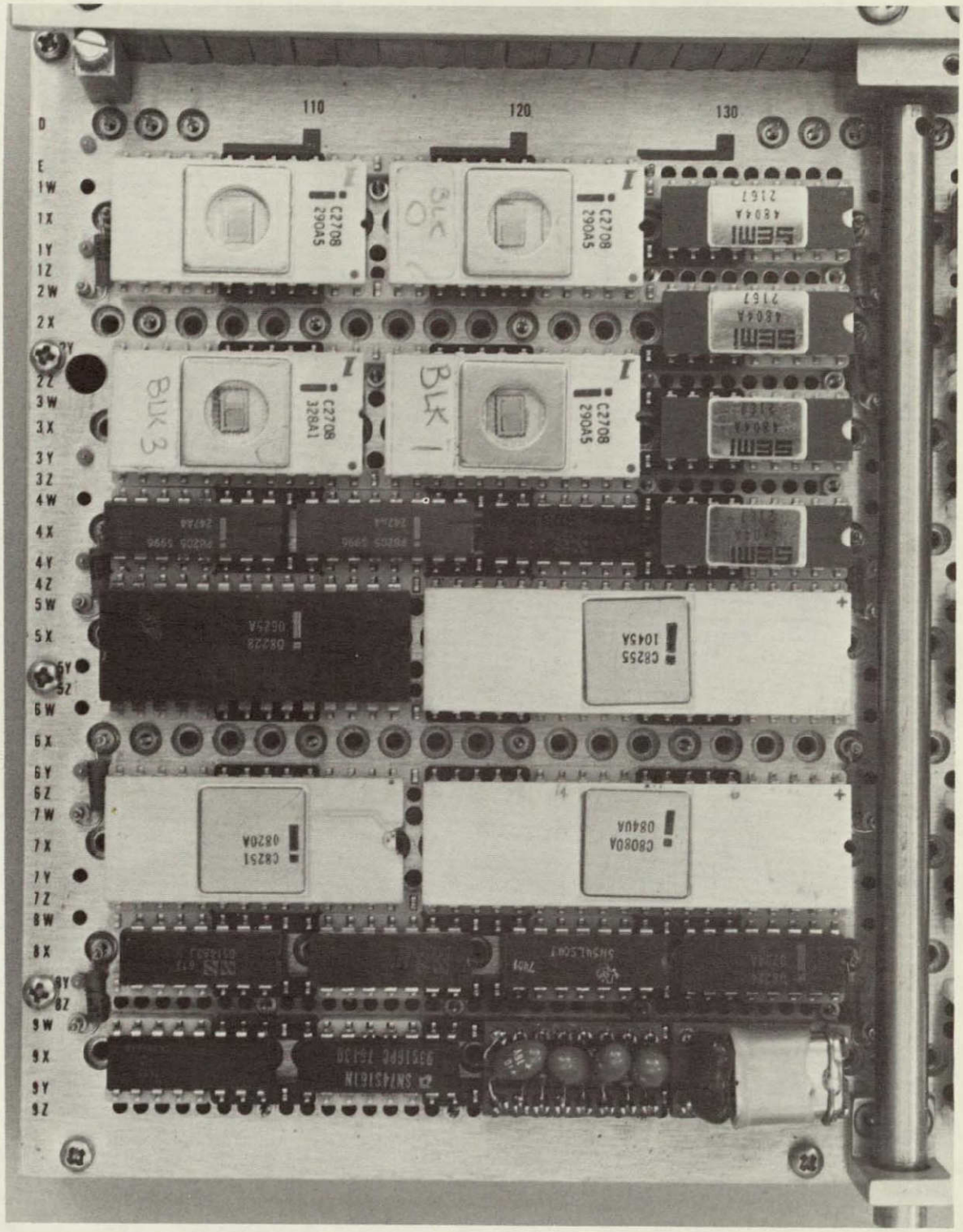

Fig. 27. Subchassis modified for microprocessor application

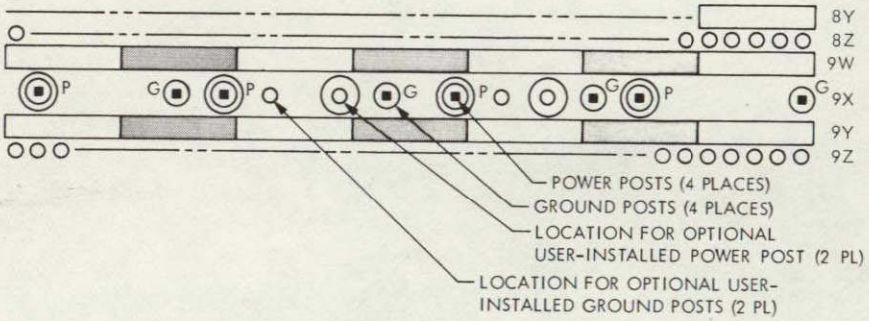

Fig. 28. Proposed subchassis 9457999-3 with ground pins alternated with power pins

DM

26-Meter S-X Conversion Project

V. B. Lobb
DSN Engineering Section

The 26-meter S-X Conversion Project provides for the conversion of an existing 26-meter S-band subnet to a 34-meter S- and X-band subnet. The subnet chosen for conversion consists of the following stations: DSS 12 near Barstow, DSS 44 in Australia, and DSS 62 in Spain. The Conversion Project has evolved from its formative stages, where many options were considered and alternates chosen, to its present status. The main Subsystems effected by this project are the Antenna Mechanical, Antenna Microwave, and Receiver-Exciter. In addition to these, there are many project-related electronic equipments that have been added to the existing station equipment. Functional Requirements and Design Response Reviews were held. The major subsystems are essentially through the design stage with the Antenna Mechanical Subsystem completed through detail design with procurement in process.

I. Introduction

The objective of the 26-meter S-X Conversion Project is to add an X-band (8.44-GHz) receive capability to the existing 26-meter antenna S-band (2.1 to 2.3-GHz) stations and increase the station's gain capability by increasing the antenna aperture from 26-meters to 34-meters. The X-band receive capability is needed to provide adequate data returns from the outer planets and improve immunity from the increasing incidences of radio frequency interference that have been occurring at S-band. The aperture increase from the 26-meter antenna to a 34-meter antenna was to increase the antenna gain, and hence its usefulness to the MJS'77 Mission and other outer planet missions, and to enhance this subnet's offloading capability of the 64-meter subnet during cruise modes.

The selection of the subnet to be converted was made on the basis of the constraints of "shared equipment" and "single point of failure". This selection process led to a subnet of stations that were not conjoint stations. The S-X conversion schedule for the selected subnet is as follows: DSS 12 (Goldstone) shall be completed by 1 December 1978, DSS 44 (Australia) shall be completed by 1 April 1980, and DSS 62 (Spain) shall be completed by 1 October 1980.

The main modifications occur in the Antenna Mechanical, Microwave and Receiver-Exciter Subsystems with other project-related station electronics to be added. These modifications are shown in Table 1 and are described in further detail in the following text.

II. Background of the 26-meter S-X Conversion Project

The project's formative stage started in an exploratory discussion held on 14 January 1975, between representatives of the Telecommunications Science and Engineering Division and TDA Engineering Office personnel. This meeting outlined the following early project assumptions for preliminary estimates as to the project's cost:

(1) Use of a Block IV receiver.

(2) Use of a Coherent Reference Generator Assembly.

(3) An enlarged primary reflector with shaping.

(4) S-X simultaneous operation (2-way S-band; coherent X-band downlink).

(5) Microwave hydrogen frequency reference from DSS 14 to DSS 12.

(6) The S-X 26-meter subnetwork is comprised of stations 12, 42, and 61.

(7) No X-band uplink.

(8) Planetary ranging to be included.

A 26-meter upgrade study team was formed on 29 April 1975 for the purpose of preparing budget guidelines and a detailed Implementation Plan, including the cost and schedule for an August 1975 OTDA and JPL-TDA Budget Review.

Four meetings were held with members of the study team reporting work progress and action items. The net result of this study was an Implementation Plan for $7.4 million for hardware that concerned three major Subsystems (Antenna Mechanical, Antenna Microwave, and Receiver-Exciter). It did not include station electronic equipment. In addition to this basic plan, there were three main options proposed. These options were an aperture increase, shaping, and a 65-kW S-band transmitter, which had a total cost of $3.5 million.

A meeting was held on 27 August 1975 after the plan was presented to OTDA for the purpose of reviewing the configuration and costs for a "baseline system" (a bare minimum requirement program). This meeting and subsequent study by team members resulted in many options and alternates being evaluated and either selected or rejected. At this stage the required station electronic equipments were added.

After this study effort was completed and the November 1975 OTDA Review meeting was held, the following decisions were made in December 1975:

(1) Recommended stations were DSS 12, DSS 44, and DSS 62.

(2) Authorized immediate initiation of design for DSS 12.

(3) The described antenna diameter is to be 34-meter. The 34-meter design will be reviewed prior to proceeding with the hardware.

(4) Schedule to be per Fig. 1.

(5) Defer all performance enhancement options.

(6) Baseline implementation to be per Table 2.

The site selection factors, as differentials, are shown in Table 3 with indicated selected stations.

The main options that were deferred were the 65-kW S-band transmitter and antnenna shaping. The baseline concept included the use of existing S-band microwave components such as switches, diplexers, filters, and maser. The use of the existing Block III Receiver-Exciter Subsystem modified to receive X-band was selected. The deferred options were as follows:

(1) Electric drives for the antenna.

(2) Antenna thermally painted.

(3) Facility modifications at DSS 13 for cone assembly testing.

(4) Increased S-band doppler frequency range.

(5) 3-Hz loop for the Receiver-Exciter Subsystem.

(6) Remote control for S-X and S-S translators.

(7) Remote control for S-band polarization.

Thus the 26-meter S-X Conversion Project was initiated with the start of design of hardware for DSS 12 and the Project budgeted in the FY-76 WAD. Using the previous work of the study team, the assigned personnel from the Telecommunications Science and Engineering Division and the TDA Engineering Office embarked on the development of a Data System Development Plan (DSDP) for the Project, which was completed and published on 1 July 1976.

III. Project Description

The addition of X-band receive capability to stations involves the following changes: a dual S- and X-band reflex microwave feed; the addition of an X-band maser; the addition of an X- to S-band down converter and X-band test translator for use with the existing Block III Receiver-Exciter Subsystem; the addition of an X-band harmonic filter to the existing S-band transmitter to prevent internal station interference. The microwave components will be housed in a new dual cone shell, which will support the reflex feed reflectors.

Within the station control room, the new X-band receive capability requires the addition of a second string of doppler extractors (for X-band) and two ranging channels, one for S-band and the other for X-band. Having this dual S- and X-band doppler and range (radio metric data) capability requires the introduction of cesium frequency standards and a minicoherent reference generator to provide the long-term frequency stability required to navigate spacecraft to outer planets. The X-band radio metric data needs to be processed in real-time and recorded. This will be provided by the addition of a Planetary Ranging Assembly, communication buffer, coded multiplexer, and dual high-rate, high-density tape recorders. The above functions are shown on a functional block diagram, Fig. 2.

The aperture increase from 26-meters to 34-meters requires extensive changes to the structure. These changes, along with changes to the shaft angle encoders and servo electronics, are shown on Fig. 3.

The DSS 44 station (originally a part of the STDN) is an X-Y antenna configuration, but the modifications still apply except for those associated with raising the antenna. Instead of raising the antenna structure, the topography is such that benching out of the hillside adjacent to the antenna foundation will allow for the necessary sky coverage.

IV. Project Status

The Project was organized with both a Programmatic Manager and Project Manager appointed to manage the S-X conversion task effective 1 October 1976. The Project Manager, representing the TDA Engineering Office, interfaces with the Telecommunications Science and Engineering and the Applied Mechanics Divisions in the implementation of the S-X conversion task through the TDA Division representatives. The interface to Operations Division 37 is through an appointed engineer. The interface with OTDA and TDA is through the Programmatic Manager.

Following the official appointment of the managers for this task, a Management Plan for the 26-meter S-X Conversion Project was prepared. This Plan was then approved by all the above mentioned Divisions and Office Managers, and was released on 1 December 1976.

This Management Plan covers the implementation of the 26-meter S-X Conversion Project. It defines the management approach and the project staffing, scheduling, and work description, which form the basis of an interorganizational agreement for project implementation.

In response to a request by the Project Manager, the JPL Quality Assurance Office published a Quality Assurance Management Plan for the Project on 15 January 1977. This plan covered the implementation of JPL quality assurance activities in support of the project. Its purpose was to define the quality assurance management approach, work description, and staffing in accordance with the Project hardware requirements and schedules.

The progress made from the official project start date of 1 October 1976 to present follows:

A. Station DSS 12

1. **Antenna Mechanical Subsystem.** The design and detailing of the antenna mechanical components (excluding servo and control hardware) was completed. The S-X reflectors and the dual cone shell fixed price contract was awarded to Capital Westward Inc. of Los Angeles and was within 5% of the budgeted funds. The quadripod and subreflector bid packages were sent to four vendors with the award expected by 1 April 1977. The reflector backup structure extension bid package was sent to vendors with the award expected by 15 March 1977. Raising hardware for the antenna is being fabricated at Goldstone and is 40% completed. Fabrication of metal forms, coring of holes into the existing foundation, and grouting of rebar ties for the 3-meter concrete pedestals into the existing foundation is in process with completion expected by 1 April 1977.

2. **Servo and Control.** The servo-pointing effort has been primarily in evaluating existing drive and pointing capabilities, and completing an electric drive option study.

The subreflector position controls computer program and operating requirements have been defined.

The angle encoder study for life-cycle cost on 18 bits versus 20 bits was completed with the 18-bit encoder being selected. Encoder prototype hardware was installed and tested on the antenna at the DSS 13 station.

3. **Antenna Microwave Subsystem.** The radio frequency instrumentation design was completed. The monitor receiver prototype test was completed. All long-lead items are in procurement with cryogenic accessory instrumentation procurement initiated.

Design of the Microwave Cone Assembly, which has been designated the SXD (S-band, X-band, Dual) cone assembly, was completed. The integration of maser and receiver components into this design has started. All long-lead components and materials are in procurement with some X-band feed parts in fabrication.

The X-band maser housing design was completed. Fabrication of maser parts and superconducting magnet was completed.

The microwave switch control configuration design is 50% complete.

4. **Receiver-Exciter Subsystem.** The engineering model for new module types has been completed, including breadboard testing and complete design documentation. The new module types are the frequency shifter, doppler mixer, doppler reference, frequency distribution, and frequency multiplier.

The new converter and translator assemblies for the engineering model are in the assembly stage with completion expected 1 March 1977. The modified control room cabinets for the exciter and control are in the manufacturing stage with modifications to be completed by 1 May 1977. Manufacturing of the same modules for operational equipment is 25% complete.

5. **Other Project-Related Electronics.** The design of the minicoherence reference generator has been started and is 15% complete. The coded multiplexer and GCF wideband NASCOM terminal has been rescheduled to suit a change in funding. The system cable design has been initiated by starting the detailed Subsystems Functional Block Diagram and the initial data base listing of system cables.

B. Stations DSS 44 and DSS 62

1. Antenna Mechanical. The design analysis of the reflector backup extension for DSS 44 is completed with member sizes determined. The analysis of the lower wheel and pedestal is in progress. The design layouts of the backup structure extension is in process with fabrication detail drawings to be started by the vendor on 21 February 1977.

All the design and detail drawings for DSS 62 are the same as those for DSS 12, except those for the pedestal and foundation interface hardware. These design drawings are 70% complete.

2. **Antenna Microwave and Receiver-Exciter.** The design and documentation of the Antenna Microwave and Receiver-Exciter modifications for DSS 44 and DSS 62 are essentially the same as those for DSS 12, hence the drawings for DSS 12 will be applicable to DSS 44 and DSS 62. However, the Antenna Microwave Subsytem will require some additional minor design and documentation to fit DSS 44 since the electronic room is a different size and in a different location on the antenna.

C. Transfer Plan

A Transfer Plan has been written and covers the transfer of the hardware and software to operations of the 26-meter S-X Conversion Project. The purpose of the plan was to establish guidelines and dates of milestones for hardware and software, documentation, spares, testing, etc., so that operations receives adequate support on a definite schedule to accept transfer of the S-X conversion equipment. The plan's hard objective is the transfer of all the hardware prior to shipment unless specifically directed otherwise by the Program Office. The Transfer Plan will be issued on 1 May 1977.

D. Project Schedule and Resources

The overall project schedule, as currently planned and in process, is shown on Fig. 4. The progress made is shown by the black shading and is effective as of 1 April 1977. The detail schedule of the individual hardware components is shown on Fig. 5, and again progress can be checked by the indicated shading for an effective date of 1 April 1977. The resource plan for the project for hardware is shown in Table 4 for an effective date of 1 October 1976, which was the official project start date.

Table 1. New or modified station equipment

Electronics		Antenna mechanical
Microwave Dual S-X reflex feed X-band maser Remote calibration	Tracking Planetary Ranging Assembly S- and X-band range demodulators	Extend diameter to 34 meters; Raise pedestal height 3 meters (10 ft)
Receiver-exciter X-to-S down converter X-band test translator X-band doppler extractor	Telemetry Wideband communications buffer and I/V converter High-rate tape recorders	Replace quadripod and subreflector
Transmitter X-band harmonic filter	GCF JPL Wideband Assembly NASCOM Wideband Assembly Interface to GHS for monitoring	Add dual cone shell and S-X reflectors
DIS (monitor) interface frequency and timing Cesium frequency standard Mimicoherent reference generator S-X UPS/FTS Assembly Interface FTS to mini-CRG and cesium frequency standard		Reinforce structure and add counterweight mods
		Angle encoder replacement
		APS replacement servo electronics

Table 2. Cost[a] summary of baseline items

Item	12	DSS 44 and 62	Total base
Antenna mechanical	867	1624	2491
Microwave	606	1146	1752
Antenna feed	93	–	93
XMTR/harm filter	75	70	145
Receiver/Exciter Assembly	635	650	1285
Ranging demodulator	44	177	221
Planetary ranging	–	105	105
Intrasite frequency distribution	277	–	277
Wideband data	98	174	272
Welding	91	179	270
Angle encoders	41	–	41
Extension to 34 m	507	752	1259
Cesium standard	–	50	50
Equipment total	3334	4927	8261

[a]Costs are in $k.

Table 3. Site selection factors (differential only)

Service to flight projects	Goldstone		Australia		Spain	
	DSS 11	DSS 12	DSS 42	DSS 44	DSS 61	DSS 62
Eliminate OPS schedule constraints	0	0	$1903k (6 my/y X 10 y)	0	0	0
Eliminate shared equipment constraints	0	0				0
Implementation	0	0	$909k		$909k	0
Maintenance (personnel)			638k (2 my/y X 10 y)		1160k (3 my/y X 10 y)	0
Eliminate single-point failure by adding control room facility	0	0	560k	0	560k	0
Implementation costs:						
Antenna	$200k	0	0	$91k	0	$50k
Equipment	0	0	0	98k	0	98k
NASCOM	0	0	0	96k	0	96k
Sites selected		X		X		X

Table 4. Equipment funding[a] summary (3 stations)

Task 59 equipment	DSS		
	12	44 and 62	Total
Antenna mechanical (C of F)		993	993
Antenna mechanical (R&D)	1531	1842	3373
Microwave	652	1165	1817
Antenna feed	71	–	71
FTS-UPS Equipment	50	94	144
XMTR/harmonic filter	59	70	129
Receiver/exciter	749	675	1424
Ranging demodulator	44	177	221
Planetary ranging	–	105	105
Minicoherence reference generator	104	180	284
Recording (TPA/GCF)	41	82	123
Wideband data	67	85	152
Cesium standard	73	152	225
Total	3441	5620	9061

[a]WAD A, $k obligation. 1 OCT 76

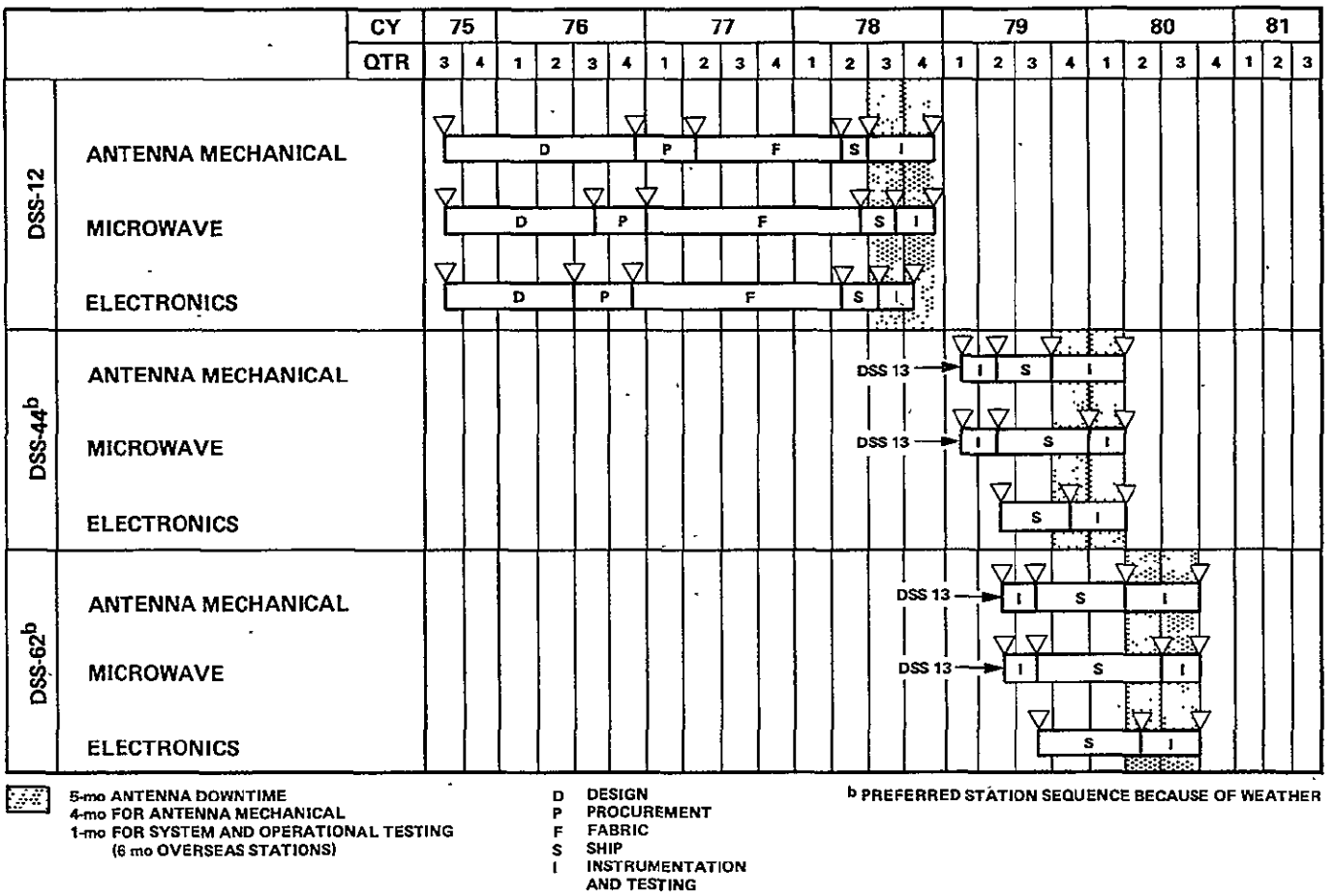

5-mo ANTENNA DOWNTIME
4-mo FOR ANTENNA MECHANICAL
1-mo FOR SYSTEM AND OPERATIONAL TESTING
(6 mo OVERSEAS STATIONS)

D DESIGN
P PROCUREMENT
F FABRIC
S SHIP
I INSTRUMENTATION AND TESTING

b PREFERRED STATION SEQUENCE BECAUSE OF WEATHER

Fig. 1. Preliminary 26-meter S-X conversion schedule

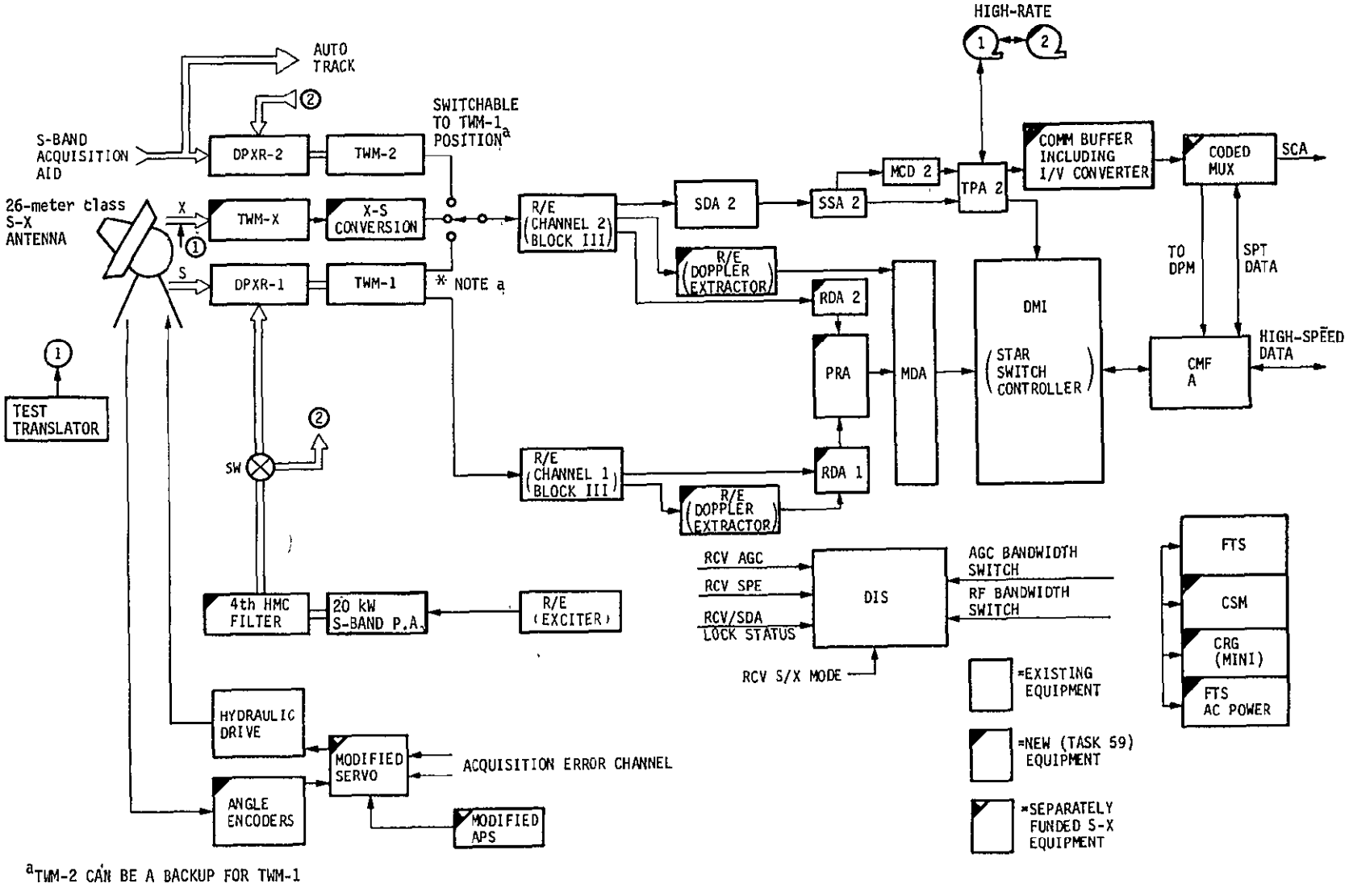

Fig. 2. 26-meter S-X Conversion Project — functional block diagram

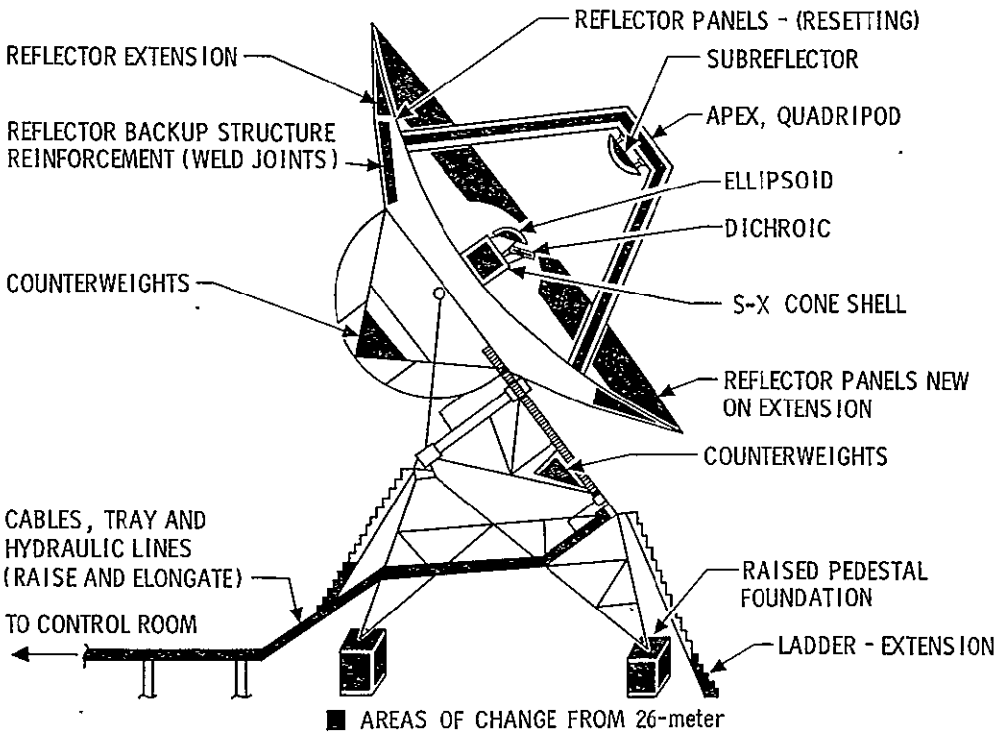

Fig. 3. Structural changes to Antenna Mechanical Subsystem for extension to 34 meters

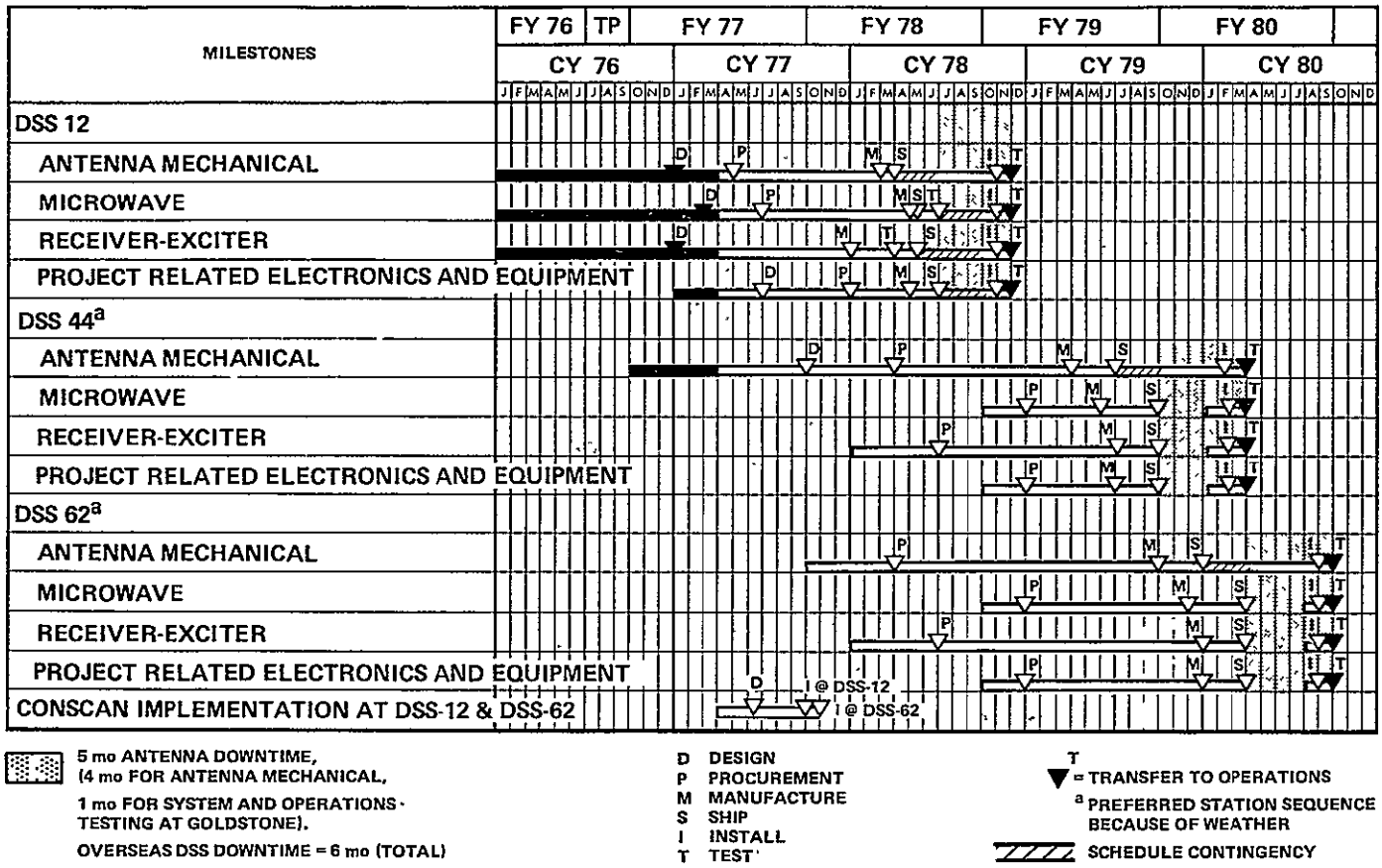

Fig. 4. 26-meter S-X Conversion Schedule

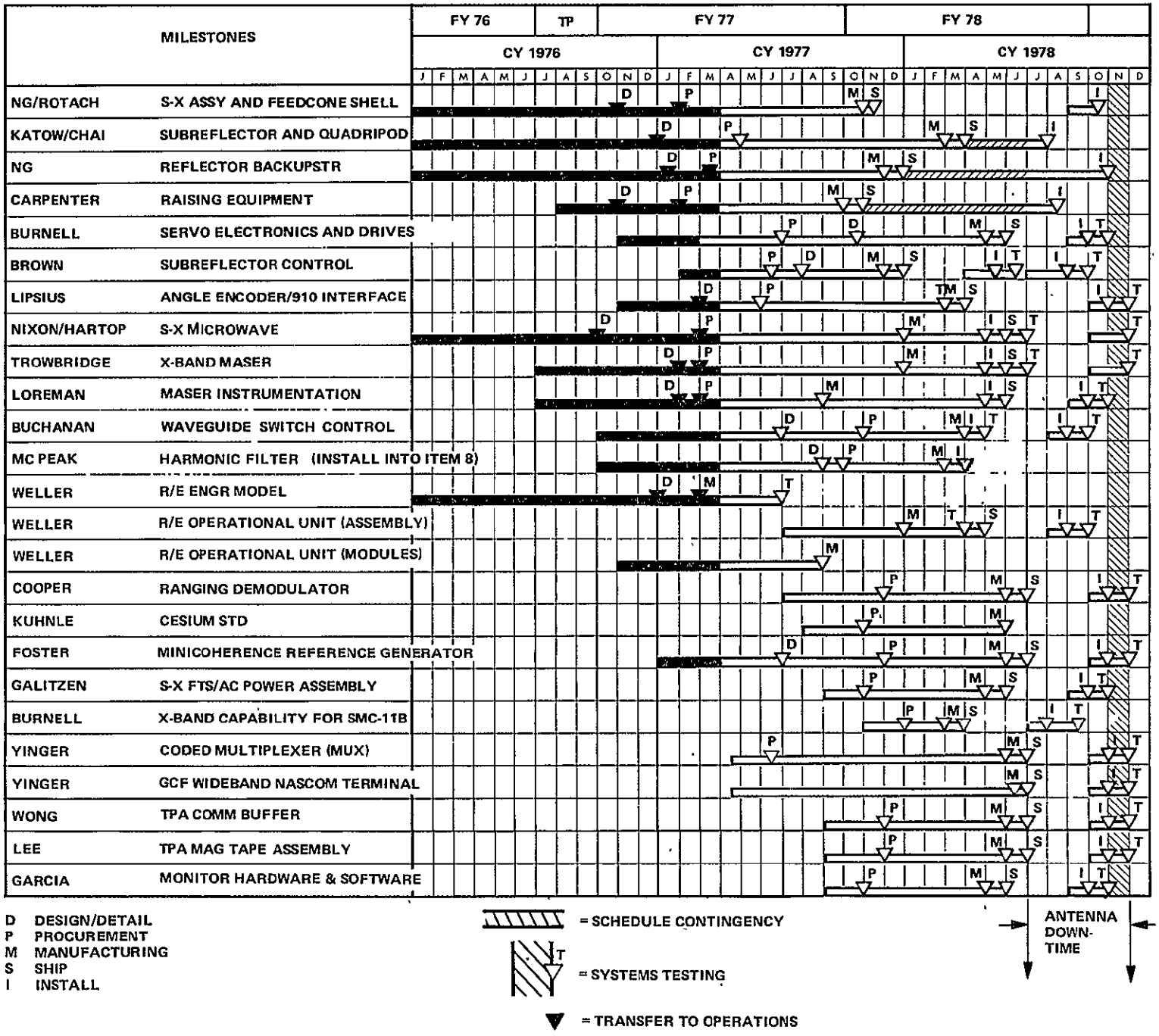

Fig. 5. 26-meter S-X conversion DSS 12 overall schedule

Piping Design Considerations in a Solar-Rankine Power Plant

F. L. Lansing
DSN Engineering Section

Two of the main parameters in sizing the piping of a solar power plant are presented. These two parameters are the working pressure of the vapor leaving the solar collectors, and the type of working fluid used. Numerical examples for each case are given using the graphical Moody friction charts and the analytical Darcy-Weisbach equation. Different working pressures of steam vapor in the solar collector-turbine pipe connection indicate their major role in the design. The size variation was found not to be in linear proportion to vapor density variations. On the other hand, high molecular weight organic fluids such as R-11 and R-113, when compared with water, have shown insignificant changes in piping sizes.

I. Introduction

The major factors associated with the proper design of the piping system in a solar-driven power plant are the selection of the working fluid itself, allowable pressure losses, and the temperature levels in the cycle. The type of working fluid in the thermodynamic cycle could be either water or, for reasons to be explained later, an organic fluid similar to that used in refrigeration machines. Examples of these organic fluids are refrigerant R-113, as used in a prototype described in Ref. 1, or refrigerant R-11, which is used in Ref. 2. The allowable pressure losses in the lines are usually limited by the designer to keep the pumping power to a minimum value. The upper temperature limit in the power cycle depends on the type of solar collector used. It varies from 90°C for flat plate collectors to more than 160°C for medium concentration types. The lower temperature limit in the power cycle varies with the ambient temperature and the type of cooling medium used in the condenser.

Rather than the technical consideration of the thermodynamic cycle and its performance characteristics, this study is related to the size parameters encountered in the piping design only. The economic feasibility of building a solar-driven power plant depends on the installation cost, which in turn depends

on the size of the various plant components and their connecting piping, which constitutes a large percentage of the installation cost. Therefore, a thorough investigation is needed to study the relative importance of piping in the plant cost analysis.

The study is divided into two main sections. The first section is a comparative piping design between a solar-powered power plant, with its low-pressure and low-temperature capability of producing steam, and the opponent case, the fuel-powered, high-pressure and high-temperature conventional power plant. The working fluid will be water in both cases. The second section is a comparison of the piping design when water is used versus an organic substance at the same operating conditions of a given power plant:

II. Friction in Pipes

The selection of a pipe size to transmit a fluid from one end to another, as shown in Fig. 1, depends on the following parameters:

(1) Type of the flowing fluid.

(2) Initial operating pressure.

(3) The allowable pressure drop or the allowable friction rate. The friction rate is defined as the pressure drop per unit equivalent pipe length.

(4) Total equivalent pipe length in the longest run, adding the effects of valves, bends, fittings, etc.

(5) The mass flow rate through the pipe.

Many charts and tables are available in the literature to help the designer select the proper pipe diameter most suitable for the job, with specific information on the above five parameters. The data given in Refs. 3 and 4 were used throughout this work.

The basic formula used to construct a pipe selection chart is the Darcy-Weisbach formula, expressed as

$$\frac{\Delta P}{L} = \frac{f}{d} \cdot \frac{U^2}{2} \cdot \rho \tag{1}$$

where

P = the end-to-end pressure drop along the pipe, N/m^2

L = the equivalent pipe length, m

d = the inner pipe diameter, m

U = the mean flow velocity, m/s

ρ = the flow. density, kg/m^3

f = the friction factor, dimensionless

Equation (1) applies for either laminar or turbulent flow. The value of (f) depends on whether the flow is laminar or turbulent, and it is in general a function of the Reynolds number (R_e) and the relative roughness. The friction factor (f) is usually plotted graphically in what is called "Moody Friction Charts". For convenience, an analytical expression has been made to accurately calculate the friction factor for the special case of smooth walled circular tubes, known as the Karman-Nikuradse equation, as follows:

$$\begin{aligned} f &= \frac{64}{R_e} && R_e \leqslant 2000 \text{ (laminar)} \\ f &= 0.316\, R_e^{-0.25} && 10^5 \geqslant R_e > 4000 \text{ (turbulent)} \\ f &= 0.184\, R_e^{-0.20} && R_e > 10^5 \text{ (turbulent)} \end{aligned} \tag{2}$$

where $R_e = \rho\, Ud/\mu$ (dimensionless) and μ is the dynamic viscosity of the fluid in kg/(m · s). Equation (2) is used throughout this article. with occasional checking with the graphical solutions given in Refs. 3 and 4 when the pipe roughness is considered.

According to the continuity equation, the mass flow rate $\dot{m}$ is given by

$$\dot{m} = \frac{\pi}{4} d^2 \cdot U \cdot \rho \text{ Kg/s} \tag{3}$$

The pump power needed to overcome the friction losses in the pipe, Fig. (1), can be written as

$$\text{friction power} = \dot{m} \left(\frac{\Delta P}{\rho}\right) \cdot \frac{1}{\eta_p}, \text{watts} \tag{4}$$

where η_p is the pump efficiency.

III. Piping Design

This part is divided into two sections: the first is a study of the effect on the piping size of varying the initial steam

pressure in the steam power plant; the second deals with the effect of varying the type of working fluid on the piping size. Each section is handled separately with its different assumptions.

A. Effect of Varying the Initial Pressure on Sizing a Steam Pipe

The necessity to work with steam in solar-powered engines at pressures close to atmospheric is due to the limited capability of low-concentration ratio collectors to obtain high-saturation temperatures. Since the specific volume of dry saturated vapors is inversely proportional to the temperature or the pressure, the effect of operation at low pressure or low temperature on the piping design has to be studied for its size impact.

Let us visualize a power plant whose boiler section is located at some distance (L) from the turbine-condenser, as shown in Fig. 2, and is capable of producing steam in a dry and saturated condition, at the desired pressure. The mass flow rate ($\dot{m}$) through the lines is kept unchanged, independent of the boiler pressure. Also, since the condenser temperature and pressure are dependent only on the cooling medium temperature, which is kept constant, the feed water line need not be resized when the boiler pressure is changed. The only piece of piping that is dependent on the boiler pressure is that connection from the boiler to the turbine. This steam line always needs a heavy thermal insulation and, because of its large size, it is the most expensive piece of piping in the power plant. This piping cost is proportional to its diameter, and constitutes a major part of the installation cost.

The following numerical values were used to construct Table 1 as an example for the study:

steam pressure range	10 to 148 N/cm^2 absolute
condition of steam at boiler exit	dry and saturated
mass flow rate $\dot{m}$	2268 kg/h (5000 lb/h)
maximum allowable friction rate, ($\Delta P/L$)	4.5 N/cm^2 per 100 m (2 psi/100 ft)
condensation temperature	40°C

Selection of the above friction rate ($\Delta P/L$) was based on the practice of designing steam pipes and is kept in the range of, but not exceeding, 4.5 N/cm^2 per 100 m for a first design trial. The following remarks can be abstracted from Table 1:

(1) The largest pipe diameter required to transmit the flow at different pressures is proportional to the specific volume, but not in linear form. For instance, a 12.7-cm (5-in.) nominal diameter pipe is sufficient to carry the steam at atmospheric pressure (10.13 N/cm^2) while a 7.62-cm (3-in.) nominal diameter pipe is required to carry the same flow rate at the same maximum allowable friction rate at a pressure of ~ 148 N/cm^2 (~ 14 atmospheres). Although the specific volume decreased by a factor of 12.4 to 1 from its value at atmospheric pressure, the necessary pipe diameter has decreased by a factor of 5/3 or 1.67 to 1 only. In Fig. 3, the selected pipe diameter is plotted versus the initial steam pressure. The dotted line does not represent any curve fitting to the points abstracted from Table 1, but rather shows how steep the change is at the low pressure range from 10 N/cm^2 to 45 N/cm^2. The main difference between the rate of decrease of the specific volume and the rate of decrease of the pipe diameter is due to the steam velocity that has acquired another rate of decrease at higher pressures to keep the pressure lost in friction below the maximum permissible rate listed.

(2) The shaft power needed to support the flow against the pipe friction, as given by Eq. 4, indicates that the larger the specific volume, the larger the friction power will be for the same mass flow rate and pressure drop. This is evidenced in Table 1, where the friction power is equal to 40.5 kW/100 m for 10.13 N/cm^2 (atmospheric pressure) (No. 1 in Table 1) versus 3.3 kW/100 m for 148 N/cm^2 (14 atmospheres) (No. 4 in Table 1). On the other hand, higher steam pressures imply a higher enthalpy potential difference in the turbine nozzles, and more work output from the power plant. For example, for dry and saturated (d.s.) steam at 10 N/cm^2 pressure, a 75 percent turbine isentropic efficiency, and a condensation temperature of 40°C, the example plant can produce 180 kW compared with 377 kW when d.s. steam at 148 N/cm^2 pressure is used.

It appears from the above that if a hypothetical plant is constructed with an equivalent pipe length of 100 m between the boiler section and the turbine, the friction horsepower in the first case of Table 1 would represent 22 percent of the turbine output, but only 1 percent of the turbine output for the 4th case in Table 1. The piping designer might then search for another criterion to compare the pipe sizes since this comparison based on the same friction rate (or same pressure drop) might prove satisfactory for steam heating purposes, but not suitable for power plants.

(3) An alternative procedure that might be considered for comparing the sizes of steam pipes in steam power

plants is to keep the ratio of friction power to turbine power within a certain percentage value. For example, if the ratio in case 4, Table 1, proved to be an acceptable friction power ratio, i.e., ~ 1 percent of the turbine power for every 100-m equivalent length, then case 1, Table 1, has to change its friction power from 40.5 kW/100 m to 1.8 kW/100 m. This last step necessitates an increase in the nominal pipe diameter from 12.7 cm (5 in.) to 25.4 cm (10 in.), as found from the friction chart, Ref. 3. The friction rate is then dropped from 2.8 N/cm^2 per 100 m to 0.09 N/cm^2 per 100 m, and the friction power drops from 40.5 kW/100 m to 1.3 kW/100 m and the ratio of the pipe friction power to the turbine power becomes 1.3/180 or 0.7 percent per 100 m.

A summary of the above findings follows: If for two steam power plants the piping connecting the boiler to the turbine is compared where one plant is working with dry and saturated (d.s.) steam at 10 N/cm^2 (atmospheric pressure) versus 148 N/cm^2 (14 atmospheres) for the other, then:

(1) The specific volume of steam in the first plant is 12.4 times the specific volume of steam in the second.

(2) The largest nominal diameter yielding the same maximum allowable friction rate ($\Delta P/L$) is 12.7 cm (5 in.) for the first and 7.62 cm (3 in.) for the second, a diameter ratio of 1.67 to 1.

(3) The largest nominal diameter yielding the same maximum allowable ratio of friction horsepower to turbine power is 25.4 cm (10 in.) for the first and 7.62 cm (3 in.) for the second; a diameter ratio of 3.33 to 1. In both cases, the diameter ratio of (2) and (3) is not the same as the specific volume ratio.

B. Effect of working fluids other than water

The idea of using Rankine power cycles with working fluids other than water was initially put under investigation to benefit the automotive industry, and only recently has attention been directed to coupling them with solar energy. A number of studies (for example, Ref. 5) have shown that the use of high-molecular-weight fluids, ranging from 60 to 300, leads to compact turbomachinary for low-power levels below 500 kW. Theoretically, a fluid vapor that has a high molecular weight has 3 properties: (1) a small specific volume, (2) a small isentropic expansion enthalpy drop, and (3) a small sonic velocity. The second property requires a large mass flow increase for a given power output, which may be offset by the first property. Also, the second property creates low nozzle velocities, low blade-tip speeds, and thus low rotational speed, a characteristic that is desirable for small units. The third property may make the flow in the blade passage supersonic, which is complicated. Whether high-molecular-weight fluids are superior in performance or not, it is felt that more work is needed specifically for solar-powered devices.

In this section, a comparison is made between two power plants working on the same thermodynamic cycle, which is chosen to be the Rankine cycle, the same temperature limits, and having the same net power output, but employing two different working fluids. In one case, water is used and in another case either one of the organic fluids, refrigerant R-11 or refrigerant R-113 is used. These two organic fluids were claimed by some researchers (Refs. 1 and 2) to be superior to water, both in performance and economics, for operation in low-temperature power cycles. The reason behind making this comparison is to justify the large or small differences, if they were found, between any of these two organic fluids versus water in a solar-Rankine power cycle. The following parameters were kept unchanged in a numerical example:

(1) Thermodynamic cycle: simple Rankine with no superheat.

(2) Working fluids: water, R-11, R-113.

(3) Condition of fluid entering the turbine: saturated vapor.

(4) Condition of fluid entering the pump: saturated liquid.

(5) Net power plant output: 100 kW_e.

(6) Electric generator efficiency: 90 percent.

(7) Evaporation temperature: 100°C (212°F).

(8) Condensation temperature: 40°C (104°F).

(9) Isentropic efficiency of compression or expansion processes: 75 percent.

The results of the thermodynamics of the cycle are given in Table 2. The following remarks are made from Table 2:

(1) The thermal efficiency of the Rankine cycle appears to have a weak relationship with the type of working fluid or the pressure range in the cycle. It is also evident from Table 2 that working with water produced a 10 percent increase in the thermal efficiency compared with refrigerants R-11 and R-113. This result is simply due to the large latent heat of vaporization that water possesses over any other fluid. The heat added in the Rankine cycle consists of two parts: a sensible heat

part at constant pressure, and a latent heat part at constant temperature and pressure. Therefore, the isothermal portion of the total heat addition is larger for water than for any other fluid. The rankine cycle will approach the idealizations set by Carnot's principle as more and more heat is added or rejected in reversible isothermal processes.

(2) For a specific power output, such as 100 kW_e output in the example, the mass flow rate in the case of water is 1/13.74 times that required for R-11, or 1/14.88 times that required for R-113. Again, this small water flow is due to the extremely large latent heat of vaporization for water compared to R-11 or R-113. At first glance, it may appear to the designer that water piping can be smaller in size than the comparative organic fluids. On the other hand, water vapor has a very large specific volume compared to R-11 or R-113. For example, the specific volume of dry and saturated steam at the turbine inlet is 71.7 times that for R-11 vapor, or 50.1 times that for R-113 vapor. However, the designer will find that the water vapor discharge (mass flow X specific volume product) is only 5.23 times that for R-11 vapor, or 3.37 times that for R-113 vapor. The only key left in designing the piping for each fluid is the allowable friction loss as described below.

(3) The design of steam piping connecting the boiler to the turbine could first be made using the data in Table 2 and the friction charts of Ref. 3 as follows. Taking the mass flow rate of 1388 kg/h (3060 lb/h) of dry and saturated steam at atmospheric pressure from Table 2, and an arbitrary maximum friction rate of 0.34 N/cm^2 per 100 m (0.15 psia/100 ft), the largest nominal pipe diameter is found to be 20.32 cm (8 in.). This corresponds to an inner diameter of 20.272 cm (7.981 in.), a flow velocity of 19.985 m/s (3934 ft/min), a Reynolds number of 202,740 and a friction factor (f) for smooth pipes of 0.016. The result of this selection is a friction rate of 0.10 N/cm^2 per 100 m, and a friction power rate of 0.86 kW/100 m for a smooth pipe or 1.2 kW/100 m if 40 percent allowance is made due to pipe roughness, resulting in a friction power on the order of 1 percent of the turbine power output for every 100 m of equivalent pipe length.

(4) Tables 3 and 4 were constructed for refrigerants R-11 and R-113, respectively, using the data in Table 2 and Eqs. 1, 2, 3 and 4. The following findings are made:

(a) When the maximum permissible friction rate ($\Delta P/L$) was the same for all the fluids concerned, the size of the pipe connecting the boiler to the turbine was found the same and equaled 20.32 cm (8 in.) for the 100 kW_e power plant example.

(b) If, on the other hand, the design was based on an equal ratio of friction power to total plant power (or equal friction power in the case of comparing two plants of the same power output), the design pipe diameter was found equal to 15.24 cm (6 in.) for R-11 vapor versus 20.32 cm (8 in.) for both water vapor and R-113 vapor. This corresponds to a friction power rate of less than or equal to ~1 percent of the total plant power per 100-m equivalent length

IV. Conclusions

Comparisons made were based on the assumption that the most expensive piece of piping in the power plant was that piece connecting the solar collectors (or boiler) to the turbine section. The following conclusions can be reached:

(1) Pipe size differences due to different working pressures can be a major factor in the design, while pipe size differences due to different working fluids are minor ones.

(2) The points in favor of using water as the working fluid in power plants over the selected organic fluids are numerous. From the point of view of thermodynamic behavior in the cycle, cost, nonflammability, and nontoxicity, water is the superior fluid.

References

1. Barber, R. E., "Solar Air Conditioning Systems Using Rankine Power Cycles – Design and Test Results of Prototype Three Ton Unit", *Proceedings, Institute of Environmental Science*, Vol. 1, pp. 170-179.

2. Biancardi, F., and Meader, M., "Demonstration of a 3-Ton Rankine Cycle Powered Air Conditioner", *Proceedings of the Second Workshop of the Use of Solar Energy for Cooling of Buildings,* held at UCLA, August 1975.

3. *Carrier System Design Manual and Handbook*. Carrier Air Conditioning Company, Syracuse, New York, Parts 3 and 4.

4. Mark's *Standard Handbook for Mechanical Engineers*, 7th Edition, McGraw Hill Book Co., Sec. 3.

5. Bjerklie, J., and Luchter, S., "Rankine Cycle Working Fluid Selection and Specification Rationale," paper 690063 presented at SAE Automotive Engineering Congress, Jan. 1969.

Table 1. Sizing a steam pipe at different initial pressures with constant flow and friction rates

Case no.	Initial pressure, N/cm^2 (psi) absolute	Specific volume v, m^3/kg	Largest[a] nominal diameter, cm (in.)	Inner[b] pipe diameter, cm	Flow velocity[c] U, m/sec	Viscosity μ, kg/m · h	Friction[d] factor f (smooth pipes)	$(\Delta P/L)$ calculated for smooth pipes, N/cm^2/100 m	$(\Delta P/L)$[a] working value, N/cm^2/100 m	Friction power,[a] kW/100 m	Total plant power with the same flow rate,[e] kW	Friction power to total plant power ratio per 100 m
1	10.13 (14.7)	1.673	12.7 (5)	12.819	81.64	0 043	0.0132	2.0	2 8	40.5	180	0.22
2	20.48 (29 7)	0.858	10.16 (4)	10.226	65.82	0 0457	0 0128	3.0	4.2	30.8	233	0.13
3	44.61 (64.7)	0.416	8.89 (3 1/2)	9.012	41.08	0.0493	0.0127	3.0	4.2	14.9	289	0.05
4	148 03 (214.7)	0.135	7.62 (3)	7.793	17.83	0.0553	0.0126	2 0	2.8	3.3	377	0 01

[a]Taken from steam pipe charts, Ref. (3).

[b]Taken from pipe standards Tables, Ref. (3).

[c]Using Eq 3 this article.

[d]Using Eq. 2 this article.

[e]Based on condenser temperature of 40°C and turbine isentropic efficiency of 75 percent

Table 2. Comparison between water and organic fluids R-11 and R-113 in the performance of a solar-Rankine engine

Type of working fluid	Water	R-11	R-113
Molecular weight	18.0	137.4	187.4
Heat addition, Wh/kg	696.5	55.8	51.5
Net work output, Wh/kg	80.04	5.83	5.38
Rankine thermal efficiency, percent	11.49	10.45	10.45
Carnot's thermal efficiency, percent between 40°C and 100°C	16.08	16.08	16.08
Isentropic enthalpy drop in the turbine, Wh/kg	106.77	7.99	7.29
Solar-boiler pressure, N/cm^2	10.13	81.82	44.28
Ratio of boiler pressure to condenser pressure	13.735:1	4.718:1	5.658:1
Mass flow rate ($\dot{m}$) to produce 100 kW$_e$, kg/h (lb/h)	1,388 (3060)	19,069 (42,040)	20,660 (45,545)
Specific volume (v) of d.s. vapor at turbine inlet m^3/kg (ft^3/lb)	1.673 (26.801)	0.0233 (0.3735)	0.0334 (0.5347)
Discharge (area X velocity product) at turbine-boiler pipe, m^3/s	0.6452	0.1234	0.1917

Table 3. An example of piping design for refrigerant R-11 vapor

Nominal pipe diameter,[a] cm (in.)	Inner diameter, cm	Cross sectional area, cm^2	Velocity[b] U, m/s	Reynolds[c] number, R_e $\times 10^{-6}$	f (smooth pipes)	$\Delta P/L$ (smooth pipes), $N/cm^2/100$ m	Friction horsepower, kW/100 m
10.16 (4)	10.226	82.13	15.027	4.777	0.0085	4.02	6.711
12.70 (5)	12.819	129.07	9.562	3.811	0.0089	1.36	2.274
15.24 (6)	15.405	186.39	6.622	3.171	0.0092	0.56	0.932
20.32 (8)	20.272	322.76	3.824	2.410	0.0097	0.15	0.254

[a]Steel pipe Schedule 40.

[b]At a flow rate of 19,069 kg/h and a specific volume of 0.0233 kg/m^3.

[c]At a viscosity μ of 0.0497 kg/m • h.

Table 4. An example of piping design for refrigerant R-113 vapor

Nominal pipe diameter,[a] cm (in.)	Inner diameter, cm	Cross sectional area, cm^2	Velocity[b] U, m/s	Reynolds Number[c] R_e, $\times 10^{-6}$	f (smooth pipes)	$\Delta P/L$ (smooth pipes), $N/cm^2/100$ m	Friction horsepower, kW/100 m
12.70 (5)	12.819	129.07	14.851	4.685	0.0085	2.19	5.67
15.24 (6)	15.405	186.39	10.284	3.898	0.0088	0.90	2.34
20.32 (8)	20.272	322.76	5.939	2.963	0.0093	0.25	0.63

[a]Steel pipe Schedule 40.

[b]At flow rate ($\dot{m}$) of 20660 kg/h and a specific volume of 0.0334 m^3/kg.

[c]At a viscosity μ of 0.0438 kg/m • h.

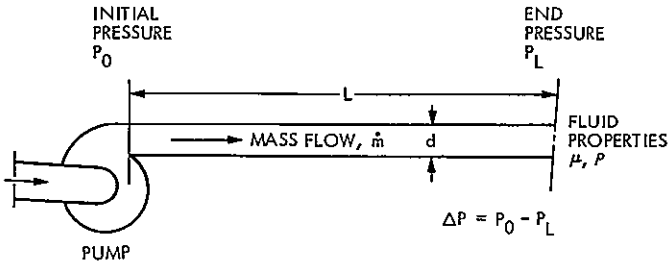

Fig. 1. Pipe schematic

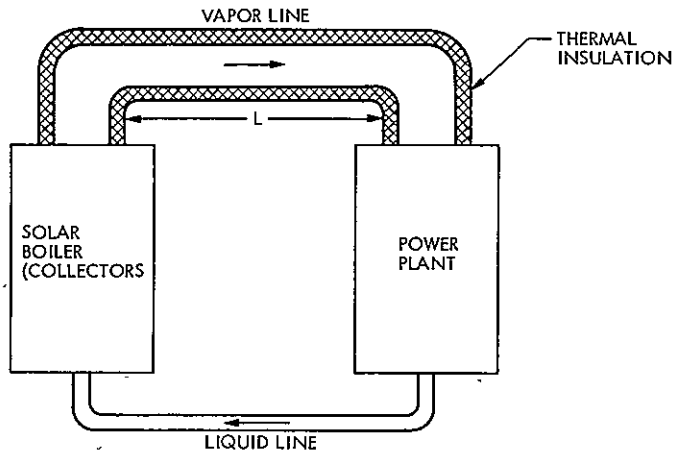

Fig. 2. A solar boiler, working at different pressures, is located at a distance *L* from the power plant

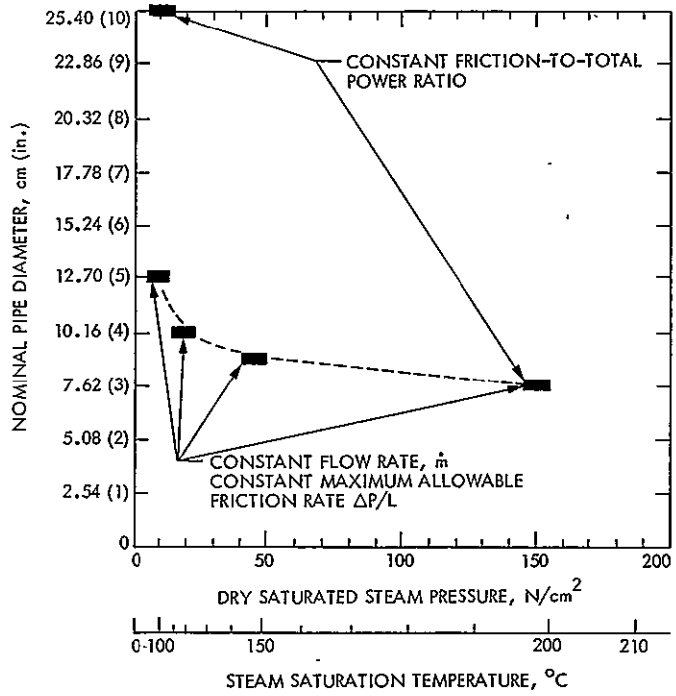

Fig. 3. The effect of varying the initial steam pressure on the pipe design with (1) constant friction rate, and (2) constant friction-to-total power ratio

D19

N78-15086

Selectable Polarization at X-Band

R. W. Hartop
Radio Frequency and Microwave Subsystems Section

The X-band feeds in the DSN are being upgraded to include selectable polarization in time for the Voyager missions to the outer planets.

I. Introduction

The 64-meter antenna stations of the DSN are equipped with X-band receiving (XRO) cone assemblies (Ref. 1). The X-band feed within the cone operates through the dichroic plate in conjunction with the S-band polarization diverse (SPD) cone assembly. The X-band feed has been required to provide right-hand circularly polarized (RCP) reception only. The entire feed structure is easily removable from the cone assembly as a unit, and provision was made in the original mechanical design to facilitate future upgrades such as the present one.

II. XRO Feed Mod II

Figure 1 shows the Mod II X-band feed which will replace the existing feed. Two complete assemblies have been fabricated and will be implemented at DSS 14 and DSS 43 during the second and third quarters of 1977. One of the original feeds from these stations will be rebuilt with new parts added to provide the third unit at DSS 63 for implementation in the fourth quarter.

Compared to the original feeds, the Mod II feed has the following major items added: two circular waveguide rotary joints, drive motor and gear reducer, gear assembly, two microswitches, and a polarization control junction box. The overall length of the feed remains the same since circular waveguide spacing sections were designed into the original feed to readily permit such modifications. Thus, there is no significant increase in antenna noise temperature compared to the original feed. Figure 2 is a close-up of the drive gear assembly. The circular steel plate is firmly attached to the lower rotary joint flange (identical to the upper rotary joint visible in the center of the picture) and is precisely stopped at its CW and CCW travel limits by the two blocks that contact the worm gear housing. The large gear is spring-loaded to the drive plate so that motor coast after microswitch activation winds up the gear springs and holds the polarizer securely in position despite antenna movement or vibration. Rotating the polarizer 90 degrees changes the polarization from RCP to LCP or vice versa. The measured ellipticity of the Mod II feed assembly is shown in Fig. 3 over a wide bandwidth. It is less than 0.7 dB over the presently required bandwidth of 8.4 to 8.5 GHz.

Since the mechanism requires about seven seconds to complete its travel, holding relays are incorporated in the junction box to insure that a momentary command from the control room panel results in a complete 90-degree movement and microswitch interlock activation.

Electrically the mechanism functions like a standard DSN waveguide transfer switch. This allows the polarizer to be controlled from a spare receptacle on the cone-mounted switch control junction box. Thus, positions may be assigned for RCP and LCP that correspond to positions 1 and 2 of a waveguide switch, and all indicator and interlock circuits are fully compatible.

III. Summary and Future Work

The Mod II XRO feed assembly that will provide remotely selectable RCP/LCP diversity for Voyager has been described. Transfer, shipment, and installation of the first two units is in progress, and the third and last unit is scheduled for implementation before the end of 1977.

Development work is beginning on a prototype orthogonal mode transducer for a Mod III XRO feed that will permit simultaneous RCP and LCP reception (and future transmission). Because of the mechanical design of the XRO cone assembly and feed, additional upgrades of this kind can be made periodically without difficult cone changes that consume valuable station time.

Reference

1. Hartop, R. W., "X-Band Antenna Feed Cone Assembly," in *The Deep Space Network Progress Report*, Technical Report 32-1526, Vol. XIX, pp. 173-175, Jet Propulsion Laboratory, Pasadena, Calif., Feb. 15, 1974.

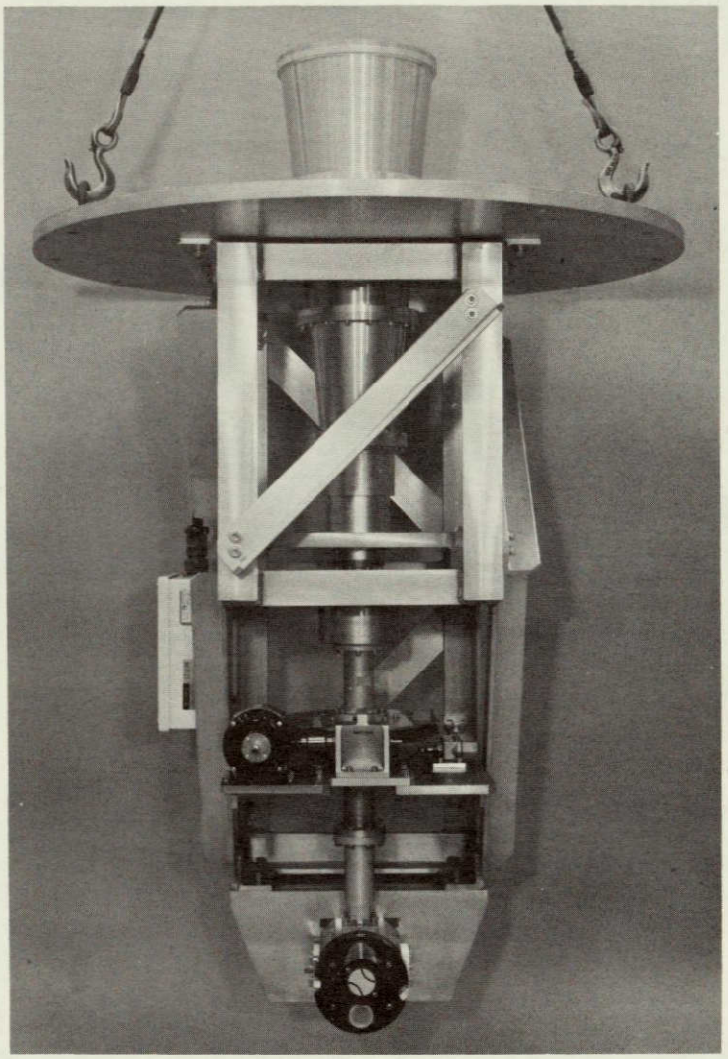

Fig. 1. XRO Mod II Feed Assembly

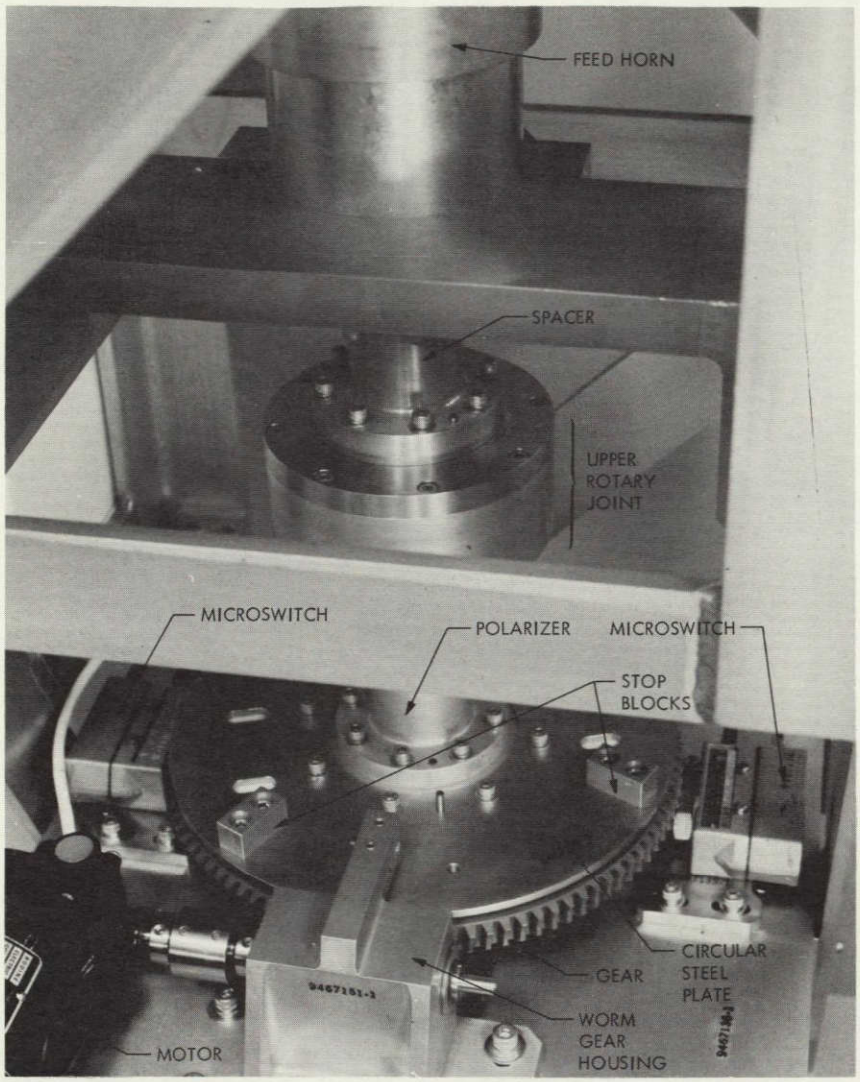

Fig. 2. Polarization drive mechanism

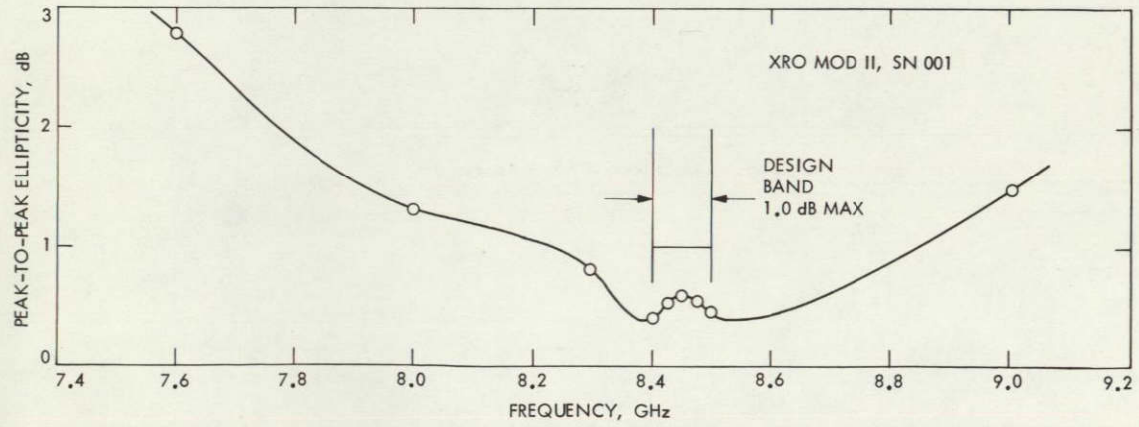

Fig. 3. Feed ellipticity

D20

N78-15087

VLBI Validation Project

W. J. Ross
Deep Space Network Operations

This article summarizes the DSN operations support of the first session of a series of yearly sessions being conducted by the VLBI Validation Project. It covers the period November 1976 through January 1977 wherein two training and three operational experiments were conducted at the Deep Space Communications Complex (DSCC) at Goldstone, California.

I. Introduction

The VLBI (Very Long Baseline Interferometry) Validation Project Task was established in response to a letter of January 2, 1976, from NASA Headquarters. A plan was subsequently developed leading to a comparison of VLBI techniques with laser ranging systems by conducting a series of vector measurements using common benchmark locations at continental distances (Goldstone, Haystack, and the McDonald Observatory) with an accuracy goal on the order of 5 cm.

The major activities included in the Validation Task are:

(1) An initial measurement of intra-Goldstone baselines and comparing with existing survey data for self-validation.

(2) An improved measurement of intra-Goldstone baselines to demonstrate short baseline accuracy with advanced system technology and comparison with improved survey to establish an upper bound on error sources.

(3) Compatibility testing and readiness tests at Goldstone in preparation for long baseline tests.

(4) Measurement of benchmark locations at Goldstone, McDonald, and Haystack using VLBI advanced systems technology.

(5) Intercomparison between VLBI and laser measurement at benchmark locations at Goldstone, McDonald, and Haystack.

The operational objectives for the first VLBI Validation Project session were to:

(1) Demonstrate reliable three station operation by Goldstone Complex personnel.

(2) Provide project experience to better plan succeeding tests.

(3) Identify and correct problem areas.

II. Operations

A. Training

The Goldstone Complex operations commenced with two personnel training experiments. For the first experiment, the Radio Science Support Group personnel participated primarily as observers during an OTDA Platform Parameters Source Survey VLBI experiment. For the second training exercise, the same personnel configured the equipment and conducted the experiment under the guidance of experienced JPL Tracking Systems and Applications Section personnel. Configuring the VLBI equipment, and solving hardware and procedural problems, provided excellent training for the Support Group but little data were obtained.

B. Experiments

The training activities were followed by three operational experiments conducted during December 1976 and January 1977. The results were satisfactory in that useful data were acquired during 77 percent of the scheduled experiment periods. The remainder of the time was used to set up, calibrate the system and de-implement the equipment following the experiments.

III. Scheduling

Combinations of the four DSN Goldstone stations (stations 11, 12, 13, and 14) were scheduled for the training exercises and the operational experiments. The experiments were spaced so as to allow time for evaluating the operational performance and equipment problems and taking corrective action prior to the subsequent experiment. Table 1 shows the hours scheduled, the stations involved, and the dates the activities occurred. For the last experiment, time was scheduled to allow the equipment to be installed on a non-interference basis in the station control rooms during the preceding station activity. This was of enough benefit to justify continuing the practice for future VLBI Validation Project experiments.

IV. Personnel

The training and operational experiments were supported by the Radio Science Support Group personnel, the stations' operations crews, and by experienced Tracking Systems and Applications Section personnel who not only acted as instructors and/or monitors of the experiments, but also provided the valuable assistance required to set up and calibrate the configuration at each station.

V. Configuration

The equipment configuration used to support the operational experiments is shown in Fig. 1.

The MK 0 (48-kHz VLBI Data Recording System) was the prime source of data. The MK II Recording Terminal was used primarily to train the supporting personnel for future project activities and therefore the data obtained was not processed.

The Bandwidth Synthesis (BWS) equipment consisted of three separate units; the MK II consisted of six separate units; and the MK 0 consisted of an Analog to Digital (A-D) VLBI Adapter and Signal Coupler connected to the station XDS 920 digital computer. By the last experiment, some of the BWS and MK II units had been installed in small portable cabinets (or modularized), which reduced the complexity of the configuration and helped to reduce the setup time.

All synthesizers used to generate local oscillator (LO) signals were referenced to the station Hydrogen Maser Frequency Standard where available; otherwise, the station Rubidium Frequency Standard was used. The 5-MHz signal for the VLBI receiver local oscillator was obtained from the MK II Recording Terminal distribution system for convenience. The VLBI receivers were located in the station antenna assemblies and obtained the S-band signal from the Travelling Wave Maser via an isolation coupler. The 50-MHz IF signal went via coaxial cable to the attenuator assemblies located in the respective station control rooms.

The F3 signal was 50 MHz, which converted the 50-MHz IF to baseband. F1 and F2 were selected to result in 24-kHz upper and lower sideband signals, which were sequentially sampled and sent to the A-D VLBI adapter connected to the XDS 920 computer for sampling, digitizing, formatting, and recording. The tapes were then sent to Pasadena for correlation and processing.

VI. Problems

Some problems were encountered during setup and during the experiments. Three examples and their solutions are listed below:

(1) One VLBI receiver local oscillator failed during setup. This unit multiplies the 5 MHz to 2240 MHz to convert the S-band signal (2290 MHz) to the 50-MHz IF. An emergency substitution was made by using the Block III receiver LO chain for this one experiment.

(2) Both digital tape units failed within a few minutes of each other at one station. The backup XDS 920 computer was then substituted for the remainder of the experiment.

(3) The 24-kHz signal to the A-D VLBI adapter was found to be too low for satisfactory data recording. This was caused by a 50-ohm input impedance Spectrum Analyzer being inadvertently connected across the high impedance line. The Spectrum Analyzer was disconnected as soon as the cause was discovered.

Other problems which were encountered during the experiments were rapidly corrected.

VII. Summary

The objectives of the first VLBI Validation Project session were met. The Goldstone personnel are better prepared to conduct subsequent project experiments and the equipment has been partially modularized. Permanent installation of the VLBI equipment in control room racks is planned for subsequent project sessions.

Table 1. Training and experiment schedule

Purpose	Date	Time, hours	DSS			
			11	12	13	14
Training	11 November	8	X		X	
Training	29 November	8			X	X
Experiment 1	6 December	12	X		X	X
Experiment 2	29 December	8	X	X		X
Experiment 3	24 January	9	X		X	X

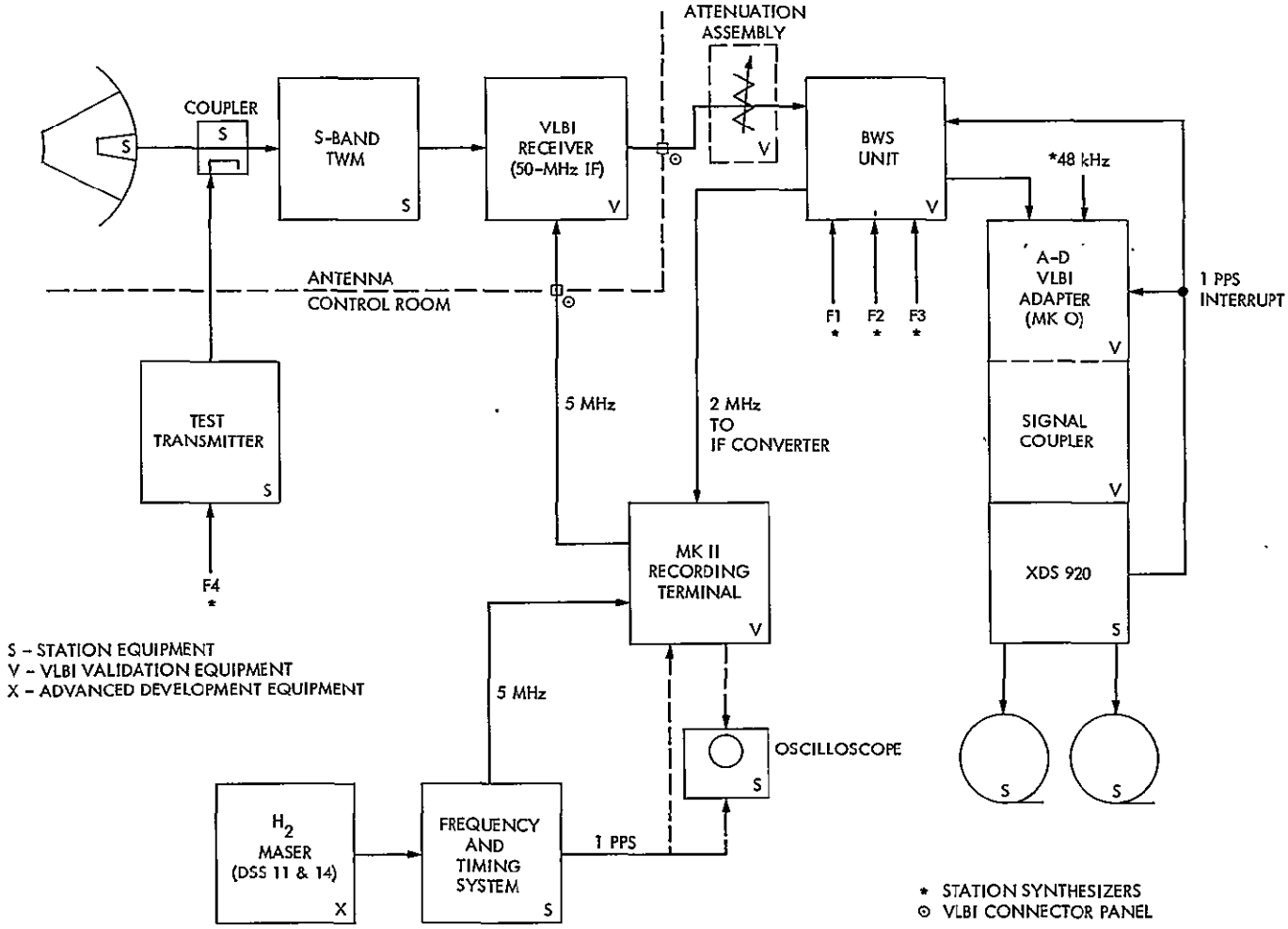

Fig. 1. VLBI Validation Project station configuration for Session 1

R21

N78-15088

A Method for Reducing Software Life Cycle Costs

W. O. Paine and J. C. Holland
Quality Assurance DSN, MCCC and Mechanical Hardware Section

The advent of new hardware and software tools permits a new approach to preparing, presenting, and maintaining software specifications and corresponding source programs. The method described could significantly reduce many of the associated costs compared with techniques-now in general use in industry.

I. Introduction

Software life-cycle costs typically include all of the manpower, equipment usage, and documentation costs necessary to design, implement, and maintain computer software throughout its life. Indirect costs, which are often excluded from this grouping, are the net consequences to operations resulting from the use of the "finished" software. Thus, if software is placed into use while still seriously in error, the indirect cost to operations could be greater than the typical total life cycle cost. On the other hand, correct and well designed software, delivered and used in a timely manner, could yield a significant saving to an operational activity. Effective ways of reducing typical costs while maintaining or improving software quality should lead to an improvement in indirect costs.

When software costs are closely examined, it is seen that skilled manpower is now the major contributor and is the most rapidly increasing cost (Ref. 1). Within the range of such human activities, it appears that designing and testing efforts are the major parts and that the underlying planning, analyzing, and communicating aspects of this effort are major portions. Thus, any real reduction in software life cycle costs must make highly skilled human effort more efficient, especially on large, complex, and long-lasting software projects. When these skilled human functions are examined closely, it is seen that critical factors include the way one communicates with oneself and then with others and finally with computers. Thus, there has been a long and active proliferation of programming languages and, more recently, a number of programming design languages to supplement older methods, such as flowcharting. One way to achieve cost reduction is to provide documentation tools whose use increases the effectiveness of skilled humans (Ref. 2).

II. Proposed Method

A. Conceptual Principles

The conceptual principles that must be met are:

(1) The design document and resulting computer code should be as closely connected as possible, both physically and in descriptive terms.

(2) The design should be readily understood by the non-programming "user" or "client" who provided the original requirements.

(3) The design and code should be readily understood and found comparable by all programmers involved in the preparation and verification of the software throughout its life.

(4) The complete design and source program document should be in a machine-readable form, such that it may be readily stored and processed on one computer. At some point it should be kept on a common single storage device such as a tape or a disk. Thus, it should be possible to also move a copy of the entire machine-readable document at once to an alternate processor for more convenient use, special testing or printing.

(5) Document updating methods should force some consideration of possible updating of both the design and source code on every occasion.

(6) There should be an automatic annotation on each page of the document showing the date of the update version number, and clearly identifying changes made from the previous version.

(7) Pagination and other systematic identification to reveal design structure should be at least semi-automatically produced for accuracy, consistency, and cost-saving convenience.

(8) The method should be independent of the choices made for programming languages and target computers.

B. Hardware and Software Tools

The fairly recent advent of important new hardware and software tools permits the solution shown in Subsection C. However, other tools are available which would allow other approaches to satisfying the conceptual principles given in Subsection A. In any event, a few new and/or expanded software tools would be required to achieve the systematic, operational use of the proposed method. The cost of producing the new software tools should be a very small fraction of the potential savings and certainly would be significantly less than the cost of a compiler or an assembler.

In the proposed method, tools which were conveniently at hand were used to illustrate the approach. Perhaps better or more suitable tools may become available later. The key hardware tool employed is the IBM 3800 (laser) printer. It is described in Refs. 3 and 4. However, for our purposes, it is enough to note that it permits 20 type fonts, up to 204 characters per line and up to 12 lines per vertical inch (2.54 cm). The laser (non-impact) principle yields printing of exceptional quality, approaching that of true graphics arts. The number of multiple copies needed may be specified by a single card with each use, and bursting and trimming are also under program control. The overall capability and flexibility of this printer would allow entire finished detailed design documents, including graphics, to be done at one time.

The key software design tool employed for this example is a program design language currently available on the JPL UNIVAC 1108 called SDDL (for Software Design and Documentation Language) (Ref. 5). In an operational system, code positioning would be either semi- or completely automatic as code is developed to fulfill design statements.

C. Details of the Proposed Method

Three new modes of displaying software under development, or as permanent documentation for field-released versions, are shown in Figs. 1 through 3.[1]

The first of the display modes (see Fig. 1) offers the ability to explicate the nature of the program and its structure in terms of natural language. This feature has the great advantage of eliminating the need for condensing identifiers into obscure mnemonics or restricting the commands to a set of reserved words known to any specific compiler or assembly language. The invented delimiters "DO.UNTIL" and "END.DO" of Fig. 1 serve to indicate a loop within the CMSP1 program, a fact established by a simple directive to SDDL (discussed below).

The flexibility of this language is demonstrated by the definition of the word "EXECUTE" as an indication of calling a subroutine, a fact indicated by the horizontal arrows terminating upon empty parentheses. It is assumed here that the documentation and programming are still under development, and the subroutines referred to have not yet been defined. Words such as "SET" in the instruction "SET STOP = FALSE," which might in some cases be viewed as auxiliary and only for the purpose of aiding readability, are admissible in such a flexible language as SDDL, just as is the usage of the "END.IF" to delimit the logic of an "IF ... THEN ... ELSE ... ENDIF" paragraph. It should be noticed also that the auxiliary word "THEN" is omitted in Fig. 1. The invented delimiter "FINIS" marks the termination of each program module.

[1] Figures 1, 2, and 3 are constrained by printing space in this publication. In operational practice the limits would permit up to 204 characters per 13.6-in. (34.5-cm) line and either 6, 8 or 12 lines per inch (2.54 cm).

The SDDL processor automatically indents the text presented to it in a manner which reflects the underlying structure, as set forth by the definitions of modules, blocks, and escapes within that language. The user may override or modify this indentation by the use of further directives, if he so desires.

The second mode of display afforded by the combination of SDDL and the capability of the IBM 3800 printer is that of the combined SDDL and generated object code – in an interleaved manner – as shown in Fig. 2. The SDDL language allows for the separation of source statements as an arbitrary point designed by a pound sign (#). The portion of the statement to the right of the pound sign is right-justified on the printed output, and is reserved for comments (i.e., has no effect on the structuring of the SDDL statements, as seen by this language processor, with respect to modules, blocks or other structures). The object-language statements, in whatever language is appropriate, may be coordinated with the SDDL statements by placing them in these fields. Auxiliary directives to the SDDL processor may be used to justify certain fields of the object language to certain margins for the sake of uniformity.

The third mode of presentation of the documentation, as shown in Fig. 3, involves a side-by-side listing of the program design language and the completed object code. Here the SDDL statements may, if desired, contain code numbers allowing coordination of these statements with the finished object code. Because of the presence of embedded code modules which may be developed separately (and displayed separately, as in the second mode described above), the final object program and its associated SDDL code will not necessarily present the simple correspondence afforded by the interleaved listing of the previous mode. The use of identifying numbers would, nevertheless, allow the two forms of the same program to be associated in a statement-by-statement manner.

III. Advantages of the Method

The method, when compared with many existing techniques, offers several advantages. By placing both the structured design and resulting code on a single page such that they may be read separately *or* together meets the needs of all users of the document while reducing production and maintenance costs. The designer and programmer, while working in both the development and maintenance modes, are encouraged to read, compare, and maintain both parts of the finished document. It is expected that the clarity and convenience alone would make the method attractive to both end users and implementers. The auditing of code vs design (Ref. 6) would become more efficient. Finally, a step is taken in the direction of allowing future semi-automation in software validation and verification, by virtue of the fact that such a well-structured presentation lends itself well to the processing of inductive assertions.

References

1. Gilb, T., *Software Metrics,* Winthrop, Cambridge, Mass., 1977.
2. Tausworthe, R., *Standardized Development of Computer Software*, SP 43-29, pp. 1-8, Jet Propulsion Laboratory, Pasadena, Calif., July 1976.
3. *Introducing the IBM 3800 Printing Subsystem Audit Programming*, IBM Manual GC26-3829-4, November 1976.
4. *IBM 3800 Printing Subsystem Programmer's Guide*, IBM Manual GC26-3846-1, September 1976.
5. Kleine, H., *SDDL-Software Design & Documentation Language*, Publication 77-24, Jet Propulsion Laboratory, Pasadena, California, May 15, 1977.
6. Holland, J. C., and Paine, W. O., "An Error-Minimizing Software Audit Technique," in *The Deep Space Network Progress Report 42-32*, pp. 201-221, Jet Propulsion Laboratory, Pasadena, California, Apr. 15, 1976.

```
                                                    SSD-DMC-5084-0P
                                                    MODULE NAME     CMSP1
                                                    DATE          7/15/76
                                                    REV    A      9/15/76
PROGRAM  CMSP1

 EXECUTE INITIALIZATION                  ------------------------------------>(( ))

 DO.UNTIL ENDRUN = TRUE

   EXECUTE FIRST.PROGRAM.STAGE           ------------------------------------>(( ))

   IF STOP = TRUE

     SET STOP = FALSE

   ELSE

     IF COMMAND.VALIDATION = TRUE

       EXECUTE SECOND.PROGRAM.STAGE      ------------------------------------>(( ))

     ELSE
     END.IF

     IF STOP = TRUE

       SET STOP = FALSE

     ELSE

       EXECUTE THIRD.PROGRAM.STAGE       ------------------------------------>(( ))

     END.IF
   END.IF
 END.DO

 EXECUTE TERMINATION.PROGRAM             ------------------------------------>(( ))

FINIS
```

TITLE	DATE	INT'S
PREPARED		
CHECKED		
APPROVED		

Fig. 1. Program design language sample

```
                                                    SSD-DMC-5084-0P
                                                    MODULE NAME     CMSP1
                                                    DATE           7/15/76
                                                    REV    A       9/15/76
PROGRAM  CMSP1

 EXECUTE INITIALIZATION                        PREEX  EQU $        INSERT CODE

 DO.UNTIL ENDRUN = TRUE                        CMS20  EQU $

   EXECUTE FIRST.PROGRAM.STAGE                 PS1    EQU $        INSERT CODE

   IF STOP = TRUE                                     TBMB,FLAG    STOP,CMS60

     SET STOP = FALSE                                 OBMM,FLAG    STOP

   ELSE

     IF COMMAND.VALIDATION = TRUE              CMS60  TBMB,FLAG    VALDTE,CMS80

       EXECUTE SECOND.PROGRAM.STAGE            PS2    EQU $        INSERT CODE

     ELSE
     END.IF

     IF STOP = TRUE                            CMS80  TBMB,FLAG    STOP,CMS120

       SET  STOP = FALSE                                OBMM,FLAG    STOP
                                                        BRU          CMS130
     ELSE

                                               CMS120 EQU $
       EXECUTE THIRD.PROGRAM.STAGE             PS3    EQU $        INSERT CODE

     END.IF
   END.IF
 END.DO                                        CMS130 TBMB,FLAG    ENDRUN,CMS20

 EXECUTE TERMINATION.PROGRAM                   CLOSE  EQU $        INSERT CODE

FINIS
```

TITLE	DATE	INT'S
PREPARED		
CHECKED		
APPROVED		

Fig. 2. Program design language with interleaved code

```
                                                    SSD-DMC-5084-OP
                                                    MODULE NAME     CMSP1
                                                    DATE          7/15/76
                                                    REV    A      9/15/76
PROGRAM  FIRST.PROGRAM.STAGE

    SET INITIAL.STAGE = NOT COMPLETED                       OBMM,FLAG   PRERTD

    ESTABLISH INTERRUPT.SUPPORT.PROCESSOR.1.TASK
                                                            REX,EST
                                                            DFC         0
                                                            DFC         @IP1
                                                            DFC         80
                                                            DFC         @LM
                                                            STM,2       IP1RCB

    ESTABLISH BACKGROUND.REAL.TIME.1.TASK
                                                            REX,EST
                                                            DFC         0
                                                            DFC         @BR1
                                                            DFC         90
                                                            DFC         @LM
                                                            STM,2       BR1RCB

    ACTIVATE INTERRUPT.PROCESSOR.1.TASK
                                                            REX,ACT
                                                            DFC         0
                                                            DFC         @IP1
                                                            DFC         0,0

    DO.UNTIL INITIAL.STAGE = COMPLETED              PS130   EQU $
                                                            TBMB,FLAG   PRERTD,PS150
                                                            HOP,PS180

        RELINQUISH                                  PS150   REX,RLNQ

    END.DO                                                  BRU         PS130

    DE-ESTABLISH  BACKGROUND.REAL.TIME.1.TASK
                                                    PS180   REX,DEEST
                                                            DFC         0
                                                            DFC         @BR1
                                                            ZRR,1
                                                            STM,1       BR1RCB

    DE-ESTABLISH  INTERRUPT.PROCESSOR.1.TASK
                                                            REX,DEEST
                                                            DFC         0
                                                            DFC         @IP1
                                                            ZRR,1
                                                            STM,1       IP1RCB

FINIS
```

TITLE	DATE	INT'S
PREPARED		
CHECKED		
APPROVED		

Fig. 3. Parallel program design language and code